
Investigating galaxies in and behind Galaxy Clusters using Strong Gravitational Lensing

Anna Monna



Investigating galaxies in and behind Galaxy Clusters using Strong Gravitational Lensing

Anna Monna

Dissertation der Fakultät für Physik

Dissertation of the Faculty of Physics

der Ludwig-Maximilians-Universität München

at the Ludwig Maximilian University of Munich

für den Grad des

for the degree of

Doctor rerum naturalium

vorgelegt von Anna Monna

presented by

Munich, December 2014

1st Evaluator: Prof. Dr. Ralf Bender

2nd Evaluator: Prof. Dr. Jochen Weller

Date of the oral exam: 24 Feb 2015

Zusammenfassung

Der Gravitationslinseneffekt ist eine einzigartige Technik, um die Verteilung von dunkler Materie in den Strukturen des Universums - von Galaxien, Galaxiengruppen und Galaxienhaufen bis hin zur großräumigen Struktur des Universums selbst - zu untersuchen. Dieser Effekt erlaubt es uns, die projizierte Massenverteilung von Objekten, die als Gravitationslinse wirken, zu kartographieren und so die Verteilung der andernfalls unsichtbaren dunklen Materie zu beleuchten. So lässt sich zum Beispiel die Massenverteilung in Galaxienhaufen - den größten virialisierten Strukturen im Universum - ausführlich erforschen. Der schwache Gravitationslinseneffekt untersucht die Massenverteilung in den Außenbezirken solcher Haufen, indem er die mittlere statistische Verformung vieler tausender Galaxien im Hintergrund des Haufens analysiert. Der starke Gravitationslinseneffekt hingegen ermöglicht es uns, die projizierte Massenverteilung sowie die von der Gravitationslinse erzielte Vergrößerung detailliert zu rekonstruieren. Außerdem können Galaxienhaufen Dank der Vergrößerung von Hintergrundgalaxien als Gravitationslinsenteleskope agieren, um so die Galaxienpopulation im frühen Universum zu erforschen.

Im ersten Teil meiner Arbeit benutze ich den CLASH und Frontier Fields Haufen RXC J2248, um Galaxien bei einer Rotverschiebung von $z \sim 6$ zu untersuchen. Bei dieser und höheren Rotverschiebungen erscheinen Galaxien als sogenannte "optische Dropout", da ihr Licht zu nahinfraroten Wellenlängen verschoben ist und sich von ihnen kein Fluss im UV- oder optischen Wellenlängenbereich beobachten lässt. Ich habe eine gelinste Galaxie bei $z \sim 6$ im Kern des Haufens RXC J2248 entdeckt, die als fünffach abgebildeter optischer "Dropout" in den 16 HST Filtern des CLASH surveys erscheint. Ich präsentiere eine detaillierte photometrische Analyse dieser "Dropout" um zu verifizieren, dass sie dieselben photometrischen Eigenschaften besitzen, d.h. dass es sich um multiple Abbildungen der gleichen Lichtquelle handelt. Außerdem führe ich eine Analyse des Galaxienhaufens mithilfe des starken Gravitationslinseneffekts durch, um zu zeigen, dass auch das Linsenmodell die Annahme einer fünffach gelinsten Quelle bei $z \sim 6$ unterstützt.

Im zweiten Teil meiner Arbeit nutze ich den starken Gravitationslinseneffekt im CLASH Galaxienhaufen Abell 383 um die Massenverteilung von Galaxien im Kern des Haufens zu untersuchen. Bekannte Skalierungsrelationen ermöglichen es uns, physikalische Eigenschaften der Galaxien, wie z.B. die stellare Geschwindigkeitsdispersion oder die Größe elliptischer Galaxien, mit ihrem beobachteten Lichtfluss in Verbindung zu bringen. Haufengalaxien werden jedoch von den Gezeitenkräften im Kern des Haufens beeinflusst. Das Ziel der vorliegenden Arbeit ist es, die Halo-Ausdehnung der Galaxien im Haufenkern zu messen um somit zu quantifizieren, wie viel Masse die Kernhaufengalaxien im Vergleich zu Feldgalaxien durch die Gezeitenkräfte verloren haben. Hierbei präsentiere ich einen neuen Ansatz zur Analyse des starken Gravitationslinseneffekts in Galaxienhaufen, bei dem die Geschwindigkeitsdispersion der Haufenmitglieder als zusätzliche Eingrenzung des Linsenmodells verwendet wird. Ich wende diese Methode auf A383 an, um den Massenanteil aus Galaxien von der glatteren Verteilung der dunklen Materie zu trennen und zu untersuchen, wie die Größe von Halos der dunklen Materie mit der Helligkeit der Haufengalaxien skaliert. Zudem rekonstruiere ich das Helligkeitsprofil der sogenannten "southern giant arcs" um die Eigenschaften einzelner nahe gelegener Galaxien besser einzugrenzen und um eventuelle Abweichungen von den für den Haufen gemessenen Skalierungsrelationen zu studieren.

Abstract

Gravitational Lensing is a unique technique to investigate the dark matter distribution of structures in the Universe, from galaxies, through galaxy groups, clusters, up to the large-scale structure. It allows us to map the total projected mass density of structures acting as lenses, and thus to shed light on the distribution and properties of the otherwise-invisible dark matter.

Clusters of galaxies are the largest virialized structures in the universe. Gravitational lensing analysis allows us to study their mass distribution in great detail. Weak lensing probes the mass distribution in the outskirts of clusters based on a statistical analysis of the shape distortion observed in hundreds of galaxies behind the cluster. Strong lensing, instead, allows us to reconstruct high resolution mass and magnification maps of the central region of the cluster. In addition, thanks to the lensing magnification of background sources, galaxy clusters act as *Gravitational Telescopes* and can be used to investigate the galaxy population of the early Universe at $z > 5$.

In the first part of my Thesis I use the CLASH and Frontier Fields cluster RXC J2248 to investigate sources at $z \sim 6$. At such and higher redshift galaxies appear as optical dropouts, since the light they emit is redshifted to NIR wavelengths and no flux is observed in the UV and optical filters. I discovered a $z \sim 6$ lensed galaxy in the core of RXC J2248 which appears as a quintuple lensed optical dropout in the 16 HST filters of the CLASH survey. I perform a detailed photometric analysis of these dropouts to verify that they present the same photometric properties and are actually multiple images of the same source. In addition, by performing the strong lensing analysis of the cluster core I verify that the lensing model supports the quintuple and $z \sim 6$ nature of this system.

In the second part of my Thesis I use strong gravitational analysis of the CLASH cluster A383 to probe the details of the mass distribution of galaxies in the cluster core. Well known luminosity scaling relations allow us to relate the physical properties as stellar velocity dispersion and size of the elliptical galaxies to their observed luminosity. However in clusters, galaxies suffer tidal stripping due to the interaction with other cluster members and the cluster dark matter halo. The goal of this work is to measure the galaxy halo sizes in a cluster core to quantify how much mass was stripped relative to field galaxies. Here I present a new approach to strong lensing analysis of clusters, in which I use measurements of cluster members' velocity dispersions as additional constraints in the lens modeling. I apply this analysis to Abell 383 to separate the galaxy mass content from the smooth dark matter mass component and investigate how the dark matter halo size scales with the galaxy luminosity in the cluster core. In addition I perform the surface brightness reconstruction of the southern giant arcs to improve constraints on close by individual galaxies and study possible deviations from the global scaling law measured for the cluster.

Contents

Zusammenfassung	vii
Abstract	ix
Contents	xii
1 Introduction	1
2 The ΛCDM Universe	7
2.1 Friedmann equations	8
2.1.1 Density and deceleration Parameters	9
2.2 Distances in cosmology	11
2.3 Structures in the Universe: Galaxies and Galaxy Clusters	12
2.3.1 Galaxies	15
2.3.2 Galaxy Clusters	15
3 Gravitational Lensing	21
3.1 Basics of Gravitational Lensing	22
3.2 Gravitational Lensing regimes	28
3.2.1 Strong Lensing	28
3.2.2 Weak Lensing	30
3.2.3 Microlensing	31
3.3 Parametrised Lens models	33
3.3.1 Point mass lens	33
3.3.2 Extended circularly symmetric lens	34
3.3.3 Singular Isothermal Sphere	35
3.3.4 The Nawarro, Frenk & White profile	37
3.3.5 PIEMD	38
3.3.6 dPIE	38
4 Strong Lensing analyses	41
4.1 Strong Lensing non-parametric analysis	41
4.2 Strong Lensing parametric analysis	42
4.2.1 Cluster Mass components and galaxy scaling relations	43

4.2.2	Multiple images	45
5	The CLASH Survey	47
5.1	The CLASH Cluster Sample	47
5.2	Dataset and Catalogs	48
5.3	The CLASH-VLT Spectroscopic Survey	53
6	CLASH: $z \sim 6$ young galaxy candidate quintuply lensed by the frontier field cluster RXC J2248.7-4431	55
6.1	RXC J2248.7-4431	56
6.2	Photometric Dataset	58
6.3	High- z dropouts: photometric selection	59
6.4	Quadruply lensed dropout: photometric evidence	62
6.4.1	Photometric redshift	63
6.4.2	Colour-colour diagrams	65
6.5	Quadruply lensed dropout: lensing evidence	65
6.5.1	Multiple images	68
6.5.2	Results	68
6.6	The central image	71
6.7	Physical properties	72
6.8	Summary and Conclusions	75
7	High-z galaxy selection in the CLASH survey	79
7.1	Spectroscopic confirmation of the quintuple lensed galaxy in RXC J2248 . . .	79
7.2	Stellar contaminants for $z \sim 6 - 8$ photometric candidates in the CLASH survey	82
8	Constraining the galaxy mass content in cluster cores	83
8.1	A383	84
8.2	Photometric and Spectroscopic Dataset	85
8.3	Cluster members	87
8.4	Strong Lensing recipe	89
8.4.1	Multiple images	90
8.5	Pointlike models	91
8.6	Surface Brightness reconstruction	99
8.7	Discussion and Conclusions	102
9	Summary and Conclusions	111
	Bibliography	126
A	SED Fitting Results for the $z \sim 6$ quintuple lensed galaxy in RXC J2248	127
	Publications	133
	Acknowledgments	135

Introduction

*Così tra questa Immensità s'annega il pensier mio:
e il naufragar m'è dolce in questo mare.*
(In this Immensity my mind is drowned:
and it's pleasant to be shipwrecked in such a sea.)

Giacomo Leopardi

Since thousands of years we have been looking through the sky wondering about the origin and properties of the Cosmos. Based on what we could observe with our eyes, several models have been proposed to describe the observed motion of extraterrestrial objects as the Sun, the stars and planets. The invention of the Telescope and its application to observe the sky in the XVII century, allowed us to resolve bodies in the Solar System, follow details of their motion and to establish their heliocentric configuration. Since then huge steps were done towards a better knowledge of our Universe, of the bodies which populate it, and the physics which governs it.

In the last decades observations have shown that our universe consists of only few percentage ($\sim 5\%$) of the matter that we can directly observe with our instruments, i.e. the baryonic matter. The rest of its content is associated with non-baryonic matter, called *dark matter* (here and after DM) ($\sim 22\%$) and to the energy which drives the observed accelerated expansion of the Universe ($\sim 73\%$), and is dubbed *dark energy* (e.g. see Komatsu et al., 2011). The existence of DM was probed through rotation curves of galaxies, which are flat in the outskirts, implying the need of another matter component in addition to the observed baryonic one (e.g. see Rubin & Ford, 1970). Also numerical simulations of galaxy clustering require DM to reproduce the observed large scale structure (LSS) of the Universe (see Springel et al., 2005).

Clusters of galaxies play a fundamental role to test cosmological models and structure formation, and to investigate the properties of DM. They are the most massive structures gravitationally bound and DM is their dominant mass component. Combining several independent techniques (X-ray, weak and strong lensing, stellar kinematics, etc.) is necessary to robustly constrain the DM density profile of galaxy clusters (see Sand et al., 2002, 2004; Newman

et al., 2011; Umetsu et al., 2012). While X-ray and kinematic analyses need to assume that clusters are in hydrostatic equilibrium, gravitational lensing requires no assumptions on the dynamical state of the clusters. This technique is unique to investigate the mass distribution of structures in the Universe, from galaxies, through groups and clusters of galaxies, up to the large scale structure (e.g., Schneider, 2003; Bartelmann, 2010; Kneib & Natarajan, 2011). The paths deflection of light passing through the potential of clusters is generated by the total mass of the object acting as lens, i.e. by the combined gravitational action of the baryonic and dark component. Strong and Weak lensing analyses probe the density profiles on different radial scales of galaxy clusters and allow to trace their dark matter distribution from the inner region ($r < 50$ kpc) up to several Mpc, respectively (e.g. see Newman et al., 2009; Zitrin et al., 2011). It allows also to investigate the small scale mass distribution associated with galaxies in clusters (e.g., see Eichner et al., 2013; Monna et al., 2014b) and in fields (Rusin et al., 2003; Brimiouille et al., 2013).

In the case of galaxy clusters acting as lenses, the cluster DM component is usually assumed to follow descriptions obtained from numerical simulations, such as an elliptical Navarro-Frank-White (NFW, Navarro et al. (1997)) halo or alike. The galaxy mass component of the cluster is given by all the cluster member masses which are typically modelled as power-laws, isothermal spheres or their variants. The combination of the baryonic and DM components yields the total projected surface mass density, which is the quantity probed in the lensing analysis. In that respect, it is difficult to properly separate the baryonic and DM galaxy components, as lensing probes only their joint contribution and degeneracies exist between the different parameters which could explain the same set of constraints. To infer the masses of the galaxies directly from the light, typically, luminosity-velocity-dispersion-mass scaling relations are used. Physical properties of elliptical galaxies are globally well described through luminosity relations which relate them to their observed luminosity both for galaxies in field and in clusters. The Fundamental Plane (see Bender et al., 1992; Dressler et al., 1987; Djorgovski & Davis, 1987; Faber et al., 1987) gives the relation between effective radius r_e , central stellar velocity dispersion (σ_0^*) and mean surface brightness I_e within r_e of elliptical galaxies. σ_0^* is related to the galaxy luminosity L through the Faber-Jackson relation ($L \propto \sigma_0^\alpha$) (Faber & Jackson 1976). However, it has been shown that bright galaxies, like the brightest cluster galaxies (BCGs), can deviate substantially from the scaling relation (see von der Linden et al., 2007; Postman et al., 2012b; Kormendy & Bender, 2013).

The central stellar velocity dispersion σ_0^* of galaxies is found to be a good estimator of the central velocity dispersion of their DM halo σ_0 . Indeed, independent measurements of the halo velocity dispersion σ_0 , e.g. from strong lensing (see Eichner et al., 2013), show a great agreement with photometric and spectroscopic measurements of σ_0^* .

The luminosity scaling relations are measured both for galaxies in clusters (e.g., see Newton et al., 2011; Eichner et al., 2013; Grillo et al., 2014) and in fields (e.g., see Brimiouille et al., 2013) using strong and weak lensing analyses, respectively. In Eichner et al. (2013) we analysed the halo properties of the galaxies in MACS1206.2-0847 by performing a detailed strong lensing analysis of the cluster. We broke the degeneracy between the halo velocity dispersion σ and size r_{tr} , improving the constraints on the $\sigma - r_{tr}$ relation through the surface brightness reconstruction of the giant arc in the core of the cluster. However, the large scatter in the Fundamental Plane (or, Faber-Jackson relation) inherently introduces modelling biases in lensing analyses which inevitably assume an analytic scaling relation for the M-L- σ planes. Actual velocity dispersion measurements of galaxies (typically, elliptical cluster members) al-

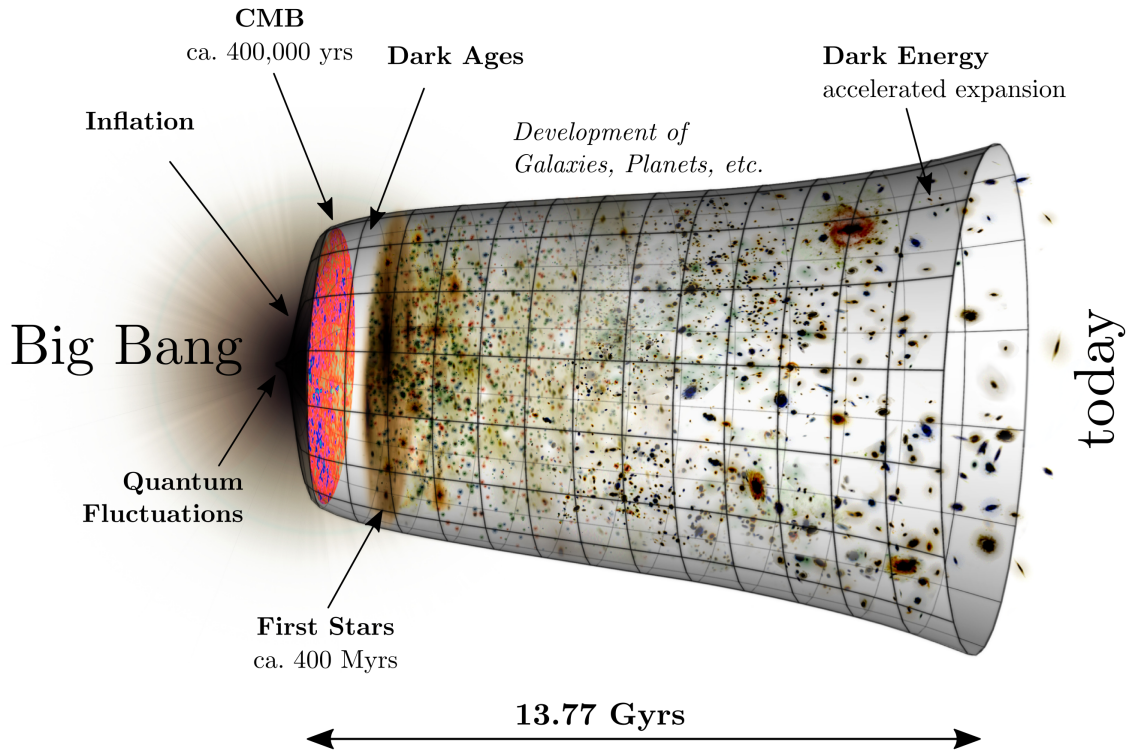


Figure 1.1: Diagram of the evolution of the Universe from the Big Bang explosion to the present epoch. Credit: NASA/WMAP Science Team (modified).

low a direct estimate of their enclosed mass on small scales, through the virial theorem that reduces to $\rho(r) = \frac{\sigma^2}{2\pi Gr}$ for an isothermal sphere, for example. At larger scales the density profiles have to deviate from an isothermal sphere, since the mass of the galaxy halo has to be finite. One introduces a truncation radius in the density profile, which describes at which scale the turnover from a $\rho \propto r^{-2}$ to $\rho \propto r^{-4}$ profile takes place. If galaxy halos are modelled in this way, and if velocity dispersions are measured, the halos are completely described up to their truncation parameter. These mass estimates can be input individually for each lens galaxy instead of applying an idealised analytic scaling relation. This will especially be significant for bright and massive cluster galaxies governing the lens, i.e. galaxies within, or close to, the critical curves, as these affect the lensing properties the most.

Clusters of galaxies acting as gravitational lenses provide also an efficient technique to investigate the Universe behind them. They act as gravitational telescopes and when the magnification is large enough, they can allow us to detect faint distant galaxies. Investigating the properties of the galaxies populating the high- z Universe is crucial to verify the evolutionary theory of the Universe.

According to the Λ -CDM model, after the Big Bang the Universe (composed of radiation, baryonic- and dark- matter) started an adiabatic expansion which caused its progressive cooling. At $z \sim 1000$ the temperature of the radiation was $T \approx 4000\text{K}$, allowing the atomic particles of the primordial plasma (protons, electrons and neutrons) to combine in atomic forms. The Universe became optically thin and this event is called *last scattering surface*,

since the radiation was not scattered and trapped by the primordial plasma anymore, but was free to travel through the Universe (see Miralda-Escudé, 2003; Loeb et al., 2008). The Cosmic Microwave Background (CMB) radiation is the observable fossil of this event. The gravitational evolution of the Universe proceeded with the formation of the first structures as a consequence of the gravitational instability of primordial matter inhomogeneities. The so-called *Dark Age* started, which is a long epoch in which structures grew hierarchically to form galaxies and clusters. The first stars were born in these structures as light-elements-massive stars emitting big amount of Ultra-Violet (UV) radiation. The UV radiation ionized the inter galactic medium (IGM) composed of neutral hydrogen (HI), generating bubbles of ionized hydrogen (HII) around the stars. This process continued as long as there was HI to ionize. This epoch is called *Epoch of Reionization*, cosmological probes support that it started at $z \lesssim 20$ and ended at $z \sim 6$, when almost all the HI was ionized (see Barkana & Loeb, 2001; Miralda-Escudé, 2003). In Fig. 1.1 we show a diagram of the evolution of the Universe from the Big Bang explosion to present day.

Gravitational Telescopes allow us to investigate galaxies at redshift $z > 5$, thus to shed light on the Reionization Epoch and on the galaxies that caused the reionization of the Universe. Blank field surveys have been used to probe the luminosity function at high redshift and investigate the properties of the galaxies populating at these epochs (e.g. Bouwens et al., 2004, 2014). The advantage of using Gravitational Telescopes is that they enable us to investigate not only the brightest galaxies, but also fainter ones thanks to the magnification induced by lensing. Up to date several lensed galaxies at $z > 5$ are identified in galaxy cluster fields, e.g., a galaxy at $z \sim 6$ lensed into 3 images in A383 (Richard et al., 2011) (spectroscopically confirmed), a lensed galaxy at $z \sim 6.56$ in A370 (Hu et al., 2002) (spectroscopically confirmed), seven lensed galaxies at $z \sim 7$ in A1703 (Bradley et al., 2012) (one of which spectroscopically confirmed), a quadruply lensed galaxy at $z \sim 6.2$ in the field of MACS0329 (Zitrin et al., 2012b), a triply lensed galaxy at $z \sim 7$ in A2218 (Kneib et al., 2004), a highly magnified galaxy at $z \sim 9.6$ (Zheng et al., 2012) in MACS1149 and a triply lensed galaxy at $z \sim 11$ in MACS0647 (Coe et al., 2012). The last two sources are the highest redshift lensed candidates detected to date, and were discovered within the Cluster Lensing And Supernovae with Hubble survey (see Cap. 5). A large sample of single and multiply lensed high- z candidate galaxies identified in the CLASH survey is described and analysed in Bradley et al. (2014).

In this Thesis I present the strong lensing analyses of two galaxy clusters of the CLASH survey, RXJ2248 and A383. I use galaxy clusters to investigate $z > 5$ galaxies lensed in their core, as well as to constrain the properties of the galaxies which belong to the lensing cluster itself. I combine detailed photometric and strong lensing analyses to carry out these analyses and also spectroscopic information when available.

This thesis is organized as follows. In Chapter 2 I introduce the cosmological scenario. In Chapter 3 I provide the basic concepts and equations of Gravitational Lensing and in Chapter 4 I describe the strong lensing analyses used to reconstruct the mass distribution of structures in the Universe and to investigate the high- z galaxies.

In Chapter 5 I introduce the CLASH survey and provide a description of the datasets I use. In Chapter 6 I present a quintuply lensed candidate young galaxy at $z \sim 6$ in the core of RXJ2248, and carry out a detailed photometric and lensing analysis to support the nature of this galaxy and to investigate its properties.

In Chapter 7 I present the spectroscopic confirmation of the quintuple lensed $z \sim 6$ galaxy

analysed in Chapter 6 and my contributions to the analysis of other high- z lensed galaxies identified in the CLASH datasets. In Chapter 8 I focus on using strong lensing analyses of the galaxy cluster A383. I use for the first time measurements of cluster members stellar velocity dispersion to fix the central density profile of cluster members and investigate the impact they have on the mass modelling. The aim of of this analysis it to improve the constraints of the galaxy mass content in the cluster core (thus on the galaxy scaling relation in the cluster), and as a consequence on the smooth dark halo as well.

In Chapter 9 I provide a summary of our analyses and conclusions.

Chapter 2

The Λ CDM Universe

The Λ -Cold Dark Matter (Λ CDM) cosmological model provides the best description of the observed Universe, which is in agreement with a large set of astronomical observations. It predicts the observed CMB anisotropy and provides a good fit of its power spectrum (Hinshaw et al., 2009; Reid et al., 2010; Komatsu et al., 2011). It reproduces the observed large scale structure and the structures clustering (Springel et al., 2005; Coil, 2013), as well as the cluster mass functions from X-ray (Mantz et al., 2010) and Strong and Weak Lensing observations (Suyu et al., 2010; Schrabback et al., 2010). It is also consistent with analysis from Supernovae Type Ia and distances measurements (Kessler et al., 2009; Riess et al., 2009b,a).

This model assumes the existence of a cosmological constant Λ , which describes the energy content of the Universe, explaining the observed accelerated expansion of the Universe. It also requires a dark matter (DM) component for the Universe matter constituents, in addition to the baryonic matter (i.e., electrons, protons and neutrons). Numerical simulations of the formation and evolution of cosmic structures support a 'cold' and 'collisionless' nature for the DM. The DM particles interact only through gravitational interaction and have small kinetic energy $v_{DM} \ll c$, thus are considered 'cold'.

The Λ CDM model assumes that the Universe is homogeneous and isotropic on sufficiently large scales and that there are no privileged positions in the Universe. This assumption is called *Cosmological Principle* (e.g., see Wu et al., 1999; Ryden, 2003).

The Universe is also in expansion, as it is proved by the Hubble flow (Hubble, 1929). The relative velocity v and proper distance d of each pair of galaxies satisfy the Hubble law

$$v = H_0 d \quad (2.1)$$

where H_0 is called the *Hubble parameter* at the present epoch.

An expanding, homogeneous and isotropic Universe is described by the Friedmann-Robertson-Walker (FRW) metric (Peebles, 1993; Weinberg, 2008):

$$ds^2 = dt^2 - a^2(t) \left[\frac{dr^2}{1 - kr^2} + r^2 d\Omega^2 \right] \quad (2.2)$$

where t is the time interval between two events, r and $\Omega = \sqrt{d\theta^2 + \sin^2\theta d\phi^2}$ are the comoving coordinates, $a(t)$ is the scale factor at time t and k is the curvature of the Universe and can assume the values (-1, 0, 1). The units are chosen so that the velocity of light is

unity. For a flat ($k=0$) and not expanding ($a(t)=1$) Universe, Eq. 2.2 gives the Minkowski metric of special relativity with $ds^2 = dt^2 - (dr^2 + r^2d\Omega^2)$.

The scale factor $a(t)$ is the function which describes the Universe's expansion and is defined such that at present day, $t_0 = 0$, it is $a(t_0) = a_0 = 1$. The proper distance $d(r, t)$ of a galaxy at the radial coordinate r and time t is given by (Weinberg, 2008)

$$d(r, t) = a(t) \int_0^r \frac{dr}{\sqrt{1 - kr^2}} = a(t) \begin{cases} \sinh^{-1}r & \text{for } k = -1 \\ r & \text{for } k = 0 \\ \sin^{-1}r & \text{for } k = 1 \end{cases} \quad (2.3)$$

thus it increases with $a(t)$. Since there are no privileged positions in the Universe, in general the proper distance of two objects increases with $a(t)$ as well. The velocity of the expansion of the proper distance $d(r, t)$ is then

$$\dot{d}(r, t) = \dot{a}(t) \int_0^r \frac{dr}{\sqrt{1 - kr^2}} = \dot{a}(t) \frac{d(t)}{a(t)} = H(t)d(t) \quad (2.4)$$

where \dot{d} and \dot{a} are the time derivatives of the proper distance and the scale factor, respectively. $H(t)$ is the Hubble parameter at the time t and, in terms of the scale factor, is written as

$$H(t) = \frac{\dot{a}}{a}. \quad (2.5)$$

The Hubble parameter $H(t)$ gives the expansion rate of the Universe at time t .

Due to the expansion of the Universe, galaxies appear to be in a recession motion with respect to us. As a consequence of the expansion, the radiation emitted by a galaxy at a certain wavelength is stretched while travelling through the Universe and its wavelength is shifted to larger values (i.e. to redder λ , thus is *redshifted*). The redshift suffered by the light is directly observable using the displacement of the wavelength λ of absorption and emission lines in the spectra of the light. The cosmological *redshift* is defined as (e.g., see Binney & Merrifield, 1998)

$$z \equiv \frac{\Delta\lambda}{\lambda} = \frac{\lambda_0 - \lambda}{\lambda} \quad (2.6)$$

where λ is the wavelength of the radiation when is emitted by the galaxy (i.e. the *restframe* wavelength) and λ_0 is the observed wavelength.

Being $\lambda = a(t)\lambda_0$, the redshift z can be expressed in terms of the scale factor $a(t)$, indeed we get

$$z = \frac{1}{a(t)} - 1. \quad (2.7)$$

The redshift of a galaxy depends directly on the recession velocity of the galaxy itself, which, given the Hubble law, is directly related to the distance of the galaxy from us. Thus redshifts are used as measure of distances.

2.1 Friedmann equations

The dynamics of the Universe is completely described by the Einstein field equations derived in the Theory of General Relativity (Einstein, 1916, 1917)

$$G_{\alpha\beta} = \frac{8\pi G}{c^4} T_{\alpha\beta} + \Lambda g_{\alpha\beta}, \quad (2.8)$$

where $G_{\alpha\beta}$ is a function of the metric and is called *Einstein tensor*, G is the gravitational constant, $T_{\alpha\beta}$ is the energy-momentum tensor which is the source of the gravitational field, Λ is the cosmological constant needed to account for the observed accelerated expansion of the Universe, and $g_{\alpha\beta}$ is the metric tensor.

Including the FRW metric in the Einstein field equations we obtain the Friedmann equations (Friedmann, 1922) which describe the evolution of the scale factor $a(t)$ as a function of the mass and radiation density ρ and pressure p of the Universe (Peebles, 1993)

$$\frac{\ddot{a}}{a} = -\frac{4\pi G}{3}(\rho + 3p) + \frac{\Lambda}{3} \quad (2.9)$$

$$\left(\frac{\dot{a}}{a}\right)^2 = \frac{8\pi G}{3}\rho + \frac{k}{a^2} - \frac{\Lambda}{3}. \quad (2.10)$$

Combining Eq. 2.9 and Eq. 2.10 and using the mass-energy conservation through the Bianchi identities, $\nabla_\alpha T^{\alpha\beta} = 0$, we get

$$\frac{d\rho}{dt} + \frac{\dot{a}}{a} \left(3\rho + \frac{3p}{c^2}\right) = 0. \quad (2.11)$$

When we assume an equation of state w of the Universe, which gives the relation between the matter density ρ and the pressure p , Eq. 2.9, 2.10 and 2.11 are the cosmological equations that describe the dynamic and state of the Universe.

2.1.1 Density and deceleration Parameters

If we consider a flat Universe ($k = 0$) with $\Lambda = 0$, the second Friedmann equation (Eq. 2.9) reads

$$H^2 = \frac{8\pi G}{3}\rho. \quad (2.12)$$

We can define the critical density as (Weinberg, 2008)

$$\rho_c = \frac{3H^2}{8\pi G} \quad (2.13)$$

which gives the present day average density of the Universe for $\Lambda = 0$, and is $\rho_c \approx 10^{-29} \text{g/cm}^3$. The ratio between the density $\rho(t)$ of the Universe and the critical density gives the cosmological density parameter $\Omega(t)$

$$\Omega_m(t) = \frac{\rho(t)}{\rho_c}. \quad (2.14)$$

Rearranging Eq. 2.10 we get

$$\frac{8\pi G}{3H^2}\rho + \frac{\Lambda c^2}{3H^2} - \frac{kc^2}{a^2 H^2} = 1 \quad \implies \quad \Omega_m + \Omega_\Lambda + \Omega_k = \Omega = 1 \quad (2.15)$$

where Ω is the density parameter, $\Omega_m = \rho/\rho_c$ is the matter density, $\Omega_\Lambda = \Lambda c^2/(3H^2)$ is the cosmological constant density and $\Omega_k = kc^2/(a^2 H^2)$ is the spatial curvature density. The matter density parameter includes the baryonic, dark matter and radiation densities, $\Omega_m = \Omega_b + \Omega_{DM} + \Omega_R$. The baryonic content of the Universe is a very small fraction ($\sim 4\%$)

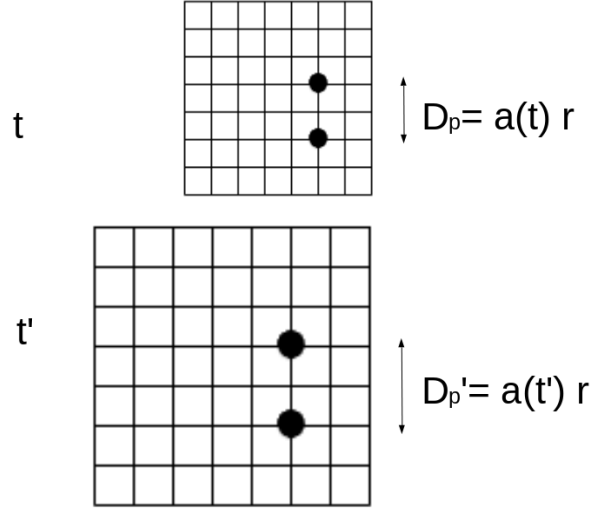


Figure 2.1: Example of proper and comoving distance at two different times t and t' for an expanding Universe with scale factor $a(t)$. The proper distance D_p between two objects increases as the Universe expands while the comoving distance r is constant.

of the total density of the Universe, while the DM content is $\sim 22\%$. The density component associated with the cosmological constant Λ contributes the most to Ω , being $\sim 70\%$ of the density parameter (see Komatsu et al., 2011).

The ratio of the first and second Friedmann equations (Eq.2.9,2.10) defines the *deceleration parameter* q (Peebles, 1993)

$$q \equiv -\frac{\ddot{a}a}{\dot{a}^2} = \frac{\Omega_m}{2} - \Omega_\Lambda. \quad (2.16)$$

Its name is due to historical reasons, since when it was introduced the Universe was thought to be in a deceleration phase. Through Supernovae Type Ia analyses q can be measured and such analyses confirmed that the Universe is in an accelerated expansion, i.e. $q < 0$ (e.g., see Riess et al., 1998).

Since decades the measurements of the cosmological parameters have been of great interest for the scientific community. The analysis of the the CMB anisotropies is sensitive to the parameters of the Universe. The most recent constraints on the cosmological parameters are resulting from long and expensive spaced-based surveys aimed to measure the CMB anisotropies, the Wilkinson Microwave Anisotropy Probe (WMAP) (Komatsu et al., 2014) and the *Planck* (Planck Collaboration et al., 2013) space mission. Combining the measurements of these two surveys, it results that our Universe is flat, in an accelerated expansion and its energy-mass content is dominated by an unknown *dark* component. According to WMAP and *Planck* measurements, the present day value for the Hubble parameters is $H_0 = 67.3 \pm 1.2 \text{ km s}^{-1}\text{Mpc}^{-1}$, and the density parameters are $\Omega_m = 0.315_{0.018}^{0.016}$ and $\Omega_\Lambda = 0.685_{0.016}^{0.018}$ (Planck Collaboration et al., 2013; Komatsu et al., 2014).

In the work presented in this thesis, we assume a standard cosmological Λ -CDM model with flat spatial geometry, with $H_0 = 70 \text{ km s}^{-1}\text{Mpc}^{-1}$, $\Omega_m = 0.3$ and $\Omega_\Lambda = 0.7$.

2.2 Distances in cosmology

In this section we provide the main distances defined and used in Cosmology (e.g., see Peebles, 1993; Weinberg, 2008). We will refer to the distance of galaxies, but they apply to all the objects in the Universe. Let us first define the dimensionless Hubble parameter $E(z)$, which will be useful to define the cosmological distances. Combining the first Friedmann equation Eq. 2.9 with Eq. 2.15 we get

$$H(t)^2 = H_0^2 \left[\frac{\Omega_m}{a^3} + \frac{\Omega_k}{a^2} + \Omega_\Lambda \right] \quad (2.17)$$

and in terms of redshift (see Eq. 2.7)

$$H(z)^2 = H_0^2 \left[\Omega_m(1+z)^3 + \Omega_k(1+z)^2 + \Omega_\Lambda \right]. \quad (2.18)$$

We can define the dimensionless Hubble parameter (Peebles, 1993; Peebles & Ratra, 2003)

$$E(z) = \sqrt{\Omega_m(1+z)^3 + \Omega_k(1+z)^2 + \Omega_\Lambda} \quad (2.19)$$

and can write

$$H(z)^2 = H_0^2 E(z). \quad (2.20)$$

Let us now consider two galaxies and see how we can define and measure their relative distance. The **comoving distance** between two galaxies at redshift z_1 and z_2 is defined as (Peebles, 1993)

$$D_c(z_1, z_2) = \frac{c}{H_0} \int_{z_1}^{z_2} \frac{dz'}{E(z')} \quad (2.21)$$

and it is constant as the Universe expands (see Fig. 2.1).

The **proper distance** of the two galaxies at the time t is defined as

$$D_p \equiv a(t) \int_0^r dr' = a(t)r. \quad (2.22)$$

Here r represents the comoving distance, which is constant with time, thus the proper distance changes as the Universe expands (see Fig. 2.1).

The **angular diameter** distance of a galaxy of intrinsic size l which subtends an angle α on the sky is defined as the ratio of l and α (Peebles, 1993). In an Euclidean space, from trigonometric considerations, the distance D of a galaxy is given by

$$D = \frac{l}{\tan \alpha} \approx \frac{l}{\alpha}, \quad (2.23)$$

where the right side equation holds for small angles ($\alpha \ll 1$). In a curved space ($k \neq 0$) the above relation is not always verified, but we can still define the angular diameter distance D_a as

$$D_a \equiv \frac{l}{\alpha}. \quad (2.24)$$

In terms of the comoving distance, it can be written as (Peebles, 1993)

$$D_a(z) = \frac{D_c(z)}{1+z} = \frac{c}{H_0(1+z)} \int_0^z \frac{dz'}{E(z')}. \quad (2.25)$$

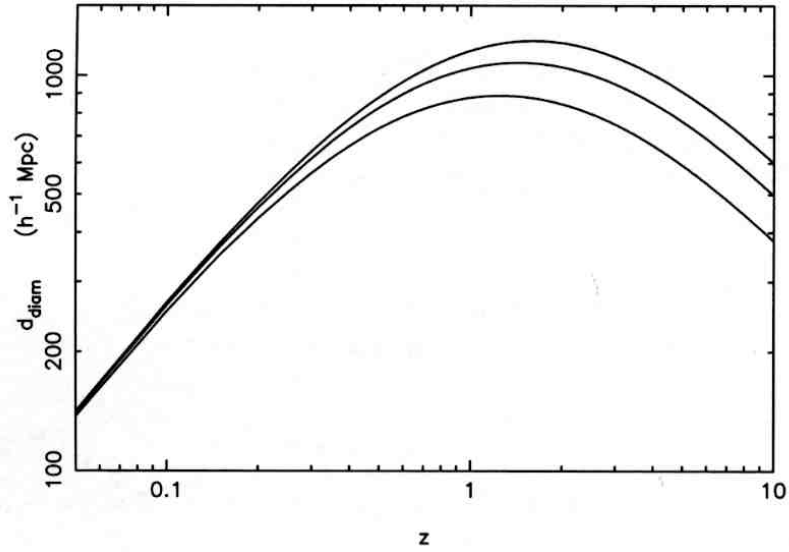


Figure 2.2: Angular diameter distance as a function of the redshift z for a flat Universe with cosmological constant Λ . From top to bottom they are shown the case of $\Omega_0 = 0.3, 0.5$ and 1 respectively. The angular diameter distance increases with redshift, it reaches a maximum value (which depends on the value of the cosmological parameters assumed) and then it decreases as z increases (figure from Liddle (2003)).

As one can see in Fig. 2.2, the angular diameter distance D_a first increases monotonically with redshift, it reaches a maximum value, which depends on the assumed cosmology, and then it starts decreasing (e.g. see Liddle, 2003). It is worth to note that the angular distances are not additive.

The angular diameter distances are the cosmological distances used in Gravitational Lensing theory, see Chapter 3.

Another distance widely used in Cosmology is the **Luminosity distance** defined by the luminosity of sources in the Universe. Let us consider a galaxy with intrinsic luminosity L . The observed flux f that we measure on Earth can be written as (Peebles, 1993)

$$f = \frac{L}{4\pi D_L^2}, \quad (2.26)$$

where D_L is the distance travelled by the light from the source to us. Thus the *luminosity distance* D_L is defined as

$$D_L = \sqrt{\frac{L}{4\pi f}}. \quad (2.27)$$

In Fig. 2.3 we show a comparison between the distances defined above as a function of the redshift. At small redshift the angular diameter, luminosity and comoving distances are very similar, and they start to differ at $z > 0.1$.

2.3 Structures in the Universe: Galaxies and Galaxy Clusters

The *Cosmological Principle* is based on the assumption that the Universe is isotropic and homogeneous on large scales, and it is satisfied on scales larger than 300 Mpc (Wu et al.,

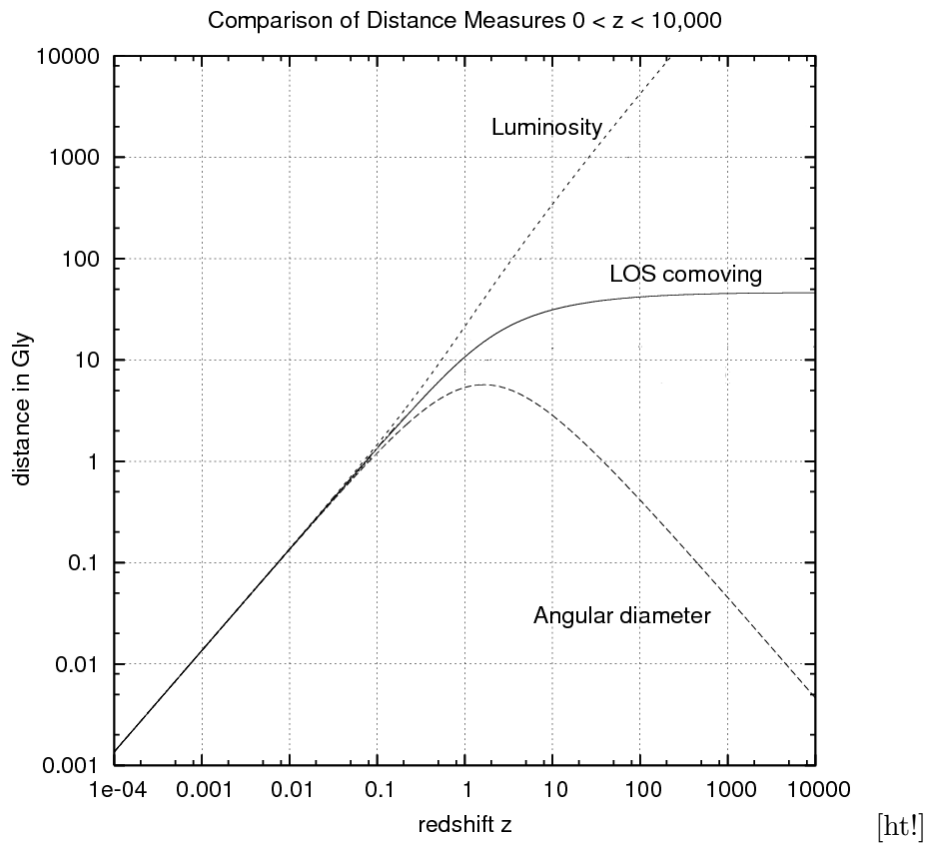


Figure 2.3: Comparison of the luminosity, comoving and angular diameter distances as a function of redshift. The assumed cosmology is $H_0 = 72 \text{ km s}^{-1} \text{ Mpc}^{-1}$, $\Omega_\Lambda = 0.732$ and $\Omega_m = 0.266$. At small redshift the three type of distances agrees with each others, and start to differ at $z > 0.1$. Figure from [http://en.wikipedia.org/wiki/Distance_measures_\(cosmology\)](http://en.wikipedia.org/wiki/Distance_measures_(cosmology)), modified.

1999). On small scales, the Universe appears not isotropic and homogeneous anymore, and it shows filaments and structures of DM and baryonic matter. In Fig. 2.4 we show the mass distribution of the Universe on different scales as it is predicted from the *Millennium* simulation¹ (Boylan-Kolchin et al., 2009). Most of the structures formed in the Universe reside in matter filaments, and the Λ CDM model reproduces their formation, evolution and distribution (e.g., see Springel et al., 2005; Boylan-Kolchin et al., 2009).

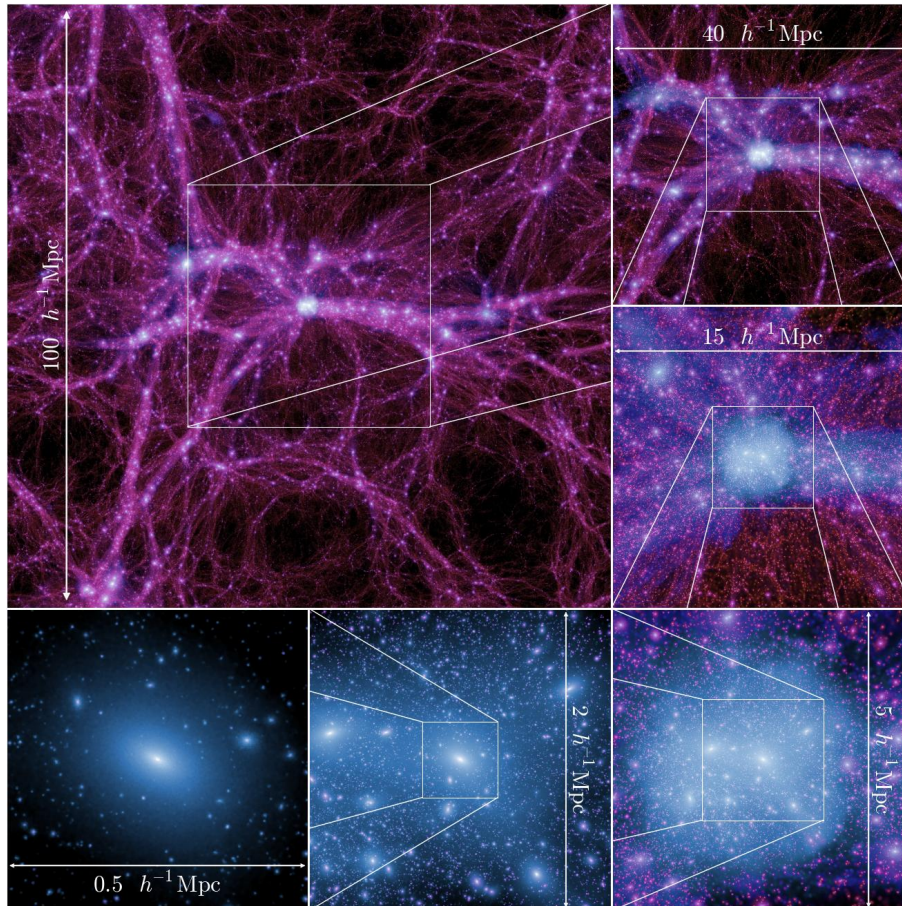


Figure 2.4: Matter distribution of structures in the Universe as predicted from the Millennium simulations on different physical scales. The simulation reproduce the mass distribution of the Universe at $z = 0$ in a volume with 100 Mpc side. Each panel is centered on the largest cluster and provide zoomed scale of the previous panel, starting from the largest scale of 100 Mpc (upper panel on the left) up to a scale of 0.5 Mpc (lower panel on the left). The structures of the Universe distribute along the mass filaments and the panels with larger scales clearly show the cosmic web of filaments and void. On small scales we can identify cluster of galaxies and the individual galaxies which reside in the cluster itself (figure from Boylan-Kolchin et al. (2009)).

¹<http://www.mpa-garching.mpg.de/galform/millennium-II/>

2.3.1 Galaxies

Galaxies are composed of dark matter and billions of stars and have masses between $10^8 - 10^{12} M_{\odot}$. In 1936 Hubble (Hubble, 1936) proposed a morphological classification of the galaxies based on their observed structures, which is commonly used today. They are divided in four main classes, depending on whether they appear as smooth elliptical galaxies (classified as *Ellipticals*, E), if they have a bulge and a disk (classified as *Lenticulars*, $S0$), or whether they have substructures like arms (*Spiral galaxies*, S) and bars (*Spiral barred*, SB) or if they show irregular structures (*Irregular galaxies*, Irr) (e.g., see Binney & Merrifield, 1998). This classification is known as Hubble sequence (or Hubble tuning fork) and is shown in Fig. 2.5. It was thought to be representative of the evolutionary sequence of the galaxies, so the ellipticals, lying on the left side of this sequence were called *early type* galaxies (ETGs), while those on the right side were referred to as *late type* galaxies (LTGs). Although this evolutionary interpretation of the Hubble sequence is completely discredited, the *early-late* type nomenclature is still used. Thus, according to their position along the Hubble tuning fork, ellipticals and lenticulars are also defined as *early type* galaxies, while the spirals and irregulars are also called *late type* galaxies.

Analyses of the luminosity profiles of galaxies showed that galaxies satisfy empirical laws which relate their physical properties to their luminosity, and which depend on the galaxy type. The Fundamental Plane (see Bender et al., 1992; Dressler et al., 1987; Djorgovski & Davis, 1987; Faber et al., 1987) is an empirical law which relate the luminosity L_e , central velocity dispersion σ_0 and mean surface brightness I_e of elliptical galaxies as

$$L_e \propto \sigma_0^{\alpha} I_e^{\beta} \quad (2.28)$$

where L_e and I_e are the luminosity and the mean surface brightness interior the effective radius R_e , which is the radius containing half of the total light of the galaxy. In particular the Faber-Jacksons (Faber & Jackson, 1976) relation relate the luminosity of elliptical galaxies to the power to the four of their central stellar velocity dispersion σ_0

$$L_e \propto \sigma_0^4. \quad (2.29)$$

A similar relation applies to spiral galaxies, which are found to follow the Tully-Fischer relation (Tully & Fisher, 1977), which relate the luminosity of the galaxy to its rotational velocity as follow

$$L \propto v_{rot}^4. \quad (2.30)$$

2.3.2 Galaxy Clusters

Galaxies are distributed in fields, groups and clusters and their morphological and dynamical properties are affected by the environment around them (e.g., see Dressler, 1980).

Underdense environments are dominated by late type galaxies, groups of galaxies host both late and early type ellipticals, while galaxy clusters are mainly populated by ellipticals and $S0$.

Groups of galaxies are defined when two up to tens of galaxies are gravitationally bound. Our galaxy, the Milky Way, is a spiral which reside in the galaxy group called *Local Group*. It counts ~ 40 galaxies, mainly dwarf ellipticals and spirals (Binney & Merrifield, 1998). Groups of galaxies show a large variety of dynamical states, and can be found as virialized objects,

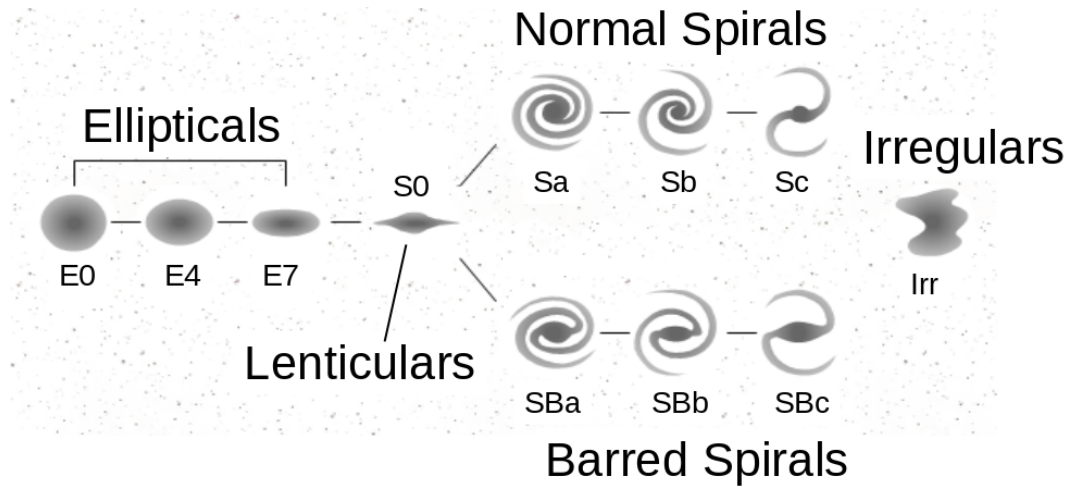


Figure 2.5: Diagram of the Hubble sequence. Figure from <https://conceptdraw.com/a2353c3/preview>, modified.

but also as recently formed or yet collapsing systems.

Clusters of galaxies are the largest bound and virialized systems of the Universe. They host hundreds of galaxies, mainly early-types. These constitute only 1-2% of the cluster's total mass. The main component is the smooth large scale dark matter halo which is $\sim 80\%$ of the cluster, and the left $\sim 18\%$ is associated with ionized intergalactic gas. The total masses of clusters ranges around $10^{14} - 10^{15} M_{\odot}$ (e.g., see van Paradijs & Bleeker, 1999; Murdin, 2001; Rosati et al., 2002). Fig. 2.6 shows an example of an optical image of a galaxy cluster. It is a HST color composite image of the galaxy cluster RXC J2248 from the Cluster Lensing and Supernovae survey with Hubble (CLASH, see Chap. 5 Postman et al., 2012a). The redder galaxies are the early type cluster members, while bluer source are foreground or background galaxies. The highly elongated sources are lenses images in the core of the cluster (see Fig. 6.1 in Chap. 6 for a zoom in the core of the cluster, where all the known multiple images are labelled). Fig. 2.7 shows the total surface mass distribution of the same cluster, as reconstructed from the joint weak and strong lensing analysis by Merten et al. (2014). Probing the mass distribution of galaxy clusters has a key role in testing cosmological models and structure formation (e.g., see Weller et al., 2002; Allen et al., 2004; Vikhlinin et al., 2009), as well as for understanding the properties of the dark matter (DM) (e.g. see Markevitch et al., 2004; Clowe et al., 2006). Cosmological simulations of formation and growth of structures, from the primordial density fluctuations up to the galaxy clusters at $z = 0$, show a great agreements with observations (e.g., see Meneghetti et al., 2014; Merten et al., 2014; Umetsu et al., 2014). In the Λ CDM scenario, the mass profile of galaxy clusters is on average described with the universal Navarro Frank and White (NFW) profile, where $\rho \propto r^{-\beta}$, with $\beta = -1$ on small scales and $\beta = -3$ on large scale (see Chapter 3.3.4 Navarro et al., 1997, 2010). The density in the core of clusters' halos depends on the density of the Universe at the epoch of the halo's formation. However measurements of the inner density slope have given different and sometimes inconsistent results (see Sand et al., 2004; Bartelmann & Meneghetti, 2004).

Different techniques are used to investigate the mass distribution of galaxy cluster, as X-ray, Weak- and Strong- Lensing, stellar kinematic analyses. Each of this technique relies on differ-

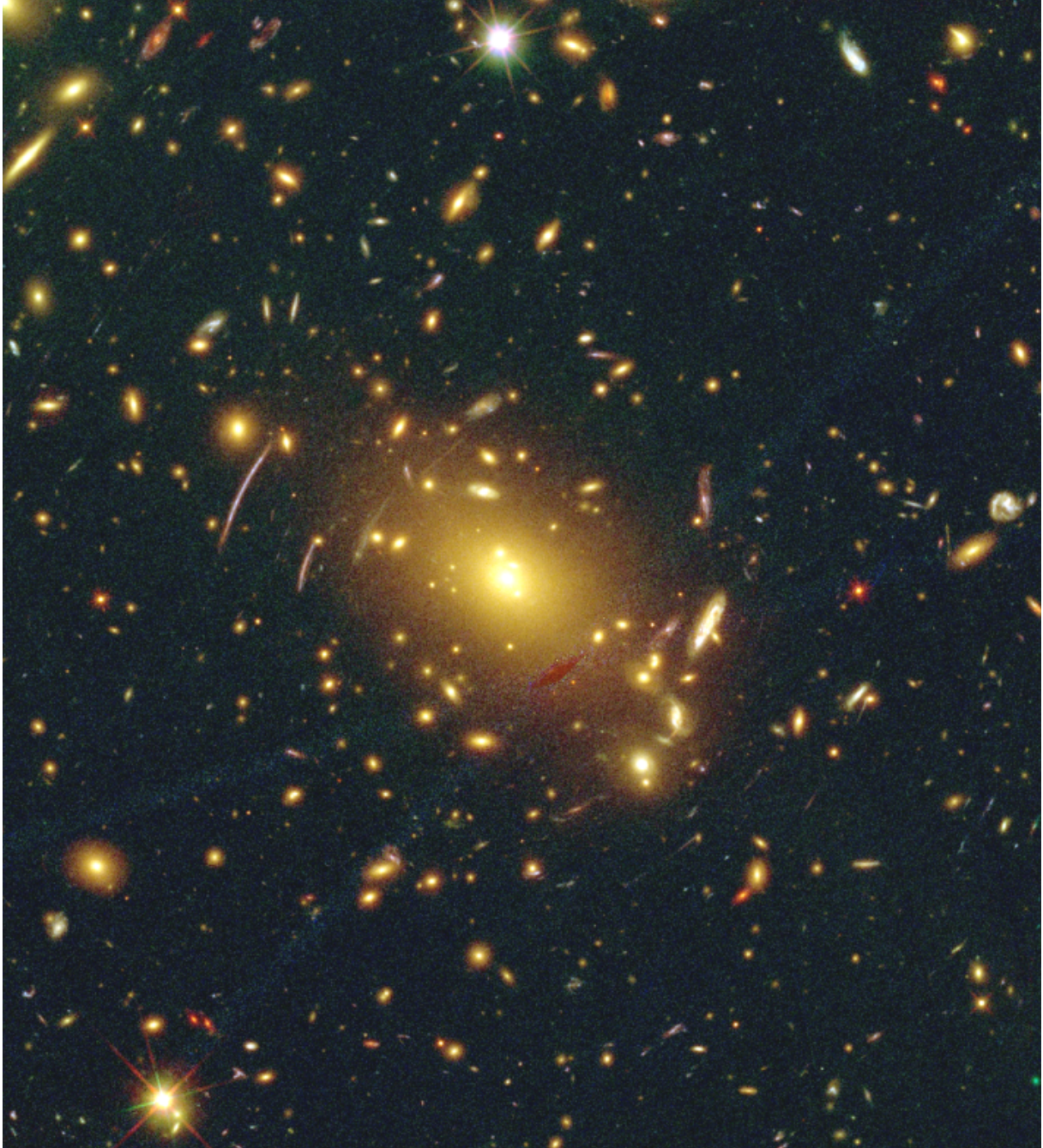


Figure 2.6: $2' \times 2'$ colour composite image of RXC J2248.7-4431 core, from the HST 16-band of the CLASH survey: Blue=F435w+F475w; Green=F606w+F625w+F775w+F814w+F850lp; Red=F105w+F110w+F140w+F160w.

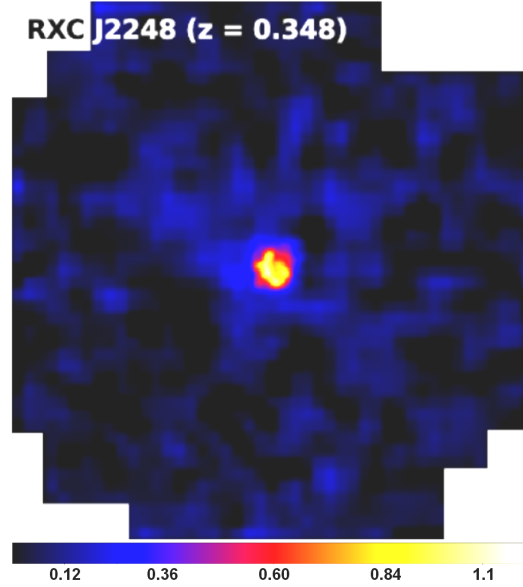


Figure 2.7: Surface density map of the total mass of RXC J2248.7-4431 covering a field of $25' \times 25'$ centred on the cluster (i.e. the SUBARU field, from Merten et al., 2014). The color scale give the lensing convergence k , which is the ratio of the surface density Σ and the critical density Σ_{cr} (see Chapter 3 for the definition of these quantities). The core of the cluster, shown in the optical color image Fig. 2.6, corresponds to the red-yellow colors.

ent physical phenomena which occur in clusters, as for example the thermal Bremsstrahlung of the intracluster gas, or the deflection of light passing through the cluster potential. Combining all these techniques is necessary to robustly constrain the DM density profile of galaxy clusters from the inner region up to large radial distances (~ 2 Mpc) (see Sand et al., 2002, 2004; Newman et al., 2009, 2011; Umetsu et al., 2012).

X-ray analyses measure the galaxy cluster mass distribution through the emission of the hot intracluster medium (ICM) (e.g., see Gioia et al., 1990; Pierre et al., 2004; Sarazin, 1988). The intracluster ionized gas has temperature of $10^7 - 10^8$ K and generates X-ray emission through thermal Bremsstrahlung, with peak at wavelengths of $0.1-100\text{\AA}$ (e.g., see Rybicki & Lightman, 1979). Assuming that the cluster is isothermal, in hydrostatic equilibrium and has spherical symmetry, the density profile of the gas can be described with the β -model (Sarazin, 1988)

$$\rho_{gas}(r) = \rho_0 \left[1 + \left(\frac{r}{r_c} \right)^2 \right]^{-\frac{3\beta}{2}} \quad (2.31)$$

where ρ_0 is the central density of the gas, r_c is a core radius and the parameter β is given by the ratio of the kinetic and thermal energy of the gas. The X-ray surface brightness profile of the cluster follows a similar profile

$$I_{Xray}(r) = I_0 \left[1 + \left(\frac{r}{r_c} \right)^2 \right]^{-3\beta + \frac{1}{2}}, \quad (2.32)$$

where I_0 is a normalization factor. β and r_c can be measured from the X-ray surface brightness

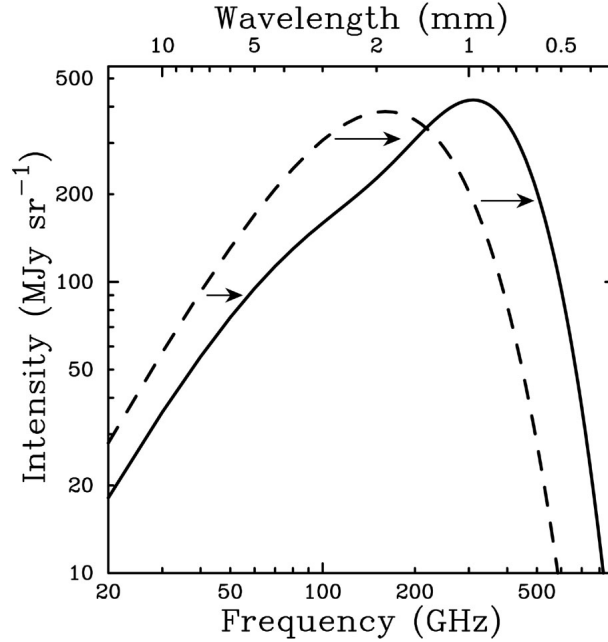


Figure 2.8: Comparison of the undistorted CMB spectrum (dashed line) and the distorted one (black line) which passed through a galaxy cluster. Photons with frequency lower than $\nu_{SZ} = 218$ GHz are boosted to higher frequencies due to the inverse Compton scatter with the hot free electrons of the intracluster gas. Figure from Carlstrom et al. (2002).

maps, and thus the gas density profile of the cluster can be estimated. Then the total mass of the cluster can be calculated as

$$M(< R) = -\frac{k_B T}{G\mu m_p} \left[\frac{d \ln \rho_{\text{gas}}}{d \ln r} + \frac{d \ln T}{d \ln r} \right] r, \quad (2.33)$$

where k_B is the Boltzmann constant, μ is the mean molecular weight of the gas, m_p is the mass of the proton and T is the gas temperature.

One disadvantage of the X-ray analyses is that they require assumptions on the thermal and hydrodynamic state and on the shape of the cluster which can introduce systematics in the mass measurements.

The thermal *Sunyaev-Zel'dovich Effect* (SZ Sunyaev & Zeldovich, 1972) offers another technique to measure the mass of galaxy clusters. The hot intracluster gas has free electrons which interact with the CMB radiation passing through the cluster. The interaction that takes place is the inverse Compton effect in which the free electrons scatter the CMB photons with low frequencies ν to higher frequencies (see Fig.2.8). The turn-over frequency is $\nu = 218$ GHz and it is peculiar for this effect and independent of the redshift of the cluster. Comparing the spectrum of the CMB passing through clusters with the CMB spectrum in the field nearby the clusters, allows to measure the SZ flux, which is directly proportional to the projected density of the intracluster gas along the line of sight (see Carlstrom et al., 2002). Thus, as for the X-ray analysis, the total mass distribution of the cluster can be estimated once the density profile of the intracluster gas is known. The advantage of using the SZ effect resides in its independence from the redshift, unlike the X-ray analysis, which is affected by the cosmological dimming. However only massive galaxy clusters can be investigated through

the SZ effect, since only those ones produce a strong enough signal that can be measured by present day instruments.

Differently to the X-ray and SZ analyses, which measure the intracluster gas mass in galaxy clusters, Gravitational Lensing analyses probe the total mass distribution of the cluster, i.e. both the dark and baryonic components, from the central region up to several Mpc from the cluster center. In the inner region ($r < 0.5$ Mpc), strong lensing analysis allow to trace in details the mass profile clusters' core using as constraints multiple images and giant arcs generated by the cluster. The mass distribution on larger scales (up to ~ 3 Mpc from the cluster cores) is measured with weak lensing analysis. This technique uses a statistical approach to estimate the weak distortion imprinted in the shape of hundreds of galaxies behind the cluster which have large angular separation from the cluster centre (See Chap.3 for more details on both techniques). Compared to other methods used to measure the mass of clusters, Gravitational Lensing needs no assumptions on the hydrodynamic state, which makes it a powerful tool to investigate the mass content of clusters. However lensing is sensitive to the total projected mass along the line of sight, thus structures which are between the observer, the cluster acting as lens and the lensed sources, can affect the lensing mass measurements.

Gravitational Lensing

The General Theory of Relativity developed by Albert Einstein in the beginning of the 20th century (see, Einstein, 1916; Weinberg, 1972) predicts that massive bodies, due to their gravitational mass, generate a distortion of the space-time in their nearby. Light traveling in the Universe, according to Fermat Principle, follows the extremal path in the space-time (called *geodesics*). When the space-time is distorted by a massive body, the light passing close to this body follows the geodesics which are curved according to the distortion imprinted in the space-time by the body itself. The deflection of light rays emitted by a source aligned or almost aligned with a massive body is a proof of the curvature of the space-time caused by gravitational masses. During the solar eclipse in May 1919, the deflection of a solar light ray grazing the surface of the Moon was measured (e.g., see Will, 2014). The deflection was due to the gravitational action of the Moon, which was in between the light source (the Sun) and the observer (on the Earth). The measured deflection angle was double the value predicted by Newton's theory, in agreement with the predictions from the General Relativity (Eddington, 1920). This was the first observational evidence of the General Relativity.

Nowadays, the deflection of light caused by the space-time distortion in presence of a massive body is commonly observed in astronomical images and it is fully described by the General Relativity. Such kind of events are referred to as Gravitational Lensing phenomena.

In this Chapter we summarise the physical and mathematical basics of Gravitational Lensing Theory.

Gravitational lensing is widely used in Cosmology, with different applications, as investigating structures in the Universe or constraining the cosmological parameters. It allows to probe the total mass distribution of objects acting as lens, thus it is used to constrain the dark matter distribution of the lenses. In addition, since lensing causes magnification of sources behind the lens, it allows to investigate properties of faint distant sources in details. Finally, gravitational lensing is used also to constrain the Cosmological Parameters adopted to describe the Universe, since, as we will see in the next sections, it directly depends on the assumed cosmology.

3.1 Basics of Gravitational Lensing

Gravitational lensing theory provides a complete analytic description of lensing phenomena at the first order using few simplifying hypotheses (e.g., see Schneider et al., 1992; Narayan & Bartelmann, 1996).

First of all, it assumes that **a weak stationary gravitational field** is associated with the lens. This means that the Newtonian potential of the lens is small ($\phi_{lens} \ll c^2$) and that the relative velocities of the components of the lensing system (i.e. source, lens and observer) are small with respect to the light velocity ($v_S, v_L, v_O \ll c$) (Narayan & Bartelmann, 1996).

Then it assumes that the physical size of the lens is much smaller than the distances between lens, source and observer. This allows to describe the 3D mass distribution of a lens with a 2D surface density distribution (i.e. the projection of the 3D mass along the line of sight). This assumption is called **thin lens approximation**.

These assumptions always hold in astrophysical lensing systems. For example, if we consider a source at redshift $z \sim 1$ lensed by a galaxy cluster at redshift $z \sim 0.3$, the distances between source, lens and observer are of the order of Gpc. However typical sizes of clusters are of order of Mpc, thus we can reasonably use a surface mass density to describe the lens. In addition, galaxy clusters have potentials $|\phi| \ll 10^{-4}c^2 \ll c^2$ (see Narayan & Bartelmann, 1996).

With these assumptions, we can describe the 4 dimensional space-time using the Minkowski metric and assume that locally, at the position of the lens, it is perturbed by the gravitational potential of the lens ϕ as follows (Schneider et al., 1992)

$$ds^2 = \left(1 + \frac{2\phi}{c^2}\right) c^2 dt^2 - \left(1 - \frac{2\phi}{c^2}\right) (d\vec{x})^2. \quad (3.1)$$

In Fig. 3.1 we present a typical lensing diagram, with a lens placed at the angular-diameter distance D_d and a source at the distance D_s . According to the thin screen approximation, the light emitted by the source S travels undisturbed until it reaches the lens plane. Here, due to the gravitational potential of the lens, the deflection of the light takes place and then the light continues its travel again undisturbed.

We note that the angular diameter distances are not additive, thus $D_d + D_{ds} \neq D_s$. However, being the physical sizes additive we can write $\vec{\theta}D_d + \hat{\alpha}D_{ds} = \vec{\beta}D_s$.

The real position of the source on the sky is given by the angular position $\vec{\beta}$. Due to the gravitational deflection, the observer sees the source at the apparent angular position $\vec{\theta}$. For small angles ($\vec{\theta}, \vec{\beta}, \hat{\alpha} \ll 1$), from geometry we get the following relation between deflection angle, real and observed position of the source (Narayan & Bartelmann, 1996):

$$\vec{\beta}D_s = \vec{\theta}D_s - \hat{\alpha}D_{ds}. \quad (3.2)$$

This is called *lens equation*, and is a mapping equation from the image plane to the source plane. The deflection angle $\hat{\alpha}$ contains all the information on the mass distribution of the lens since it is given by (see Narayan & Bartelmann, 1996)

$$\hat{\alpha}(\theta) = \frac{2}{c^2} \int \vec{\nabla}_{\perp} \Psi dz. \quad (3.3)$$

where Ψ is the gravitational potential of the lens and $\vec{\nabla}_{\perp} \Psi$ is the gradient of Ψ perpendicular to the light path. This relation is similar to the expression for the deflection of a light

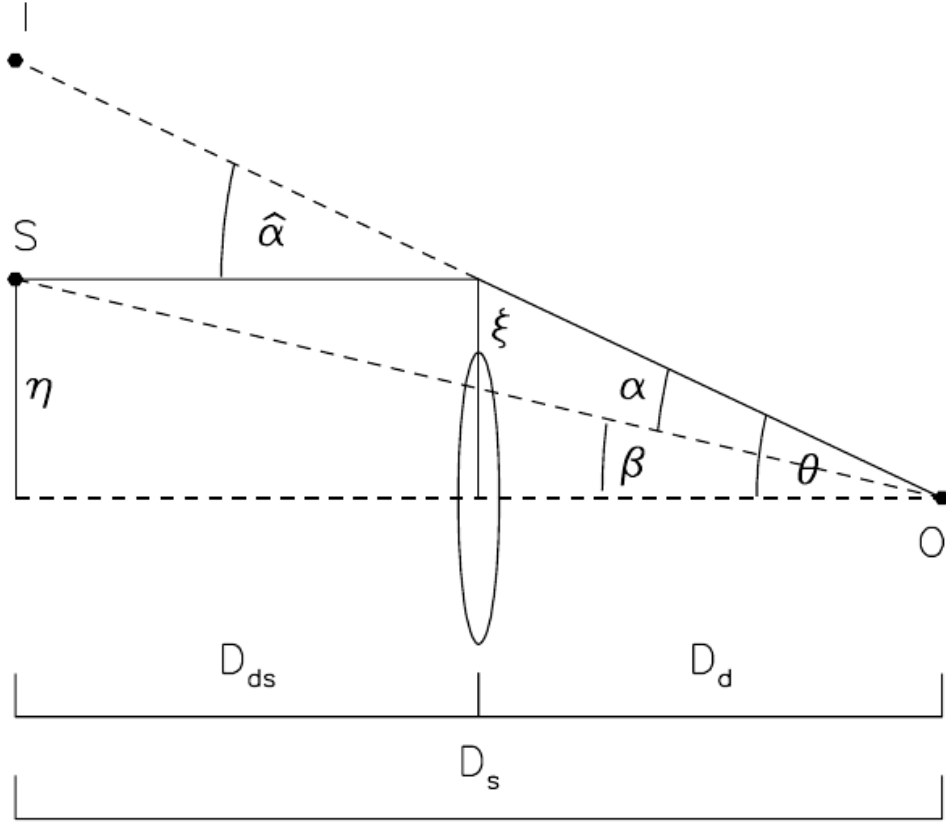


Figure 3.1: Diagram of a gravitational lensing system. Due to the gravitational lensing deflection, the observer sees the source in the position I on the lens plane, while its actual position is S, on the source plane. Due to the *thin lens approximation* we can assume that the deflection takes place in correspondence of the lens plane, and that the light emitted by the source travel undisturbed before and after this deflection. The dashed line is the optical axis of the system, and is perpendicular to the lens and source planes, passing through the observer position. The angular positions on the source and lens planes are measured relative to this axis, and are given by optical geometric relations (see text for more details). Figure from Narayan & Bartelmann (1996).

ray traveling through a medium with non constant refraction index $n = n(l)$

$$\vec{\alpha} = - \int \vec{\nabla}_{\perp} n(l) dl. \quad (3.4)$$

For a ray of light traveling through a weak gravitational field ϕ , we can define the effective refraction index of the field $n = 1 - 2\phi/c^2$, and then the deflection is given by

$$\vec{\alpha} = 2/c^2 \int \vec{\nabla}_{\perp} \phi dl. \quad (3.5)$$

Using the *thin lens approximation* we describe the mass of the lens through its surface density Σ , which is the projection on the lens plane of the lens density $\rho(\vec{r})$ (see Narayan & Bartelmann, 1996)

$$\Sigma(\vec{\xi}) = \int \rho(\vec{\xi}, z) dz \quad (3.6)$$

where $\xi = D_d\theta$.

Then the deflection angle is given by

$$\hat{\alpha}(\vec{\xi}) = \frac{4G}{c^2} \int \frac{(\vec{\xi} - \vec{\xi}')\Sigma(\vec{\xi}')}{|\vec{\xi} - \vec{\xi}'|^2} d^2\xi'. \quad (3.7)$$

For a symmetric circular lens with constant Σ it reads

$$\alpha(\xi) = \frac{D_{ds}}{D_s} \frac{4G}{c^2} \frac{\Sigma\pi\xi^2}{\xi} \Rightarrow \alpha(\theta) = \frac{4\pi G\Sigma}{c^2} \frac{D_{ds}D_d}{D_s} \theta. \quad (3.8)$$

We can introduce the *critical surface density* Σ_{cr} as (see Narayan & Bartelmann, 1996)

$$\Sigma_{cr} = \frac{c^2}{4\pi G} \frac{D_s}{D_{ds}D_d} \quad (3.9)$$

and then the deflection angle for a symmetric circular lens with constant Σ becomes

$$\hat{\alpha}(\theta) = \frac{\Sigma}{\Sigma_{cr}} \theta. \quad (3.10)$$

If the lens has $\Sigma > \Sigma_{cr}$ then $\alpha > \theta$, and the source is *strongly* deflected. In this case we are in the *Strong Gravitational Lensing* regime, where highly deformed images and also multiple images of the same source are generated.

If $\Sigma \ll \Sigma_{cr}$ then $\alpha < \theta$, and we are in the so-called *Weak Lensing* domain. The deflection imprinted in the light is *weak* generating only small distortions in the image shape. We note that the critical density depends only on the distance between the lens, the source and the observer, and thus on the cosmology that they refers to. In Section 3.2 we present in more details the different lensing regimes.

We now define the reduced deflection angle (see Narayan & Bartelmann, 1996)

$$\vec{\alpha}(\vec{\theta}) = \frac{D_{ds}}{D_s} \hat{\alpha}(\vec{\theta}), \quad (3.11)$$

which allows to write the lens equation as follows

$$\vec{\beta}(\vec{\theta}) = \vec{\theta} - \vec{\alpha}(\vec{\theta}). \quad (3.12)$$

From this expression of the lens equation, we see that lensing is sensitive to the angular diameter distance ratio D_{ds}/D_s . In Fig. 3.2 we plot the distances ratio D_{ds}/D_s as a function of the source redshift and for fixed lens redshift. We plot the cases of a lens at redshift $z = 0.189$ and $z = 0.348$ (which correspond to the redshifts of the galaxy clusters Abell 383 and RXC J2248, presented in Chap. 8 and 6, respectively). The ratio D_{ds}/D_s gets approximately flat for sources at high redshifts, which introduce a degeneracy between the lensing configuration and source redshifts. Then we introduce the *effective lensing potential* $\psi(\vec{\theta})$ (see Narayan & Bartelmann, 1996), defined as a rescaled projection of the three-dimensional Newtonian potential on the lens plane

$$\psi(\vec{\theta}) = \frac{D_{ds}}{D_s D_d} \frac{2}{c^2} \int \Psi(D_d \vec{\theta}, z) dz. \quad (3.13)$$

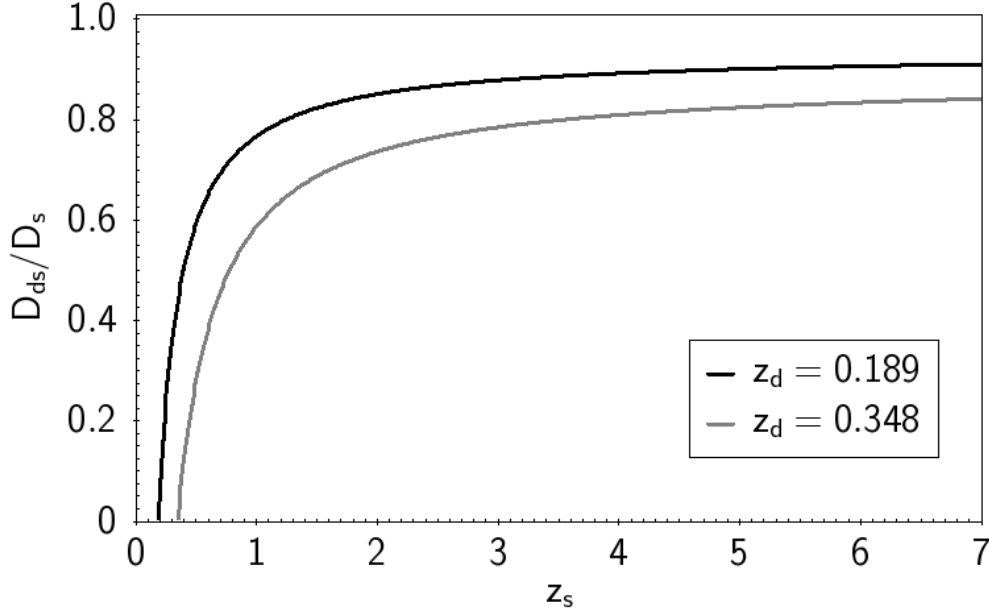


Figure 3.2: The ratio of the distances D_{ds} and D_s as a function of the redshift of the source z_s and constant lens distance. In black we plot the case $z_d = 0.189$ and in gray the case $z_d = 0.348$. Lensing is sensitive to the angular diameter distance ratio which gets approximately flat for sources at high redshifts.

The gradient of ψ along $\vec{\theta}$ is equal to the reduced deflection angle:

$$\begin{aligned}\vec{\nabla}_{\theta}\psi(\vec{\theta}) &= \vec{\nabla}_{\theta}\frac{D_{ds}}{D_s D_d}\frac{2}{c^2}\int\Psi(D_d\vec{\theta},z)dz = \vec{\nabla}_{\perp}\frac{D_{ds}}{D_s}\frac{2}{c^2}\int\Psi(D_d\vec{\theta},z)dz = \\ &= \frac{D_{ds}}{D_s}\frac{2}{c^2}\int\vec{\nabla}_{\perp}\Psi(D_d\vec{\theta},z)dz = \alpha(\vec{\theta}).\end{aligned}\quad (3.14)$$

Thus

$$\vec{\nabla}_{\theta}\psi(\vec{\theta}) = \alpha(\vec{\theta}).\quad (3.15)$$

In addition, the Laplacian of ψ is directly proportional to the so-called *convergence* function $\kappa(\vec{\theta})$, defined as the ratio between the surface density $\Sigma(\vec{\theta})$ and the critical surface density Σ_{cr}

$$\vec{\nabla}_{\theta}^2\psi = 2\frac{\Sigma(\vec{\theta})}{\Sigma_{cr}} \equiv 2\kappa(\vec{\theta}).\quad (3.16)$$

Strong lensing occurs where the surface mass density $\Sigma(\vec{\theta})$ is larger than the critical surface density Σ_{cr} , thus where the convergence $\kappa(\vec{\theta}) > 1$: this condition marks the *strong lensing* domain, while $\kappa(\vec{\theta}) \ll 1$ marks the region of *weak lensing* regime.

As previously stated, the lens equation is a *mapping equation* which maps each surface element $\delta\vec{\theta}$ of the image plane into a surface element $\delta\beta(\vec{\theta})$ on the source plane as follows

$$\delta\vec{\beta} = \frac{\partial\vec{\beta}}{\partial\vec{\theta}}\delta\vec{\theta} = \left(\delta_{ij} - \frac{\partial\alpha_i(\vec{\theta})}{\partial\theta_j}\right)\delta\vec{\theta} = \left(\delta_{ij} - \frac{\partial^2\psi(\vec{\theta})}{\partial\theta_i\partial\theta_j}\right)\delta\vec{\theta} = A\delta\vec{\theta}.\quad (3.17)$$

The indexes $i, j = 1, 2$ are for the 2-D components of the angles on the lens and the source planes. The matrix A corresponds to the Jacobian matrix of the transformation (see Narayan

& Bartelmann, 1996).

For simplicity in the calculation we adopt the following shorthand notation for the second derivatives of the effective potential

$$\frac{\partial^2 \psi(\vec{\theta})}{\partial \theta_i \partial \theta_j} \equiv \Psi_{ij}. \quad (3.18)$$

Using the Jacobian matrix A , we define the so-called *Shear* matrix as (see Narayan & Bartelmann, 1996)

$$\begin{aligned} \left(A - \frac{1}{2} \text{tr} A \cdot I \right)_{ij} &= \delta_{ij} - \Psi_{ij} - \frac{1}{2} (1 - \Psi_{11} + 1 - \Psi_{22}) \delta_{ij} \\ &= -\Psi_{ij} + \frac{1}{2} (\Psi_{11} + \Psi_{22}) \delta_{ij} = \begin{pmatrix} -\frac{1}{2} (\Psi_{11} - \Psi_{22}) & -\Psi_{12} \\ -\Psi_{12} & \frac{1}{2} (\Psi_{11} - \Psi_{22}) \end{pmatrix} \\ &= - \begin{pmatrix} \gamma_1 & \gamma_2 \\ \gamma_2 & -\gamma_1 \end{pmatrix} \end{aligned} \quad (3.19)$$

This matrix describes the asymmetric distortion of the shape of lensed images. $\vec{\gamma} = (\gamma_1, \gamma_2)$ is the *shear* pseudo-vector². Its components are:

$$\gamma_1(\vec{\theta}) = \frac{1}{2} (\Psi_{11} - \Psi_{22}) \quad (3.20)$$

$$\gamma_2(\vec{\theta}) = \Psi_{12} = \Psi_{21} \quad (3.21)$$

while the eigenvalues of the shear matrix are

$$\pm \gamma = \pm \sqrt{\gamma_1^2 + \gamma_2^2} \quad (3.22)$$

It exists a particular coordinate rotation by an angle ϕ for which we can write the shear matrix as (see Narayan & Bartelmann, 1996)

$$- \begin{pmatrix} \gamma_1 & \gamma_2 \\ \gamma_2 & -\gamma_1 \end{pmatrix} = -\gamma \begin{pmatrix} \cos 2\phi & \sin 2\phi \\ \sin 2\phi & -\cos 2\phi \end{pmatrix} \quad (3.23)$$

Since

$$\frac{1}{2} \text{tr} A = \left[1 - \frac{1}{2} (\Psi_{11} + \Psi_{22}) \right] \delta_{ij} = \left(1 - \frac{1}{2} \Delta \Psi \right) \delta_{ij} = (1 - \kappa) \delta_{ij}, \quad (3.24)$$

thus the Jacobian matrix can be written as

$$A = \begin{pmatrix} 1 - \kappa - \gamma_1 & -\gamma_2 \\ \gamma_2 & 1 - \kappa + \gamma_1 \end{pmatrix} = (1 - \kappa) \begin{pmatrix} 1 & 0 \\ 0 & 1 \end{pmatrix} - \gamma \begin{pmatrix} \cos 2\phi & \sin 2\phi \\ \sin 2\phi & -\cos 2\phi \end{pmatrix}. \quad (3.25)$$

With this expression we decomposed the Jacobian matrix A into an isotropic component, proportional to the convergence κ , and an anisotropic component, proportional to the shear γ . This clarifies the physical meaning of both these quantities. The convergence describes the isotropic magnification of the lensed images relative to the source. On the other hand the

²It is a 'pseudo-vector' since its components are elements of a 2×2 tensor and not components of a vector.

shear describes the anisotropic deformation which causes that the shapes of the images are stretched along a particular direction, given by the phase of $\vec{\gamma}$.

Finally, lensing phenomena are achromatic, since the gravitational deflection affects the light in the same way at all the wavelengths. There are no absorption nor emission processes associated with lensing, thus the surface brightness of the source is conserved. However, we saw that lensed images are rescaled and stretched with respect to the source, and this means that the solid angles they subtend are different from the one of the source. Thus, from the Liouville theorem, we conclude that the fluxes of the lensed images are magnified or demagnified (Schneider et al., 1992).

The total magnification μ of the lensed images is given by

$$\mu = \frac{1}{\det A} = \frac{1}{(1 - \kappa)^2 - \gamma^2} \equiv \frac{1}{H(\vec{\theta})}. \quad (3.26)$$

The sign of μ is related to the parity of the images: if the lensed image at the position $\vec{\theta}_i$ has $\mu(\vec{\theta}_i) > 0$, then it has the same parity as the source, that means the same symmetry (*even parity*). If $\mu(\vec{\theta}_i) < 0$ then the lensed image has a mirror symmetry with respect to the source (*odd parity*).

The family of points where the magnification is formally infinite on the image plane (i.e. where $\det A(\vec{\theta}) = 0$) defines the so-called *critical lines*. Defining λ_t, λ_r as

$$\lambda_r = \frac{1}{\mu_r} = 1 - \kappa + \gamma, \quad (3.27)$$

$$\lambda_t = \frac{1}{\mu_t} = 1 - \kappa - \gamma, \quad (3.28)$$

the critical lines are where $\lambda_t = 1/\mu_t = 0$ and by $\lambda_r = 1/\mu_r = 0$. $\lambda_t = 0$ and $\lambda_r = 0$ defines the *tangential* and *radial critical lines* respectively. Lensed images forming close to these lines are strongly distorted tangentially and perpendicularly to the curves respectively.

Mapping these curves in the source plane through the lens equation we get the so-called *caustic lines*. A source which lies close to a tangential caustic line will be mapped close to a tangential critical line showing a strong tangential distortion, and similarly a source lying close to a radial caustic will result in a radial lensed image.

Finally, due to gravitational lensing, deflected light rays will take longer time to reach the observer than unperturbed rays. The lensing time delay has two components. A *geometric* component which is due to the different path followed by the lensed rays with respect to the path of unperturbed rays. This is directly proportional to the square of the angular separation between the source and the image. Then there is a *gravitational* time delay component. This is associated with the *slowing down* of the photons traveling through the gravitational field of the lens and is given by the effective lensing potential. The total lensing time delay function reads as (see Narayan & Bartelmann, 1996)

$$t(\vec{\theta}) = \frac{1 + z_d}{c} \frac{D_s D_d}{D_{ds}} \left[\frac{1}{2} (\vec{\theta} - \vec{\beta})^2 - \psi(\vec{\theta}) \right], \quad (3.29)$$

where z_d is the redshift of the lens.

3.2 Gravitational Lensing regimes

Gravitational lensing phenomena are classified in three main fields, *Strong, Weak and Microlensing*, depending on the positions of the source, the lens and the observer and on the astronomical objects acting as lenses.

When the source, lens and observer are almost aligned the gravitational distortion is large, the lensed images show a strong distortion of their real shape and also multiple images of the same source can be generated. In this case we are in the 'strong lensing' regime.

Sources which are far from the line of sight (l.o.s.) of the system suffer a weaker distortion due to the gravitational lensing. These sources show weak deformation of their real shape because of the gravitational distortion, appearing for example more elliptical and with a different orientation than the real one. These cases are classified as 'weak lensing'.

With strong and weak lensing we refer to events in which the lenses are extragalactic object, as a galaxy or a cluster of galaxies.

'Microlensing' takes place if the lens is compact (i.e. a star or a planet), and if lens and source move at timescales that we can observe. In this case the angular separations between the lensed images and the lens itself are too small to be resolved and the only observable lensing effect is a variation of the apparent magnitude of the source. Microlensing can occur on galactic scales (e.g. microlensing by a star or a planet in the Milky Way) or with extragalactic objects (e.g. microlensing of QSOs by stars in a foreground galaxy).

3.2.1 Strong Lensing

Strong lensing events occurs when a source is aligned or almost aligned with the lens and the observer. In this case the light emitted by the source is passing through the region where the distortion of the gravitational field generated by the lens is high. Thus the light paths are highly curved and the deflection angles α are large (but still smaller than $\sim 1'$). Depending on the geometry and properties of the system, the lens equation, Eq 3.2, can allow multiple solutions θ_i , which means that multiple images of the same source can be generated. In addition, if the source is extended, the light bundles are differentially deflected, leading to the formation of highly distorted images, called arclets or giant arcs. The higher distortion and magnification occur when the sources are close to the caustics in the source plane. In this case the multiple images and arcs are generated close to the critical lines in the image plane. If source, lens and observer are perfectly aligned, the source is mapped into the so-called *Einstein Ring*. In astrophysical systems, the configuration of a perfect alignment along the line of sight is rare, although there are several examples of observed Einstein Rings in literature. If the source is slightly off from the line of sight, then the Einstein Ring breaks into multiple images highly distorted in direction tangential to the l.o.s.

If Fig.3.3 we show a colour image of the core of the galaxy cluster MACS0329. This is an example of galaxy cluster strong lensing. Several lensing features are observed in the core of this cluster, as multiple images and tangential arcs. Since lensing is achromatic, the lensed images preserve the colour of the source, and multiple images will have the same colours in colour composite images, unless the source have intrinsically spatial colour variation, or if extinction processes take places along the light paths of the different multiple images. Moving to the outskirts of the cluster, we also find an example of galaxy-galaxy strong lensing (shown in the cut-out in Fig. 3.3) composed of a giant arc and its counter images. In this system,

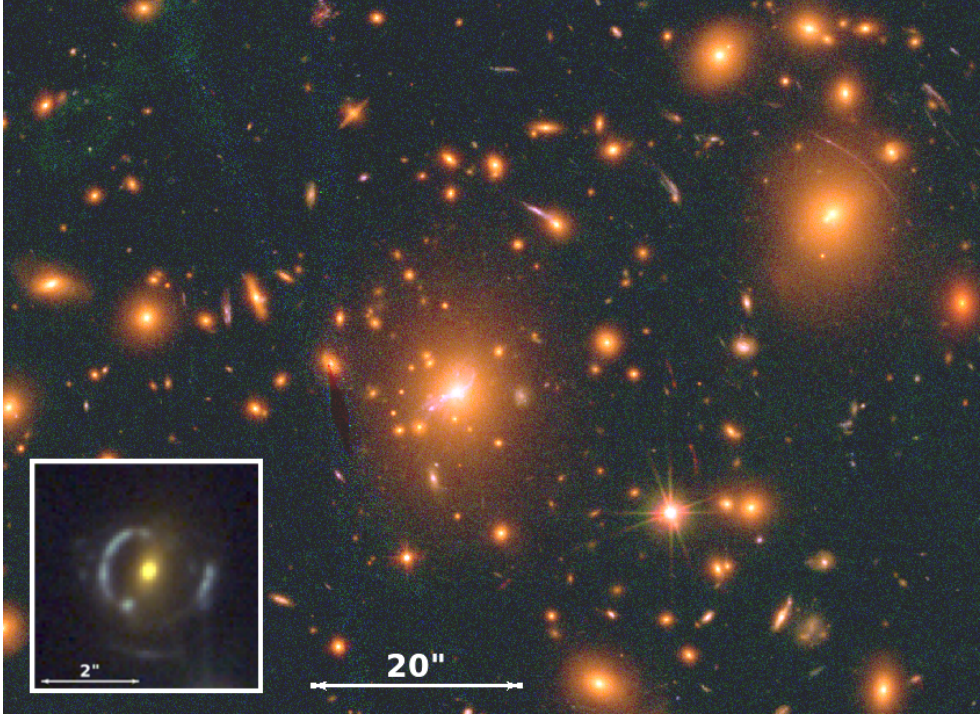


Figure 3.3: RGB colour composite image of the core of the galaxy cluster MACS2129. The image is generated using CLASH photometric images as follows: Blue=F435W+F475W, Green=F606W+F625W+F775W+F814W+F850LP, Red=F105W+F110W+F140W+F160W. Several strong lensing features can be identified as tangential arcs, which appear highly distorted, and multiple images, which are distorted images with the same colours. All the multiple images identified in the core of this cluster are presented in Zitrin et al. (2012a), in which the discovery of a quadruply lensed galaxy at redshift $z \sim 6.2$ is presented. The cut-out in the left corner presents a galaxy-galaxy lensing system observed at $\sim 1.5'$ south of the cluster BCG. The colour of the cut-out is blueish since it is slightly outside the WFC3IR FOV, thus it has no red component in the RGB image (see Section 5.2 for more details on the CLASH photometric dataset).

if the source and the lens-galaxy were perfectly aligned we would have observed an Einstein Ring.

The radius of an Einstein Ring is called Einstein Radius θ_E and it is a direct observable of strong lensing. If the lens is a point mass (i.e. we assume that all the mass of the lens is concentrated in the centre of the lens) and the source is aligned along the line of sight, the Einstein Radius is given by (see Sec 3.3.1)

$$\theta_E = \left(\frac{4GM}{c^2} D \right)^{\frac{1}{2}} \approx \left(\frac{M}{10^{11} M_\odot} \right)^{\frac{1}{2}} \left(\frac{D}{Gpc} \right)^{\frac{1}{2}} \quad (3.30)$$

where G is the gravitational constant, M is the mass of the lens, c the speed of light and D is the ratio of the distances $D = D_{DS}/D_S D_D$ (see Narayan & Bartelmann, 1996). When multiple images are generated, the order of the angular separation of the counter images is $\approx 2\theta_E$. Thus, given the observed θ_E in lensing systems, if the distances of the lens and the source are known, we can roughly estimate the mass of the lens and vice versa. For a Galaxy Cluster having $M \sim 10^{14} M_\odot$ at $z_{cl} = 0.1$ lensing a galaxy at $z_s = 1$, we would expect $\theta_E \sim 30''$. If the lens is a galaxy of mass $M \sim 10^{11}$ at redshift $z_l = 0.1$, for a source at $z_s = 1$

we would observe $\theta_E \sim 3''$.

The relative positions (angular separations and redshifts) of the lens and the lensed images are direct observables and give astrometric constraints in the lensing systems. In photometric datasets the relative fluxes of multiple images can be directly measured providing other constraints for strong lensing analyses. If the lensed sources have intrinsic time variability in the light emission, this can be observed in a time delay of the lensed images. The time delays observed in multiple images allows to estimate the Hubble constant H_0 (e.g., see Schneider et al., 1992; Narayan & Bartelmann, 1996; Suyu et al., 2013). For a Singular Isothermal Sphere (SIS, 3.3.3) lens, the time delay observed in two multiple images A and B is given by (Schneider et al., 1992; Narayan & Bartelmann, 1999, see)

$$\Delta t_{SIS} = \frac{1}{2} \frac{D_D D_S}{c D_D S} (1 + z_d) (\theta_A^2 - \theta_B^2) \quad (3.31)$$

where $\theta_{A,B}$ are the observed positions of the multiple images. Δt_{SIS} is directly proportional to the ratio of the distances between the source, lens and observer, and thus to the cosmology used to define these distances. Using the multiple images time delays to investigate H_0 mainly applies to galaxy-galaxy system, in which the angular separation of multiple images is of the order of few '' ($\theta_e \sim 1''$).

The main application of strong sensing is to trace the total mass distribution in the inner regions of the lens. The mass profiles can be constrained to high precision when a lot of lensing observables are used. In addition, using appropriate assumptions on the dark and baryonic mass components of the lens, strong lensing can allow to disentangle these two mass components, and thus completely constrain the dark matter distribution of the lens.

3.2.2 Weak Lensing

Weak lensing occurs when gravitational deflection is small and causes weak distortions of the shape of the galaxies behind the lens, see the example shown in Fig. 3.4. Galaxy clusters as well as individual galaxies cause weak lensing effects.

It probes the mass distribution of the lens to larger radii than strong lensing. In addition, also the Large Scale Structure causes observable weak distortions in background galaxies. In this case the lensing distortion (i.e. the change of the ellipticity of individual galaxies due to lensing) is of the order of 0.1 – 1% and it is called *cosmic shear*.

In the weak lensing regime, the distortion of the ellipticity e and orientation $P.A.$ of the galaxies lying behind the lens, is proportional to the local shear $\vec{\gamma}(\vec{\theta})$ (e.g., see Hoekstra & Jain, 2008). Let us consider a circular galaxy, behind a galaxy cluster, which is at the position $\vec{\theta}$ where $\kappa\vec{\theta}, \gamma\vec{\theta} \ll 1$. Due to the weak lensing distortion of the shape of the galaxy, this does not appear circular but with ellipticity $e > 0$. The axes of the observed ellipse are given by (see Narayan & Bartelmann, 1996)

$$a = \frac{r}{1 - \kappa - \gamma} \quad (3.32)$$

$$b = \frac{r}{1 - \kappa + \gamma}. \quad (3.33)$$

The observed ellipticity of the galaxy reads

$$e = \frac{a - b}{a + b} = \frac{\gamma}{1 - \kappa} \approx \gamma, \quad (3.34)$$

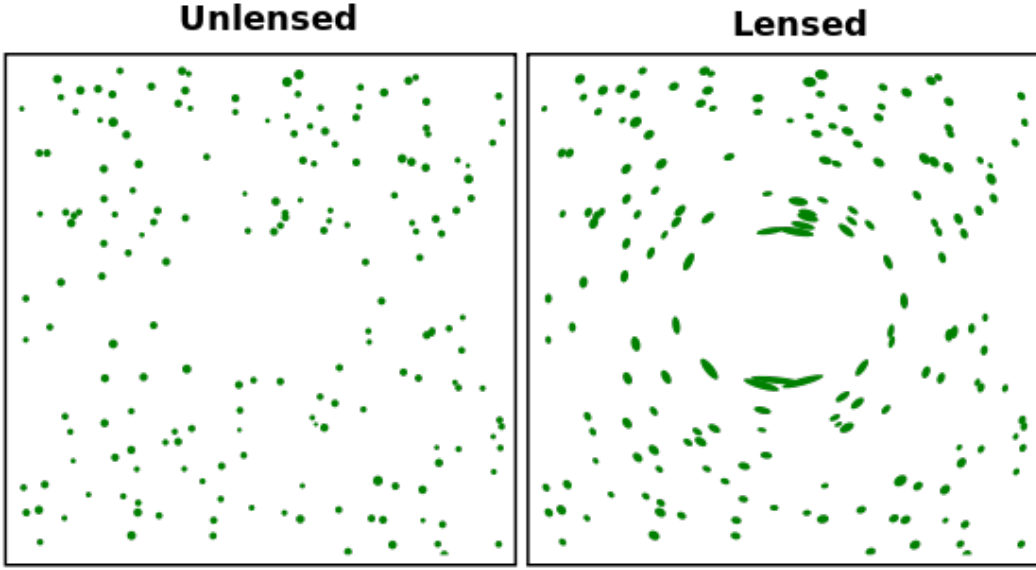


Figure 3.4: Example of the weak lensing distortion induced at large angular separation from a gravitational lens. The left panel shows a galaxy field in absence of gravitational lensing, while the right one the same field when a massive body is between the field galaxies and the observer. Figure from http://en.wikipedia.org/wiki/Weak_gravitational_lensing, modified.

that is, the observed ellipticity of the background circular galaxy gives a direct measurement of the local shear.

Here we assumed that the lensed galaxy has circular symmetry, which is an hypothesis not generally satisfied by galaxies. However, weak lensing applies to a large field behind the lens, and the number density of background galaxies usually ranges between tens and hundreds galaxies per arcminute². A statistical approach is used to investigate the weak distortions imprinted on the shape of the weakly lensed galaxies. Thus, we can reasonably assume that the background galaxies are randomly oriented and that the average intrinsic ellipticity over all these galaxies is zero, $\langle e \rangle = 0$. Due to weak lensing distortion, the average measured ellipticity of background galaxies around the position $\vec{\theta}$ is not zero, and it gives the average shear in $\vec{\theta}$ (Narayan & Bartelmann, 1996)

$$\langle e \rangle = \langle g \rangle \equiv \left\langle \frac{\gamma}{1 - \kappa} \right\rangle, \quad (3.35)$$

where g is called *reduced shear*. The observed $\vec{\gamma}$ and the lensing potential ψ are related by Eq.3.20 and Eq.3.21. Thus, by measuring the shear across the field around the lens, the lensing potential and the convergence $\kappa(\vec{\theta})$, and then the lens mass distribution, can be mapped.

3.2.3 Microlensing

Microlensing events are transient phenomena which occur when a (galactic) massive object, as a star or a massive compact halo object (MACHO), during its proper motion passes in front of a distant source, as a Quasar, a star or a planet. When the lens and the background source are aligned, strong lensing occurs, and multiple images are generated. Given the order of distances between lens and source (~ 10 kpc for galactic microlensing, and ~ 1 Gpc for extragalactic microlensing) the typical separation between the multiple images $\Delta\theta \approx \theta_E$ is

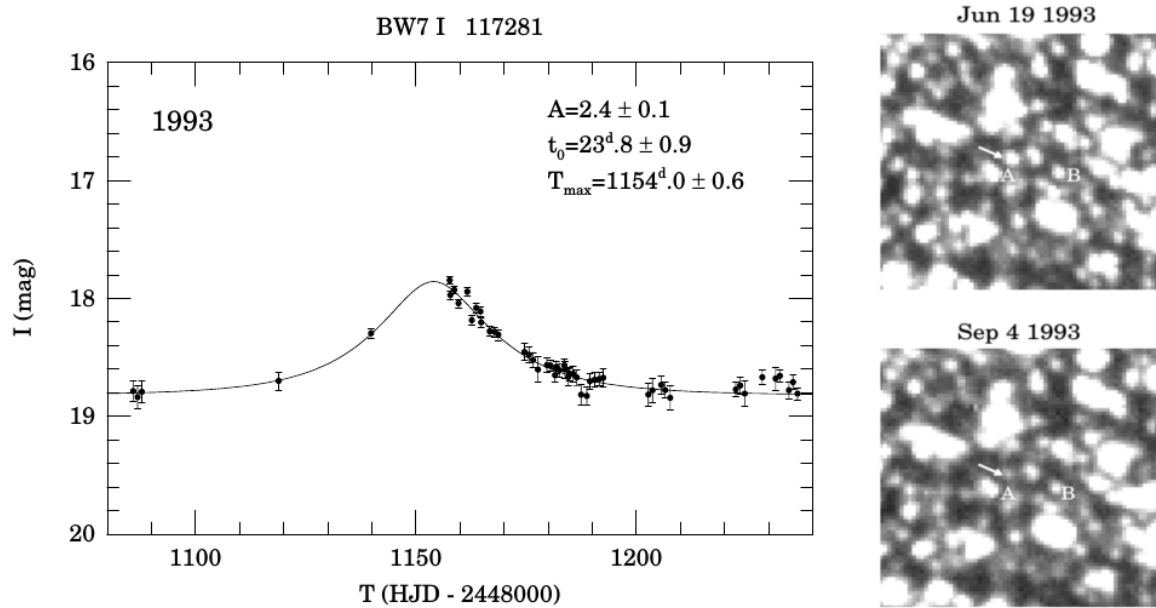


Figure 3.5: First microlensing event observed in the direction of the Galactic bulge in 1993 by the Optical Gravitational lensing Experiment (OGLE) survey (Udalski et al., 1993). The left diagram shows the light curve of the lensed star, with the observed points (black dots) and the best fitting curve. The panel on the right shows a field of $30'' \times 30''$ centred on the lensed star (pointed by the arrow) in the I -band. Two comparison stars are marked with A and B . Two different observation epochs are shown, one in which the star is highly magnified (on June the 19th, 1993), and the other in which it is not magnified (on September the 4th, 1993). The lens is likely associated with a M-dwarf star with mass of $\sim 0.3M_{\odot}$

of the order of milliarcseconds, and is not resolvable (e.g., see Paczynski, 1996). However, due to the magnification induced by lensing, the apparent brightness of the source changes as the lens moves in front of the source. The observed flux of the lensed source varies with timescales ranging from seconds to years. Thus, by monitoring the light curves of objects in dense stellar fields, microlensing effects can be identified.

Microlensing is used to investigate the population of MACHOs in the Galaxy halo, which are massive but faint astronomical objects, and also to discover extrasolar planets, (see e.g. Wambsganss, 2006). Fig. 3.5 shows the light curve and the *I*-band image of a microlensing event observed in direction of the galactic bulge, reported by Udalski et al. (1993).

3.3 Parametrised Lens models

In this section we present the analytic mass profiles most commonly used to describe the mass components in Strong Lensing analyses. First we introduce simple lensing configurations and then move to more complex ones in order to describe realistic lensing phenomena due to galaxy-galaxy or galaxy-clusters lensing.

3.3.1 Point mass lens

Let us consider a point mass lens of mass M_p at redshift z_d which lenses a source at redshift $z_s > z_d$. Such a system has circular symmetry and the lensing analysis is reduced to a one-dimension problem. For simplicity we use as the one-coordinate system the direction along the line of sight. The gravitational potential of the lens is $\Psi = -GM_p/r$, thus the deflection angle reads (see Narayan & Bartelmann, 1996)

$$\hat{\alpha}(\xi) = \frac{2}{c^2} \int \vec{\nabla}_\perp \Psi dz = \frac{4GM_p}{c^2 \xi} = \frac{4GM_p}{c^2 D_d \theta} \quad (3.36)$$

where $\xi = D_d \theta$ is the impact parameter.

The lens equation writes as

$$\beta = \theta - \frac{4GM_p}{c^2 D_d \theta} \frac{D_{ds}}{D_s} = \theta - \frac{\theta_E^2}{\theta}, \quad (3.37)$$

where we have introduced the Einstein radius defined as

$$\theta_E \equiv \sqrt{\frac{4GM_p}{c^2} \frac{D_{ds}}{D_d D_d}}. \quad (3.38)$$

This equation admits two solutions

$$\theta_\pm = \frac{1}{2} \left[\beta \pm \sqrt{\beta^2 + 4\theta_E^2} \right]. \quad (3.39)$$

Thus, for a source at the position β two lensed images are generated. If the source is perfectly aligned with the lens, i.e. $\beta = 0$, then $\theta_\pm = \pm\theta_E$, the so-called *Einstein Ring*, with radius θ_E , is generated.

The magnifications of the images are

$$\mu_\pm = \frac{1}{2} \pm \frac{\frac{\beta}{\theta_E}^2 + 2}{2 \frac{\beta}{\theta_E} \sqrt{\frac{\beta}{\theta_E}^2 + 4}} \quad (3.40)$$

For $\beta \rightarrow \infty$, Eq.3.39 and Eq.3.40 give

$$\begin{cases} \theta_- \rightarrow 0; & \mu_- \rightarrow 0 \\ \theta_+ \rightarrow \beta; & \mu_- \rightarrow 1. \end{cases} \quad (3.41)$$

The image with mirror-symmetry, θ_- , disappears. Increasing the angular separation between the source and the lens, we move from strong to weak lensing regime, where we have no multiple images but only weak distortion of the image shape.

3.3.2 Extended circularly symmetric lens

The formalism of the point mass lens is easy and straightforward, but can be applied to describe only systems in which the lens is massive and compact, e.g. microlensing systems. For galaxy-galaxy and galaxy-cluster lensing systems, the lenses which we aim to describe have extended mass distributions. Let us consider an axially symmetric mass distribution, with surface mass density $\Sigma(|\theta|)$. As before, such a system can be converted to a one-dimension problem. The gravitational potential and the deflection angle for such a lens are (see Narayan & Bartelmann, 1996)

$$\psi = -\frac{GM(<\theta)}{D_d\theta}, \quad \hat{\alpha}(\theta) = \frac{4GM(<\theta)}{c^2 D_d\theta}. \quad (3.42)$$

The lens equation reads

$$\beta(\theta) = \theta - \frac{M(<\theta)}{\pi D_d^2 \theta \Sigma_{cr}} = \theta - \frac{\theta_E}{\theta}, \quad (3.43)$$

where $M(<\theta)$ is the lens mass enclosed within the radius $D_d\theta$, Σ_{cr} is the critical surface density of the system and the Einstein radius is defined as

$$\theta_E = \frac{1}{D_d} \left(\frac{M(<\theta)}{\pi \Sigma_{cr}} \right)^{\frac{1}{2}}. \quad (3.44)$$

The Jacobian matrix A , in polar coordinates (θ, ϕ) , is

$$\begin{aligned} A &= \begin{pmatrix} 1 - \frac{\partial^2 \psi}{\partial \theta^2} & -\frac{\partial}{\partial \theta} \left(\frac{1}{\theta} \frac{\partial \psi}{\partial \phi} \right) \\ -\frac{\partial}{\partial \theta} \left(\frac{1}{\theta} \frac{\partial \psi}{\partial \phi} \right) & 1 - \frac{1}{\theta} \frac{\partial \psi}{\partial \phi} - \frac{1}{\theta^2} \frac{\partial^2 \psi}{\partial \phi^2} \end{pmatrix} = \\ &= \begin{pmatrix} 1 - \frac{1}{\pi D_d^2 \Sigma_{cr}} \frac{\partial}{\partial \theta} \left(\frac{M(<\theta)}{\theta} \right) & 0 \\ 0 & 1 - \frac{1}{\pi D_d^2 \Sigma_{cr}} \left(\frac{M(<\theta)}{\theta^2} \right) \end{pmatrix} = \begin{pmatrix} \frac{d\beta}{d\theta} & 0 \\ 0 & \frac{\beta}{\theta} \end{pmatrix} \end{aligned} \quad (3.45)$$

The radial and tangential critical lines are defined by the family of points where $\det|A| = 0$, that is where the two (diagonal) elements of the Jacobian matrix are zero. Both critical lines are circular for this spherical mass case. If the mass distribution is singular, i.e. $M \rightarrow \infty$ for $r \rightarrow 0$, the radial critical line reduces to a point coincident with the centre of the lens. If it is not singular, for example because it has a core radius, then the radial critical line is given by $d\beta/d\theta = 0$ and is a circle with radius

$$\theta_R = \frac{1}{D_d} \left(\frac{M(\theta_R)}{\pi \Sigma_{cr}} \right)^{\frac{1}{2}} \left(\frac{1}{\frac{2\Sigma(\theta_R)}{\Sigma_{cr}} - 1} \right). \quad (3.46)$$

The tangential critical line is given by $\beta = 0$ and is circular with radius θ_E .

From the Eq.3.43, we find that points of the tangential critical line ($\theta = \theta_E$) are mapped in $\beta = 0$ on the source plane, i.e. the tangential caustic is a point centred on the lens, while the radial critical line is mapped on a circular caustic.

The total number of multiple images depends on the position of the source with respect to the caustics. If the lens is non-singular, the number of multiple images is $n = 2m + 1$, where m is the number of caustics that include the source. Thus, if the source is within the radial caustic, three multiple images are formed, while if it is outside this caustic, then only one image is observed. In Fig.3.6,3.7 we show a diagram of the multiple images predicted as a function of the source position with respect to the caustics for a non singular mass distribution with circular symmetry. We present both the case of a point-like source, in Fig.3.6, and of an extended source, in Fig.3.7. In Fig.3.6 we present the case of a point-like source. In this case simply point-like multiple images are generated. If the lensed source is extended, due to the differential deflection of the rays of the source, the lensed images show large distortion of their shape along the tangential (if the source is close to the tangential caustic) or radial (if the source is close to the radial caustic) direction. When the source is approaching a caustic, the respective lensed images will be seated on the respective critical line and a *fold* images is observed, which is two multiple images merged into one. If the lens is described with a singular mass profile ($\rho \rightarrow \infty$ for $r \rightarrow 0$), the central image is has $\mu = 0$ and thus is not observed. If the central singularity is removed by introducing a core radius r_c , the magnification of the central image is not zero anymore and it becomes observable (see Narayan & Bartelmann, 1996). For non singular mass profiles, the location and relative magnification of the central image bring constraints on the steepness of the density profile. Thus, when the central images are observed, they add important constraints on the lens mass profile. However, central images are usually difficult to detect, since the central region of the lens are too bright. For example, the cores of galaxy clusters are dominated by bright elliptical galaxies, which can prevent the detection of the central multiple images. (e.g., see Narayan & Bartelmann, 1996).

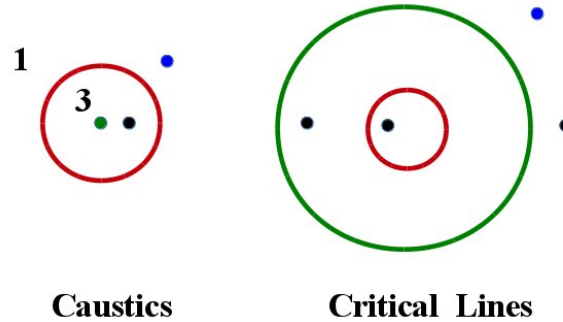


Figure 3.6: Diagram of the critical lines and caustics for a non singular axially symmetric lens. In red we plot the radial caustic and critical line, while in green we plot the tangential ones. For a point-like source within the radial caustic (in black) three images are produced, while when the source is outside the radial caustic (in blue) only one image is observed.

3.3.3 Singular Isothermal Sphere

The Singular Isothermal Sphere (SIS, see Narayan & Bartelmann, 1996) mass model assumes that the components of the mass distribution (e.g. the stars, or the dark matter) behave like

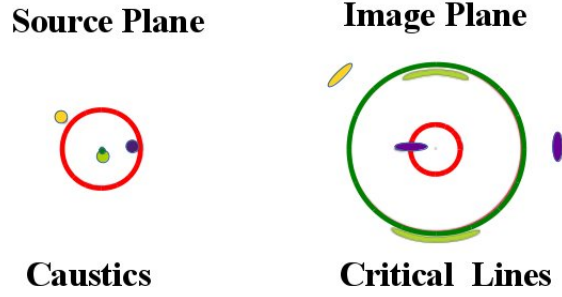


Figure 3.7: Same Diagram as in Fig. 3.6. Here we present the multiple images generated for an extended source. As before, if the source lies within the radial caustic three multiple images are generated. If the source is close to the radial caustic (purple one), a radially elongated image is generated near the radial critical line (for a the source approaching the caustic it is a fold image) and a tangentially elongated image is generated outside the tangential critical line. When the source is close to the tangential point-like caustic it produces two tangentially distorted images near the tangential critical line. An extended source which lies outside the radial caustic has no multiple images, but is only distorted in the tangential direction. This distortion gets smaller as the angular separation of the source from the lens gets larger. Image from <http://gravitationalensing.pbworks.com/w/page/15553257/Strong%20Lensing>, modified.

an ideal gas which follows the equation of state $p = \rho kT/m$, where p is the pressure, ρ the mass density, m the mass and T is the temperature of the particles. In thermal equilibrium T is directly proportional to the velocity dispersion σ_v of the particles (i.e. of the stars), as $kt = m\sigma_v^2$. If we assume that the gas is isothermal, then $T = \text{constant}$ and also σ_v is constant across the mass distribution. The equation of hydrostatic equilibrium gives

$$\frac{1}{\rho} \frac{dp}{dr} = -\frac{GM(r)}{r^2}, \quad \frac{M(r)}{dr} = 4\pi r^2 \rho, \quad (3.47)$$

where $M(r)$ is the mass inside the radius r .

The density profile for such mass distribution is then

$$\rho(r) = \frac{\sigma_v^2}{2\pi G r^2}, \quad (3.48)$$

and the surface mass density is

$$\Sigma(\theta) = \frac{\sigma_v^2}{2GD_d\theta}. \quad (3.49)$$

The total mass within a radius θ is given by

$$M(< \theta) = \frac{\pi\sigma_v^2 D_d \theta}{G}. \quad (3.50)$$

From Eq. 3.42 we get the deflection angle

$$\hat{\alpha} = 4\pi \frac{\sigma_v^2}{c^2}, \quad (3.51)$$

which results independent from θ . The convergence $\kappa(\theta)$ and shear $\gamma(\theta)$ are both

$$\kappa(\theta) = \gamma(\theta) = \frac{\theta_E}{2\theta}, \quad (3.52)$$

where the Einstein radius is

$$\theta_e = 4\pi \frac{\sigma_v^2 D_{LS}}{c^2 D_S} = \hat{\alpha} \frac{D_{LS}}{D_S} = \alpha. \quad (3.53)$$

For sources inside the Einstein ring (i.e., for $\beta < \theta_E$) the lens equation admits the two solutions

$$\theta_{\pm} = \beta \pm \theta_E. \quad (3.54)$$

The respective magnifications are

$$\mu_{\pm} = \frac{\theta_{\pm}}{\beta} = \left(1 \mp \frac{\theta_E}{\theta_{\pm}}\right)^{-1}. \quad (3.55)$$

A third central image is theoretically predicted, but it has $\mu = 0$ (due to the central singularity of the mass profile), and is not observable. If the source is outside the Einstein ring, $\beta > \theta_E$, only one image is observed at the position $\theta = \beta + \theta_E$.

The SIS profile has a simple analytic form and is suitable to describe dark halos of galaxies and clusters (e.g., see Binney & Tremaine, 1987). Its density goes as $\rho \propto r^{-2}$ and implies a constant rotational velocity

$$v_{rot}^2(r) = \frac{GM(r)}{r} = 2\sigma_v^2 \quad (3.56)$$

which reproduces the observed flat rotation curves of galaxies.

3.3.4 The Navarro, Frenk & White profile

The Navarro Frenk & White (NFW) model is a general density profile resulting from N-body simulations of dark matter halos. It provides good fits for halo masses within $10^9 - 10^{15} M_{\odot}$ and is generally used to describe the halo mass distribution of galaxies and cluster of galaxies (Navarro et al., 1997).

The density profile for spherical symmetry reads

$$\rho(r) = \frac{\rho_s}{\left(\frac{r}{r_s}\right) \left(1 + \frac{r}{r_s}\right)^2} \quad (3.57)$$

and is defined through the scale radius r_s and the characteristic density of the halo ρ_0 . At small radii $r \ll r_s$, the density goes as $\rho(r) \propto r^{-1}$, while $\rho(r) \propto r^{-3}$ for $r \gg r_s$. Compared to the SIS profile, for which the density follows r^{-2} , the NFW profile is flatter in the inner region of the halos and gets steeper in the outskirts.

NFW parametrize the mass of the halos using M_{200} , which is the mass within a virial radius r_{200c} . This is the radius of the sphere centred on the halo, which has an average density of 200 times the critical density of the Universe, i.e. $\langle \rho \rangle = \rho_{200c} \equiv 200\rho_c$ (Navarro et al., 1997). Numerical simulation shows that r_{200c} separate the virialized and infall region of the halo (Cole & Lacey, 1996; Navarro et al., 1997). The ratio r_{200c}/r_s defines the *concentration* of the mass distribution

$$c \equiv r_{200c}/r_s. \quad (3.58)$$

This parameter provides the mean cosmic density at the time when the halo formed. Thus by measuring it one can constraint the cosmological parameters.

By integration of $\rho(r)$ along the line of sight we get the surface mass density (e.g., see Bartelmann, 1996):

$$\Sigma(x) = \frac{2\rho_s r_s}{x^2 - 1} f(x), \quad \text{with} \quad x = \frac{D_d \theta}{r_s} \quad (3.59)$$

with

$$f(x) = \begin{cases} 1 - \frac{2}{\sqrt{x^2 - 1}} \arctan \sqrt{\frac{x-1}{x+1}} & (x > 1) \\ 1 - \frac{2}{\sqrt{1-x^2}} \operatorname{arctanh} \sqrt{\frac{1-x}{1+x}} & (x < 1) \\ 0 & (x = 1) \end{cases} \quad (3.60)$$

3.3.5 PIEMD

Circular symmetric profiles have a simple analytic profiles which allow a simple solution of the lensing equations. However galaxies and clusters have mass distributions more irregular than spherical profiles. A first step to better describe the real mass profile of these objects is to allow for elliptical iso-surface density contours.

The Pseudo Isothermal Elliptical Mass Distribution (PIEMD) (Kassiola & Kovner, 1993) has density profile given by

$$\rho(r) = \frac{\rho_0}{1 + \frac{r}{r_c}} \quad (3.61)$$

with a core with radius r_c and central density of ρ_0 . The profile is called *pseudo-isothermal* since for $r > r_c$ the density goes as $\rho \propto r^{-2}$, as the isothermal sphere. Its projected surface density is

$$\Sigma(R) = \frac{\sigma^2}{2G} \left(\frac{1}{\sqrt{r_c^2 + R^2}} \right), \quad (3.62)$$

where σ is the velocity dispersion of the DH. R is the 2D radius, given by $R^2 = x^2/(1+e)^2 + y^2/(1-e)^2$ for an elliptical profile with ellipticity e . For elliptical mass distribution with core radius, lensing measures the Einstein parameter Θ_E , which corresponds to the Einstein radius θ_E when the ellipticity and core radius go to zero ($e, r_{core} \rightarrow 0$).

3.3.6 dPIE

The 'dual Pseudo Isothermal Elliptical mass distribution' (dPIE, see Elíasdóttir et al., 2007) is a two component PIEMD profile which has both a core radius r_c and a scale radius r_{tr} . The density profile is

$$\rho(r) = \frac{\rho_0}{\left(1 + \frac{r}{r_c}\right) \left(1 + \frac{r}{r_{tr}}\right)} \quad (3.63)$$

with $r_{tr} > r_c$. The profile is isothermal ($\rho \propto r^{-2}$) for $r_c < r < r_{tr}$ and the scale radius r_{tr} , also called *truncation radius*, marks the region where the density slope changes from $\rho \propto r^{-2}$ to $\rho \propto r^{-4}$. The projected surface mass density for this profile is

$$\Sigma(R) = \frac{\sigma^2}{2GR} \frac{r_{tr}^2}{(r_{tr}^2 - r_c^2)} \left(\frac{1}{\sqrt{1 + r_c^2/R^2}} - \frac{1}{\sqrt{1 + r_{tr}^2/R^2}} \right) \quad (3.64)$$

where $R^2 = x^2/(1+e)^2 + y^2/(1-e)^2$ as for the PIEMD mass profile. The total mass for this profile is given by

$$M_{tot} = \frac{\pi\sigma^2}{G} \frac{r_{tr}^2}{r_{tr} + r_c}, \quad (3.65)$$

which, for $r_c \rightarrow 0$, reduces to

$$M_{tot} = \frac{\pi\sigma^2 r_{tr}}{G}. \quad (3.66)$$

For vanishing core radius, the r_{tr} corresponds to the radius containing half of the total mass of the galaxy (see Appendix A3 in Elíasdóttir et al., 2007). Thus r_{tr} can be considered as a half mass radius.

In Fig.3.8 we present examples of multiple images produced by elliptical lenses with core radius. For profiles with core radius, the tangential caustic is not point-like, as for the case of SIS, and sources within both the tangential and radial caustics are quintuply lensed (the number of multiple images is $n=2m+1=5$ being $m=2$, see Sec.3.3.2).

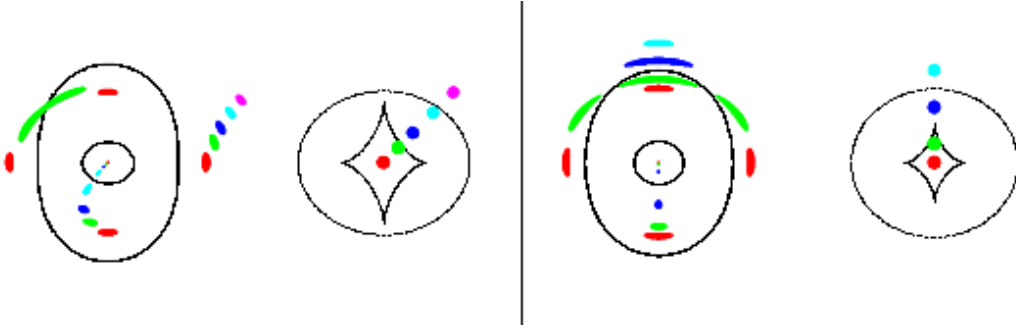


Figure 3.8: Diagram of multiple images produced by an elliptical lens with core radius for a source moving from the centre of the system to the outskirts. Left panel: case of a source crossing a fold caustic. In this panel the diagram on the left shows the image plane with the critical lines and the multiple images generated, while the diagram on the right presents the source plane with the caustics and the source position. Depending on the position of the source with respect to the caustics different configuration of multiple images are predicted (source and respective multiple images are shown with the same colours). Right panel: same as left panel but for a source crossing a cusp caustic (Figure from Narayan & Bartelmann, 1996).

Strong Lensing analyses

Gravitational lensing and its modelling are some of the most popular and important means to map the mass distribution of structures in the Universe from galaxies, through galaxy groups and clusters, and up to the large-scale structure (eg., Schneider, 2003; Bartelmann, 2010; Kneib & Natarajan, 2011). One of the main motivations to use lensing is its ability to map the total projected mass density of the lens and thus shed light on the distribution and properties of the otherwise-invisible dark matter (DM).

The work presented in this Thesis is based on strong lensing parametric analyses of the core of massive clusters of galaxies. In this chapter we describe in general the strong lensing mass modelling techniques, focussing in particular on the technique we use later on.

Strong lensing analyses aim to solve the lens equation (Eq. 3.12) for the observed lensed images at the positions θ_i , to put constraints on the surface density of the lens and thus to trace its mass profile.

In order to model the mass distribution of galaxy clusters using strong lensing, two approaches are used. The first, often dubbed *non-parametric*, elegantly makes no prior assumptions on the underlying mass distribution of the lens, but due to the typical low number of constraints usually yields a low-resolution result lacking prediction power (see, Abdelsalam et al., 1998; Diego et al., 2005; Coe et al., 2008). Alternatively, *parametric* mass modelling exploits prior knowledge or assumptions regarding the general form of the lens mass distribution, using parametrised mass model to describe the lens. The mass parameters are iterated for by producing many mass models each with a different set of parameter values, and looking for the solution which best reproduces the observed lensing features used as constraints. Despite their model dependence, these methods allow for a very-high spatial resolution result, and typically exhibit high prediction power to reproduce additional constraints such as multiple images not used as input (see, Jullo et al., 2007; Zitrin et al., 2009; Monna et al., 2014a).

4.1 Strong Lensing non-parametric analysis

Strong lensing non-parametric mass modelling makes no prior (or few) assumptions on the mass distribution of the lens (e.g. Saha & Williams, 1997; Diego et al., 2005; Coe et al., 2010). The surface mass density $\Sigma(\vec{\theta})$ (or directly the effective potential $\psi(\vec{\theta})$, depending on the particular method) is tessellated into a regular (or irregular, Coe et al. (e.g. 2008, 2010)) grid of smaller elements Σ_j . It assumes that the effective lensing potential $\psi(\vec{\theta})$ and

the deflection $\alpha\vec{\theta}$ are linear functions of the surface density and thus, for example, the lens equation for the observed image i can be written as

$$\vec{\beta}_i = \vec{\theta}_i - A_{i,j}\Sigma_j. \quad (4.1)$$

The matrix A_i gives the deflection at the position of the images i as a function of the tessellated surface density Σ_j . This technique has an high level of flexibility, since the underlying mass distribution of the lens is not restricted to an analytic mass profile, and different mass distributions can be explored. However, this also implies an high level of degeneracy for the mass distributions which reproduce the observed multiple images. (e.g., see Natarajan & Kneib, 1997; Kassiola et al., 1992).

4.2 Strong Lensing parametric analysis

Strong lensing parametric analyses use analytic mass profiles to describe the mass distribution of the lens. For galaxy cluster lensing, the total cluster mass is usually composed of two main components. A large scale components describes the smooth large scale dark halo of the cluster and the intra-cluster gas. A secondary component describes the sub-structures of the cluster, as the galaxies. Their contribution to the lensing ability of a cluster is not negligible, since they contribute to $\sim 10\%$ of the total cluster mass (see Natarajan & Kneib, 1997). Moreover, bright cluster members close to lensed multiple images or arcs have a direct impact on the local lensing potential and on the distortion imprinted in the lensed sources. The inclusion of these galaxies in the lensing modelling allows a better reproduction of the observed multiple lensed features and helps to reconstruct more realistic cluster mass distribution (e.g., see Kassiola et al., 1992). A third component is also used to describe the *external shear*. It takes into account the external contribution to the light deflection caused by the environment in which the lens resides.

The analytic profiles of the mass components are defined through a set of parameters which we need to constrain in the lensing analysis. For example, the large scale dark halo is often modelled with a Navarro-Frenk-White (NFW) profile, characterized by a scale radius r_s and density ρ_s of the halo (see Sec. 3.3). Each mass component, i.e. the smooth dark halo, the external shear and each cluster member included in the model, introduces several parameters related to the particular analytic profile used, other than the parameters related to position, orientation and ellipticity.

Given the total set of parameters \mathbf{p} of the mass components, the lens equation reads

$$\vec{\beta}_i = \vec{\theta}_i - \vec{\alpha}(\vec{\theta}, \mathbf{p}), \quad (4.2)$$

where $\vec{\theta}_i$ are the positions of the lensed images use to constrain the cluster mass.

The number of free parameters grows rapidly as we add mass components to the cluster and, as a consequence, a large number of constraints is needed as well.

Strong lensing parametric analyses search for the set of parameters \mathbf{p} which better reproduces the observed multiple images. It uses a standard χ^2 minimization of the observed and predicted positions of the multiple images.

Eq. 4.2 can be solved in the source or in the image plane. Solving it in the source plane is faster and easier, since the observed images positions $\vec{\theta}_i$ are projected in the source plane and

then the minimization is performed on the source positions β_i . However the astrometric uncertainties are known on the image plane and not on the source plane, thus a correct analysis requires the minimization to be performed in the image plane.

In source plane the χ^2 is defined as

$$\chi_{src}^2 = \sum \left(\frac{\vec{\beta} - \beta_i(\vec{\theta}_i)}{\mu_i \sigma_i} \right)^2 \quad (4.3)$$

where β is the unknown position of the source, β_i are the projections in the source plane of observed positions θ_i , σ_i are the positional errors of the i -th image and μ_i are the respective lensing magnifications. This minimization is usually performed to restrict the space of free parameters which lead to a good reproduction of the observed images and then the analysis is performed through minimization in the image plane.

The χ_{img}^2 defined in the image plane is

$$\chi_{img}^2 = \sum \left(\frac{\vec{\theta}(\vec{\beta}) - \vec{\theta}_i}{\sigma_i} \right)^2. \quad (4.4)$$

The minimal χ^2 provides the values of the free parameters \mathbf{p} for which the scatter between the observed and the predicted positions of the lensed images is minimal.

To perform the strong lensing analyses of clusters of galaxies we use the strong lensing parametric mass modelling software 'Gravitational Lens Efficient Explorer' (GLEE), developed by S. H. Suyu and A. Halkola (Suyu & Halkola, 2010; Suyu et al., 2012). Given information as positions and redshifts of multiple images and using analytic models to describe the mass profiles of the lenses, the code yields the best fitting model which reproduces the observed images. It uses a simulated annealing minimisation in the source and/or image planes. A Monte Carlo Markov Chain (MCMC) sampling is then used to find the most probable parameters and uncertainties for the model. In addition, the surface brightness reconstruction of lensed images can be performed through a linear inversion method (see Warren & Dye, 2003). It reconstructs the pixellated brightness distribution of the source, with regularization of the source intensity through a Bayesian analysis (see Suyu et al., 2006, for a detailed description of this technique).

4.2.1 Cluster Mass components and galaxy scaling relations

In order to model the total mass distribution of galaxy clusters using the strong lensing parametric analysis, we consider the cluster as composed of two main components, a smooth large scale dark halo which describes the cluster dark halo and the intra cluster gas, and the cluster galaxy component composed of the small scale sub-halos associated with the galaxies. We describe the smooth dark halo (DH) mass component of the cluster with a PIEMD profile (see Sec. 3.3.5). The PIEMD projected surface density is

$$\Sigma(R) = \frac{\sigma^2}{2G} \left(\frac{1}{\sqrt{r_c^2 + R^2}} \right), \quad (4.5)$$

where σ is the velocity dispersion of the DH and r_c is its core radius. $R^2 = x^2/(1+e)^2 + y^2/(1-e)^2$ gives the 2D radius for the elliptical profile with ellipticity e .

The velocity dispersion tunes the amplitude of the mass of the halo and can be converted to the Einstein radius of the system. For a singular isothermal sphere the θ_E and velocity dispersion of the halo are related by

$$\theta_E = 4\pi \left(\frac{\sigma}{c}\right)^2 \frac{D_{ds}}{D_s} = \Theta_E \frac{D_{ds}}{D_s} \quad (4.6)$$

where θ_E and Θ_E are in arcseconds, c is the speed of light, D_S is the distance of the lensed source and D_{LS} is the distance between the lens and the source. Θ_E is the *Einstein parameter*, which corresponds to the Einstein radius for an hypothetical source which satisfies $D_{LS}/D_S = 1$. Using strong lensing analyses we measure the Einstein parameters Θ_E associated with the mass distribution of the lens. Non singular elliptical mass distribution, Θ_E corresponds to the Einstein radius when the ellipticity and core radius go to zero ($e, r_{core} \rightarrow 0$). In this work we use the Einstein parameter Θ_E to describe the mass amplitude of the lens halos.

The galaxy components are modelled with dPIE profiles (see Sec. 3.3.6) which have projected surface mass density

$$\Sigma(R) = \frac{\sigma^2}{2GR} \frac{r_{tr}^2}{(r_{tr}^2 - r_c^2)} \left(\frac{1}{\sqrt{1 + r_c^2/R^2}} - \frac{1}{\sqrt{1 + r_{tr}^2/R^2}} \right) \quad (4.7)$$

where $R^2 = x^2/(1+e)^2 + y^2/(1-e)^2$, e is the ellipticity, σ is the halo velocity dispersion, r_c and r_{tr} are the core and scale radius respectively. We adopt vanishing core radii for the galaxies' profiles, so that we have only 2 free parameters (the velocity dispersion σ and the truncation radius r_{tr}) for each galaxy. The number of cluster members in the cluster core is usually large (~ 100), thus the galaxy mass component introduces a large number of free parameters in the lensing model. To reduce this large number of free parameters, we adopt luminosity scaling relations to scale the velocity dispersions σ and the truncation radii r_{tr} of the galaxies with respect to their luminosity, as in Halkola et al. (2007) and Eichner et al. (2013).

Given the Faber-Jackson relation, the central velocity dispersion of early type galaxies is proportional to a power law of the luminosity. Thus for the cluster member we adopt

$$\sigma = \sigma_{GR} \left(\frac{L}{L_{GR}} \right)^\delta \quad (4.8)$$

where the amplitude σ_{GR} is the velocity dispersion of a reference galaxy halo with luminosity L_{GR} .

Following Hoekstra et al. (2003), Halkola et al. (2006, 2007) and Limousin et al. (2007), we assume that the truncation radius of galaxy halos scales with luminosity as

$$r_{tr} = r_{tr,GR} \left(\frac{L}{L_{GR}} \right)^\alpha = r_{tr,GR} \left(\frac{\sigma}{\sigma_{GR}} \right)^{\frac{\alpha}{\delta}} \quad (4.9)$$

where $r_{tr,GR}$ is the truncation radius for a galaxy with luminosity L_{GR} . Given Eq. 4.8 and Eq. 4.9, once we fix the exponent δ and α , the free parameters, used to tune the galaxy

mass contribution to the total cluster mass, are reduced to the velocity dispersion σ_{GR} and truncation radius $r_{tr,GR}$ of the reference galaxy.

The total mass-to-light ratio for a galaxy scales as

$$\frac{M_{tot}}{L} \propto L^\epsilon \propto \sigma^{\frac{\epsilon}{\delta}} \quad (4.10)$$

and it is constant for $\epsilon = 0$. Combining Eq. 3.66, 4.8 and 4.9, the total mass scales as

$$M_{tot} \propto \sigma^2 r_{tr} \propto \sigma^{2+\frac{\alpha}{\delta}}. \quad (4.11)$$

Therefore, from Eq. 4.10 and Eq. 4.11, we obtain the following relation for the exponents

$$\alpha = \epsilon - 2\delta + 1, \quad (4.12)$$

which means that if we have knowledge of two of them, we can derive the third one. In the following we will go through some considerations which will help us to fix the value of these exponents.

For elliptical galaxies in clusters, the exponent δ has measurements between 0.25 and 0.3, depending on the filter in which the photometry is extracted (see Ziegler & Bender, 1997; Fritz et al., 2009; Kormendy & Bender, 2013; Focardi & Malavasi, 2012). Measurements from strong and weak lensing analyses yield $\delta = 0.3$ (see Rusin et al., 2003; Brimiouille et al., 2013). Concerning the truncation radius of galaxies in clusters, theoretical studies predict that in dense environment it scales linearly with the galaxies velocity dispersion (see Merritt, 1983) and, given Eq. 3.66, this yields $M_{tot} \propto \sigma^3$. However, from Eq. 4.10, the total galaxy mass can be written as $M_{tot} \propto \sigma^{\frac{\epsilon+1}{\delta}}$, and thus we conclude that $\epsilon = 3\delta - 1$.

In summary, we expect δ to be within $[0.25, 0.3]$, which implies ϵ to be within $[-0.3, 0.2]$. The lower limit $\epsilon = -0.3$ is the case in which the galaxy halos mass has a value as expected for completed stripping process (e.g., see Merritt, 1983). On the contrary, $\epsilon = 0.2$ is the case in which the galaxies have suffered no stripping at all and fulfill the scaling relations in fields (e.g., see Brimiouille et al., 2013).

For relaxed galaxy clusters we expect the galaxy halos stripping processes to be completed in the core. However, to take into account still ongoing halo stripping, as we did in Eichner et al. (2013), we fix the exponents of the mass to light luminosity relations to $\epsilon = 0$, which is in between the value expected for not yet started, and completed stripping halos. Given Eq. 4.12, implies

$$\alpha = 1 - 2\delta. \quad (4.13)$$

In Eichner et al. (2013) we confirmed that using $\delta = 0.3$ or $\delta = 0.25$ does not affect the results on the halos sizes.

Once we fix the exponents of the luminosity scaling relations, the only parameters we need to determine to define the galaxy mass component are the amplitudes of the scaling relations, σ_{GR} and $r_{tr,GR}$.

Finally, we also allow for an external shear component, to take into account the large scale environment contribution to the lensing potential.

4.2.2 Multiple images

To constrain the mass distribution of cluster cores through strong lensing analyses we use the information available from photometric and spectroscopic datasets on the lensing feature

identified in the cluster field.

Using photometric data, lensed images can be identified in the core of clusters thanks to the distorted shape they have due to the lensing effect. In addition, when multiband imaging data are available, we take advantage that lensing is achromatic, to identify multiple images of the same source which are expected to show similar colours.

The observed positions θ_i and relative fluxes of the multiple images are the main constraints used in strong lensing analyses, since they all depend the mass distribution of the lens and on the redshifts of the lensed sources. The positions of the multiple images can be measured with accuracy given the high resolution images of present day instruments. In this work we perform analyses of cluster cores using Hubble Space Telescope (HST) multiband datasets, which have pixelscale of 65 milliarcseconds (mas) per pixel. However, Host (2012) and D'Aloisio & Natarajan (2011) show that, on cluster scales, multiple image positions are usually reproduced with accuracy ~ 1 -2 arcseconds due to density fluctuations along the line of sight. Grillo et al. (2014) show that a higher precision can be reached through detailed strong lensing analysis of cluster cores. They predict the positions of the observed multiple images in the core of MACS J0416 with a median offset of $0.3''$. Starting with realistic uncertainties on the multiple images positions is important in the modelling procedure, because underestimating such errors will lead to underestimated uncertainties on the mass model free parameters. Thus we adopt a positional uncertainty of $1''$ on the multiple images positions, even though from the HST images we can estimate such positions with an accuracy of $0.065''$.

Spectroscopic measurement of the redshift of the lensed sources is also a strong constraints, since it allows to place the D_S of the sources. When we lack of spectroscopic measurements, photometric redshift measurements, when robust, can supply the sources redshifts, or at least they can provide a starting value for the z_S which can be then optimized in the lensing analysis.

The relative fluxes of the multiple images also give constraints for the lensing analysis, being the surface brightness of the sources preserved. However, for highly extended images, the magnification can vary strong across the images, and thus to estimate the unmagnified flux is usually be trivial.

In the analyses presented in this Thesis we will use as constraints the observed positions of the multiple images and their spectroscopic redshifts, when available. When lacking of spectroscopic z_s we estimate the photometric redshifts of the multiple images using the SED-fitting routine **LePhare**¹ (Arnouts et al., 1999; Ilbert et al., 2006) (see Sec.a383-rxj2248 for more details).

¹<http://www.cfht.hawaii.edu/~arnouts/lephare.html>

The CLASH Survey

The work presented in this thesis has been performed using high spatial resolution Hubble Space Telescope (HST) data from the “Cluster Lensing And Supernovae with Hubble” Survey (hereafter CLASH), see Postman et al. (2012a).

By combining space-based and ground-based photometric and spectroscopic observations (Rosati et al. 2015, in prep.) of 25 massive galaxy clusters, this survey aims to investigate and characterize structures in the Universe. Through strong and weak lensing analyses, the deep and high resolution photometric data together with the spectroscopic measurements of cluster members, field galaxies and lensing features are used to constrain in details the total mass distribution and concentration of clusters of galaxies, as well as the small scale mass distribution associated with the galaxies in the clusters.

Moreover, since galaxy clusters act as *Gravitational Telescopes*, the survey aims to identify and investigate the high redshift ($z > 5$) galaxies lensed by the clusters to constraints the population of the high redshift Universe. Finally, space-based parallel observations of fields around the 25 targeted clusters are taken to detect Type-Ia Supernovae out to redshift $z \sim 2.5$ to improve the constraints on their evolution and in general on the dark energy equation of state.

5.1 The CLASH Cluster Sample

The full CLASH cluster sample contains 25 massive galaxy clusters. 20 of these clusters were selected using X-ray archival data. Since one of the main goal of the survey is to investigate the mass distribution and concentration of galaxy clusters, no lensing information was used to select these 20 clusters to avoid any bias deriving from lensing, as preferentially alignments along the line of sight. These are massive clusters, having $T_x \geq 5$ keV. In addition they are dynamically relaxed, as their X-ray images reveal well defined surface brightness peaks with concentric isophotes. They show low ellipticity contours in the X-ray maps, and their BCGs lie at projected distance $r \lesssim 20$ kpc from the X-ray centroid.

The other 5 clusters of the sample were selected as gravitational lenses with an exceptional lensing strength (they have large Einstein radii, $\theta_E > 35''$ for a source at $z_s = 2$). These were selected mainly for their power to magnify high redshift galaxies and thus to shed light on the high redshift Universe.

The 25 galaxy clusters span the redshift range $0.18 < z_{cl} < 0.90$ and have masses between

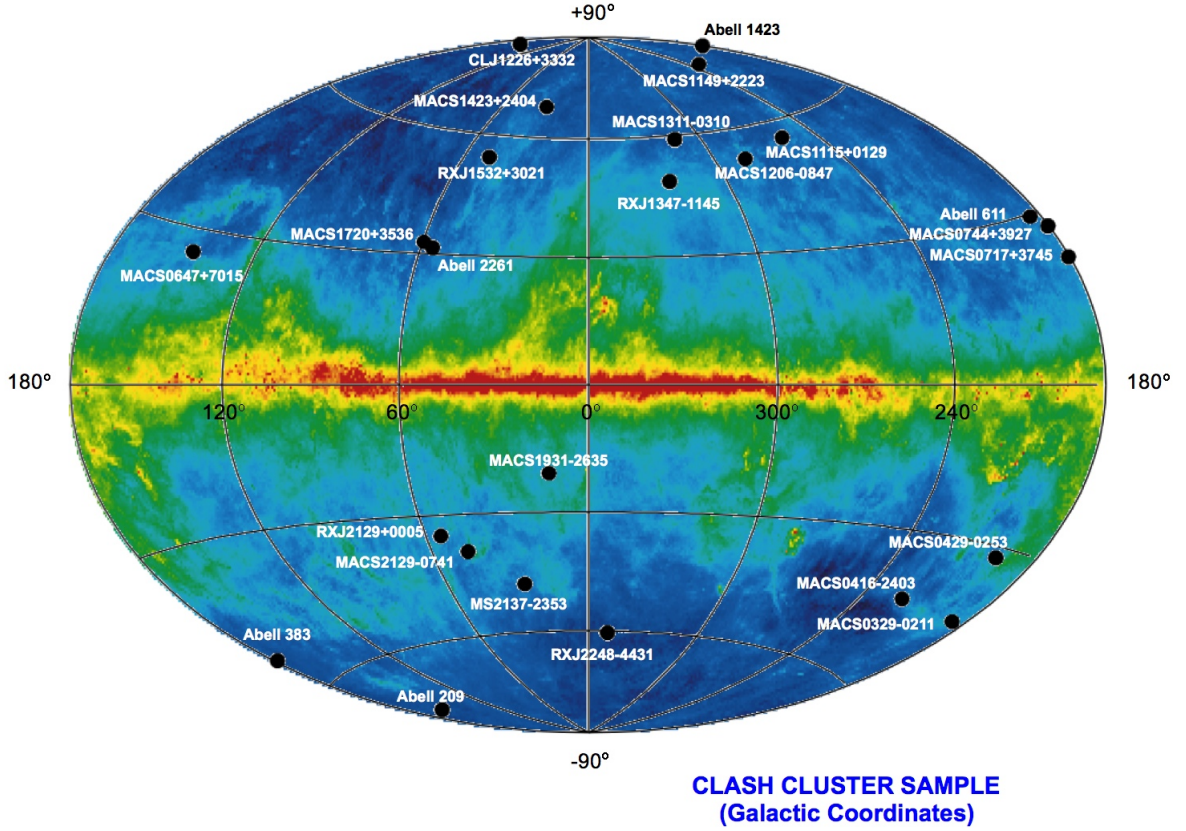


Figure 5.1: Distribution of the CLASH clusters on the sky map, in galactic coordinates (source: <http://www.stsci.edu/postman/CLASH/>).

~ 5 to $\sim 30 \times 10^{14} M_{\odot}$, thus they allow to probe the cluster concentration $c(M, z)$ on a wide range of M and z .

In Fig.5.1 we show the position of the 25 CLASH clusters on the sky. In Tab. 5.1 we provide the list of the clusters with their coordinates and redshifts.

5.2 Dataset and Catalogs

The CLASH survey is a 524-orbit Multi-Cycle-Treasure program (Postman et al., 2012a). The observations were taken over a 3 annual HST observing periods, corresponding to cycles 18, 19 and 20. The clusters were observed in 16 broadband filters covering the wide wavelength range of 2000-17000Å from the near-ultraviolet (NUV) to the near-infrared (NIR) using the Advanced Camera for Surveys (Ford et al., 2003, ACS,) and the Wide Field Camera 3 (Kimble et al., 2008, WFC3) mounted on HST. The NUV range is covered with 4 broadband filters of the NUV channel of WFC3 (WFC3/UVIS), the optical range with 7 filters of the ACS/WFC and the NIR range is covered with 5 filters of the NIR channel WFC3/IR. In Fig. 5.2 the transmission curves of the 16 filters are shown.

A wide photometric dataset is crucial to accurately measure photometric redshifts z_{ph} (Jouvel et al., 2014; Postman et al., 2012a), in particular for lensed and high- z sources, which are

Cluster	RA (J2000)	Dec (J2000)	z_{cl}	CLASH-VLT
Massive Relaxed X-ray selected Clusters:				
Abell 209	01:31:52.54	-13:36:40.4	0.206	yes
Abell 383	02:48:03.40	-03:31:44.9	0.187	yes
MACSJ0329-0211	03:29:41.56	-02:11:46.1	0.450	yes
MACSJ0429-0253	04:29:36.05	-02:53:06.1	0.399	yes
MACSJ0744+3927	07:44:52.82	+39:27:26.9	0.686	no
Abell 611	08:00:56.82	+36:03:23.6	0.288	no
Abell 963	10:17:03.60	+39:02:49.0	0.206	no
MACSJ1115+0129	11:15:51.90	+01:29:55.1	0.355	yes
MACSJ1206-0847	12:06:12.09	-08:48:04.4	0.439	yes
CLJ1226+3332	12:26:58.25	+33:32:48.6	0.890	no
MACSJ1311-0310	13:11:01.80	-03:10:39.8	0.494	yes
RXJ1347-1145	13:47:31.05	-11:45:12.6	0.451	yes
MACSJ1423+2404	14:23:47.88	+24:04:42.5	0.545	no
RXJ1532+3021	15:32:53.78	+30:20:59.4	0.363	no
MACSJ1720+3536	17:20:16.78	+35:36:26.5	0.387	no
Abell 2261	17:22:27.18	+32:07:57.3	0.224	no
MACSJ1931-2635	19:31:49.62	-26:34:32.9	0.352	yes
RXJ2129+0005	21:29:39.96	+00:05:21.2	0.234	yes
MS2137-2353	21:40:15.17	-23:39:40.2	0.313	yes
RXJ2248-4431	22:48:43.96	-44:31:51.3	0.348	yes
High Lensing Efficiency Clusters:				
MACSJ0416-2403	04:16:08.38	-24:04:20.8	0.396	yes
MACSJ0647+7015	06:47:50.27	+70:14:55.0	0.584	no
MACSJ0717+3745	07:17:32.63	+37:44:59.7	0.548	no
MACSJ1149+2223	11:49:35.69	+22:23:54.6	0.544	no
MACSJ2129-0741	21:29:26.06	-07:41:28.8	0.570	yes

Table 5.1: List of the 25 clusters observed within the CLASH survey: column (1) cluster, column (2)-(3) coordinates of the cluster centre, column (4) cluster redshift, column (5) included in the CLASH-VLT survey, see 5.3.

often too faint to be spectroscopically observed in reasonable exposure times. The knowledge of the redshifts of lensed sources is necessary to robustly trace the mass distribution in the core of galaxy clusters using strong lensing. Accurate z_{ph} estimations of $z > 1$ sources allow to select robust high- z photometric candidates and investigate the properties of the galaxy population of the high- z Universe. The range covered by the 16 HST filters allow to identify the Lyman limit (at the restframe wavelength $\lambda = 912\text{\AA}$) and Lyman- α line (at the restframe wavelength $\lambda = 1216\text{\AA}$) from $z \sim 1.5$ up to $z \sim 10$. In particular, the NUV filters allow to break the degeneracy in the z_{ph} estimations between the Balmer break of early type galaxies at $z \sim 0.2$ and the Lyman break of star-forming galaxies at $z \sim 3$, while the NIR filters allow to break the same degeneracy between early type galaxies at $z \gtrsim 1$ and star-forming galaxies at $z \gtrsim 5$.

Each cluster was observed with 20 orbits, divided between the HST/ACS and HST/WFC3 filters. All the filters together cover a field of view (FOV) of ~ 4.08 square arcminutes centred on the clusters. While the clusters were observed with one of the HST camera, parallel observations were taken with the other camera at ~ 6 arcminutes distance from the cluster centre. The parallel field observations are used to search for the Type-Ia Supernovae out to $z \sim 2.5$. The observing times were set up to reach a 10σ depth of 26 AB mag in all the filters except for the F814W and the F160W filters for which the 10σ depth of ~ 27 AB mag was required to identify high- z lensed candidate.

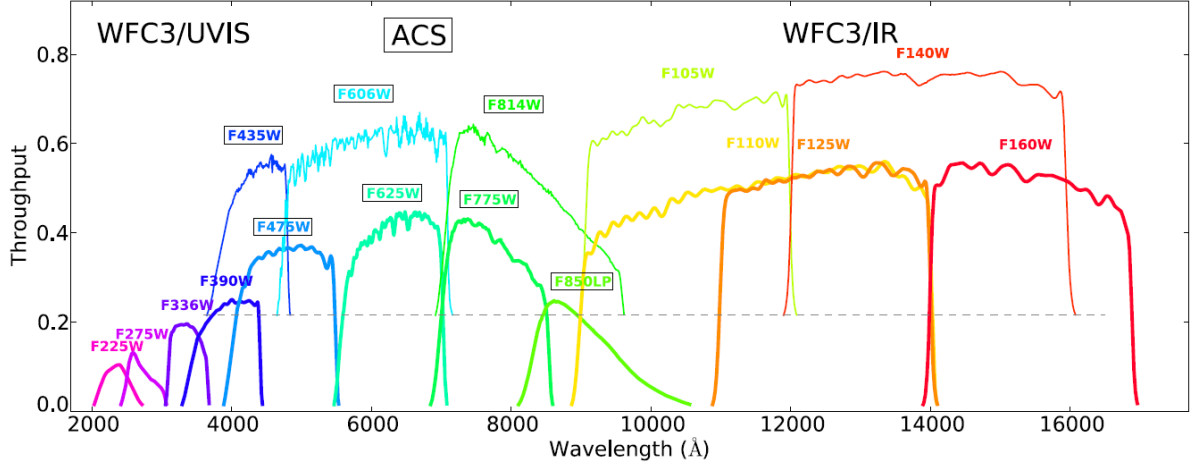


Figure 5.2: Throughput curves of the 16 HST/ACS and HST/WFC3 filters used in the CLASH survey. Some of the filters overlap with each others, thus for clarity in the plot some filters are shown with a vertical offset of 0.2 (dashed line) (see Postman et al., 2012a).

The images acquired for each cluster are processed with the `MoosaicDrizzle` pipeline (Koekemoer et al., 2011), which co-adds and aligns the several exposures in each filter. To add and align the images the pipeline uses deep ground-based catalogues as starting reference, then it iterates the alignment process using the CLASH images themselves, to reduce shifts and rotations between the exposures. The final products of the pipeline are mosaic drizzled science images, with respective inverse variance images, which are used as weight maps for each filter. For each cluster two different sets of images are generated with different pixelscale, one drizzled to 30mas/pixel and the other to 65mas/pixel.

All the reduced images, as well as the raw data, are public and available at the `stsci archive`¹. For each cluster the photometric catalogues of the sources extracted in the images are also public. The catalogues are produced using `SExtractor 2.5.0` (Bertin & Arnouts, 1996), which detect sources in each image and extract their photometry. It is run in *dual mode*, which means that one chosen image is used to detect the sources (this is called *detection image*) and then the photometry for all these sources is extracted respectively in each image of the dataset. For the detection it is required to have at least 9 contiguous pixels at the observed background RMS (i.e. `DETECT_MIN_AREA=9`).

Two catalogues are generated: one using as detection image the weighted sum of all the ACS and WFC3/IR images and the other using the weighted sum of all the WFC3/IR. The latter one is created with the aim to identify $z > 6$ sources, which are detected only in the NIR images. Each catalogue provides the isophotal photometry in all the CLASH filters for each detected source. They are given the isophotal fluxes (in electron/seconds) and the respective AB magnitudes with their uncertainties computed as:

$$\text{mag} = \text{zeropoint} - 2.5 * \log_{10}(\text{flux}) \quad (5.1)$$

$$\delta\text{mag} = 2.5 * \log_{10}(1 + \delta\text{flux}/\text{flux}) \quad (5.2)$$

¹<http://archive.stsci.edu/prepds/clash/>

Filter	Instrument	λ_{eff} (nm)	Width (nm)
F225W	WFC3/UVIS	235.9	46.7
F275W	WFC3/UVIS	270.4	39.8
F336W	WFC3/UVIS	335.5	51.1
F390W	WFC3/UVIS	392.1	89.6
F435W	ACS/WFC	432.8	29.8
F475W	ACS/WFC	474.7	42.0
F606W	ACS/WFC	592.1	67.2
F625W	ACS/WFC	631.1	41.5
F775W	ACS/WFC	769.2	43.4
F814W	ACS/WFC	805.7	65.2
F850LP	ACS/WFC	903.3	52.6
F105w	WFC3/IR	1055.2	265.0
F110W	WFC3/IR	1153.4	443.0
F125W	WFC3/IR	1248.6	284.5
F140W	WFC3/IR	1392.3	384.0
F160W	WFC3/IR	1536.9	268.3

Table 5.2: List of the 16 HST filters of the CLASH survey: column (1) filters included in the survey, column (2) HST instrument, (3) effective wavelength and (4) width of the filter.

The zeropoints and dust extinctions are also provided for each filter. In addition the photometric redshifts measured from the observed photometry are given together with their 95% confidence level. These are computed with *Bayesian Photometric Redshifts* (BPZ, Benítez, 2000), which is a spectral energy distribution (SED) fitting code. The photometric redshift are intended only for galaxies.

Jouvel et al. (2014) perform a detailed analysis of the improvements in computing photometric redshifts using a such wide photometric dataset as the CLASH one. They used both the publicly available SED fitting codes BPZ and *LePhare* to estimate the photometric redshifts for galaxies and lensing features observed in the field of MACS J1206.2-0847, for which the spectroscopic redshift is known. They reach a precision in the redshift prediction of 3%(1+z) for the lensed arcs and of 4%(1+z) for the galaxies in the cluster field, see Fig. 5.3

In the work presented in this thesis we use multiband photometric catalogs that we generate using similar parameters as for the public CLASH catalogs, but modified to match our needs in function of our scientific goals. Using *SExtractor* 2.5.0 (Bertin & Arnouts, 1996), we create multiband photometric catalogues of galaxy fluxes extracted within 0.6" (9 pixels) diameter aperture. We run *SExtractor* in dual image mode, using as detection image the weighted sum of all the WFC3IR images.

We also estimate independently the photometric redshifts for cluster members and lensing features, using the spectral energy distribution (SED) fitting code *LePhare*² (Arnouts et al., 1999). The package computes photometric redshifts through a standard χ^2 fitting method to fit the observed fluxes with template spectra, where the χ^2 is defined as (Ilbert et al., 2006)

$$\chi^2(z, T, A) = \sum_{f=1}^{N_f} \left(\frac{F_{\text{obs}}^f - A \times F_{\text{pred}}^f(z, T)}{\sigma_{\text{obs}}^f} \right)^2 \quad (5.3)$$

where the index f refers to the filters of the dataset, N_f is the number of filters, F_{obs}^f is

²<http://www.cfht.hawaii.edu/~arnouts/lephare.html>

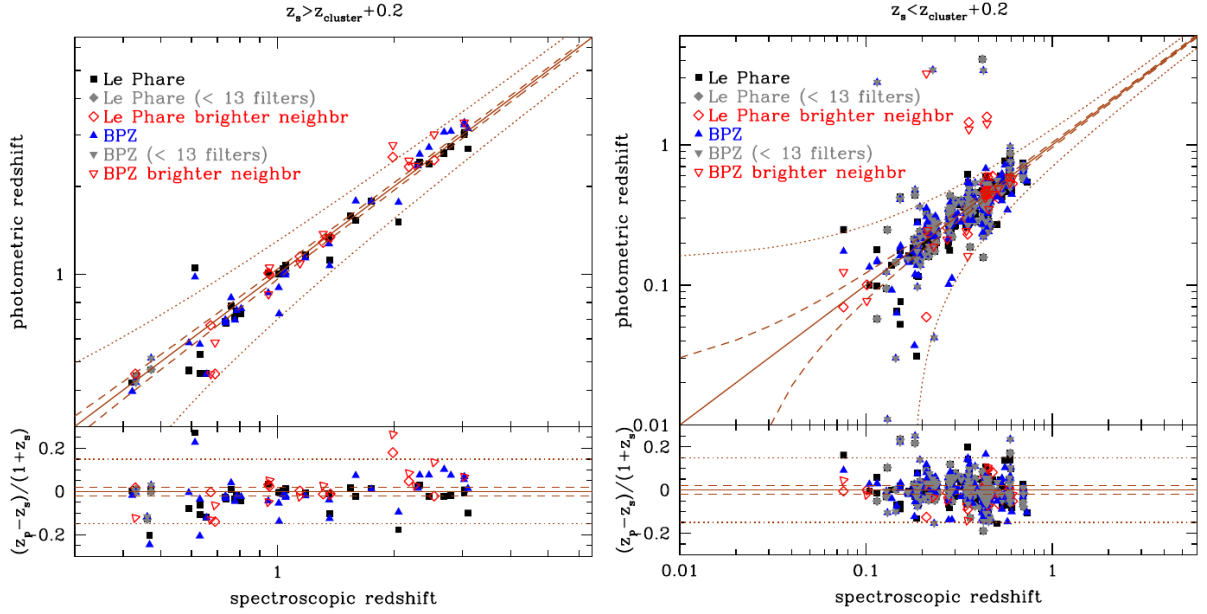


Figure 5.3: Spectroscopic versus photometric redshifts for lensed galaxies (at $z_s > z_{cl} + 0.2$, left panel) and cluster members and foreground galaxies (with $z_s \leq z_{cl} + 0.2$, right panel) in the field of MACS J1206. Black squares and blue triangles are results from LePhare and BPZ respectively, for galaxies which have secure spectroscopic redshift and which are detected at least in 7 bands, with $S/N > 10$ in the F775W filter. Gray diamonds and triangles are galaxies with secure redshift observed in less than 13 bands. Red empty diamonds and triangles are galaxies with a brighter neighbor within $3''$. Figure from Jouvel et al. (2014).

the observed flux, σ_{obs}^f is its error, $F_{\text{pred}}^f(z, T)$ is the estimated flux for the redshift z and the spectral type T , and finally A is a normalization factor. The photometric redshift is computed by searching for the solution (z, T, A) for which the χ^2 is minimal.

Galaxy, QSO and star SED templates can be used in the templates set; moreover, extinction laws, emission lines and constraints on the range of redshift, age, absolute magnitude and other physical parameters can be included in the fitting procedure (see Arnouts et al., 1999; Ilbert et al., 2006).

The output files give the photometric redshift values for the best fits each for the star, QSO and galaxy templates: in particular for the galaxy solutions, LePhare computes the redshift probability distribution function ($\text{PDF}(z)$) and gives also the secondary solution from the $\text{PDF}(z)$, if available.

We adopt as galaxy template set the COSMOS libraries (Ilbert et al., 2009), which include 31 templates describing SEDs of ellipticals, spirals and starburst galaxies. To take into account the extinction due to the interstellar medium (ISM) we apply the Calzetti extinction law (Calzetti et al., 2000) to the starburst templates, and the SMC Prevot law (Prevot et al., 1984) to the Sc and Sd templates. We also include emission lines, and add prior information on the redshift distribution: for that the code uses an $N(z)$ prior by type computed from the VVDS survey (see Ilbert et al., 2006). As QSOs template set we use the SWIRE library (Polletta et al., 2006; Hatziminaoglou et al., 2005; Gregg et al., 2002) including type 1, type 2, Seyfert 1.8 and Seyfert 2 AGN templates. Finally as stellar templates we adopt the Pickles stellar library (Pickles, 1998), which include all the normal spectral types, plus metal-poor F-K dwarves and G-K giants.

Greisel et al. (2013) carried out a systematic analysis of luminous red galaxies from the Sloan Digital Sky Survey (SDSS) with $0 < z < 0.5$, which shows that local SED templates do not match within appropriate level the observed colours for galaxies at different redshifts, due to the evolution of the SEDs with redshift. Thus we expect that, using **LePhare** libraries to estimate the cluster members photo- z , we predict different colours from what we actually observe in some filters. Indeed when we estimate the photometric redshift for the sources extracted in our images, the cluster appears to be at $z \sim 0.4$ from the z_{ph} histogram. One way to account for the template mismatch of red SEDs at the $z_{\text{cl}} = 0.348$ is to apply some offsets correction to our photometry. To estimate these offsets we use the sample of spectroscopically confirmed cluster members. In **LePhare** they are estimated through a colour adaptive method which finds the template that best fits the observed photometry given the fixed z_{sp} of the galaxies, and minimizes the offset between the observed and predicted magnitudes in each filter.

5.3 The CLASH-VLT Spectroscopic Survey

The CLASH Very Large Telescope Survey (CLASH-VLT) is a panoramic spectroscopic survey of the 14 CLASH clusters which are in the southern hemisphere (Rosati et al., in prep.). It is a Large Program (*Dark Matter Mass Distributions of Hubble Treasury Clusters and the Foundations of Λ CDM Structure Formation Models*, LP186.A-0798, P.I. Rosati P.) of 200 hours of observing time with the VISual Multi-Object Spectrograph (VIMOS, Le Fèvre et al., 2003) mounted on the ESO-VLT. The survey aims to measure the spectroscopic redshift for ~ 500 cluster members, over 3-5 Mpc from the centre of each clusters, to perform accurate dynamical analyses and reconstruct the mass profiles of the CLASH clusters. In addition it aims to follow up lensed features and high- z magnified candidates identified in the field of the clusters. The spectroscopic measurements of lensing features helps to put stronger constraints in the lensing analysis and thus to achieve higher accuracy on the cluster mass distribution. Finally robust high- z photometric candidates magnified by the clusters are selected in the CLASH multiband dataset for spectroscopic follow up with VIMOS to confirm their high- z nature and investigate their spectral properties.

The observations are taken with Low Resolution Blue (LR-Blue) and Median Resolution Red (MR-Red) grisms. The LR-Blue grism covers the wavelength range 3700-6700Å with resolution of 28Å, while the MR-Red grism covers the λ range 4800-10000Å with resolution of 13Å. The masks have slits of 1'' width. Each cluster is observed with 4 to 8 pointings, depending if mainly bright sources are targeted, as cluster members, or if longer total exposure time are required to measure the redshift of faint targets, as can be the lensed sources. In each pointing, one of the 4 quadrants of VIMOS always observes the cluster core, to have deeper spectra for the sources in the core. The other three quadrants are rotated in each pointing to cover in total as much is possible the field around the cluster core. are used to follow up lensing features, cluster and field galaxies and high- z candidates.

The acquired spectra are processed using the Vimos Pipeline Graphical Interface (VIPGI, Scodreggio et al., 2005) for standard reduction (bias and sky subtraction, flat-fielding) and for wavelength calibration.

In Table 5.3 the list of the cluster observed within the CLASH-VLT survey is provided, with respective information on the observation status, and preliminary redshifts results.

Cluster	Run	Observing Time	Status	Cluster members	Lensed images
Abell 383	C P86	13:33:45	Complete	234	8
MACS1206	C P86	16:36:00	Complete	613	17
RXJ1347	C P86	8:56:30	Complete	342	11
MACS2129	D P87	9:10:30	Complete	48	16
MS2137	D P87	18:20:00	Complete	416	13
MACS0329	E P88	10:42:15	Complete	108	6
MACS1115	E P88	14:48:00	Complete	502	17
Abell 209	E P88	12:17:30	Complete	521	13
MACS0416	E P88	11:17:30	Complete	844	12
MACS0429	E P88	0:00:00	Deleted	0	0
MACS1931	F P89	11:17:00	Complete	251	8
RXJ2129	F P89	12:14:00	Complete	0	10
RXJ2248	F P89	17:30:00	Complete	1045	15
MACS1311	F P89	0:00:00	In Progress	0	0

Table 5.3: Summary of the 14 CLASH clusters targeted with VIMOS: column (1) cluster, column (2) VIMOS observation period, column (3) Total observing time, column (4) status of the observations, column (5)-(6) number of redshifts resulting from the preliminary reduction of the completed observations for the cluster members and lensed sources.

MACS0429 was removed from the sample of clusters to observe.

CLASH: $z \sim 6$ young galaxy candidate quintuply lensed by the frontier field cluster RXC J2248.7-4431

A. Monna^{1,2}, S. Seitz^{1,2}, N. Greisel^{1,2}, T. Eichner^{1,2}, N. Drory^{2,3}, M. Postman⁴, A. Zitrin⁵, D. Coe⁴, A. Halkola, S. H. Suyu⁶, C. Grillo⁷, P. Rosati⁸, D. Lemze⁹, I. Balestra², J. Snigula^{1,2}, L. Bradley⁴, K. Umetsu⁶, A. Koekemoer⁴, M. Bartelmann⁵, N. Benítez¹⁰, R. Bouwens¹¹, T. Broadhurst¹², M. Donahue¹³, H. Ford⁹, O. Host⁷, L. Infante¹⁴, Y. Jimenez-Teja¹⁰, S. Jouvel^{15,16}, D. Kelson¹⁷, O. Lahav¹⁵, E. Medezinski⁹, P. Melchior¹⁸, M. Meneghetti¹⁹, J. Merten²⁰, A. Molino¹⁰, J. Moustakas²¹, L. Moustakas²⁰, M. Nonino²², W. Zheng⁹

¹University Observatory Munich, Scheinerstrasse 1, 81679 Munich, Germany

²Max Planck Institute for Extraterrestrial Physics, Giessenbachstrasse, 85748 Garching, Germany

³Instituto de Astronomía, Universidad Nacional Autónoma de México, Avenida Universidad 3000, 04510, D.F. Mexico

⁴Space Telescope Science Institute, 3700 San Martin Drive, Baltimore, MD 21208, USA

⁵Institut für Theoretische Astrophysik, ZAH, Albert-Ueberle-Str. e 2, 69120 Heidelberg, Germany

⁶Institute of Astronomy and Astrophysics, Academia Sinica, P.O. Box 23-141, Taipei 10617, Taiwan

⁷Dark Cosmology Centre, Niels Bohr Institute, University of Copenhagen, Juliane Maries Vej 30, 2100 Copenhagen, Denmark

⁸ESO-European Southern Observatory, D-85748 Garching bei München, Germany

⁹Department of Physics and Astronomy, The Johns Hopkins University, 3400 North Charles Street, Baltimore, MD 21218, USA

¹⁰Instituto de Astrofísica de Andalucía (CSIC), Camino Bajo de Hueter 24, Granada 18008, Spain

¹¹Leiden Observatory, Leiden University, P. O. Box 9513, 2300 RA Leiden, The Netherlands

¹²Department of Theoretical Physics, University of the Basque Country, P. O. Box 644, 48080 Bilbao, Spain

¹³Department of Physics and Astronomy, Michigan State University, East Lansing, MI 48824, USA

¹⁴Departamento de Astronomía y Astrofísica, Pontificia Universidad Católica de Chile, V. Mackenna 4860, Santiago 22, Chile

¹⁵Department of Physics & Astronomy, University College London, Gower Street, London WC1E 6 BT, UK

¹⁶Institut de Ciències de l'Espai (IEEC-CSIC), Bellaterra (Barcelona), Spain

¹⁷Observatories of the Carnegie Institution of Washington, Pasadena, CA 91 101, USA

¹⁸Center for Cosmology and Astro-Particle Physics; The Ohio State University, 191 W. Woodruff Ave., Columbus, Ohio 43210, USA

¹⁹INAF-Astronomical Observatory of BOLOGNA, Via Ranzani 1, 40127 Bologna, Italy

²⁰Jet Propulsion Laboratory, California Institute of Technology, MS 169-327, Pasadena, CA 91109, USA

²¹Siena College, 515 Loudon Road, Loudonville, NY 12211, USA

²²INAF-Osservatorio Astronomico di Trieste, via G.B. Tiepolo 11, 40131 Trieste, Italy

This Chapter is a reproduction of the paper *CLASH: $z \sim 6$ young galaxy candidate quintuply lensed by the frontier field cluster RXC J2248.7-4431* published on the *Monthly Notices of the Royal Astronomical Society Main Journal*, Volume 438, Issue 2, p.1417-1434. Submitted on August, the 11th 2013, accepted for publication on November, the 25th 2013 (Monna et al., 2014a).

AM and SS conducted the analysis presented in this Chapter. TE and NG performed the Strong Lensing and SFH-fitting analyses, respectively. SHS and AH provided the software used to perform the Strong lensing analysis. MP performed the BCG subtraction. All the authors contributed with input to the general discussion.

We present a quintuply lensed $z \sim 6$ candidate discovered in the field of the galaxy cluster RXC J2248.7-4431 ($z \sim 0.348$) targeted within the Cluster Lensing and Supernova survey with Hubble (CLASH) and selected in the deep HST Frontier Fields survey. Thanks to the CLASH 16-band HST imaging, we identify the quintuply lensed $z \sim 6$ candidate as an optical dropout in the inner region of the cluster, the brightest image having $\text{mag}_{\text{AB}} = 24.81 \pm 0.02$ in the f105w filter. We perform a detailed photometric analysis to verify its high- z and lensed nature. We get as photometric redshift $z_{\text{ph}} \sim 5.9$, and given the extended nature and NIR colours of the lensed images, we rule out low- z early type and galactic star contaminants. We perform a strong lensing analysis of the cluster, using 11 families of multiple lensed images identified in the HST images. Our final best model predicts the high- z quintuply lensed system with a position accuracy of $0.8''$. The magnifications of the five images are between 2.4 and 10, which leads to a delensed UV luminosity of $L_{1600} \sim 0.4L_{1600}^*$ at $z = 6$. We also estimate the UV slope from the observed NIR colours, finding a steep $\beta = -2.89 \pm 0.25$. We use singular and composite stellar population SEDs to fit the photometry of the high- z candidate, and we conclude that it is a young (age < 300 Myr) galaxy with mass of $M \sim 10^8 M_{\odot}$, subsolar metallicity ($Z < 0.2Z_{\odot}$) and low dust content ($A_V \sim 0.2 - 0.4$).

6.1 RXC J2248.7-4431

RXC J2248 is a very massive galaxy cluster ($M_{200} > 2.5 \cdot 10^{15} M_{\odot}$) at $z = 0.348$ (Guzzo et al., 2009), see Fig. 6.1. It is part of the ROSAT-ESO Flux-Limited X-ray (REFLEX) survey galaxy cluster sample, and it is the second brightest cluster in this survey, with a luminosity of $L \sim 3 \times 10^{45} \text{ erg s}^{-1}$ in the rest frame 0.1-2.4 KeV interval (Guzzo et al., 2009). Gómez et al. (2012) confirmed 51 cluster members with spectroscopic observations taken with the Gemini Multi-Objects Spectrograph (GMOS), from which they estimate the mean effective velocity dispersion and redshift of the cluster to be $\sigma = 1660_{-150}^{+230} \text{ km/s}$ and $z = 0.3461_{-0.0011}^{+0.0010}$. The galaxy density, obtained using spectroscopically confirmed and candidate (selected from the colour magnitude diagram) cluster members, combined with the X-ray isophotes, reveals several substructures and an elongation in NW-SE direction. The X-ray analysis shows that the X-ray peak emission is shifted by $37'' \pm 9''$ with respect to the galaxy density peak. The combination of optical, spectroscopic and X-ray analysis thus reveals traces of recent merging activities. Gruen et al. (2013) performed a multi-wavelength weak lensing analysis of this cluster using deep UBVRIz imaging data from the ESO-2.2m Wide Field Imager, with a total integration time of about 50 hours. They accurately measured the 2D mass distribution and mass profile for scales larger than 500 kpc, out to 4 Mpc. Their mass map shows that the main dark matter halo is centred on the brightest cluster galaxy (BCG), and that dark matter substructures in and around the cluster coincide with galaxy density substructures, dominated by red galaxies. Fitting the dark halo with an NFW profile, they obtain the values $c_{200m} = 2.6_{-1.0}^{+1.5}$ and $M_{200m} = 33.1_{-6.8}^{+9.6} \cdot 10^{14} M_{\odot}$, in agreement with previous X-ray and SZ estimates. Due to its strong lensing strength, RXC J2248 is selected in the sample of 6 galaxy clusters of the deep Frontier Fields (FF) HST survey¹, which aims to map the cluster dark matter to the highest precision and derive magnification maps to investigate the high redshift Universe.

¹<http://www.stsci.edu/hst/campaigns/frontier-fields/>

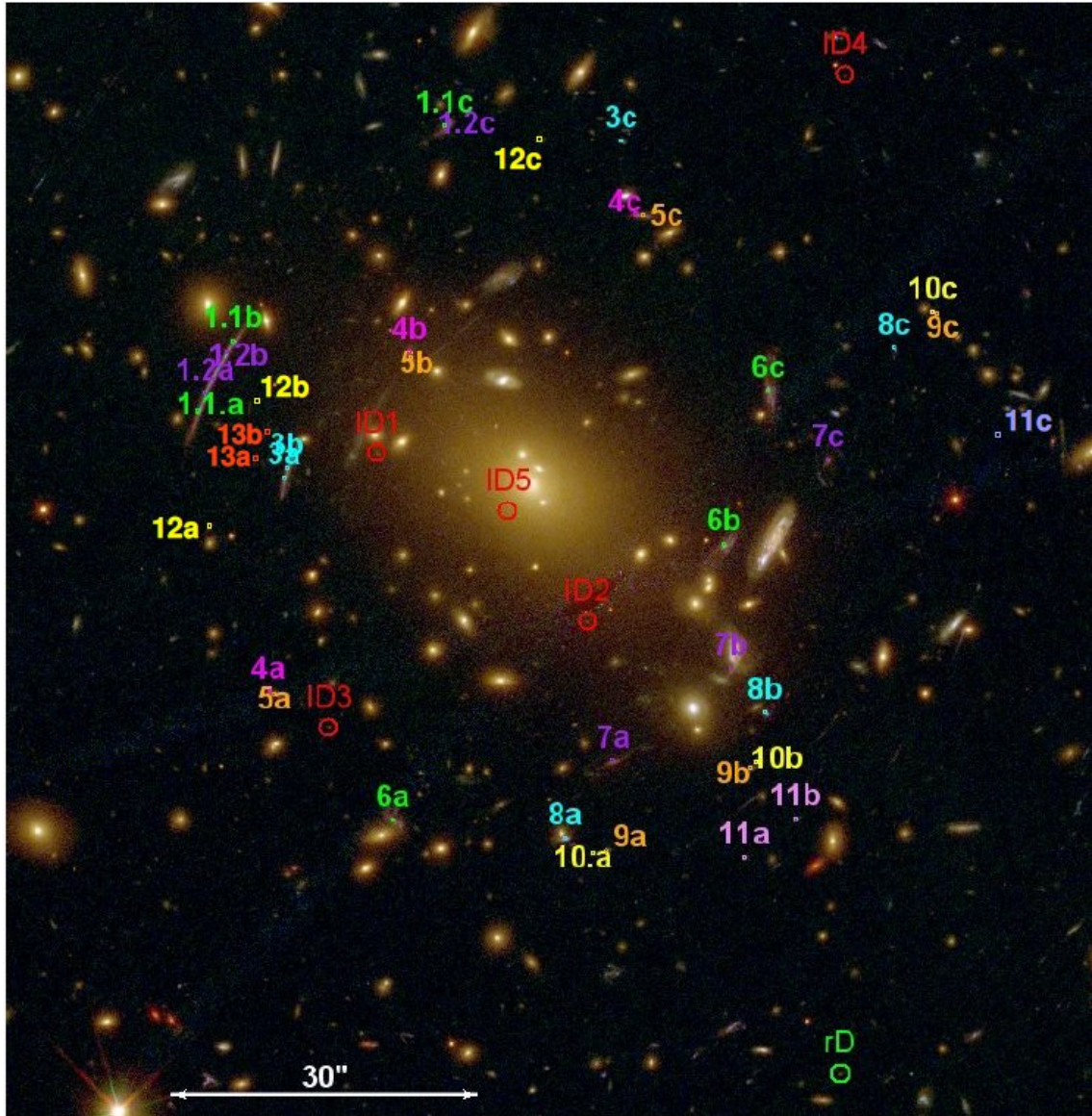


Figure 6.1: $1.7' \times 1.7'$ colour composite image of RXC J2248.7-4431 core, from the HST 16-band of the CLASH survey: Blue=F435w+F475w; Green=F606w+F625w+F775w+F814w+F850lp; Red=F105w+F110w+F140w+F160w. We label the multiple lensed systems used in the strong lensing analysis (see Sec. 6.5). The systems 12, 13 and the lensed image 11.c are new systems recently identified in the model. We verified that including these systems in the model is not changing significantly the final best model nor the errors on the model parameters (see Sec. 6.5 for more details). The red circles (ID1-5) label the quintuply lensed dropout candidate at $z \sim 6$. The central image ID0 is selected after removing the BCG light (see Sec. 6.6). With rD we label the other r-dropout candidate at $z \sim 5$ identified through photometric selection (see Sec. 6.3).

Filter	Total time (s)	Instrument	5σ Depth
f225w	7148	WFC3/UVIS	25.43
f275w	7274	WFC3/UVIS	25.44
f336w	4718	WFC3/UVIS	25.74
f390w	4740	WFC3/UVIS	26.47
f435w	4102	ACS/WFC	26.35
f475w	2064	ACS/WFC	26.77
f606w	3976	ACS/WFC	27.07
f625w	4128	ACS/WFC	26.60
f775w	4058	ACS/WFC	26.30
f814w	8136	ACS/WFC	26.94
f850l	6164	ACS/WFC	25.84
f105w	2815	WFC3/IR	26.86
f110w	2515	WFC3/IR	26.87
f125w	1509	WFC3/IR	26.88
f140w	2312	WFC3/IR	26.93
f160w	3520	WFC3/IR	26.96

Table 6.1: RXC J2248 CLASH Dataset summary: column (1) filters included in the survey, column (2) total observation time in seconds, column (3) HST instrument, column (4) the 5σ magnitude depth within $0.6''$.

The Chapter is organized as follows. In Section 6.2 we present the photometric data and redshifts. In Section 6.3 we provide an overview of the dropout selection procedure we use and present the $z > 5$ candidates selected in the field of RXC J2248, including the multiply lensed $z \sim 6$ galaxy. In Section 6.4 we discuss the photometric evidence supporting the lensed high- z nature of our candidate. In Section 6.5 we provide the strong lensing analysis of the cluster, and we show that the lensing model predicts our candidate to be at high redshift. In Section 6.6 we present the fifth (central) image of the system, identified thanks to the lensing model and detected after subtracting the BCG light from the images. In Section 6.7 we analyse the physical properties of the $z \sim 6$ candidate and compare it with other similar systems analysed in the CLASH survey. In Section 6.8 we present our summary and conclusions.

6.2 Photometric Dataset

RXC J2248.7-4431 was observed between September 2012 and October 2012 within the CLASH survey. In Tab. 6.1 we provide the complete list of the filters of the photometric dataset with the respective total exposure time and depth. The images have pixel scale of $65\text{mas}/\text{pixel}$ and cover a FOV of $\sim 3.4' \times 3.4'$ in the ACS images and $\sim 2' \times 2'$ in the WFC3IR images. For the sources extracted in our images, we estimate independent photometric uncertainties in each filter, both for aperture- and iso- photometry to compare with the **SExtractor** uncertainties, and we find that the **SExtractor** errors are underestimated by a factor between 2 and 4. In the paper we adopt the formal **SExtractor** uncertainties on the photometry, being aware that they are underestimated by such a factor. Moreover we compute the flux detection limit in each band by measuring the fluxes within 3000 random apertures of $0.6''$ diameter within the image FOV. We then fit a gaussian to the flux measurement histogram, estimate the 1σ width and obtain the 5σ limiting magnitudes. The results are given in Tab. 6.1.

6.3 High- z dropouts: photometric selection

Star forming galaxies at high redshift are known as Lyman Break Galaxies (LBGs, see Steidel et al., 1996b; Dunlop, 2013), because of the strong break in the SED at the Lyman- α wavelength ($\lambda_{\text{Ly}\alpha} = 1216\text{\AA}$ restframe) due to the intergalactic medium (IGM) absorption: the UV flux emitted at $\lambda < \lambda_{\text{Ly}\alpha}$ is absorbed by the neutral hydrogen (HI) of the intergalactic medium (IGM) along the path travelled by the light, causing a peculiar break in the observed SED of these sources at the redshifted $\lambda_{\text{Ly}\alpha}$. This effect is known as ‘‘Gunn-Peterson trough’’: the optical depth τ_{GP} of Lyman- α photons is directly proportional to the HI density in the IGM. At high redshift ($z > 5$), a tiny amount of HI (for example a fraction $x_{\text{HI}} \sim 10^{-4}$) leads to a complete absorption of UV photons with $\lambda < \lambda_{\text{Ly}\alpha}$ (see Fan et al., 2006). Thus candidate galaxies at redshift $z > 5$ can be identified in photometric datasets using the so called ‘dropout technique’ (Steidel et al., 1996a; Steidel, 1996), which aims to identify the Lyman- α break in galaxy SEDs through colour analyses. In particular, for galaxies at $z > 5$ the Lyman break is redshifted to the near infra-red spectral range, and these sources are expected to be not detected in the UV and optical filters (see Fig. 6.2).

The optical dropout nature cannot be used alone to identify high- z galaxies, since other galaxies mimic the same photometric behaviour: these are early-type galaxies at lower ($z \sim 1$) redshift, for which the dropout is due to the restframe 4000 \AA break, caused by the stellar photospheric opacity shortward of 4000 \AA . In this case the flux blueward this break can be fainter than the detection limit, leading to none detection in the optical filters (see Kriek et al., 2006). To discriminate between high- z star-forming and low- z early-type galaxies we need to measure the colours at wavelength redder than the observed break: indeed comparing the SEDs of star-forming galaxies at redshift $z > 5$ and early-type galaxies at $z \sim 1.5$, the colours at wavelengths larger than the dropout filter are expected to be blue for the former and red for the latter, see Fig. 6.2.

As described in Sec. 6.2, we build the multiband photometric catalogue of fluxes in 0.6’’ diameter apertures. We use the weighted sum of all the WFC3IR images as the detection frame since our aim is to identify sources at $z > 5$ which are expected to be detected in the NIR filters. Moreover, since high- z candidates are expected to have small size (e.g., the galaxy half light radius at $z = 6$ is expected to be $r_{\text{hl}} \sim 1\text{kpc}$, see Bouwens et al. (2004)), we use a DETECTION_MIN_AREA of 9 pixels as the minimum number of pixels above the threshold. Our catalogue of sources extracted in the WFC3IR_total image counts 7767 objects: of course, given the small DETECTION_MIN_AREA for the extraction, several of these sources are spurious detections due to background fluctuations, but most of them will be automatically removed from our sample through our dropout selection procedure.

To select optical dropout candidates at $z > 5$, we compute photometric redshifts with **LePhare** (see Sec. 5.2) using the multiband catalogue of aperture fluxes, and using the 1σ detection limit as upper limit when sources are not detected in a filter. Then we select all the sources with first or secondary galaxy z_{ph} solution higher than 5.

We use the starbust (SB) colour-redshift tracks to define the colour criteria that sources need to satisfy as high- z candidates. In the UV continuum range (1250 – 2600 \AA), SB SEDs follow the law $F_{\lambda} \propto \lambda^{\beta}$ (see Calzetti et al. 1994), with an expected mean $\beta = -2$ at $z \sim 6$ (see appendix in Bouwens et al. 2012). Thus we generate SB SEDs with UV continuum slope $\beta = -1, -2, -3$, and compute the colour expected for these templates in the CLASH filters as a function of the redshift in the range $z \in [0, 12]$. In Fig. 6.3 we plot the SB redshift tracks with $\beta = -1, -2, -3$ in the optical and NIR colours diagram, together with the tracks of an

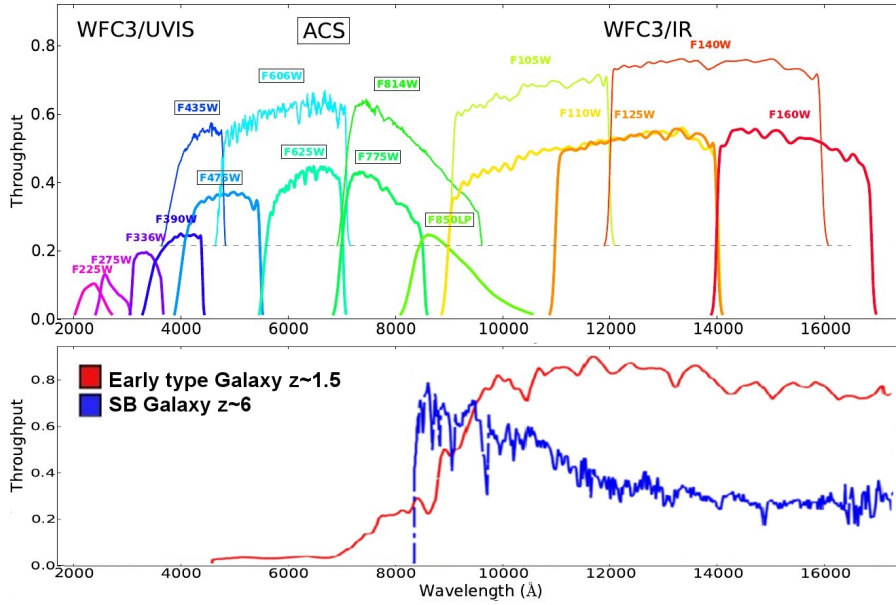


Figure 6.2: Upper panel: transmission curves of the HST/ACS and HST/WFC3 filters used in the CLASH survey. Lower panel: Comparison of a star-forming SED redshifted to $z = 6$ (in blue) and an early-type galaxy at $z = 1.5$ (from the COSMOS library, Ilbert et al., 2009). In both cases the strong spectral break falls in the same NIR range, and both these kind of sources appear as optical dropouts. At λ redder than the break the SEDs differ, thus the NIR photometry can be used to discriminate between high- and low- z dropouts.

early type galaxy (in red) and a SB galaxy (in green) from the COSMOS library (Ilbert et al., 2009). Referring to SB tracks we find that the colours for star forming galaxies at $z > 5$ are expected to be (see Fig. 6.3):

$$(i_{775} - Y_{105} > 0.8) \wedge (Y_{105} - J_{125} < 0.5). \quad (6.1)$$

We check the optical and NIR colours of our high- z candidates (all the galaxies with primary or secondary z_{ph} solution) and reduced the sample to objects matching these colour criteria. Moreover we require that all the dropouts have detection fainter than the 5σ detection limit in the filters bluer than the f775w. Finally we perform a visual check to remove obvious stellar contaminants (galactic M, L and T dwarf stars) and spurious detections, like objects at the images edges, or stellar sparks.

Our final sample yields 5 high- z candidate dropouts. All of them are extended sources with detection $> 5\sigma$ in the NIR filters (see Tab. 6.2 for the aperture photometry in the CLASH HST filters); in Fig. 6.3, we plot their colours in the NIR colour-colour diagram, together with starburst galaxy colours-redshift tracks. In Tab. 6.3 we summarize the photometric redshift results from LePhare: all the candidates have only photometric redshift solution at high redshift $z_{\text{ph}} > 5$ for galaxy templates. In Fig. 6.4, we present the postage stamp images from the f435w to the f160w filter. The four objects ID1-ID4 have the lowest wavelength detection in the i band: ID1-3 are first detected in the f814w filter with magnitude $> 5\sigma$ and ID4 is detected with magnitude $> 3\sigma$ in the f814w filter and $> 5\sigma$ in the f850lp filter. They have all similar photometric redshift of $z \sim 5.9$ with a well defined peak in the PDF(z), see Sec. 6.4, and their positions on the cluster FOV suggest that they can be a system of multiple images

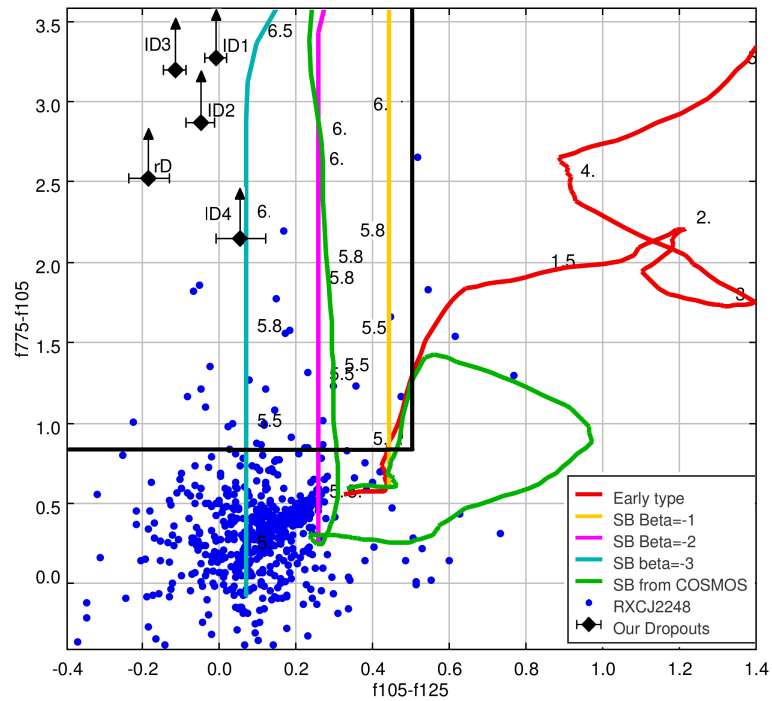


Figure 6.3: Optical and NIR colours diagram for the sources in the field of the CLASH cluster RXC J2248. In blue we plot all the sources extracted in the WFC3IR FOV, in black our high- z dropout candidates. We also plot the colour-redshift tracks for the SB galaxies that we generated with UV continuum slope $\beta = -1, -2, -3$ (in yellow, magenta and light-blue respectively), for a SB (in light green) and an early type (in red) templates from the COSMOS library (Ilbert et al., 2009). The black lines enclose the diagram region satisfying the colour criteria for $z > 5$ candidates from Eq. 6.1.

ID	f625	f775	f814	f850	f105	f110	f125	f140	f160
ID1	> 26.6	> 26.3	25.83 ± 0.01	25.05 ± 0.07	24.81 ± 0.02	24.77 ± 0.02	24.82 ± 0.02	24.87 ± 0.02	24.89 ± 0.02
ID2	> 26.6	> 26.3	26.39 ± 0.01	24.99 ± 0.07	25.22 ± 0.03	25.21 ± 0.02	25.27 ± 0.03	25.43 ± 0.03	25.52 ± 0.03
ID3	> 26.6	> 26.3	26.10 ± 0.01	25.04 ± 0.07	24.89 ± 0.02	25.00 ± 0.02	25.01 ± 0.02	25.19 ± 0.02	25.30 ± 0.03
ID4	> 26.6	> 26.3	> 26.9 ^a	25.95 ± 0.16	25.94 ± 0.05	26.14 ± 0.05	25.88 ± 0.05	26.14 ± 0.05	26.37 ± 0.06
rD	> 26.6	25.9 ± 0.1	25.72 ± 0.01	25.44 ± 0.10	25.57 ± 0.04	25.62 ± 0.03	25.75 ± 0.04	25.60 ± 0.03	25.80 ± 0.04

Table 6.2: Summary of the photometry extracted within apertures of $0.6''$ diameter for the dropouts selected in the field of RXC J2248. We present only the filters from f625w to f160w; where the object are not detected, we give the 5σ detection limit. In all the filters of our dataset bluer than f625, all the dropouts are not detected. See Tab. 6.1 for the 5σ limit for all the filters. Here we provide the SExtractor formal error; the true errors are estimated to be a factor 2-4 larger than the SExtractor ones (see Sec. 6.2).

^aID4 is fainter than the 5σ detection limit in the f814, but is brighter than the 3σ limit.

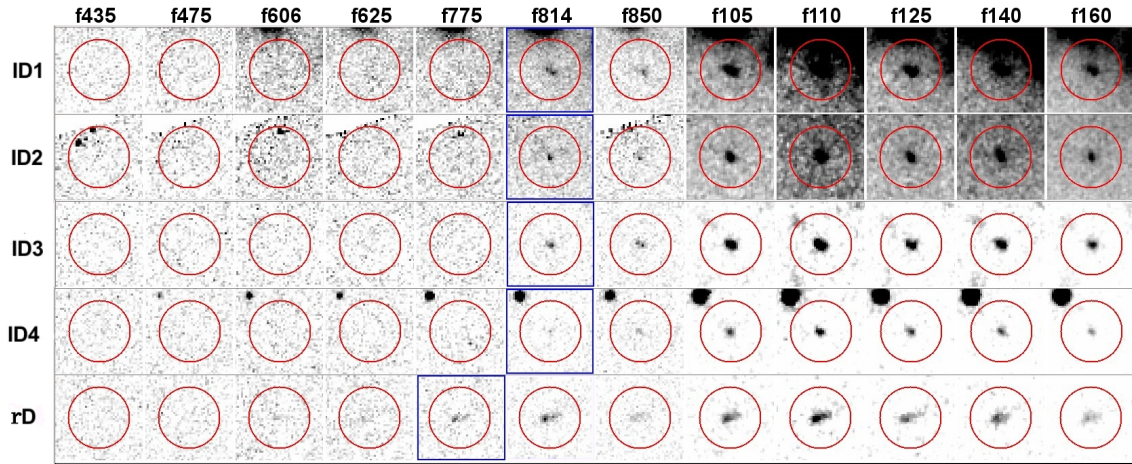


Figure 6.4: Postages of the dropouts candidate at $z > 5$ in the HST filters from the f435 to the f160w. The first four objects (ID1 – 4) are the candidate $z \sim 6$ multiple lensed system: for this system the first detection band is the f814w, while in the bluer filters there is not significant detection ($\text{flux} < 5\sigma$). The last object (rD) is a r-band dropout, with first significant detection in the f775w filter. The red circles have diameters of $2''$, i.e. ~ 3 times the aperture diameter where we perform the photometry.

of the same source lensed by the cluster. The other high- z candidate (rD) is dropout in the r band, with first detection $> 5\sigma$ in the f775w filter. It has primary solution for the photometric redshift at $z \sim 5$.

In the following sections we will focus on the system ID1-4 to verify its high- z multiple lensed nature through photometric and lensing analyses.

6.4 Quadruply lensed dropout: photometric evidence

The four high- z lensed candidates are i_{f775} dropouts: none of them is detected in the filters bluer than the f814w, in which ID1-3 are clearly first detected with detection $> 5\sigma$, while ID4 is detected with detection higher than 3σ . Moreover they are detected in all the WFC3IR bands (see Fig. 6.4). The image ID1 is the brightest among the ID1 to ID4, but it is also the one with a highly contaminated photometry since it is close to two very bright early-type galaxies (the distance from the centre of the closer galaxy is $\sim 1.7''$). ID4 is the faintest image and the furthest from the cluster centre (thus we expect it to be the least magnified), moreover it is close ($\sim 1.5''$) to a star. ID2 and ID3 are the images with the best photometry,

ID	RA(J2000)	DEC(J2000)	z_{GAL} [68%C.L.]	χ^2/dof	z_{QSO}	χ^2_{QSO}	χ^2_{Star}	Det Band
ID1	342.18906	-44.53003	5.69 [5.65 – 5.73]	3.4	6.00	6.5	10.1	f814w
ID2	342.18106	-44.53461	5.87 [5.85 – 5.90]	4.8	5.88	14.3	14.2	f814w
ID3	342.19089	-44.53746	6.01 [5.95 – 6.04]	4.3	6.00	20.1	19.4	f814w
ID4	342.17130	-44.51981	5.95 [5.87 – 6.01]	3.7	6.20	4.3	6.4	f814w($< 3\sigma$)
rD	342.17145	-44.54686	5.03 [4.94 – 5.10]	2.6	4.88	5.9	4.3	f775w

Table 6.3: Summary of the photometric redshift computed with LePhare for the 5 dropouts selected in the field of RXC J2248. Col.1 ID; Col.2-3 coordinates; Col. 4-5 first z_{ph} best solution with the respective 68% confidence level intervals and reduced χ^2 for galaxy fitting; Col. 6-7 QSO z_{ph} best solution and reduced χ^2 ; Col. 8 χ^2 for the best stellar fit; Col. 12 is the first detection band. All the reduced χ^2 are estimated using the formal SExtractor photometric errors in the SED fitting, which are likely to be 2-4 times lower than the true photometric errors.

since both are in isolated regions: we will refer to these images when using the photometry to estimate physical properties of this system. We also check the detection of these images in mosaic mid IR imaging data in the channel1 ($3.6\mu\text{m}$) and channel2 ($4.5\mu\text{m}$), obtained from HST observations with the Infrared Array Camera (IRAC) from the survey "Use of massive clusters as cosmological lenses"(PI: G. Rieke, program ID 83). Since our candidates are in the inner region of the cluster, the contamination from the cluster members is very high in the mid-IR photometry. Indeed ID1 is completely embedded in the light of the two nearby galaxies. At the positions of ID2 and ID3 it is possible to identify the lensed galaxies, but the S/N is too low to allow for extraction of robust photometry, and also reliable upper limit values are difficult to estimate due to the crowding in the field of the images. Finally ID4, the faintest of our system, is not detected in any of the two channels.

6.4.1 Photometric redshift

As described in Sec. 5.2, we compute the photometric redshifts with LePhare using the COSMOS galaxy templates library and photometry within 9 pixels aperture: for the ID1-4 dropouts, we obtain only high- z solution at $z \sim 5.9$ with reduced χ^2/DOF between 2.7 and 4.8, see Tab. 6.3. The four high- z candidates are best fitted with the same starburst (SB) galaxy template, the SB11 template from the COSMOS library. ID1 and ID4 best fits are obtained applying the $\text{SB}_{\text{calzetti_bump2}}$ extinction law with colour excess $E(\text{B-V})=0.2$: such reddening can be related to the light contamination by the two close early type galaxies for ID1, and to the nearby red galactic star for ID4. The other two objects of our system, ID2 and ID3, require no extinction in the best fit.

For the QSO templates, we use the SWIRE QSO library including the two Seyfert templates, see Sec. 5.2. The best QSO fits are still for a $z \sim 6$ source: in particular when we include the two Seyfert galaxy SED in the QSO templates, we get a best fit for $z_{\text{QSO}} \sim 6$ with χ^2/DOF lower than the galaxy best fit, while if we only include the pure AGN templates, we still get best $z_{\text{QSO}} \sim 6$, but with χ^2/DOF higher than the galaxy z_{best} (see Tab. 6.1).

As stellar templates we use the Pickles library Pickles (1998): the stellar SED fit give the worst results, as shown in Tab. 6.3. This, in addition to the extended nature of the candidates, support the exclusion of red dwarf galactic star contaminants. See Tab. 6.3 for a complete summary of the z_{ph} estimations for the ID1-4 candidates.

As we described, we get only high- z solutions for our candidates when we run the SED fit on the z range $[0, 12]$. Thus to investigate what the values for a low redshift scenario would be, we force the z_{ph} to be lower than 4 when we run LePhare. With this constraint we get $z_{\text{ph}} \sim 1.3$ for all the four dropouts, but with $\chi^2/\text{DOF} > 10$ due to the bad fit in the NIR

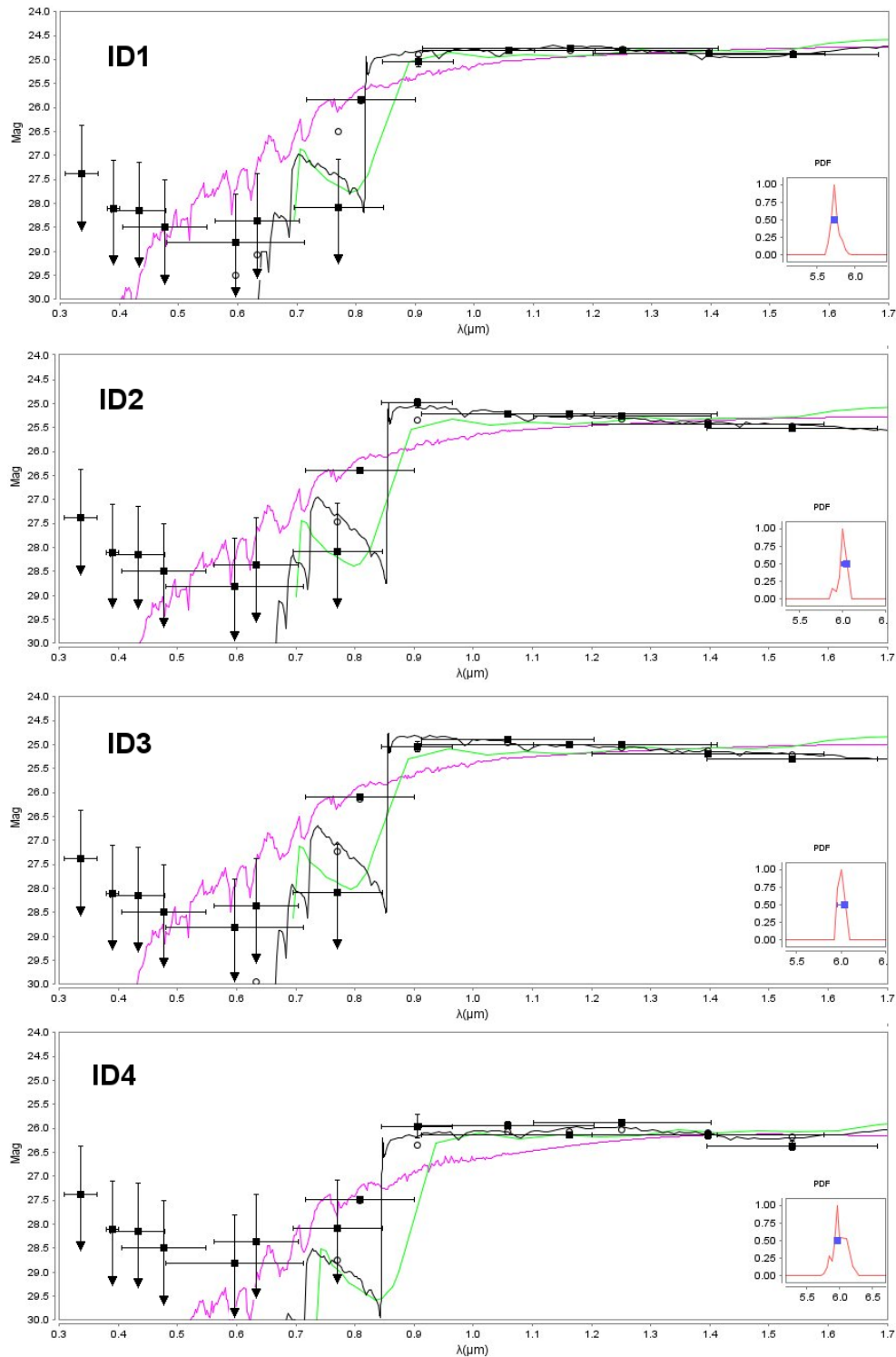


Figure 6.5: SED Fit for the best results from LePhare. The black squares are the observed magnitudes; the open circles are the predicted magnitudes; arrows represent upper limits in the detection; the black, green and magenta lines are the Galaxy, Quasar and Stellar templates respectively. The Probability Distribution Function (PDF) of the redshift for the Galaxy template is given in the lower right corner of each SED-fit.

filters. Actually if we totally exclude the WFC3IR photometry, using only fluxes up to the f850lp filter, we get good fits for $z_{\text{ph}} \sim 2$ with reduced χ^2/DOF within 0.3 and 2: in this case the predicted NIR fluxes are ~ 1 mag brighter than the observed ones. In Fig. 6.5 we present the best SED fit results from LePhare. The high- z photometric solutions we get for these sources are in agreement with the photometric redshift provided in the CLASH public catalogue² for RXC J2248, except for the ID2 candidate, for which a $z_{\text{ph}} \sim 0.09$ is obtained. The photometry for this source is extracted in a `iso_mag` aperture of 89 pixels, while in our catalogue we extract the photometry within aperture of 9 pixels, i.e. an area of ~ 64 pixels. Thus, given the larger area used for the photometry, the different photo- z results can be due to contamination by the BCG light or to the very close ACS chip gaps in the `Mosaicdrizzle` images.

6.4.2 Colour-colour diagrams

To assure the robustness of dropout high- z candidates and to rule out low- z contamination, namely by early-type galaxies at $z \sim 1.3$, we analyse the NIR colours of our high- z candidates in the colour-colour diagram. In Fig. 6.3 we show the optical and NIR colours diagram for the sources extracted in the FOV of RXC J2248, the high- z dropouts that we select in this field and the colour–redshift tracks of star-forming galaxies (with $\beta = -1, -2, -3$) with which we compare the colours of our dropouts. Our four candidates ID1-4 all lie in the region defined with the colour criteria of Eq. 6.1: they present blue NIR colours in the bands redder than the dropout one, in agreement with the colours expected for high- z star-forming galaxies. Moreover we compute the UV-slope from the NIR photometry (see Bouwens et al. 2012):

$$\beta = 3.09((Y_{105} + J_{125})/2 - H_{160}) - 2 \quad (6.2)$$

and we find that our candidates have a mean $\beta = -2.89 \pm 0.25$, in agreement with the UV continuum slope of star-forming galaxies.

We also compare all the NIR colours of the 4 dropouts with each other, to support their lensed nature on the basis of photometry. As shown in Fig. 6.6, the colours of the 4 dropouts are all consistent within 4 times the `SExtractor` formal errors.

The photometric dropouts selection presented in this Section allows to identify robust high- z candidates. We applied it to a subsample of the CLASH clusters, A383, MACS0329, MACS2129, MS2137 and MACS1149, and verified that it leads to the the selection of other known high- z candidates. Between the several high- z optical dropouts collected, we selected the already known $z \sim 6$ double lensed in the core of A383 (Richard et al., 2011), the quadruply lensed $z \sim 6.2$ galaxy in the core of MACS0329 (Zitrin et al., 2012b) and the magnified $z \sim 9.6$ galaxy in MACS1149 (Zheng et al., 2012).

6.5 Quadruply lensed dropout: lensing evidence

Given the positions of the ID1-4 candidates in the field of the cluster (see Fig. 6.1), we investigate the possible multiply lensed nature of the system. Therefore we now derive a strong lensing model of RXC J2248 to verify quantitatively whether they are lensed images of the same background source.

²<http://archive.stsci.edu/prepds/clash/>

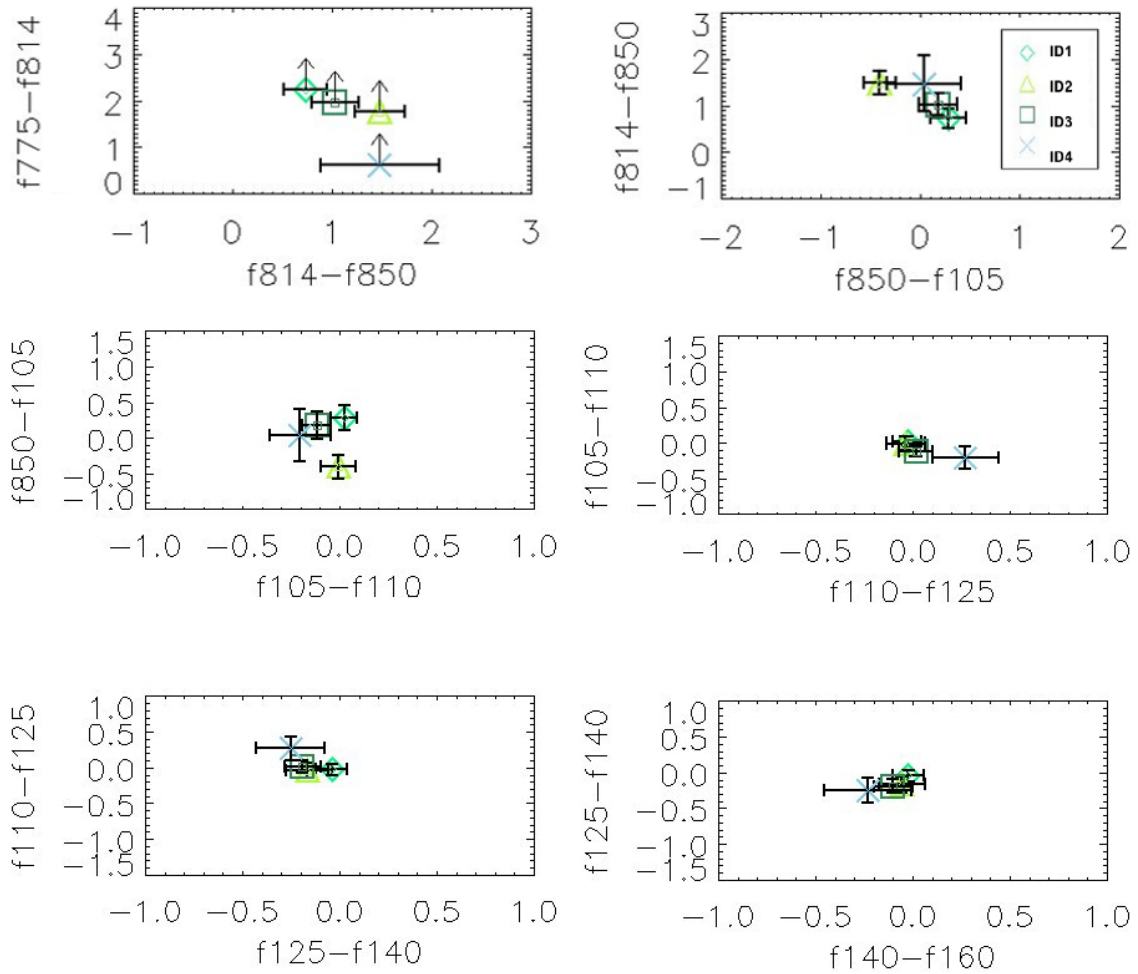


Figure 6.6: HST NIR colour-colour plot of the four high- z lensed candidates using photometry in $0.6''$ aperture. In the first panel we show the colours over the dropout filter (the arrows represent lower limit). The colours are consistent within $4\times$ the formal `SExtractor` errors, which correspond to our estimated true photometric errors in the aperture (see Sec. 6.2).

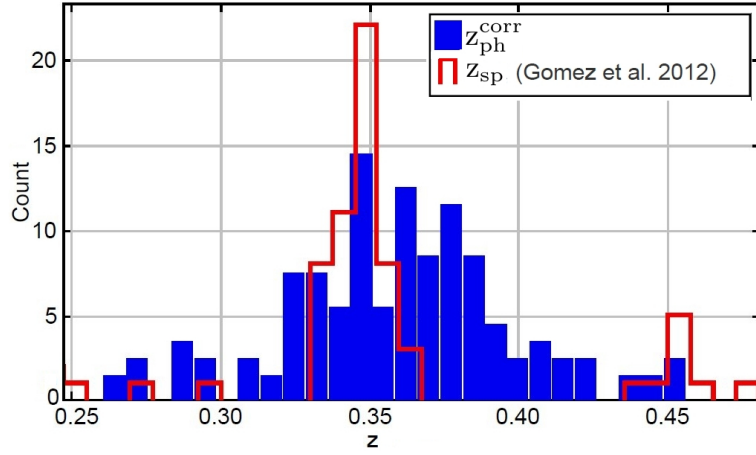


Figure 6.7: Redshift distribution of sources extracted in the WFC3IR FOV of RXC J2248. In blue we plot the distribution of the corrected photometric redshifts $z_{\text{ph}}^{\text{corr}}$ computed with LePhare for sources with $f775w_mag_best < 23$, within the range $z_{\text{ph}} = [0.25, 0.45]$. In red we plot the distribution of spectroscopic redshift from Gómez et al. (2012). In the z_{ph} distribution a clear peak is identified in correspondence of the spectroscopic z_{cl} .

We model the inner mass profile of the cluster with the strong lensing modelling software GLEE developed by S. H. Suyu and A. Halkola (Suyu & Halkola, 2010; Suyu et al., 2012), see Chapter 4 for details.

The smooth dark halo (DH) mass component of the cluster is described by a PIEMD profile (see 3.3.5), while the galaxy components are modelled with dPIE profiles with vanishing core radius (see 3.3.6). We use 16 cluster members from the spectroscopic sample (Gómez et al., 2012), which are in our WFC3IR FOV, to compute the magnitude offsets expected in our filters, and apply these offsets to the observed photometry to compute the photometric redshift for the cluster member galaxies (see Sec. 5.2). The offsets we get are not significant (< 0.03 mag) in the filters from $f606w$ to $f160w$, while they are higher (between 0.1 and 0.36 mag) in the blue filters (from $f475w$ to $f225w$) showing that the adopted templates do not describe the early type restframe SEDs well for wavelengths smaller than 3500\AA . In Fig. 6.7 we plot the histogram of the offset corrected $z_{\text{ph}}^{\text{corr}}$ for the bright ($f775w_mag_best < 23$) galaxies extracted in our images, which clearly shows a peak at the cluster redshift $z_{\text{cl}} \sim 0.35$ when using the estimated magnitude offsets. We select 64 bright cluster member candidates with $z_{\text{ph}}^{\text{corr}}$ in the range $[0.25, 0.45]$ and $f775w_mag_best < 23$ best fitted with early type templates, all of them lying on the red sequence in the colour–magnitude diagram (see Fig. 6.8). Together with the spectroscopically confirmed members, we get 80 cluster members to include as the galaxy component in performing the strong lensing mass model of the cluster. For the galaxy luminosity scaling relations, we use as exponents $\delta = 0.25$ and $\alpha = 0.5$ respectively for the velocity dispersion and the truncation radius relations. We use the observed fluxes in the $f814w$ band as a tracer for the luminosity L of the cluster members. For the ellipticities and orientations we use the values estimated with SExtractor in the same band (assuming that the dark matter halo ellipticities of the cluster galaxies are equal to their surface brightness ellipticities). The BCG is optimized independently to robustly account for its contribution to the total mass profile.

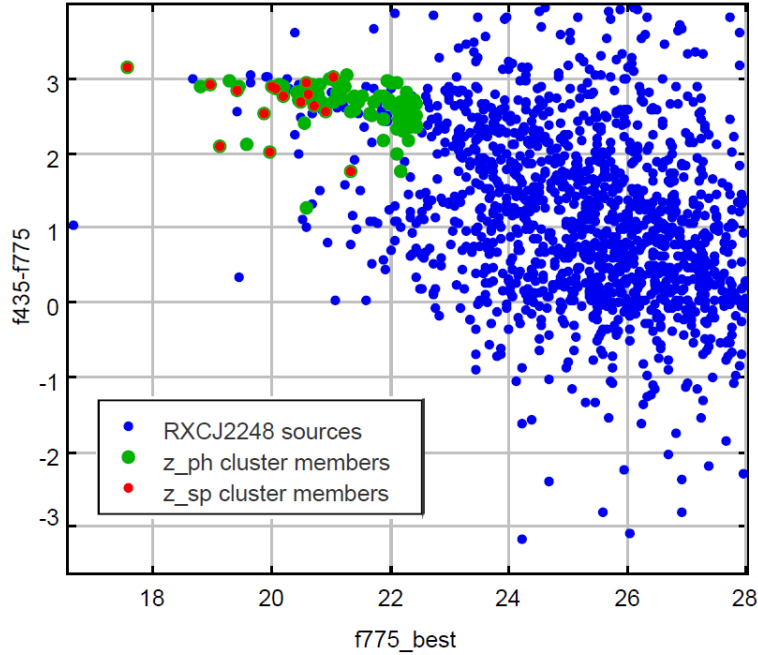


Figure 6.8: Colour magnitude diagram for sources extracted in the WFC3IR FOV of RXC J2248. We plot the colour from the aperture magnitudes f435w and f775w, versus the SExtractor mag_best in the f775w filter. Blue circles are all the sources extracted in the WFC3IR FOV; Red circles are the spectroscopic confirmed cluster members from Gómez et al. (2012); Green circles are cluster member candidates with $z_{\text{ph}} \in [0.25, 0.45]$ and $f775w_mag_best < 22.5$. We select 86 bright cluster member candidates within the $2' \times 2'$ WFC3IR FOV, which almost all lie on the red sequence of the cluster.

6.5.1 Multiple images

Since we lack spectroscopic confirmation of multiple image systems, we use the wide CLASH photometric dataset to select multiple images based on similarity of surface brightness, morphology and photometric redshift: we identify 11 candidate multiple lensed systems, for a total of 32 multiple images (see Fig. 6.1). We first use the most obvious systems (1 to 4) to build a preliminary strong lensing model based on these images. Then we iteratively include more multiple image systems (5 to 11) and build optimized models, predicting further multiple images. In total, we use 11 multiple image systems, without counting the high redshift lensed candidate system (see Tab. 6.4). We adopt a positional uncertainty of $1''$ on the multiple images positions.

For completeness, in Tab. 6.4 and Fig. 6.1 we also present two new lensed systems recently identified in the central region of the cluster. All these new multiple images are well predicted by our model, with only exception for 12c. We verify that including these systems in our model is not significantly affecting the result from our strong lensing analysis.

6.5.2 Results

We optimize the mass model using the 11 multiple image systems in Tab. 6.4 as constraints, getting the best fitting model which reproduce the positions of the observed multiple lensed images with $\chi_{\text{tot}}^2 = 10.8$ (having 18 degrees of freedom) in the image plane. Then we run the MCMC to sample the most likely parameters for the model.

Table 6.4: RXC J2248 CLASH Multiple image systems

Id	RA	Dec	z_{ph}	z_{lensing}
1.1a	342.19585	-44.52889	1.22	1.19
1.1b	342.19450	-44.52702	1.22	1.19
1.1c	342.18646	-44.52119	1.22	1.19
1.2a	342.19560	-44.52843	1.24	1.20
1.2b	342.19479	-44.52732	1.24	1.20
1.2c	342.18630	-44.52107	1.24	1.20
3a	342.19257	-44.530729	1.28	1.26
3b	342.19247	-44.53046	1.28	1.26
3c	342.17974	-44.52157	1.28	1.26
4a	342.19315	-44.53653	1.34	1.40
4b	342.18781	-44.52732	1.34	1.40
4c	342.17919	-44.52353	1.34	1.40
5a	342.19294	-44.53659	1.44	1.40
5b	342.18774	-44.52747	1.44	1.40
5c	342.17889	-44.52361	1.44	1.40
6a	342.18843	-44.54002	1.48	1.46
6b	342.17580	-44.53253	1.48	1.46
6c	342.17417	-44.52837	1.48	1.46
7a	342.18005	-44.53842	1.10	1.02
7b	342.17553	-44.53589	1.10	1.02
7c	342.17193	-44.53024	1.10	1.02
8a	342.18187	-44.54049	2.00	1.98
8b	342.17427	-44.53710	2.00	1.98
8c	342.16940	-44.52722	2.00	1.98
9a	342.18032	-44.54083	2.96	2.81
9b	342.17476	-44.53858	2.96	2.81
9c	342.16780	-44.52628	2.96	2.81
10a	342.18078	-44.540891	2.98	2.87
10b	342.17462	-44.538418	2.98	2.87
10c	342.16792	-44.52621	2.98	2.87
11a	342.17504	-44.54102	2.94	2.97
11b	342.17315	-44.53999	2.94	2.97
11c	342.16557	-44.52954	3.04	-
12a	342.19555	-44.53213	1.91	-
12b	342.19392	-44.52870	1.79	-
12c	342.18278	-44.52152	2.73	-
13a	342.19369	-44.53012	1.58	-
13b	342.19333	-44.52941	1.58	-

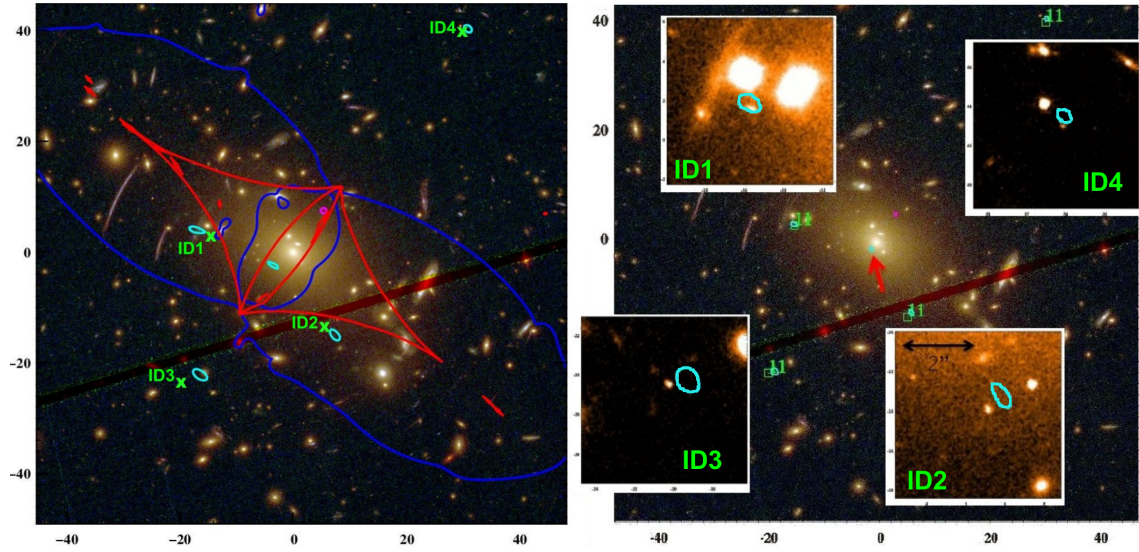


Figure 6.9: HST colour composite images of the inner region of RXC J2248. **Left Panel:** critical lines (in blue) and caustics (in red), for a source at $z=6$, for the best model that we obtain using as constraints the multiple images given in Tab. 6.4 (excluding the high- z system). In light green we show the high- z system, while in light blue the images that this model predicts for a source at $z=6$, assuming a radius of $0.25''$. **Right Panel:** Images predicted from the final best model, in which we also include the high- z system in the modelling. We show the zoom on the predicted images ($4.5'' \times 4.5''$) in the HST/f110w image. The red arrows indicate the position of the 5th central image predicted for this system.

We use this mass model of RXC J2248 to analyse the multiple imaging for a source at $z \sim 6$ and we find that the model predicts a 4 multiple images configuration very close to the one that we observe (see Fig. 6.9). We also test the prediction assuming that the source of this system is at low- z . From *LePhare* we get $z_{\text{ph}} = 1.3$ when we force the photometric redshift solution to be at low- z (see Section 6.4). For such redshift of the source, the model predicts lensed images which have no correspondence with sources observed in the field of the cluster, thus supporting that the lensed system is at high redshift.

In addition, we verify that independent mass modelling with the full light-traces-mass method of Zitrin et al. (2009), supplied to us by private communication, supports the identification of multiple images outlined here, as well as the $z \sim 6$ solution for the quadruply lensed source.

Once we tested that our model predicts the observed high- z multiple lensed system, we perform a new strong lensing model of the cluster, using this time also the high- z quadruply lensed system ID1-ID4 in the modelling. For the redshift of this system we use a starting value of $z = 6$ and allow it to vary within the range $z = [5.5, 6.5]$ throughout the modelling process. After the minimization and the MCMC runs, we get a final model of the cluster with $\chi^2 = 12.97$ with 23 degrees of freedom. For the cluster-scale halo, we get an offset of $\delta x = -0.5_{-1.6}^{+1.7}$ arcseconds, $\delta y = -0.4_{-1.4}^{+1.3}$ arcseconds with respect to the BCG, axis ratio of $b/a = 0.5_{-0.06}^{+0.07}$ and position angle $\text{P.A.} = -37.8_{-1.4}^{+1.3}^\circ$. The cluster mass is flatter in the centre with a core radius of $\sim 17 \pm 4''$, and it has an Einstein radius $\theta_E = 31.2_{-3.7}^{+2.8}$ arcseconds for a source at $z_s = 2$, which gives a central velocity dispersion of $\sigma = 1210_{-71}^{+54}$ km/s for a singular isothermal sphere. The BCG is well centred on the DH, its axis ratio is $b/a = 0.86 \pm 0.03$, the major axis has an offset of $\sim 10^\circ$ with respect to the DH orientation, and has a velocity

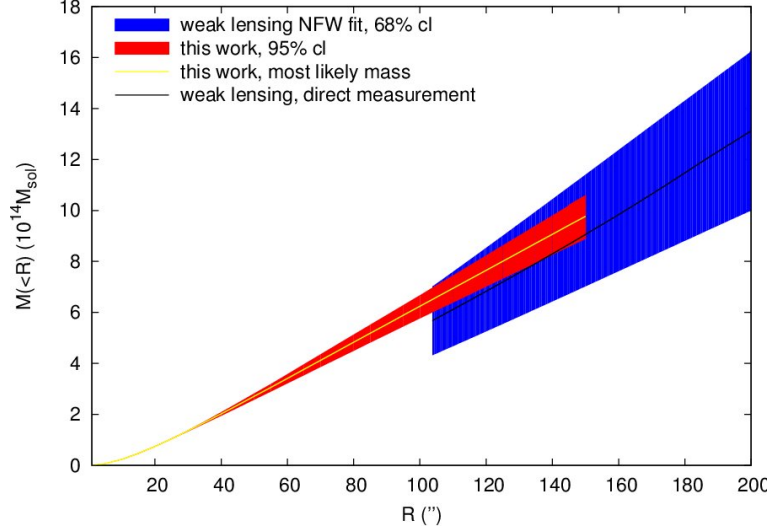


Figure 6.10: Cumulative projected mass profile of RXC J2248. We compare results from the strong lensing (this work) and weak lensing Gruen et al. (2013) analysis. In yellow we plot the most likely mass from the strong lensing analysis with 2σ uncertainties (red area) obtained using from the MCMC sample. In black we plot the weak lensing measurements from Gruen et al. (2013) with the uncertainties from the best NFW fit model (blue area). The predictions from both lensing analyses are in good agreement in the radial region where they overlap.

dispersion of $\sigma = 276_{-125}^{+79}$ km/s. The total mass of the cluster is $M_{\text{tot}} = 2.3 \times 10^{14} M_{\odot}$ within the Einstein radius, for a source at $z_s = 2$. To compare our mass prediction with the weak lensing results from Gruen et al. (2013), we calculate the most likely mass and its 1σ uncertainties by taking 200 random MCMC sample points. We derive the surface mass density and measure the projected mass up to $2.5'$ for each model and measure their projected mass within different apertures. The prediction from both lensing analyses are in good agreement in the radial region where they overlap, (see Fig. 6.10). Our best model of the cluster predicts the 4 multiple lensed high- z system with an accuracy of $0.8''$ on the observed positions. The magnifications induced by the cluster for this system are $\mu_{\text{ID1}} = 10. \pm 74$, $\mu_{\text{ID2}} = 5.8 \pm 0.7$, $\mu_{\text{ID3}} = 6.0 \pm 1.5$ and $\mu_{\text{ID4}} = 2.4 \pm 0.2$. The magnification of the brighter image, ID1, is not well constrained due to its position very close to the critical lines. In proximity of the critical lines, the magnification gradient rapidly vary, leading to high uncertainties in the magnification in correspondence of small uncertainties in the position. We estimate the relative magnification of ID2 and ID3 to be $\mu_{23} = 0.96 \pm 0.11$, which is in agreement with the observed fluxes ratio within 4 times the **SExtractor** photometric errors.

Finally, comparing the previous model, and the final one with the high- z system, we found that including or omitting the high redshift candidate system does not significantly alter the results for the cluster mass model.

6.6 The central image

As we show in Fig. 6.9, our final best model predicts a central fifth image for our high- z system, as we also expect from lensing theory. This central image is $\sim 3.5''$ away from the BCG, thus it is completely embedded in the BCG light. However, we find that, in the NIR

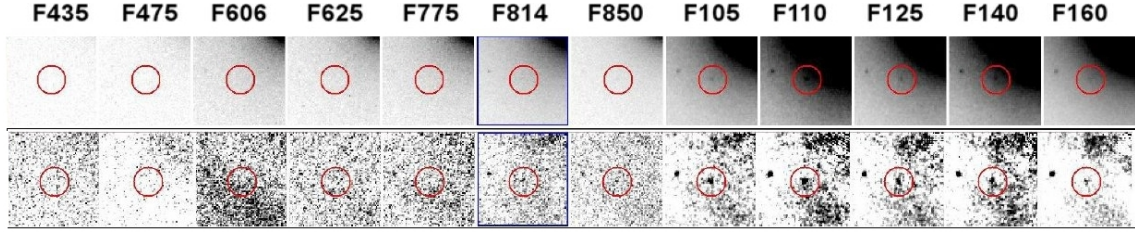


Figure 6.11: Postage stamps of the central image that we discover thanks to the strong lensing prediction and the subtraction of the cluster BCG. **Upper panel:** HST/ACS and HST/WFC3IR postage of $4'' \times 4''$ centred on the position predicted from lensing for the 5th image of the high- z system, where a source is actually observed in the NIR images. **Lower panel:** same as the upper panel, but for the images after the BCG subtraction: in this case there is a clear detection in the NIR filters, but also in the f814w and f850lp filters there are residuals left after the BCG subtraction.

images of the CLASH dataset, a source is detected at the position predicted for the central image (see Fig. 6.11). To investigate this source we subtract the BCG light from our images. Within CLASH, we use the isophote fitting routine, SNUC, which is part of the XVIDA image processing system, to derive two-dimensional models of all early-type BCGs in the CLASH clusters. SNUC is capable of simultaneously obtaining the best non-linear least-squares fits to the two-dimensional surface brightness distributions in multiple, overlapping galaxies (see Lauer (1986)). We perform these fits independently in the 12 HST passbands acquired with the ACS/WFC and WFC3/IR cameras (the BCGs are typically not dominant in the four WFC3/UVIS bands used in CLASH). Up to ten of the brightest galaxies, including the BCG, are fitted. Other objects in this region are masked prior to the fit.

In the specific case of RXC J2248, we only fit the BCG and its three closest satellite galaxies. Residuals were typically less than 0.001 mag, indicating that all 4 of the fitted galaxies are consistent with the concentric elliptical isophote assumption used in this procedure. SNUC, however, does allow the ellipticity and position angle of the isophotes to vary with the semi-major axis.

In Fig. 6.11 we show the cutout of the central image of our lensed system for the HST/ACS and HST/WFC3IR images after the subtraction of the BCG and the satellite galaxies. After removing the BCG, this central image is clearly detected in all the NIR HST filters, while its detection in the f814w and f850lp filters is difficult to claim, given the high noise fluctuations in this two bands and their low S/N. Despite the fact that the photometry of this object is highly contaminated by the BCG light, we try to estimate the z_{ph} using the photometry extracted from the images after the BCG subtraction. The result from **LePhare** gives $z_{\text{ph}} = 5.88$ as the best solution for the galaxy SED fit. Due to the noisy photometry, the $\text{PDF}(z)$ is quite broad, but given the good lensing prediction for this image, and also the best z_{ph} value, we are confident that this source is actually the central image of our system. For this image, our best strong lensing model predicts a magnification of 2.5 ± 1.0 .

6.7 Physical properties

In this section we estimate some physical properties of the high- z galaxy quintuply lensed in the field of RXC J2248. As noted in the previous sections, the images ID2 and ID3 are the ones with the best photometry, which do not suffer any contamination by nearby sources, so

we focus on these images to estimate physical properties based on photometry. In Sec. 6.5, we estimate the magnification for ID2 and ID3 to be $\mu_{\text{ID2}} = 5.8 \pm 0.7$ and $\mu_{\text{ID3}} = 6.0 \pm 1.5$. From the best **LePhare** galaxy SED fit, we extract the UV absolute magnitude M_{1600}^{AB} for these images, and after correcting for the magnification, we get delensed absolute UV magnitudes of -19.44 ± 0.13 and -19.39 ± 0.27 respectively for ID2 and ID3. Comparing these values with the luminosity function at redshift $z=6$ as estimated in Bouwens et al. (2012), our candidates have $L_{\text{UV}} = 0.4L^*$.

In order to derive the physical properties of the system ID2&3 we perform a fit of model SEDs to the colours of ID2&3 with the SED-fitting routine **SEDfit** (Drory et al., 2004). It performs a χ^2 fit of model SEDs to the observed photometry, concurrently allowing reddening by dust following the law of Calzetti et al. (2000). As basis for the template set for the fitting we use the single stellar population (SSP) model SEDs of Bruzual & Charlot (2003, hereafter BC03) with a Chabrier IMF (Chabrier, 2003) and Padova 1994 evolutionary tracks. From these we create composite stellar populations (CSPs) with the software **galaxev**³. The star formation history (SFH) of galaxies is commonly described by a so-called ' τ model' that follows:

$$\text{SFR} \propto \exp(-t/\tau), \quad (6.3)$$

where *SFR* denotes the star formation rate, and τ the (positive) *e*-folding timescale. *t* is the time that has elapsed since the start of star formation, i.e., the age of the galaxy. This function describes well the SFHs of local galaxies, but likely does not hold for $z \gtrsim 1$ (e.g., Maraston et al., 2010; Lilly et al., 2013). In fact, Maraston et al. (2010) showed that fitting model SEDs with exponentially decreasing SFRs to star-forming galaxies at $z \sim 2$ yields unrealistic young ages because the galaxy spectrum is then dominated by the young stellar population. Moreover, they showed that τ models with negative τ lead to more physical results.

Here we create CSPs for τ models with both positive and negative τ (and therefore decreasing and increasing SFR), as these should set lower and upper limits to the SFR of the investigated galaxy. We generate CSPs with metallicities of $Z = 0.0001, 0.0004, 0.004, 0.008, 0.02 (Z_{\odot}), 0.05$ and *e*-folding timescales of $\tau = \pm 0.01, \pm 0.1, \pm 0.5, \pm 1.0, \pm 2.0, \pm 3.0, \pm 4.0, \text{ and } \pm 5.0$ Gyr for the τ model. The created CSPs were extracted at 24 different ages evenly distributed in logarithmic space between 0.1 Myr and 3 Gyr. Additionally to the CSPs, we extract SSPs with the same metallicities and ages. We set the redshift of the system ID1-4 to $z = 5.9$. For model ages that are higher than the age of the universe at redshift 5.9 the SED fitting code will assign probabilities of zero. The extinction is allowed to take values between $A_V = 0.0$ and 3.0 with steps of 0.1.

We perform the SED fitting for model sets containing the SSPs and CSPs with increasing and decreasing SFH separately, and afterwards with all models combined. The results are summarised in Tab. 6.5.

Using the SSPs models, the best fits yield subsolar metallicities (0.2 and $0.005 Z_{\odot}$ for ID2 and ID3 respectively) and very young ages (0.1 and 1.5 Myr for ID2 and ID3 respectively). The results when using the CSPs with increasing and decreasing SFR are similar to one another. The best fits yield the same values for the metallicities (0.2 and $0.005 Z_{\odot}$) and comparable small ages (0.5 and 1.5 Myr). In summary, for the three different model sets (SSPs, and CSPs with $\tau \leq 0$) the results for metallicities, extinctions, and ages are essentially the same

³<http://www.cida.ve/~bruzual/bc2003> or <http://www.iap.fr/~charlot/bc2003>

ID	τ / Gyr	Z / Z_{\odot}	age [age] / Myr	M_* [M_*] / $10^9 M_{\odot}$	β_{UV}	A_V
<i>SSPs</i>						
ID2	SSP	0.2	0.1 [0.1,45]	0.093 [0.17,0.28]	-2.90 ± 0.02	0.2
ID3	SSP	0.005	1.5 [0.1,111]	0.21 [0.034,0.79]	-2.64 ± 0.02	0.4
$\tau < 0$ model CSPs						
ID2	-1.5	0.2	0.5 [0.1,274]	0.093 [0.034,0.25]	-2.90 ± 0.02	0.2
ID3	-0.1	0.005	1.5 [0.1,301]	0.23 [0.059,0.71]	-2.62 ± 0.02	0.4
$\tau > 0$ model CSPs						
ID2	0.1	0.2	0.5 [0.1,291]	0.093 [0.034,0.27]	-2.90 ± 0.02	0.2
ID3	0.1	0.005	1.5 [0.1,383]	0.23 [0.059,0.78]	-2.62 ± 0.02	0.4
<i>all combined</i>						
ID2	-1.5	0.2	0.5 [0.1,270]	0.093 [0.033,0.26]	-2.90 ± 0.02	0.2
ID3	SSP	0.005	1.5 [0.1,330]	0.21 [0.058,0.75]	-2.64 ± 0.02	0.4

Table 6.5: Best fitting parameters from SED fitting for CSPs, SSPs, and all models combined. Positive values for τ stand for an exponentially decreasing SFR, $\text{SFR} \propto \exp(-t/\tau)$, while negative values denote an increasing SFR. We interpolate the PDF of model ages (see also Figs. A.5 to A.8 in App. A) and calculate the age interval within which the probability of a fit is 95.45% (corresponding to a 2σ confidence interval). These 2σ intervals are given in brackets in the column “age”. The same is done for the masses, where the corresponding intervals are in column “ M_* ”. Note that the age and mass values of the best fitting model do not necessarily lie in the calculated intervals.

(except for the age of ID2, which is 0.1 Myr for the CSPs, and 0.5 Myr for the SSPs). Actually this is what we would expect given the small ages resulting from the best fits. Within these short timescales ($t \ll \tau$) the galaxies could not evolve significantly which is why the stellar populations (and therefore SEDs) of the CSPs are very similar to one another and also to the SSPs. When including all models (CSPs and SSPs) in the SED fitting, we get that ID2 is better fitted by a CSP model with increasing SFR, while an SSP model is preferred for ID3. In any case, the differences in the stellar populations are, as mentioned above, not very high at these young ages which is why the results for ID2&3 are in good agreement.

All the results are shown in greater detail in App. A, Figs. A.1 to A.4, where we plot the best fitting SEDs and the likelihood distributions in parameter space, as well as in Figs. A.6 to A.8, which display the PDFs of the model ages. Through interpolation of the age PDF, we calculate that ID2&3 have ages within the interval of [0.1,330] Myr (centred on the PDF) at a 95.45% (2σ) confidence. The same was done for the masses, which we estimate to be within $[0.3, 7.5] \cdot 10^8 M_{\odot}$ at the same level of confidence. The best fitting masses and the age and mass intervals are also summarised in Table 6.5. The χ^2 values of all fitting results lie between 10 and 12.7 and differ only marginally when the underlying model set is changed.

We furthermore estimate the UV slope β (Tab. 6.5) from the best fitting SED of each run by a linear fit of $\log(\lambda)$ versus $\log(F_{\lambda})$ within $\lambda \in [1276, 2490] \text{ \AA}$ (see Calzetti et al., 1994), getting results which are in total agreement with $\beta = -2.89 \pm 0.25$ estimated using the observed NIR colours in Sec. 6.4.

We also combine the likelihoods from the SED fits of the two candidates, and the results for masses and ages are same as the previous ones. Moreover, we repeat the SED fits with SSP and CPS, using this time the combined photometry of the two lensed images ID2&ID3, and the SED fits lead to same constraints on masses and ages.

To robustly compare our results with the literature, we perform the same fitting procedure (using CSPs and SSPs models) on other known $z \sim 6$ lensed sources selected in the field of the CLASH clusters (i.e., Richard et al., 2011; Zitrin et al., 2012b; Bradley et al., 2014), for which we have the same photometry as for our candidate. The SED fitting performed in

ID	τ / Gyr	Z / Z_{\odot}	age [age] / Myr	$M_{*} [M_{*}] / 10^9 M_{\odot}$	β_{UV}	A_V	Reference
MACS0329	0.1	0.005	300 [4.7,700]	1.3 [0.2,1.5]	-2.32 ± 0.02	0.0	this work
	–	0.5	180	1	-2.50 ± 0.06	–	Z12
A383	SSP	0.005	3.5 [2.9, $1.3 \cdot 10^3$]	0.2 [0.3,11.4]	-2.03 ± 0.02	0.8	this work
	0.5	–	[640,940]	$6.3^{+2.8}_{-1.2}$	–2	–	R11

Table 6.6: Best fitting parameters for the objects of R11 and Z12. Columns are the same as in Tab. 6.5.

our work uses similar model parameters as Zitrin et al. (2012b, hereafter Z12). The main difference is in the lowest model ages, which is 0.1 Myr in our work and 5 Myr in Z12. For the $z \sim 6.2$ quadruply lensed galaxy in the field of MACS0329, we get results that are consistent with Z12, for a low mass ($M \sim 10^9 M_{\odot}$) young galaxy. Our best age (300 Myr) is slightly higher, but still consistent within the 2σ confidence level.

Richard et al. (2011, hereafter R11), unlike us, adopt in their SED fitting models a Sapeleter IMF and smaller ranges for the metallicity (Z within $[0.2, 1] Z_{\odot}$) and ages (within 10 Myr and 1 Gyr). Our best age is much younger than the age range predicted in R11, although our 2σ confidence level age interval of $\sim [3, 10^3]$ Myr covers the age range of [640,940] Myr given in R11. As a consequence, also the stellar mass is found to be quite different, given that our best value is much smaller than the mass estimated by R11 (although they are anyhow consistent within our 2σ confidence level mass interval). In table 6.6 we summarise our results for these two lensed systems, and provide the physical properties estimated in the reference works.

We also perform the SED fitting for the 208 galaxy candidates at $z \sim 6$ from Bradley et al. (2014, hereafter B13). We plot in Fig. 6.12 the best fitting ages versus masses for these candidates, together with the results we get for our system, R11 and Z12. Our candidates have age and mass similar to many young candidates from B13. In Fig.6.13 we show the histograms for best age, with the lower- and upper- age limits, for B13 and our candidates. Although the large 2σ confidence level intervals, we see that our multiple lensed system is definitely among the young sample of $z \sim 6$ galaxies. Moreover we also estimate the UV slope β from the best SED fitting templates for all the sources and we get that our candidate belongs to the sample of galaxies with very steep UV slope ($\beta \sim 2.6 - 2.9$). Moreover, although the large 2σ confidence level intervals on the ages, our SED fitting suggest a very young best age for our system, compared to the other $z \sim 6$ multiply lensed galaxies (Z12 and R11), while the Z12 and R11 have confirmed older ages, in agreements with the results from literature.

6.8 Summary and Conclusions

We report the discovery of a young quintuply lensed galaxy candidate at $z \sim 6$ in the field of the galaxy cluster RXC J2248 ($z_{cl} = 0.348$). We identify this system as four i-dropouts, plus a central lensed image which we detect once we remove the BCG from the dataset images. The lensed images have colours consistent within the errors, which are in agreement with the colour prediction for starburst galaxies at $z > 5$. Moreover, they have photometric redshift of $z \sim 6$, with a well defined peak in the PDF(z) and no photo- z solution at low- z . We perform the strong lensing analysis of the cluster, using 11 systems of multiple images as constraints, and we find that our model predicts the $z \sim 6$ multiple lensed system with an accuracy of 0.8". The magnifications predicted for the lensed images are between 2.4 and 10. Referring to the two images with the best photometry, we estimate the delensed UV luminosity to be $L_{UV} \sim 0.4L^*$ at $z = 6$. From the observed NIR colours, we estimate the UV slope of

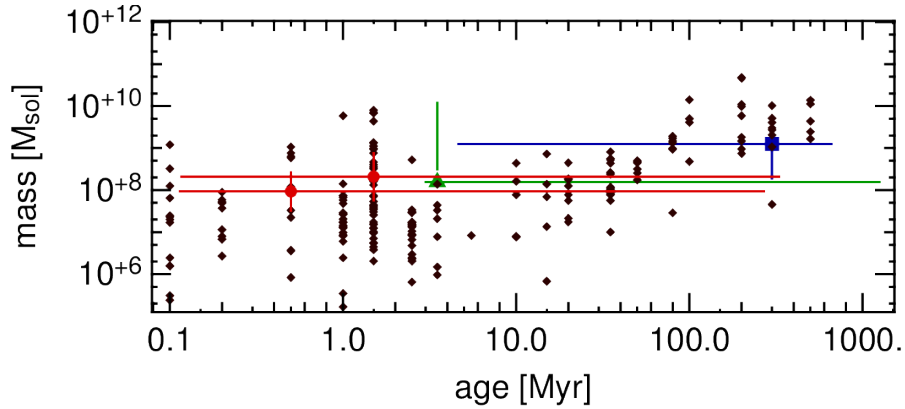


Figure 6.12: : Age and mass results for SED fitting runs with all SFHs combined on the objects from the literature and the system discussed in this paper. The plot shows the objects of R11 (green triangle), Z12 (blue square), B13 (black diamonds), and ID2&3 (red points). Error bars show the intervals in mass and age within which the total probability reads 95.45% (corresponding to a 2σ confidence interval). To improve on the clarity of the figure we did not plot the intervals for the Bradley et al. (2014) objects.

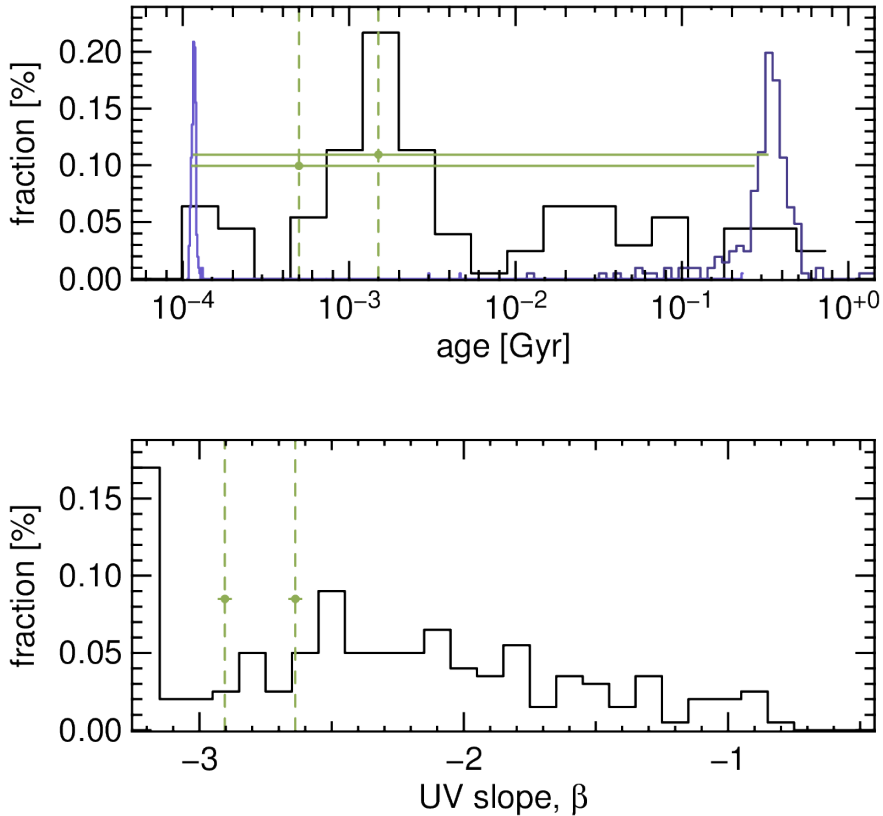


Figure 6.13: Upper panel: Histogram of the best ages for the $z \sim 6$ candidates from R11, Z12, and B13 (in black). We plot in light and dark blue the age lower and upper limits respectively for the 2σ confidence level intervals of the $z \sim 6$ candidates. In green we plot ID2&3. The 2σ confidence level intervals are too large to well constrain the ages of the sources, however our multiple lensed system surely belongs to the young sample of $z \sim 6$ galaxies. Lower panel: Histogram of the UV slope β as measured from the best fitting SED templates for the B13 candidates (in black) and for our high- z galaxy (in green).

our source to be $\beta = -2.89 \pm 0.25$. We perform a SED fitting of the observed photometry, using SSPs and CSPs SED templates, and derive that our candidate has subsolar metallicity ($Z/Z_{\odot} < 0.2$), low dust content ($A_V \sim 0.2 - 0.4$), stellar mass $M \sim 10^8 M_{\odot}$ and best age of ~ 1 Myr. Although the age is not well constrained, we can set an upper limit of ~ 300 Myr, given the 2σ uncertainties that we get.

We finally compare our predicted ages and masses, with the $z \sim 6$ candidates selected up to date in the field of all CLASH clusters, and we find that our multiply lensed galaxy has a young age and low mass, similar to some of the objects from B13. However, compared to the other known multiply lensed $z \sim 6$ galaxies, our SED fitting suggests a younger age for our multiple lensed system. This source adds to the several multiple lensed objects known at high- z , characterized for being five times lensed, with a central image identified in the very inner region of the lensing cluster. Moreover, due to its brightness (~ 25 mag) in the NIR filters it is a promising candidate for spectroscopic verification, with prospective of detection of the Ly- α and of the UV continuum. In an accompanying paper (Balestra et al. 2013), we describe the spectroscopic properties of several multiple images of this high- z system derived from a dedicated VIMOS Large Programme of follow-up of CLASH high- z objects.

High- z galaxy selection in the CLASH survey

In this Chapter we present the spectroscopic confirmation of the quintuple lensed $z \sim 6$ (Balestra et al., 2013) that we identified in the field of RXC J2248. In addition we presents our contributions to the analysis of other high- z lensed galaxies identified in the CLASH datasets.

7.1 Spectroscopic confirmation of the quintuple lensed galaxy in RXC J2248

The dropouts selection presented in the previous Chapter, was applied to several of the CLASH cluster in order to identify robust $z > 5$ lensed candidates and to follow up the brighter ones with the CLASH-VLT survey.

The quintuple lensed galaxy we identified in the core of RXC J2248, thanks to the lensing magnification, was bright enough (~ 25 mag in the F850LP filter) to be included in the target sample for the VLT/VIMOS observations of the cluster with the MR-red mask. Balestra et al. (2013) present the spectroscopic confirmation of this $z \sim 6$ galaxy, together with the analysis of the properties derived from its spectra. In addition they also provide the spectroscopic confirmation of some of the lensed systems observed in the core of the cluster, which are in excellent agreement with the prediction from our SL model presented in Cap. 6.

This lensed $z \sim 6$ galaxy is also presented in Boone et al. (2013), who detected the source in the APEX/LABOCA observation of RXC J2248, and associated its emission with a high- z lensed galaxy or to substructure in the Sunyaev-Zeldovich increment generated by the hot gas inhomogeneities of the cluster.

Here we focus on the spectroscopic confirmation and the analysis we presented in Balestra et al. (2013). The cluster was observed within the CLASH-VLT survey in June and July 2013. Only three (ID2, ID3 and ID4, see 6.1) of the five multiple images of the $z \sim 6$ lensed galaxy were included as targets of the MR-red masks, while ID1 and ID5 were excluded due to the strong light contamination of the close by cluster members. The observations were performed with 4 different pointings using the MR grism and the GG475 filter, each with 1 hour of observing time, providing final spectra with a total of 4 hours of integration time.

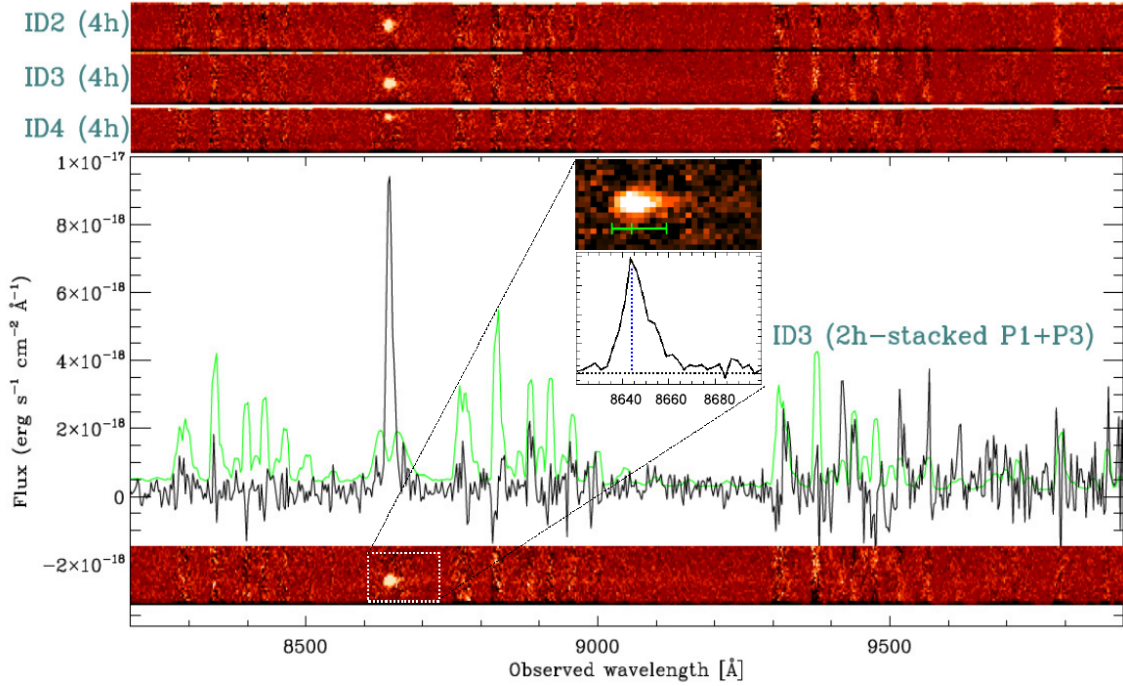


Figure 7.1: 4 hours stacked 2D VIMOS spectra of the multiple images ID2, ID3 and ID4 observed in the core of RXC J2248. The lower inset shows the 1-D and 2-D spectrum of ID3 resulting from the combination of the pointings with better seeing. The 1-D spectrum shows the emission of the high-z source in black, and of the sky in green, rescaled to arbitrary units. A zoomed cutout around the emission line observed at 8643Å is shown for the 1-D and 2-D spectrum of ID3 (figure from Balestra et al., 2013).

The pointings 1 and 3 (P1 and P3) had the best seeing conditions of $\sim 0.6 - 0.7''$, while pointing 2 and 4 (P2 and P4) had a higher seeing of $\sim 1.0 - 1.1''$. The wavelength range covered is 4800-10000Å, with resolution of 13Å. The data reduction is performed with the Vimos Interactive Pipeline Graphical Interface (VIPGI, see Scodreggio et al., 2005).

The three multiple images ID2-4 targeted all show a strong emission line at 8643Å in each of the pointing. Assuming the emission line to be the redshifted Ly-alpha line, this places the source of these multiple images at $z = 6.110$, which is consistent with the photometric and lensing prediction presented in Monna et al. (2014a), see Cap. 6.

ID3 is the brightest of the multiple images targeted with VIMOS and a faint continuum emission is detected, at 5σ level, between $\sim 8700\text{Å}$ and $\sim 9300\text{Å}$ in the pointing with better seeing, P1 and P3. The signal to noise ratio S/N of its spectrum is maximized when only P1 and P3 are combined, which is used to estimate the properties of the source from the observed emission line. Although the higher S/N, the stacked spectrum is not high enough to allow the detection of other spectral features over the emission line at 8643Å. However, star forming galaxies with large Ly α equivalent width ($EW > 50$) are expected to have very weak UV stellar absorption lines, or even to completely lack such lines (e.g. see Vanzella et al., 2009; Balestra et al., 2010). The integrated flux of the emission line (in the P1-P3 stacked spectrum of ID3) is $1.63 \times 10^{-16} \text{ergs s}^{-1} \text{cm}^2$ and the continuum emission in the $\sim 9000 - 9400\text{Å}$ range is $2.9 \times 10^{-19} \text{ergs s}^{-1} \text{cm}^2 \text{Å}^{-1}$. This implies the equivalent width of the Ly α line to be $EW = 79 \pm 10\text{Å}$, where the error is computed from the statistical uncertainties on the continuum emission. The emission line is asymmetric as it is expected in high-z galaxies due to the

intergalactic medium absorption of the radiation with observed λ lower than the redshifted Ly α wavelength, i.e. $\lambda < 8643\text{\AA}$ in this case. In Fig. 7.1 we show the 4 hours 2-D spectra for ID2-4 resulting from the stack of all the pointings P1-4. In addition we plot the 1-D and 2-D spectra of ID3 resulting from the combination of P1 and P2, and a zoomed cutout of the emission line at 8643\AA .

The observed emission is corrected by the lensing magnification computed in Sec. 6.5 (which is $\mu = 6$ for ID3), then following Kennicutt (1998), the star forming rate (SFR) is estimated from the observed Ly α and the stellar UV emission (at the restframe 1600\AA wavelength), giving $SFR(\text{Ly}\alpha) = 11M_{\odot}\text{yr}^{-1}$ and $SFR(\text{UV}) = 3M_{\odot}\text{yr}^{-1}$ respectively. The $SFR(\text{Ly}\alpha)$ is a lower limit estimation, given the IGM attenuation of probably $\sim 50\%$ of the flux of this line, but it is anyhow of the same order of the $SFR(\text{UV})$ obtained from the continuum. This can be explained by low dust attenuation combined with a very young stellar population of the galaxy and recent onset of the star forming activity (see Verhamme et al., 2008), which are all conditions consistent with the results predicted by the SED fitting presented in Sec. 6.7. From the SED fitting analysis presented in Sec. 6.7 we derived the stellar mass of the galaxy to be $\sim 2 \times 10^8 M_{\odot}$, which leads to the specific star forming rate $sSFR(\text{Ly}\alpha) = 55\text{Gyr}^{-1}$ and $sSFR(\text{UV}) = 15\text{Gyr}^{-1}$.

Given the magnification computed in Sec. 6.5 and the measured size of ID2, ID3 and ID4 as measured in the HST images, the real size of the source is estimated and gives $R_{eff} \lesssim 0.4\text{kpc}$. Thus this source is a quintuple lensed $z = 6.110$ young and compact galaxy with low dust content in the early stage of its evolution.

In addition to the $z = 6.110$ multiple images, other lensed systems, identified thanks to the CLASH photometric dataset in the core of RXC J2248, were included in the CLASH-VLT observations. The multiple images have been observed with the MR-red and LR-blue grisms and provide the spectroscopic confirmation for 10 of the 14 systems presented in Monna et al. (2014a). The spectroscopic redshifts are in excellent agreement with the photometric redshift estimations and in particular with the source redshift prediction from the strong lensing analysis (see Sec. 6.5), supporting the high accuracy of the lensing model. In Tab. 7.1 we list the photometric and lensing redshift of the multiple images, and the respective spectroscopic confirmation (see Balestra et al., 2013)

Table 7.1: Spectroscopic (Col.3), Photometric (Col.4) and Lensing (Col.5) redshifts of 10 multiple images observed in the core of RXC J2248. Column 1 and 2 give the position of the lensed images in degrees. Table from Balestra et al. (2013).

RA	Dec	z_{sp}	z_{ph}	$z_{lensing}$
22:48:43.45	44:32:04.6	6.110	$5.87^{+0.03}_{-0.02}$	6.0 (ID2)
22:48:45.81	44:32:14.8	6.110	$6.01^{+0.03}_{-0.06}$	6.0 (ID3)
22:48:41.11	44:31:11.4	6.110	$5.95^{+0.06}_{-0.08}$	6.0 (ID4)
22:48:47.00	44:31:44.0	1.229	$1.26^{+0.03}_{-0.06}$	1.19 (1.1a)
22:48:44.75	44:31:16.3	1.229	$1.22^{+0.05}_{-0.02}$	1.19 (1.1c)
22:48:46.22	44:31:50.6	1.260	$1.23^{+0.06}_{-0.06}$	1.26 (3a)
22:48:45.08	44:31:38.4	1.398	$1.53^{+0.02}_{-0.02}$	1.40 (4b)
22:48:43.01	44:31:24.9	1.398	$1.11^{+0.02}_{-0.02}$	1.40 (4c)
22:48:45.22	44:32:24.0	1.429	$1.17^{+0.10}_{-0.09}$	1.46 (6a)
22:48:41.56	44:32:23.9	3.110	$3.03^{+0.05}_{-0.05}$	2.97 (11b)

7.2 Stellar contaminants for $z \sim 6 - 8$ photometric candidates in the CLASH survey

In this section we present our contribution to the photometric analysis of $z \sim 6 - 8$ candidates selected in 18 of the CLASH clusters, described in Bradley et al. (2014). We contributed to the work presented in this paper by performing a detailed photometric redshift analysis to investigate the contamination of red galactic M, L and T dwarf stars, which appear as optical dropouts in photometric dataset (e.g., see Dunlop, 2013), to the sample of $z \sim 6 - 8$ candidates selected.

Bradley et al. (2014) select 262 candidate as $z \sim 6 - 8$ galaxies, identified through photometric redshift selection, all having $z_{\text{ph}} > 5.5$. The photometric redshifts are computed with *BPZ* using the public available CLASH catalogs¹, see Sec. 5.2. Using stars in the field of the cluster sample, an empirical PSF model is constructed which has full width half maximum (FWHM) of 0.22" in the F160W filter, and sources are considered unresolved when they have FWHM lower than this. 46 of the high- z candidates are not resolved sources, and are thus possible stellar contaminants (Bradley et al., 2014).

BPZ does not allow to use stellar templates, therefore in order to investigate the possibility of stellar contaminants we use the SED-fitting code *LePhare*. We use the same galaxy, QSO and stellar templates presented in Sec. 5.2 and same options for extinction and emission lines. In addition we include metal poor F-K dwarfs, G-K giants and M, L, T dwarfs spectra from Cushing et al. (2005) and Rayner et al. (2009) to the stellar templates.

Only for 6 of the unresolved candidates the observed photometry is better fitted by stellar templates, having $\chi_{\text{star}}^2 < \chi_{\text{gal}}^2$. Other 5 candidates get $\chi_{\text{star}}^2 \sim \chi_{\text{gal}}^2$. Of these 11 sources, three prefer a low- z solution for the galaxy templates, and have as secondary solution the high- z one. All the other unresolved candidates have *LePhare* best fit for $z > 5.5$ with galaxy templates. In summary the contamination rate from dwarf galactic stars is very low, being $\lesssim 4\%$.

¹<http://archive.stsci.edu/prepds/clash/>

Constraining the galaxy mass content in the core of A383 using velocity dispersion measurements for individual cluster members

A. Monna^{1,2}, S. Seitz^{1,2}, A. Zitrin^{3,4}, M. J. Geller⁵, C. Grillo⁶, A. Mercurio⁷, N. Greisel^{1,2}, A. Halkola, S. H. Suyu⁸, M. Postman⁹, P. Rosati¹⁰, I. Balestra^{2,11}, A. Biviano¹¹, D. Coe⁹, D. G. Fabricant⁵, H. S. Hwang¹², A. Koekemoer⁹

¹University Observatory Munich, Scheinerstrasse 1, 81679 Munich, Germany

²Max Planck Institute for Extraterrestrial Physics, Giessenbachstrasse, 85748 Garching, Germany

³Cahill Center for Astronomy and Astrophysics, California Institute of Technology, MS 249-17, Pasadena, CA 91125, USA

⁴Hubble Fellow

⁵Harvard-Smithsonian Astrophysical Observatory, 60 Garden St., Cambridge, MA 02138

⁶Dark Cosmology Centre, Niels Bohr Institute, University of Copenhagen, Juliane Maries Vej 30, 2100 Copenhagen, Denmark

⁷INAF/Osservatorio Astronomico di Capodimonte, Via Moiariello 16, I-80131 Napoli, Italy ⁸Institute of Astronomy and Astrophysics, Academia Sinica, P.O. Box 23-141, Taipei 10617, Taiwan

⁹Space Telescope Science Institute, 3700 San Martin Drive, Baltimore, MD 21208, USA

¹⁰Dipartimento di Fisica e Scienze della Terra, Univ. degli Studi di Ferrara, via Saragat 1, I-44122, Ferrara, Italy

¹¹INAF-Osservatorio Astronomico di Trieste, via G.B. Tiepolo 11, 34143 Trieste, Italy

¹²Korea Institute for Advanced Study, 85 Hoegiro, Dongdaemun-gu, Seoul 130-722, Republic of Korea

In this Chapter we present a reproduction of the paper *Constraining the galaxy mass content in the core of A383: first case study using velocity dispersion measurements for individual cluster members* accepted for publication by the *Monthly Notice of the Royal Astronomical Society Main Journal* on November, the 28th 2014.

AM and SS conducted the analysis presented in this Chapter with some contribution from AZ and CG. MJG, DGF and HSH provided the velocity dispersions measurements from the Hectospec survey. PR and IB provided the spectroscopic redshifts for cluster members and lensing features from the CLASH-VLT survey. SHS and AH provided the Strong Lensing software. MP performed the cluster members subtraction in the F775W image, used to perform the surface brightness reconstruction of the southern giant arc. All the authors contributed with input to the general discussion.

We use velocity dispersion measurements of 21 individual cluster members in the core of Abell 383, obtained with MMT's Hectospec, to separate the galaxy and the smooth dark halo

(DH) lensing contributions. While lensing usually constrains the overall, projected mass density, the innovative use of velocity dispersion measurements as a proxy for masses of individual cluster members breaks inherent degeneracies and allows us to (a) refine the constraints on single galaxy masses and on the galaxy mass-to-light scaling relation, and as a result, (b) refine the constraints on the DM-only map, a high-end goal of lens modeling. The knowledge of cluster member velocity dispersions improves the fit by 17% in terms of the image reproduction χ^2 , or 20% in terms of the *rms*. The constraints on the mass parameters improve by $\sim 10\%$ for the DH, while for the galaxy component, they are refined correspondingly by $\sim 50\%$, including the galaxy halo truncation radius. For an L^* galaxy with $M_B^* = -20.96$, for example, we obtain best fitting truncation radius $r_{tr}^* = 20.5_{-6.7}^{+9.6}$ kpc and velocity dispersion $\sigma_* = 324 \pm 17$ km/s. Moreover, by performing the surface brightness reconstruction of the southern giant arc, we improve the constraints on the r_{tr} of two nearby cluster members, which have measured velocity dispersions, by more than $\sim 30\%$. We estimate the stripped mass for these two galaxies, getting results consistent with numerical simulations predictions. In the future, we plan to apply this analysis to other galaxy clusters for which velocity dispersions of member galaxies are available.

8.1 A383

Abell 383 (A383) is a massive galaxy cluster at redshift $z = 0.189$ which presents several multiple lensed images and radial and tangential arcs in its core.

The mass distribution of this cluster has been traced through gravitational lensing analyses (see Smith et al., 2001, 2005; Sand et al., 2004), also in combination with dynamical analyses (see Sand et al., 2008). Newman et al. (2011) combined strong and weak lensing analysis with galaxy kinematics and X-Ray analyses to trace the mass distribution of the cluster out to 1.5 Mpc. They disentangled the baryonic and dark matter components in the inner region of the cluster, finding a shallow slope β for the density profile $\rho \propto r^{-\beta}$ of the dark matter on small scales. Geller et al. (2014) presented a detailed dynamical analysis of A383 using 2360 new redshift measurements of galaxies in the region around the cluster. They traced the cluster mass distribution up to about 7 Mpc from the cluster centre obtaining results that are in great agreement with mass profiles derived from weak lensing analyses, in particular at radial distances larger than R_{200} . Zitrin et al. (2011) performed a detailed strong lensing model of the cluster using the well known giant arcs and several newly identified lensed systems using the deep 16-band HST photometric dataset from the CLASH survey (Postman et al., 2012a). They used 9 lensed systems with a total of 27 multiple images to measure in detail the total mass distribution and profile in the cluster core.

In our analysis we perform an accurate strong lensing analysis of A383 using the velocity dispersion measurements for several cluster members as additional constraints. We investigate the impact of using such information on the accuracy of the lensing reconstruction, on the constraints for the individual galaxy masses and on the global $\sigma - L$ relation. In addition, we perform the surface brightness reconstruction of the southern tangential giant arc lensed between several cluster members, to set stronger constraints on the mass profiles of these individual galaxies and directly measure their size.

The Chapter is organised as follows. In Section 8.2 we describe the photometric and spectroscopic dataset, in Section 8.3 we present the photometric catalogues and the cluster

Table 8.1: Photometric Dataset summary: column (1) filters, column (2) HST instrument, column (3) total exposure time in seconds, column (4) 5σ magnitude depth within $0.6''$ aperture (see text).

Filter	Instrument	Exposure time [s]	5σ Depth
F225W	WFC3/UVIS	7343	25.76
F275W	WFC3/UVIS	7344	25.84
F336W	WFC3/UVIS	4868	26.06
F390W	WFC3/UVIS	4868	26.68
F435W	ACS/WFC	4250	26.47
F475W	ACS/WFC	4128	26.81
F606W	ACS/WFC	4210	27.06
F625W	ACS/WFC	4128	26.55
F775W	ACS/WFC	4084	26.46
F814W	ACS/WFC	8486	26.79
F850LP	ACS/WFC	8428	25.93
F105W	WFC3/IR	3620	26.81
F110W	WFC3/IR	2515	27.09
F125W	WFC3/IR	3320	26.68
F140W	WFC3/IR	2412	26.80
F160W	WFC3/IR	5935	26.81

members selection. In Section 8.4 we describe the strong lensing analysis, the mass components included in the mass model and the lensed systems used as constraints. In Section 8.5 we present the results of the strong lensing analyses performed using as constraints the observed positions of lensed images. In Section 8.6 we perform the surface brightness reconstruction of the southern giant arc which we use to refine the constraints on the mass profile of the cluster members close to the arc. Summary and conclusions are given in Section 8.7. Throughout the paper we assume a cosmological model with Hubble constant $H_0 = 70 \text{ km s}^{-1} \text{ Mpc}^{-1}$, and density parameters $\Omega_m = 0.3$ and $\Omega_\Lambda = 0.7$. Magnitudes are given in the AB system.

8.2 Photometric and Spectroscopic Dataset

As part of the CLASH survey, A383 was observed (between November 2010 and March 2011) in 16 filters covering the UV, optical and NIR range with the HST Advanced Camera for Surveys (ACS) and the HST Wide Field Camera 3 (WFC3) with its UVIS and IR cameras. The photometric dataset cover a field of view (FOV) of $\sim 2.7' \times 2.7'$ in the UVIS filters, $\sim 3.4' \times 3.4'$ in the ACS and $\sim 2' \times 2'$ in the WFC3IR images, centred on the cluster core. In Tab. 8.1 we list the filters, observing times and 5σ depths of the photometric data. We generate multi-band photometric catalogues of fluxes extracted within $0.6''$ diameter aperture using `SExtractor` 2.5.0 (Bertin & Arnouts, 1996) in dual image mode. As detection image we use the weighted sum of all the WFC3IR images.

Preliminary spectroscopic results from the first CLASH-VLT/VIMOS observations of the cluster, taken between October 2010 and March 2011 were available over a FOV of $\sim 25'$. They provided redshift measurements for 13 cluster members in the core ($r < 1.5'$) of A383 and for 4 multiply lensed systems. One of these strongly lensed systems is a double imaged $z \sim 6$ source identified in the HST CLASH data and presented in Richard et al. (2011). The cluster VLT/VIMOS observations have been completed in 2014, and the complete spectroscopic dataset will be published in Rosati et al. (in prep.).

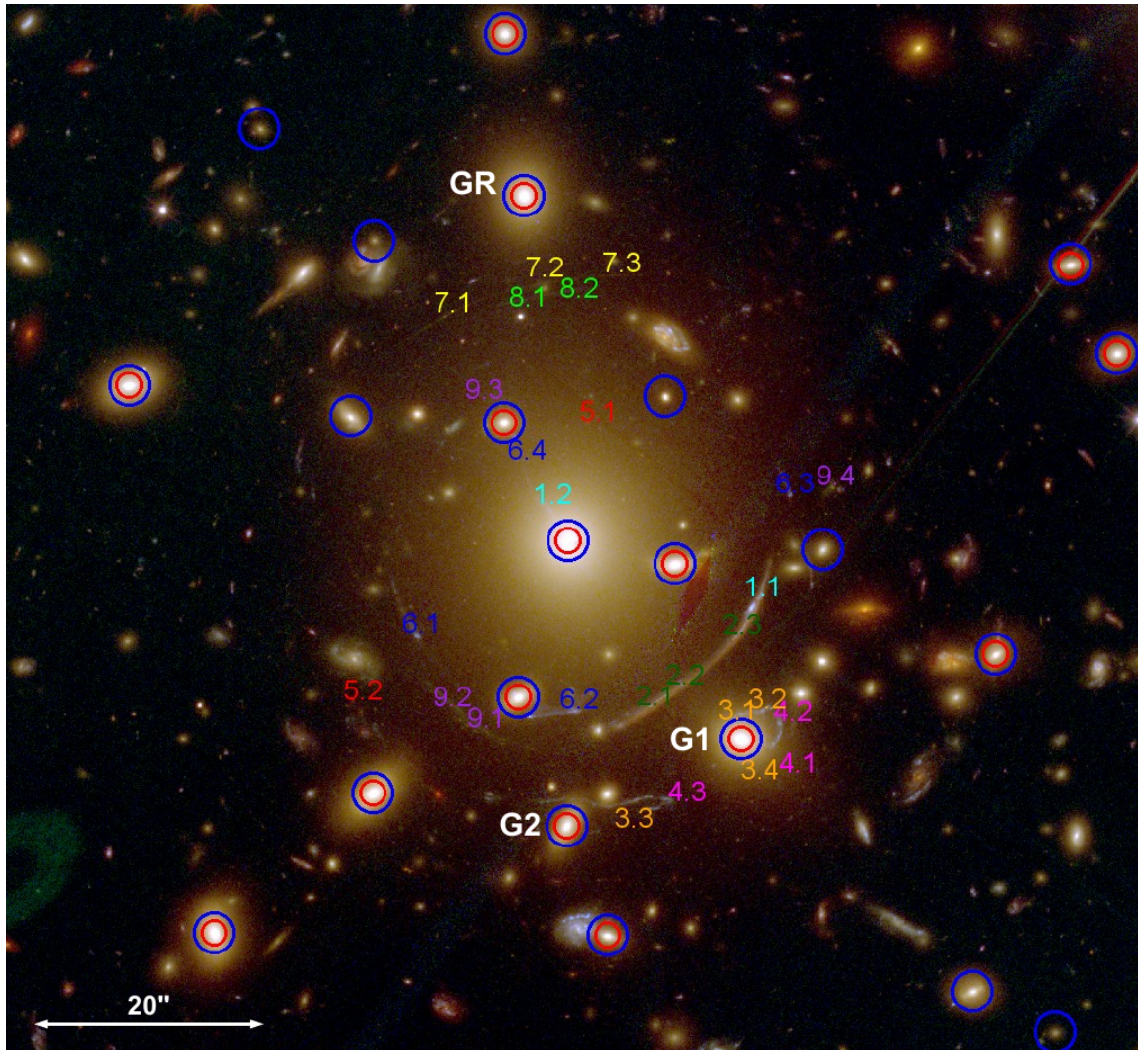


Figure 8.1: $1.5' \times 1.5'$ HST colour composite image of A383 core: Blue=F435W+F475W; Green=F606W+F625W+F775W+F814W+F850LP; Red=F105W+F110W+F140W+F160W. Blue circles label the spectroscopic confirmed cluster members in the FOV shown, while red circles label the galaxies with measured velocity dispersion. We label with GR the galaxy used as reference for the luminosity scaling relations, and with G1 and G2 the two galaxies we are modelling individually (see Sec. 8.6). The 9 multiply lensed systems used in the strong lensing analysis (see Sec. 8.4) are labelled as in Zitrin et al. (2011).

In addition, we use the sample of galaxies observed within the Hectospec redshift survey (see Geller et al., 2014). Geller et al. (2014) used Hectospec (Fabricant et al., 2005) mounted on the 6.5-meter MMT to measure 2360 redshifts within $50'$ of the centre of A383. Hectospec is a multiobject fiber-fed spectrograph with 300 fibers, with aperture of $1.5''$, deployable over a circular field-of-view with a diameter of 1° . The spectra cover the wavelength range $3500 - 9150\text{\AA}$.

During the pipeline processing based on the IRAF cross-correlation package `rvsao` (Kurtz & Mink, 1998), spectral fits receive a quality flag “Q” for high-quality redshifts, “?” for marginal cases, and “X” for poor fits. All 2360 redshifts published by Geller et al (2014) have quality Q.

To derive a velocity dispersion for a galaxy we follow the procedure outlined by Fabricant et al. (2013). We use an IDL-based software package, `ULySS`,¹ developed by Koleva et al. (2009) to perform direct fitting of Hectospec spectra over the interval 4100 to 5500 Angstroms. The effective resolution of the Hectospec spectra in this interval is $5.0\text{-}5.5\text{ \AA}$. There are 70 galaxies in the entire Geller et al. (2014) A383 survey that have velocity dispersions with errors $< 25\text{ km s}^{-1}$ and a spectral fit with reduced $\chi^2 < 1.25$. These spectra have a median signal-to-noise of 9.5 over the wavelength $4000\text{-}4500\text{ \AA}$. Among these objects, 21 are in the core of the cluster and we report them here in Table 8.2.

Jorgensen et al. (1995) empirically show that the stellar velocity dispersion σ_{obs} observed with fibers and the central stellar velocity dispersion σ_{sp} are related by:

$$\sigma_{sp} = \sigma_{obs} \left(\frac{R_{\text{eff}}}{8 \times d/2} \right)^{-0.04} \quad (8.1)$$

where R_{eff} is the galaxy effective radius and d is the fiber aperture. We estimate the effective radii of cluster members using `GALFIT` (Peng et al., 2010), fitting de Vaucouleurs profiles to the 2D surface brightness distribution of the galaxies in the HST/F814W filter. We then correct the central velocity dispersion for our cluster members according to Eq. 8.1.

In Table 8.2 we provide the coordinates, spectroscopic redshift (z_{sp}) and σ_{sp} for the sample of cluster members confirmed in the core of the cluster.

8.3 Cluster members

In order to define the galaxy component to include in the strong lensing analysis (see Chapter 4), we select cluster members in the core of A383 combining the photometric and spectroscopic datasets. We restrict our analysis to the sources in a FOV of $1.5' \times 1.5'$ centred on the cluster. In this FOV we have 34 spectroscopically confirmed cluster members (13 from VLT/VIMOS data and 21 from Hectospec data), which have $|z_{\text{sp}} - z_{\text{cl}}| < 0.01$ (see Fig. 8.1), where $z_{\text{cl}} = 0.189$ is the cluster redshift. To include in our lensing analysis also cluster members which lack spectroscopic data, we select further member candidates combining information from the cluster magnitude-colour diagram and from photometric redshifts. We compute photometric redshifts for the galaxies extracted in our dataset using `LePhare`, see Sec. 5.2. As we did in Monna et al. (2014a), in order to account for template mismatch of red SEDs (see Greisel et al., 2013), we apply offset corrections to our photometry. We use the sample of spectroscopic confirmed cluster members to estimate these photometric offsets through a colour adaptive method. In the blue filters, from f225w to f475w, the magnitude offsets are between 0.3 and 0.8 mag, showing that the templates used do not describe well

Table 8.2: List of the cluster members with measured spectroscopic redshift from the Hectospec and the VIMOS/VLT surveys. Col.1 ID; Col.2-3 coordinates Ra and Dec; Col.4 spectroscopic redshift; Col.5 measured velocity dispersion corrected according to Eq.8.1; Col.6 Effective radius.

ID	α	δ	z_{sp}	σ_{sp} [km/s]	R_{eff} [kpc]
GR	02:48:03.6	-03:31:15.7	0.194 ^a	233.1 ± 12.2	5.03 ± 0.03
BCG	02:48:03.4	-03:31:45.0	0.189 ^a	377.8 ± 15.1	10.45 ± 0.15
G1	02:48:02.4	-03:32:01.9	0.191 ^a	254.9 ± 12.8	3.35 ± 0.02
G2	02:48:03.4	-03:32:09.3	0.195 ^a	201.8 ± 15.4	1.59 ± 0.02
15	02:48:03.0	-03:30:18.2	0.188 ^a	141.9 ± 16.0	2.11 ± 0.02
16	02:48:03.0	-03:30:20.8	0.195 ^a	273.4 ± 13.5	2.35 ± 0.01
146	02:48:00.5	-03:31:21.6	0.191 ^a	121.5 ± 34.5	1.25 ± 0.01
223	02:48:02.1	-03:30:43.9	0.194 ^a	194.8 ± 11.1	3.67 ± 0.02
410	02:48:03.7	-03:31:02.0	0.182 ^a	159.6 ± 24.8	1.73 ± 0.01
658	02:48:08.5	-03:31:28.9	0.195 ^a	207.7 ± 13.4	2.49 ± 0.01
683	02:48:00.3	-03:31:29.2	0.179 ^a	164.3 ± 33.1	0.62 ± 0.01
711	02:48:05.9	-03:31:31.9	0.186 ^a	159.4 ± 13.7	1.78 ± 0.01
770	02:48:03.7	-03:31:35.0	0.190 ^a	172.1 ± 18.3	1.16 ± 0.02
773	02:48:02.8	-03:31:47.1	0.186 ^a	212.0 ± 12.3	3.16 ± 0.03
816	02:48:08.3	-03:31:39.2	0.191 ^a	192.8 ± 16.2	4.21 ± 0.05
906	02:48:03.7	-03:31:58.4	0.190 ^a	240.4 ± 20.5	1.74 ± 0.02
975	02:48:01.0	-03:31:54.7	0.192 ^a	75.0 ± 35.4	0.97 ± 0.01
1034	02:48:07.1	-03:31:46.9	0.184 ^a	81.0 ± 48.1	2.22 ± 0.01
1069	02:48:04.5	-03:32:06.5	0.196 ^a	244.6 ± 16.0	3.25 ± 0.01
1214	02:48:05.4	-03:32:18.4	0.185 ^a	212.0 ± 21.8	2.0 ± 0.01
1479	02:48:04.9	-03:32:36.7	0.183 ^a	108.5 ± 20.3	1.03 ± 0.01
208	02:48:02.6	-03:30:37.7	0.184 ^b	-	-
233	02:48:03.7	-03:30:43.2	0.186 ^b	-	-
367	02:48:06.8	-03:30:55.3	0.197 ^b	-	-
496	02:48:05.1	-03:31:10.1	0.191 ^b	-	-
601	02:48:04.5	-03:31:19.6	0.193 ^b	-	-
742	02:48:02.8	-03:31:32.8	0.188 ^b	-	-
792	02:48:04.6	-03:31:34.5	0.184 ^b	-	-
901	02:48:01.9	-03:31:45.8	0.203 ^b	-	-
1274	02:48:01.1	-03:32:23.3	0.197 ^b	-	-
1342	02:48:00.6	-03:32:26.8	0.188 ^b	-	-
1362	02:48:05.5	-03:32:30.4	0.192 ^b	-	-
1551	02:48:05.3	-03:32:44.0	0.188 ^b	-	-
1670	02:48:05.9	-03:32:53.0	0.191 ^b	-	-

^aFrom the Hectospec Survey

^bFrom the VIMOS CLASH-VLT Survey

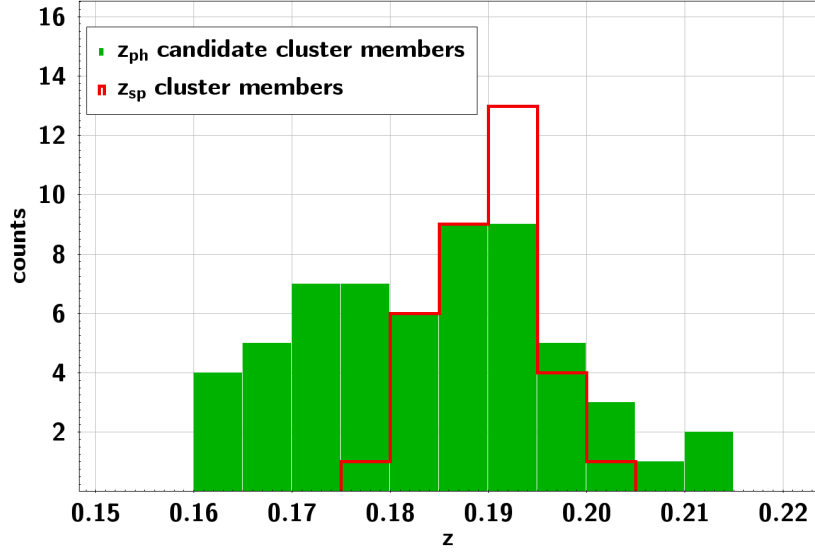


Figure 8.2: Redshift distribution of the final cluster member sample, including the photometric candidates (green histogram) and the spectroscopically confirmed members (red histogram).

the restframe SEDs of early type galaxies for wavelengths smaller than 4000\AA . In the redder filters, from f606w to f160w, the offsets are less significant (between 0.02 and 0.2 mag).

The photometric redshift and spectroscopic measurements for the relatively bright spectroscopically confirmed cluster members present small scatter: all of them fulfill $|z_{\text{sp}} - z_{\text{ph}}| < 0.02$. However, we use a larger interval of $|z_{\text{ph}} - z_{\text{cl}}| < 0.03$ to select candidate cluster members photometrically, since faint galaxies have larger photometric redshift errors in general. In addition, we require candidate cluster members to be brighter than 25 mag in the F625W filter ($F625W_{\text{auto}} < 25$) and to lie around the red sequence in the colour–magnitude diagram (having $F435W - F625W \in [1.3, 2.3]$), see Fig. 8.2, 8.3.

Our final cluster member sample in the core of the cluster contains 92 galaxies, 34 spectroscopically confirmed and 58 photometric candidates. We use this sample as galaxy component in the following strong lensing analysis (see Section 8.4).

8.4 Strong Lensing recipe

We perform the strong lensing analysis of A383 using GLEE (Suyu & Halkola, 2010; Suyu et al., 2012). The smooth dark halo (DH) mass component of the cluster is described by a PIEMD profile while the galaxy components are modelled with dPIE profiles with vanishing core radius. The luminosity scaling relations are used to scale the velocity dispersions σ and the truncation radii r_{tr} of the galaxies with respect to their luminosity. Using the sample of confirmed cluster members with measured velocity dispersions, we measured the exponent δ of the Faber-Jackson relation in the F814W band to be $\delta \sim 0.296$. Thus in lensing analysis we use $\delta = 0.3$ and $\alpha = 0.6$, given Eq. 4.13.

As reference galaxy (GR) we use the third brightest galaxy of the cluster (RAJ2000=02:48:03.63, DECJ2000=-03:31:15.7), which has $F814W_{\text{iso}} = 17.74 \pm 0.01$, $z_{\text{sp}} = 0.194$ and measured velocity dispersion $\sigma_{GR} = 233 \pm 12$ km/s. Once we fix the exponents of the luminosity scaling

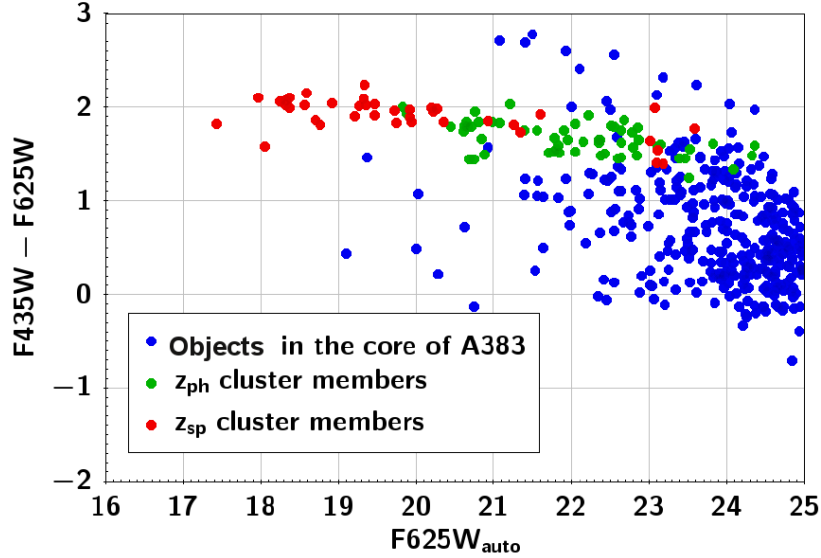


Figure 8.3: Colour magnitude diagram for the sources extracted in the core of A383. We plot the colour from the aperture magnitudes in the filters F435W and F625W, versus the SExtractor `mag_auto` in the F625W filter. Blue circles are all the sources extracted in the cluster core; in red we plot the spectroscopically confirmed cluster members and in green the photometric cluster member candidates with $z_{\text{ph}} \in [0.16, 0.22]$.

relations, being σ_{GR} measured, the only parameter we need to determine to define the galaxy mass component and tune the galaxy scaling law is $r_{tr,GR}$.

We optimise the BCG independently to better account for its contribution to the total mass profile. Moreover we independently optimise two further cluster members close to the lensed system 3-4. These galaxies have measured σ_{sp} , which combined with the strong lensing constraints from their nearby arcs, allow to directly measure their halo sizes. We call these two galaxies G1 and G2 (see Fig. 8.1). Their redshifts and measured velocity dispersions are $z_{G1} = 0.191$, $z_{G2} = 0.195$ and $\sigma_{G1} = 255 \pm 13$ km/s, $\sigma_{G2} = 202 \pm 15$ km/s, respectively (see Tab. 8.2).

To rescale σ and r_{tr} of the cluster members according to Eq. 4.8 and 4.9, we use the observed isophotal fluxes in the F814W filter. Assuming that the luminosity of the galaxies traces their dark matter halo, we adopt as ellipticities and orientations of the galaxies dark halos the values extracted with SExtractor in the F814W band.

In addition, we also allow for an external shear component, to take into account the large scale environment contribution to the lensing potential.

8.4.1 Multiple images

We use the 9 systems of multiply lensed sources presented in Zitrin et al. (2011) as constraints for our lens modelling. Four of these systems (system 1 to 4 in Tab. 8.3) are well known and spectroscopically confirmed and were used in previous lensing analyses (Newman et al., 2011; Sand et al., 2004, 2008; Smith et al., 2005). System 5 is a double lensed source at $z=6$, which has been spectroscopically confirmed by Richard et al. (2011). System 6, identified by Zitrin et al. (2011), has been followed up with VIMOS in the spectroscopic CLASH-VLT survey and confirmed to be at $z_s = 1.83$. Systems 7 to 9 lack spectroscopic data, thus we estimate

their photometric redshifts with **LePhare**. As source redshift of these systems we use the photometric redshift of the brightest multiple images with photometry uncontaminated by nearby galaxies. Altogether we have 27 multiple images of 9 background sources, of which 6 are spectroscopically confirmed lensed sources (systems 1-6). In Tab. 8.3 we list the positions and redshifts for all the images.

For the systems with spectroscopic confirmation we fix the source redshift z_{SL} in the lens modelling to the spectroscopic value z_{sp} . For the other systems the z_{SL} are free parameters. Their photometric predictions are used as starting values for z_{SL} and we optimise them with gaussian priors. As widths of the gaussian priors we adopt 3 times the uncertainties of the photometric redshifts. This is to explore a range of source redshifts z_{SL} larger than the range indicated by the 1σ uncertainties of the z_{ph} .

Using the HST photometric dataset, we can estimate the position of multiple images with a precision of $0.065''$. Host (2012) and D’Aloisio & Natarajan (2011) estimated that, on cluster scales, multiple image positions are usually reproduced with accuracy ~ 1 -2 arcseconds due to structures along the line of sight. Grillo et al. (2014) show that a higher precision can be reached through detailed strong lensing analysis of cluster cores. They predict the positions of the observed multiple images in the core of MACS J0416 with a median offset of $0.3''$. In this work, we adopt an uncertainty of $1''$ on the position of the observed multiple images to account for uncertainties due to density fluctuations along the line of sight.

8.5 Pointlike models

We now carry on with the strong lensing modelling of A383, using as constraints the observed positions and spectroscopic redshifts of the multiple images listed in Table 8.3.

In this Section we investigate how much the precision of the lens model and the constraint on the mass parameter r_{tr} of the galaxy component improve when we can use the velocity dispersion measurements of galaxies as input for the lens model.

Thus we construct two parallel models.

In the first model we scale all the galaxies with respect to GR using the luminosity scaling relations (Eq. 4.8 and left side of Eq. 4.9). We individually optimise only the BCG, the reference galaxy GR and the two galaxies G1 and G2 close to the lensed system 3-4. Their velocity dispersions and truncation radii are optimised with flat priors in the range of $[100,500]$ km/s and $[1,100]$ kpc.

In the second model we fix the velocity dispersions of the 21 cluster members from the Hectospec survey to their measured values. Their truncation radii are then given by the left side of Eq.4.9. All the other cluster members are still scaled with respect to GR according to Eq. 4.8 and Eq. 4.9. In the lens modelling we allow for some freedom for the velocity dispersions of the BCG, GR, G1 and G2, which we optimise around their σ_{sp} using gaussian priors with width equal to their spectroscopic uncertainties. Also in this case the truncation radii of these four galaxies are optimised with a flat prior within $[1,100]$ kpc.

We will refer to these two models as “pointlike models with and without velocity dispersions” (hereafter “w/ σ ” and “wo/ σ ” respectively). With “pointlike” we indicate that multiple image constraints are used as points, without accounting at this stage for surface brightness constraints.

In both cases, we optimise all the DH parameters using flat priors: the DH centre is opti-

Table 8.3: Summary of the multiply lensed systems used to constrain the strong lensing model of A383 (see also Zitrin et al. (2011)). The columns are: Col.1 is the ID; Col.2-3 Ra and Dec; Col.4 is the source redshift z_s , for systems 1-6 it is the spectroscopic redshift z_{sp} from VLT/Vimos (see text), for systems 7-9 we give the photometric redshift z_{ph} with the 3σ uncertainties estimated for the multiple image with the best photometry; Col.5 gives the strong lensing predictions for the sources redshifts from the model performed including the measured velocity dispersions, with the respective 1σ uncertainties.

Id	Ra	Dec	z_s	z_{SL}
1.1	02:48:02.33	-03:31:49.7	1.01	1.01
1.2	02:48:03.52	-03:31:41.8	"	"
2.1	02:48:02.95	-03:31:58.9	1.01	1.01
2.2	02:48:02.85	-03:31:58.0	"	"
2.3	02:48:02.45	-03:31:52.8	"	"
3.1	02:48:02.43	-03:31:59.4	2.58	2.58
3.2	02:48:02.31	-03:31:59.2	"	"
3.3	02:48:03.03	-03:32:06.7	"	"
3.4	02:48:02.30	-03:32:01.7	"	"
4.1	02:48:02.24	-03:32:02.1	2.58	2.58
4.2	02:48:02.21	-03:32:00.2	"	"
4.3	02:48:02.85	-03:32:06.7	"	"
5.1	02:48:03.26	-03:31:34.8	6.03	6.03
5.2	02:48:04.60	-03:31:58.5	"	"
6.1	02:48:04.27	-03:31:52.8	1.83	1.83
6.2	02:48:03.38	-03:31:59.3	"	"
6.3	02:48:02.15	-03:31:40.9	"	"
6.4	02:48:03.72	-03:31:35.9	"	"
7.1	02:48:04.09	-03:31:25.5	4.46 [3.71,5.09]	$4.94^{+0.30}_{-0.28}$
7.2	02:48:03.57	-03:31:22.5	"	"
7.3	02:48:03.13	-03:31:22.2	"	"
8.1	02:48:03.68	-03:31:24.4	2.3 [1.85,3.38]	$1.78^{+0.31}_{-0.23}$
8.2	02:48:03.39	-03:31:23.5	"	"
9.1	02:48:03.92	-03:32:00.8	"	$4.10^{+0.56}_{-0.68}$
9.2	02:48:04.05	-03:31:59.2	"	"
9.3	02:48:03.87	-03:31:35.0	"	"
9.4	02:48:01.92	-03:31:40.2	3.45 [3.30,3.60]	"

misredshifted within 3 arcsec from the BCG position, ellipticity within [0,1], the position angle (PA) is free to vary within 180° and the core radius within [0,60] kpc. The Einstein parameter Θ_E is optimised within [4.5, 65] arcseconds, which correspond to the velocity dispersion range [400,1500] km/s for a singular isothermal sphere. For each galaxy we fix its position, ellipticity ϵ and position angle PA to the value measured from the photometry in the ACS/F814W filter. Only for the BCG we optimise the values of ϵ and PA measured in the ACS/F814W filter with a gaussian prior with width of 0.25 and 10° respectively. Both models have 18 free parameters associated with the mass components. In Tab. 8.4 we list the results on the galaxies' and DH's parameters for both models and in the Fig. 8.5, 8.6) we provide the plots of the MCMC sampling. We here summarise the main results for both models.

The final best model wo/ σ reproduces the positions of the observed multiple images system to an accuracy of $0.5''$, with $\chi^2 = 0.6$ in the image plane. The cluster dark halo has core radius of $\sim 37.5^{+5.6}_{-7.7}$ kpc and Einstein parameter $\Theta_E = 13.3^{+2.6}_{-2.2}$ arcsec, which corresponds to the fiducial Einstein radius $\theta_E = 11.6^{+2.3}_{-1.9}$ arcsec for a source at $z_s = 2.58$. It gives a central velocity dispersion of $\sigma = 680^{+67}_{-57}$ km/s for a singular isothermal sphere. The BCG has velocity

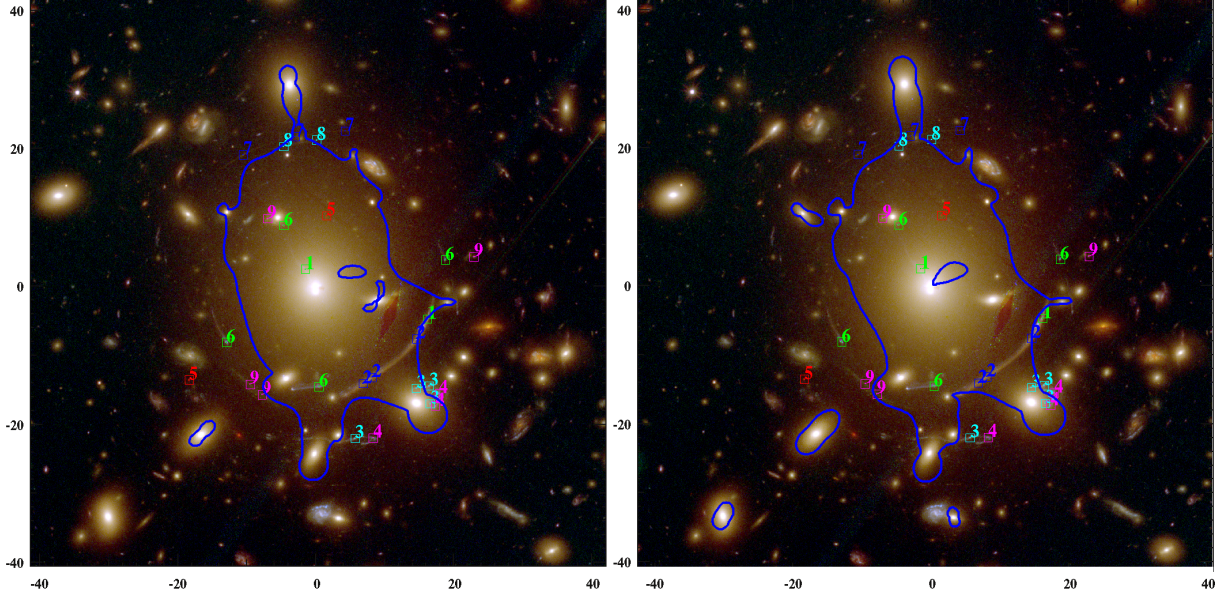


Figure 8.4: HST colour composite image of A383 core with overplotted the critical lines (in blue) for the SL models. Left panel shows the model wo/ σ , and the right panel is the model including the measured velocity dispersions. The critical lines are for a $z_s = 2.58$, which is the spectroscopic redshift measurement for the system 3-4.

dispersion of $\sigma = 395_{-44}^{+39}$ km/s and truncation radius of $r_{tr} = 53.1_{-25.0}^{+15.6}$ kpc. The predicted velocity dispersion and radii for GR, G1 and G2 are respectively $\sigma_{GR} = 214_{-32}^{+40}$ km/s, $\sigma_{G1} = 253 \pm 23$ km/s, $\sigma_{G2} = 194_{-45}^{+54}$ km/s and $r_{tr,GR} = 23.1_{-12.8}^{+29.4}$ kpc, $r_{tr,G1} = 47.8 \pm 20.9$ kpc, $r_{tr,G2} = 32.2_{-23.4}^{+31.5}$ kpc. The total mass of the cluster within the Einstein radius $\theta_E = 11.6_{-1.9}^{+2.3}$ arcsec, is $M_{tot} = 9.72 \pm 0.23 \times 10^{12} M_{\odot}$.

Including the measured velocity dispersions in the strong lensing analysis leads to a final best model with $\chi^2 = 0.5$ in the image plane, which reproduces the multiple images positions with a mean accuracy of $0.4''$. The smooth dark halo has core radius of $39.5_{-5.7}^{+5.3}$ kpc, and $\theta_E = 11.1_{-1.6}^{+2.1}$ arcsec for a source at $z_s = 2.58$, from which we get $\sigma = 667_{-47}^{+62}$ km/s for a singular isothermal sphere. The measured velocity dispersion of GR, BCG, G1 and G2 are optimised within their uncertainties. The final values for these parameters are $\sigma_{GR} = 238 \pm 15$ km/s, $\sigma_{BCG} = 379 \pm 21$ km/s, $\sigma_{G1} = 252 \pm 14$ km/s and $\sigma_{G2} = 201 \pm 20$ km/s. The predicted radii for GR, BCG, G1 and G2 are respectively $r_{tr,GR} = 13.2_{-4.3}^{+6.2}$ kpc, $r_{tr,BCG} = 58.4_{-33.2}^{+24.9}$ kpc, $r_{tr,G1} = 73.1_{-35.5}^{+38.7}$ kpc, $r_{tr,G2} = 53.2_{-36.3}^{+49.2}$ kpc. The total mass of the cluster is $M_{tot} = 9.70 \pm 0.22 \times 10^{12} M_{\odot}$ within the Einstein radius $\theta_E = 11.1_{-1.6}^{+2.1}$ arcsec for a source at $z_s = 2.58$. The results for the two pointlike models are globally in agreement within their 1σ errors. In Fig. 8.4 we show the critical lines for a source at $z = 2.58$ for both the models overplotted on the colour composite image of the cluster core. The global models are in agreement, however using the spectroscopically measured velocity dispersions of cluster members locally affects the mass distribution reconstruction. In Fig. 8.7 we plot the measured velocity dispersions σ_{sp} versus the predicted ones from SL for the model wo/ σ , and in the lower panel their ratio. They are overall in agreement within the 1σ uncertainties. Only few galaxies present a larger deviation from the measured velocity dispersions, but they are anyhow consistent at

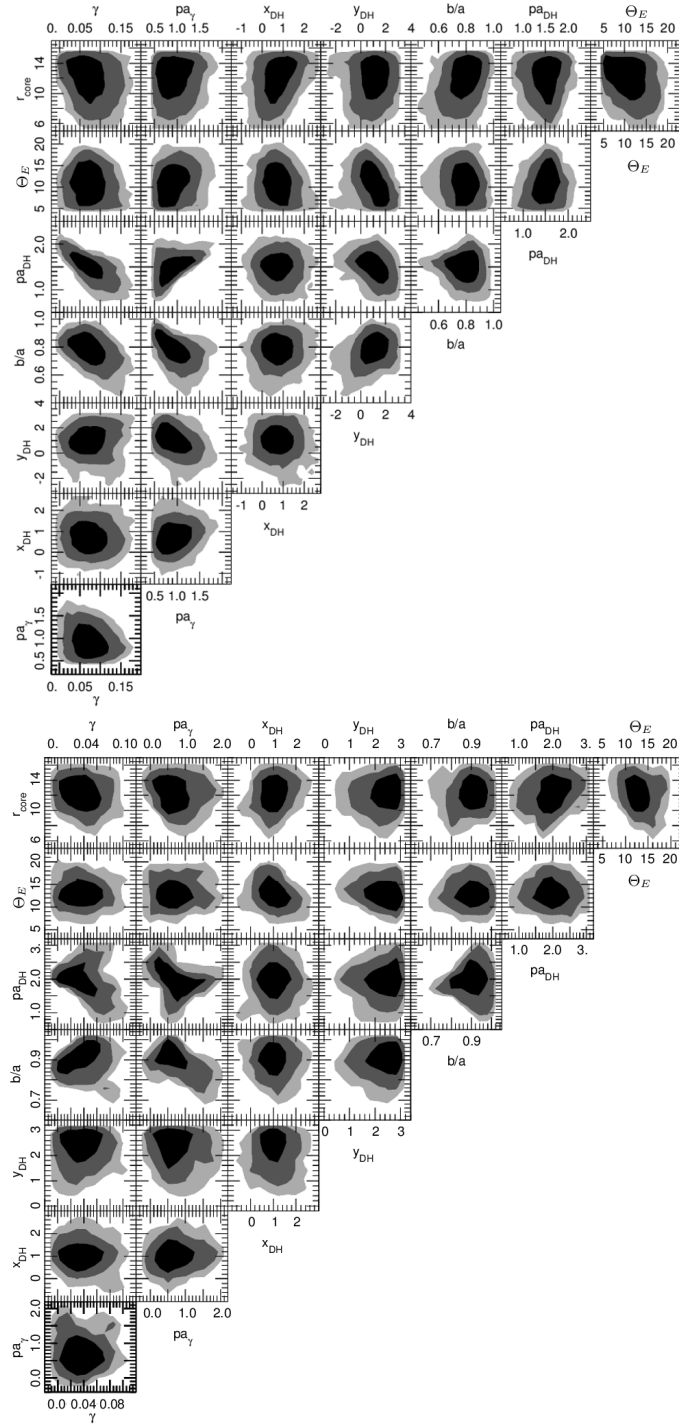


Figure 8.5: MCMC sampling of the parameters of the DH profile for the models w/σ (upper panel) and w/σ (lower panel). The gray scale corresponds to 68.3% (black), 95.5% (dark gray) and 99.7% (light gray) confidence levels. The angles pa_γ and pa_{DH} are given in radians. The central position of the DH, x_{DH} and y_{DH} , is given in arcseconds with respect to the BCG position. The DH core radius r_{core} and Einstein parameter Θ_E are in arcseconds as well.

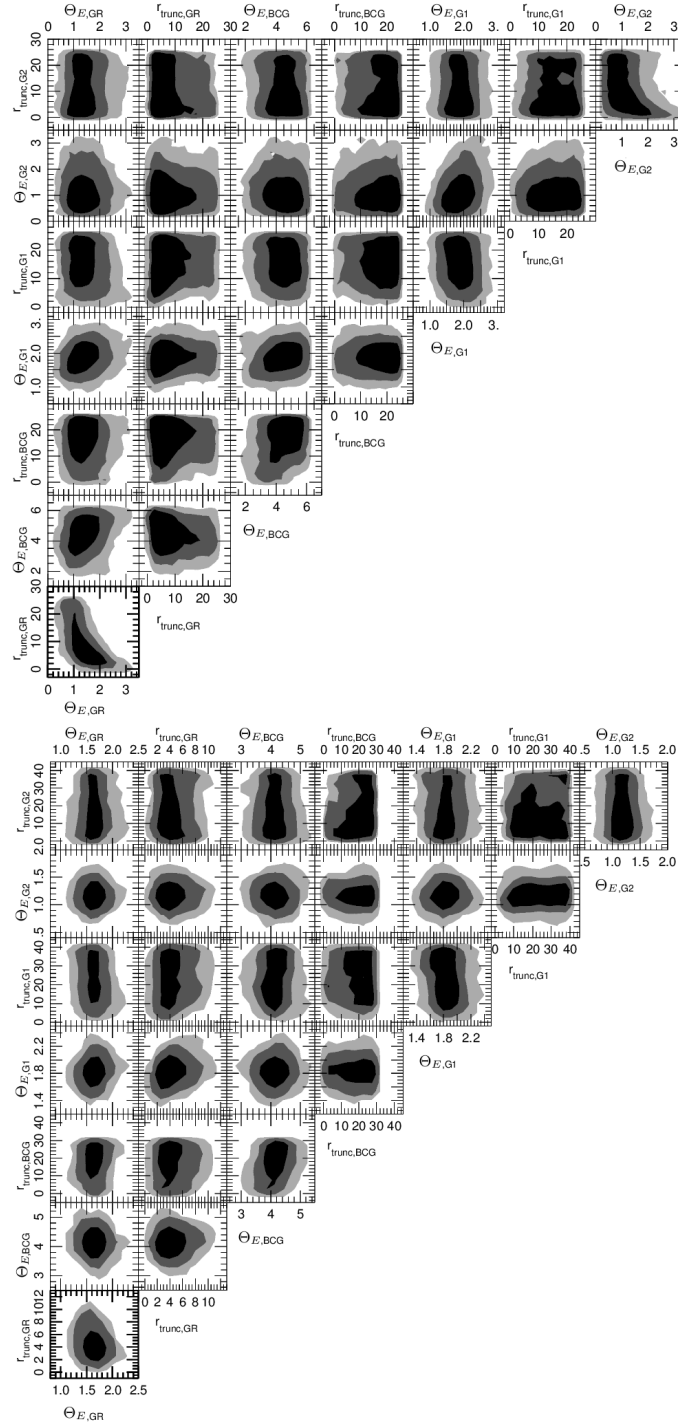


Figure 8.6: MCMC sampling of the mass profile parameters of the galaxies individually optimised (GR, BCG, G1 and G2) from the model without (upper panel) and with sigma (lower panel). The gray scale is as in Fig. 8.5. The truncation radii and Θ_E are in arcseconds. The galaxies truncation radii present large errors in the model wo/ σ , and including the measured velocity dispersions of the 22 cluster members allows to improve the constraints on the halo size of the reference galaxies by 50%.

Table 8.4: Most probable mass profiles parameters with the respective 1σ uncertainties for the smooth dark halo, the BCG, GR, G1 and G2 from strong lensing models of A383. In column (1) we give the results for the model without measured velocity dispersions and in column (2) for the model with velocity dispersions.

Param	w ₀ /σ	w/σ
External shear		
γ	0.07 ± 0.03	0.04 ± 0.02
$\theta [^\circ]$	51^{+17}_{-11}	37^{+17}_{-26}
Dark Halo		
$\delta x ["]$	0.7 ± 0.5	1.0 ± 0.4
$\delta y ["]$	1.0 ± 0.8	$2.4^{+0.4}_{-0.6}$
PA $[^\circ]$	88^{+10}_{-14}	111 ± 20
b/a	0.8 ± 0.1	0.90 ± 0.06
$\theta_E ["]$	$11.6^{+2.3}_{-1.9}$	$11.1^{+2.1}_{-1.6}$
r_{core} [kpc]	$37.5^{+5.6}_{-7.7}$	$39.5^{+5.3}_{-5.7}$
BCG		
PA $[^\circ]$	$94^\circ \pm 23^\circ$	$98^\circ \pm 9^\circ$
b/a	$0.61^{+0.18}_{-0.15}$	$0.60^{+0.17}_{-0.13}$
σ [km/s]	395^{+39}_{-44}	379 ± 21
r_{tr} [kpc]	$53.1^{+15.6}_{-25.0}$	$58.4^{+24.9}_{-33.2}$
GR		
σ [km/s]	214^{+40}_{-32}	238 ± 15
r_{tr} [kpc]	$23.1^{+29.4}_{-12.8}$	$13.2^{+6.2}_{-4.3}$
G1		
σ [km/s]	253 ± 23	252 ± 14
r_{tr} [kpc]	47.8 ± 20.9	$73.1^{+38.7}_{-35.5}$
G2		
σ [km/s]	194^{+54}_{-45}	201 ± 20
r_{tr} [kpc]	$32.2^{+31.5}_{-23.4}$	$53.2^{+49.2}_{-36.3}$

the 2σ level. These are faint galaxies (F814W_auto_mag > 18.6) which have spectroscopic velocity dispersion with uncertainties of $\gtrsim 30\%$. The velocity dispersions predicted from SL for the 4 galaxies optimised individually are in good agreement with the measured values, in particular for G1 and G2, which are well constrained through the lensed system 3-4. The velocity dispersion predicted for the reference galaxy, $\sigma_{\text{SL,GR}} = 214_{-32}^{+40}$ km/s, is slightly lower than the measured $\sigma_{\text{sp,GR}} = 233 \pm 12$ km/s, but still consistent within the 1σ errors.

From the comparison of the two pointlike models we find that lensing predictions for galaxies velocity dispersions are overall in good agreement with spectroscopic measurements. We reached a similar results in Eichner et al. (2013), where the velocity dispersions predicted from strong lensing for cluster members in the core of MACS1206 were in great agreement with the σ estimated from the Faber-Jackson relation. In Fig. 8.8, we plot the probability contours from the MCMC sampling for the truncation radius and velocity dispersion of the GR. The results from the model wo/ σ show a clear degeneracy between these two parameters (see also Eq. 3.66), which is broken only in the analysis w/ σ . The inclusion of velocity dispersion measurements allows us to improve the constraints on the galaxy sizes by $\sim 50\%$ reaching uncertainties of a few kpc on the truncation radii. The truncation radius scaling relations are

$$r_{tr,wo/\sigma} = 23.1_{-12.8}^{+29.4} \text{kpc} \left(\frac{\sigma}{214_{-32}^{+40} \text{ km/s}} \right)^{\frac{4}{3}} \quad (8.2)$$

$$r_{tr,w/\sigma} = 13.2_{-4.3}^{+6.2} \text{kpc} \left(\frac{\sigma}{238 \pm 15 \text{ km/s}} \right)^{\frac{4}{3}} \quad (8.3)$$

for the models wo/ σ and w/ σ respectively. In Fig. 8.9 we plot Eq. 8.2 and Eq. 8.3 with their 68% confidence levels. In the model wo/ σ , all the galaxies individually optimised lie within the 68% confidence levels of the scaling relation.

When we include the measured velocity dispersions in the analysis, the reference galaxy GR gets a smaller r_{tr} which is better constrained by a factor of 3 to 4. However, we get no improvement on measuring the halo size of the other galaxies individually optimised. These galaxies show a large deviation from the scaling relation. However, their truncation radii have large errors, such that these galaxies are consistent with the scaling law within $1 - 2\sigma$ errors. The truncation radius of all the other galaxies with measured σ_{sp} , are scaled with the light according to Eq. 4.9. They are all in agreement with the scaling relation at the 1σ level. The scaling law w/ σ is consistent at the 1σ level with the law obtained from the model wo/ σ , and now constraints on the truncation radii are improved by a factor of 50%.

The smooth DH parameters are consistent within the 1σ errors for both models (see Tab. 8.4). Including the velocity dispersions helps to constrain more tightly all the DH parameters, except for the PA, where the uncertainty rises by 6%. The external shear is low for both models ($\gamma_{wo/\sigma} = 0.07 \pm 0.03$ and $\gamma_{w/\sigma} = 0.04 \pm 0.02$) and in agreement within the 1σ errors. Strong lensing analyses allow high precision measurements of the projected mass profile of the lens within the observed lensing features. For both the pointlike models we obtain the same projected mass $M(< 50 \text{ kpc}) = 1.7 \pm 0.03 \times 10^{13} M_{\odot}$ enclosed within a radius of 50 kpc, which is the distance of the giant radial arcs (system 1-2) from the cluster centre. This result is in agreement with previous analysis, e.g. with Newman et al. (2011) and Zitrin et al. (2011), who find a total projected mass within $r=50 \text{ kpc}$ of $M(< 50 \text{ kpc}) = 2 \times 10^{13} M_{\odot}$ and $M(< 50 \text{ kpc}) = 2.2 \times 10^{13} M_{\odot}$, respectively (both masses are provided without errors). The global models present differences in the mass components parameters due to the different

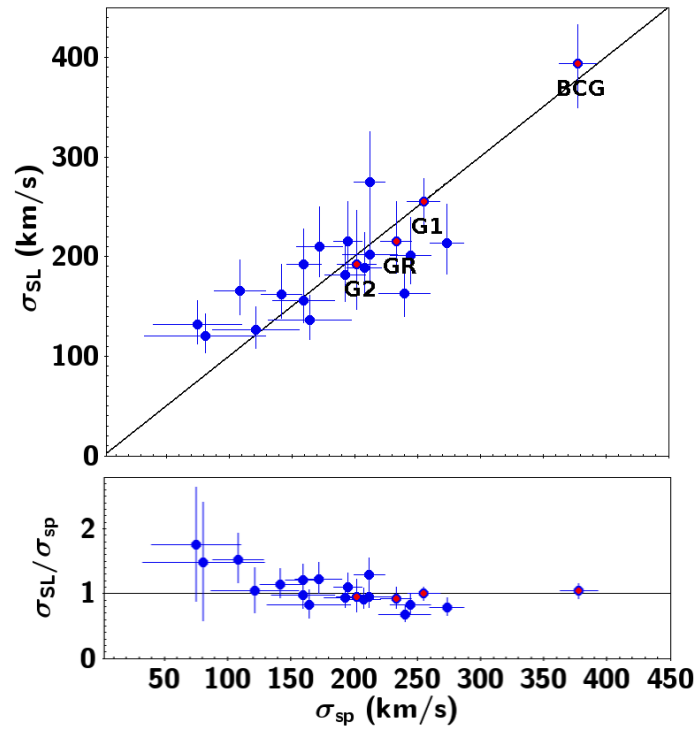


Figure 8.7: Upper panel: velocity dispersions σ_{SL} predicted from the SL analysis versus measured velocity dispersions σ_{sp} for the 21 cluster members from the Hectospec survey. Lower panel: ratio of σ_{SL} and σ_{sp} . The σ_{SL} are predicted using the scaling luminosity relation, except for the four galaxies individually optimised, GR, BCG, G1 and G2. The values predicted in the model w_0/σ are globally in agreement with the measured σ_{sp} at the 1σ level, except at low velocity dispersions where they are slightly overestimated by a factor of ~ 1.5 . We label in red the data for the galaxies individually optimised: these show an excellent agreement between the σ_{SL} and the measured σ_{sp} .

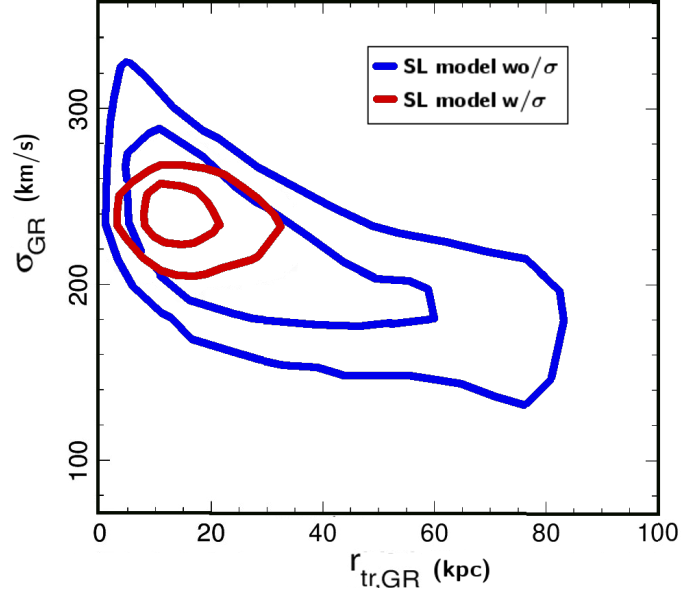


Figure 8.8: Probability Contours of the GR velocity dispersions versus the truncation radius from the MCMC sampling for the the model w_0/σ (in blue) and w/σ (in red). The knowledge of the galaxies velocity dispersions improves the constraint on the global scaling relation, tightening the constraints on the galaxy truncation radii by $\sim 50\%$.

constraints and mass components used in the different analyses, but they show agreement on the total mass predictions probed by strong lensing.

8.6 Surface Brightness reconstruction

In this section we perform the surface brightness reconstruction of the southern giant arc corresponding to the lensed systems 3-4 in the pointlike models (see Fig. 8.1). This is a lensed source at redshift $z_{\text{sp}} = 2.58$ which bends between several cluster members. For two of these galaxies, G1 and G2, we have measured velocity dispersions. By performing the surface brightness reconstruction of these arcs we aim to directly measure the truncation radii of these two cluster members, which are the only unknown parameters for the profile adopted to describe their masses.

To perform the surface brightness reconstruction, GLEE uses a linear inversion method (see Warren & Dye, 2003). It reconstructs the pixellated brightness distribution of the source, with regularisation of the source intensity through a Bayesian analysis (see Suyu et al., 2006, for a detailed description of this technique).

We reconstruct system 3-4 in the HST/ACS/F775W filter, in which the arcs are bright and at the same time the light contamination from the close cluster members is still low. In order to reconstruct only the light from the arcs and avoid contamination from nearby galaxies, we subtract the galaxies close to system 3-4 using the SNUC¹ isophote fitting routine, which is part of the XVISTA image processing system. Within CLASH, we apply SNUC to derive two-dimensional models of early-type galaxies in the CLASH clusters since it is capable of

¹see <http://astronomy.nmsu.edu/holtz/xvista/index.html> and Lauer 1986

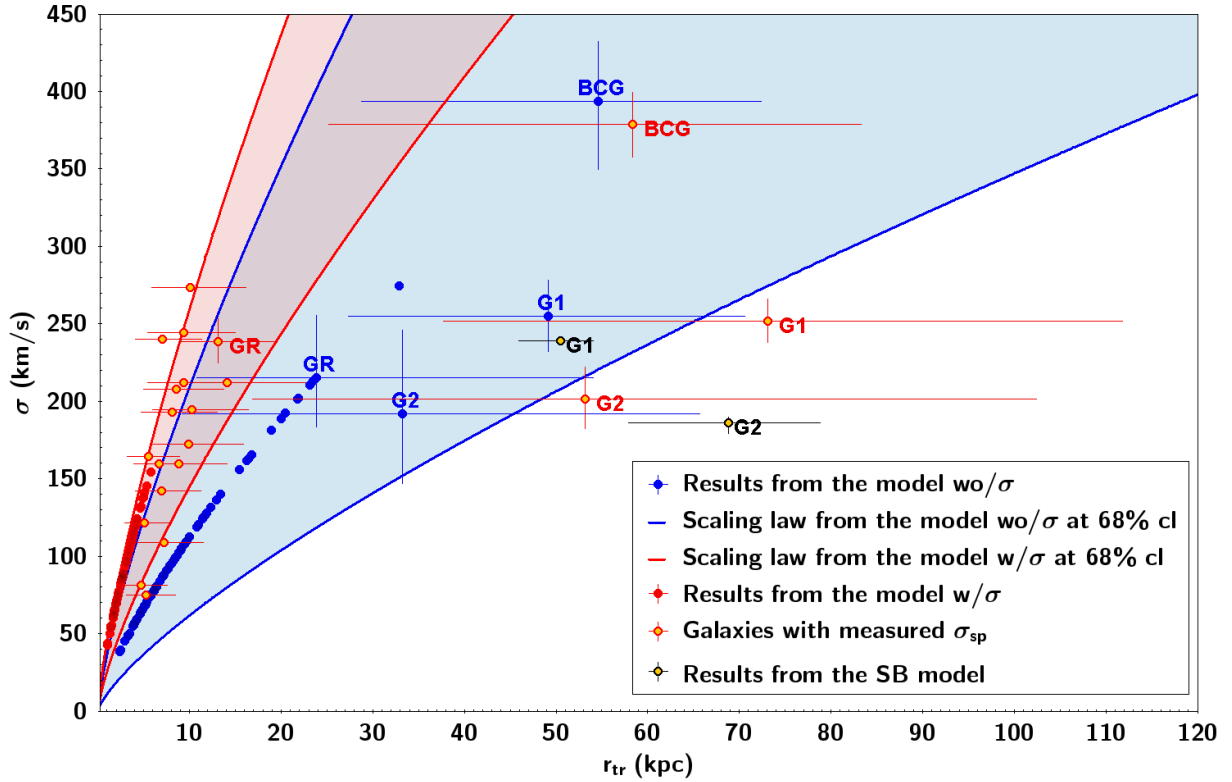


Figure 8.9: Galaxy scaling relations for the models w_0/σ and w/σ . The blue lines are the 68% confidence level for the scaling law from the model w_0/σ . All the cluster members (blue circles) are scaled according to this relation, except the 4 galaxies which we optimise individually and which are labelled with their respective ID. The 68% confidence levels of the scaling relation obtained from the model w/σ is shown in red, and the red circles are the cluster members scaled according to this relation. We plot in yellow the galaxies with measured velocity dispersion, for which the velocity dispersions are fixed to the measured σ_{sp} and only the truncation radii are scaled according to the galaxy luminosity. These galaxies scatter around the cluster σ - r_{tr} scaling relation from the model w/σ , but they are all consistent with this scaling law within the 1σ errors. The galaxies individually optimised, BCG, G1 and G2, have a large scatter from the luminosity relation, and in particular G1 and G2 present truncation radii larger than the 68% cl of the scaling law w/σ . In addition we plot in black the prediction for G1 and G2 obtained from the surface brightness reconstruction of the southern giant arc (see Sec.8.6). Also in this case these galaxies present a large deviation from the scaling relations, but the results from the three analysis are all consistent within each other for both galaxies.

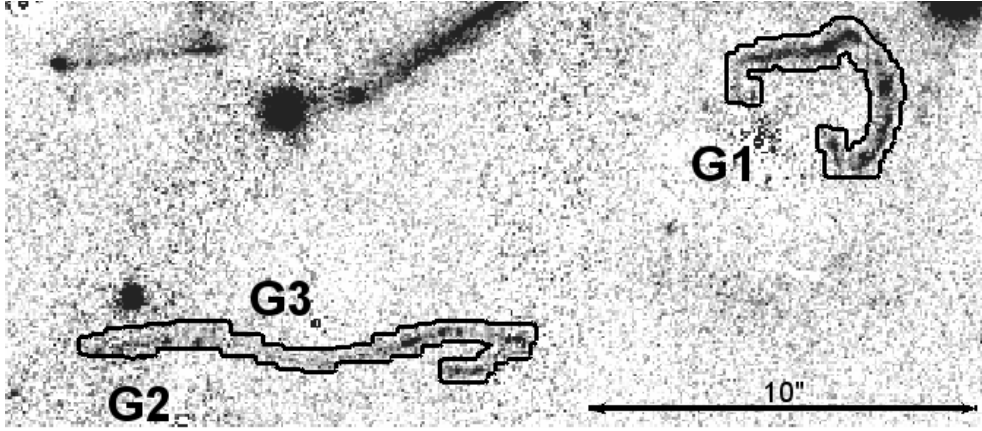


Figure 8.10: Cutout of the system 3-4 in the HST/ACS/F775W filter. In this images the three galaxies close to the system, G1, G2 and G3, are subtracted using the SNUC routine. In black we trace the contours of the area we reconstruct in the surface brightness reconstruction of this system.

simultaneously obtaining the best non-linear least-squares fits to the two-dimensional surface brightness distributions in multiple, overlapping galaxies (see Lauer 1986).

We perform the surface brightness reconstruction of the arcs where $S/N > 0.5$. In Fig. 8.10 we show the arcs in the F775W filter with the bright nearby galaxies subtracted, and we show the contours of the area we mask for reconstruction in black. When performing the surface brightness reconstruction of systems 3-4, we fix the mass profile parameters of the smooth dark halo, GR and BCG to the values obtained from the model w/σ . Then we only optimise the mass profile parameters associated with the three cluster members G1, G2 and G3 close to the arcs (see Fig. 8.10). As before, position and shape parameters of these three galaxies are estimated using the values traced by the light. For G1 and G2 we optimise the PA and b/a with gaussian prior using their 10% error as width. We also optimise their measured velocity dispersions within their uncertainties using a gaussian prior. For G3 we have no measured σ_{sp} , so we use the σ_{G3} resulting from the model w/σ , and optimise it within the 1σ uncertainties with a gaussian prior. Finally we optimise the truncation radii of these three galaxies (G1 to G3) within the wide range of [1,100] kpc with a flat prior and we also allow for a core radius for G1 and G2.

The final best model has a reduced $\chi_{img}^2 = 1.4$ from all images positions. In Fig. 8.11 we show the arc reconstructed, the original image, and the residual between these two images. The χ^2 from the pixellated surface brightness reconstruction of the southern arcs is $\chi_{SB}^2 = 0.78$. In Fig 8.12 we present the reconstruction of the unlensed source. It shows an irregular light distribution which consists of 5 clumps. The clumps A-B corresponds to the system 3 in the pointlike models, while the clumps C-D-E to system 4. Irregular light distribution seems to be common to galaxies at redshift $z > 2$. The Hubble morphological sequence applies to galaxy population from the local Universe up to intermediate redshifts $z \sim 1 - 2$ (e.g., see Glazebrook et al., 1995; Stanford et al., 2004). At higher redshifts the majority of galaxies show irregular and clumpy morphology (e.g., see Dickinson, 2000; Conselice et al., 2005; Talia et al., 2014). The source reconstructed has a size of $\sim 0.5''$, which corresponds to ~ 4 kpc at $z_s = 2.58$. Galaxies in the redshift range $z \sim 2 - 3.5$ typically have radii ranging between 1-5 kpc (e.g., see Bouwens et al., 2004; Oesch et al., 2009). Thus the size of the source

we reconstruct at $z_s = 2.58$ is consistent with value expected for galaxies at high redshift.

In Table 8.5 we list the most probable mass parameters and their respective 1σ uncertainties for G1, G2 and G3. Here we focus on the parameters for G1 and G2, to compare them with results from the pointlike models. The ellipticity and PA are stable relative to the values extracted from the light profiles for both galaxies. G1 gets a velocity dispersion of $\sigma = 239 \pm 2$ km/s, which is consistent with previous results within the 1σ uncertainties. The core radius is 1.3 ± 0.1 kpc and the truncation radius is $50.5^{+3.6}_{-4.6}$ kpc. For G2 we get $\sigma = 186^{+4}_{-7}$ km/s, $r_{core} = 0.3^{+0.3}_{-0.2}$ kpc (consistent with zero) and $r_{tr} = 68.8^{+10.0}_{-10.9}$ kpc. Performing the surface brightness reconstruction of the southern arcs allows to reach better constraints on the individual galaxies G1 and G2, as can be seen from the MCMC sampling of this model presented in Fig. 8.13. In Fig. 8.9 we plot the velocity dispersions and truncation radii of these two galaxies as resulting from the surface brightness reconstruction, to compare them with the prediction from the scaling relations obtained from the pointlike modelling. In the previous models these two galaxies get truncation radii which are several times larger than the predictions from the respective luminosity scaling laws in Eq. 8.2 and 8.3. The surface brightness reconstruction of the southern arcs leads to similar results. Both the galaxies have truncation radii larger than the respective predictions from the global scaling law. However, comparing the r_{tr} prediction for these two galaxies for the three analyses performed in this work, they are all consistent with each others within the 1σ errors. In Fig. 8.13 we plot the Monte Carlo Markov Chain sampling of the dark halo parameters for both G1 and G2. The total masses associated with the two galaxies (see Eq. 3.65) are $M_{G1} = 2.1 \pm 0.2 \times 10^{12} M_\odot$ and $M_{G2} = 1.7 \pm 1.3 \times 10^{12} M_\odot$, which are consistent with the mass estimations from the pointlike models. See Tab. 8.5 for a summary of the mass profile parameters.

To infer the amount of stripped dark matter for galaxies in cluster cores we can estimate the total mass that G1 and G2 would have if they were in underdense environments, and compare them to their total mass estimated with lensing in the cluster core. Brimiouille et al. (2013) estimated the r_{tr} - σ scaling law for early type field galaxies, getting $r_{tr,field} = 245^{+64}_{-52} h_{100}^{-1}$ kpc for a reference galaxy with $\sigma = 144$ km/s, assuming that $r_{tr} \propto \sigma^2$ in fields. Using this relation and Eq. 3.65 we can derive the mass that G1 and G2 would have in the field. Assuming that the velocity dispersion of the halos does not change when the galaxies infall in cluster and during the stripping process, we get that $M_{tot,SL}^{G1}/M_{tot,fields}^{G1} = 0.07$ and $M_{tot,SL}^{G2}/M_{tot,fields}^{G2} = 0.17$, which imply that 93% and 83% of the mass has been stripped respectively for G1 and G2. This results is in agreement with numerical simulations of tidal stripping processes (see Warnick et al., 2008; Limousin et al., 2009) which estimate that 90% of the mass is lost for galaxies in cluster cores.

8.7 Discussion and Conclusions

In this paper we measured the mass distribution in the core of A383 using pointlike lensing constraints and by reconstructing the surface brightness distribution of giant arcs. For the first time we included in the lensing analyses the measurements of velocity dispersions for 21 cluster members. These allow us to refine individually the constraints on the galaxy mass component and on the smooth dark halo mass profile.

In Sec. 8.5 we construct two parallel models, one in which we include the measured σ_{sp} and the other in which do not use such information. We find that the σ_{SL} values are globally in

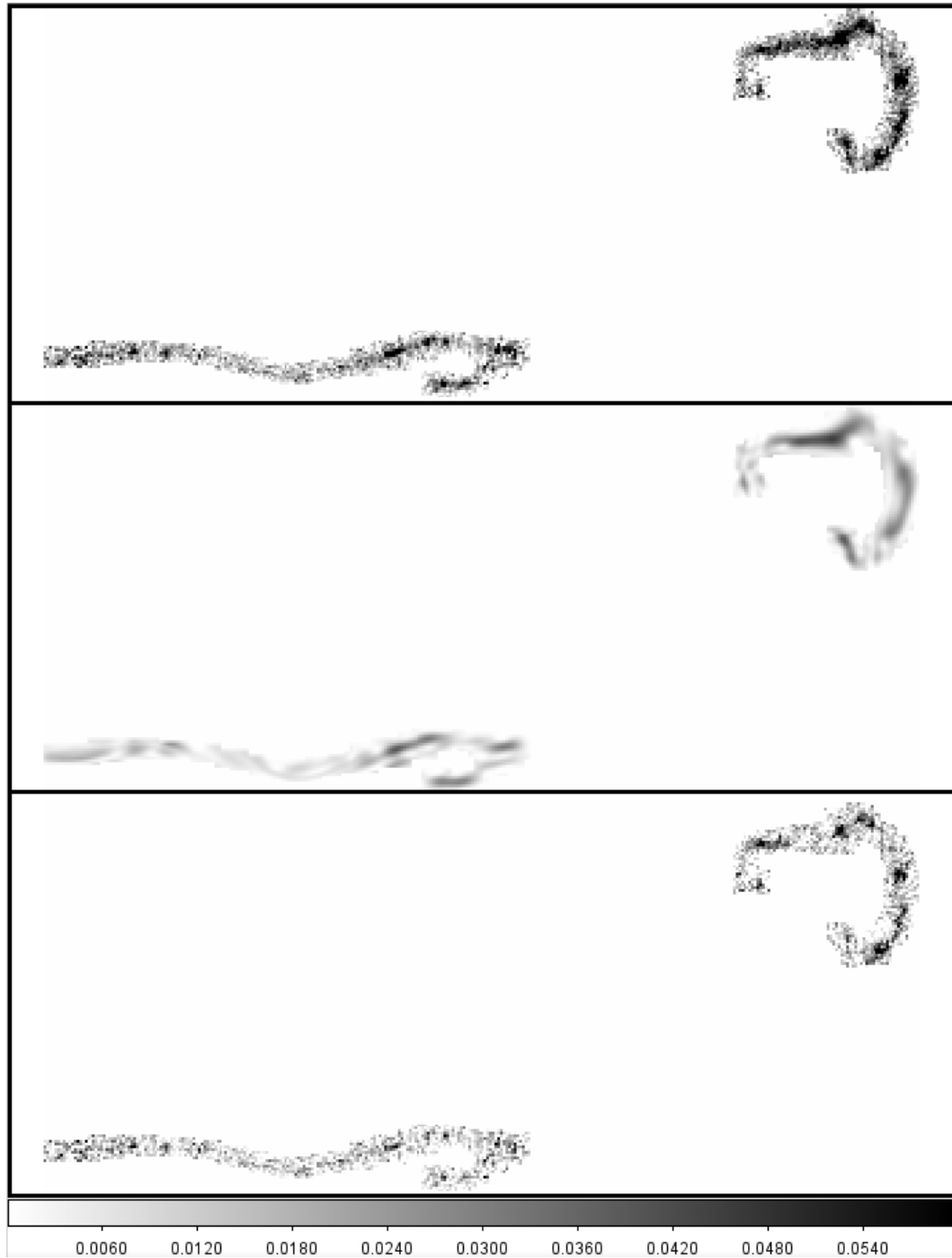


Figure 8.11: Surface brightness reconstruction of the giant southern arcs (20×10 arcsec cutout, which corresponds to $\sim 60 \times 30$ kpc at the cluster redshift). Upper panel show the arcs in the HST/ACS/F775W filter, the central panel shows the reconstruction of the arc in this filter, and the lower panel shows the residuals.

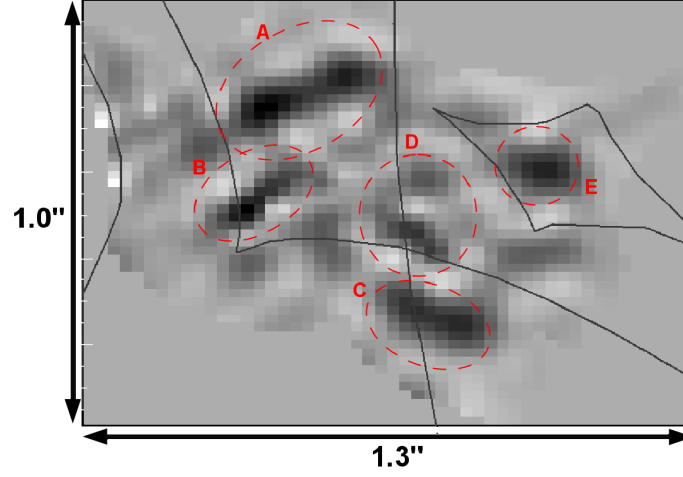


Figure 8.12: Source reconstruction of the southern arc (1.3×1.0 arcsec cutout, which corresponds to $\sim 10 \times 8$ kpc at the redshift of the source). The gray lines are the caustics. The reconstructed source is composed of 5 clumps (red dashed contours). The clumps A-B corresponds to the system 3 in the pointlike models, while C-D-E are the light reconstruction of system 4.

Table 8.5: Most probable parameters with the respective 1σ errors for the dPIE mass distribution of the cluster members close to the reconstructed giant arcs. The total mass is estimated according to Eq. 3.65

Galaxy	wo/ σ	w/ σ	Ext_model
G1			
b/a	0.8	0.8	0.82 ± 0.01
PA	151	151	150.7 ± 0.6
σ [km/s]	253 ± 23	252 ± 14	239 ± 2
r_{core} [kpc]	0.	0.	1.3 ± 0.1
r_{tr} [kpc]	47.8 ± 20.9	$56.8^{+24.8}_{-25.6}$	$50.5^{+3.6}_{-4.6}$
M [$10^{12} M_{\odot}$]	2.2 ± 1.4	$2.6^{+1.4}_{-1.5}$	2.1 ± 0.2
G2			
b/a	0.58	0.58	0.57 ± 0.01
PA	63	63	63 ± 1
σ [km/s]	194^{+54}_{-45}	201 ± 20	186^{+4}_{-7}
r_{core} [kpc]	0.	0.	$0.3^{+0.3}_{-0.2}$
r_{tr} [kpc]	$32.2^{+31.5}_{-23.4}$	$53.2^{+49.2}_{-36.3}$	$68.8^{+10.0}_{-10.9}$
M_{tot} [$10^{12} M_{\odot}$]	$0.9^{+1.3}_{-1.1}$	$1.6^{+1.8}_{-1.4}$	1.7 ± 1.3
G3			
b/a	0.93	0.93	0.57 ± 0.01
PA	65	65	65
σ [km/s]	109^{+20}_{-16}	120 ± 7	128 ± 2
r_{core} [kpc]	0.	0.	0.
r_{tr} [kpc]	$9.6^{+12.2}_{-5.3}$	$4.1^{+2.5}_{-1.7}$	2.9 ± 0.4
M_{tot} [$10^{12} M_{\odot}$]	$0.08^{+0.14}_{-0.07}$	$0.04^{+0.02}_{-0.03}$	0.04 ± 0.01

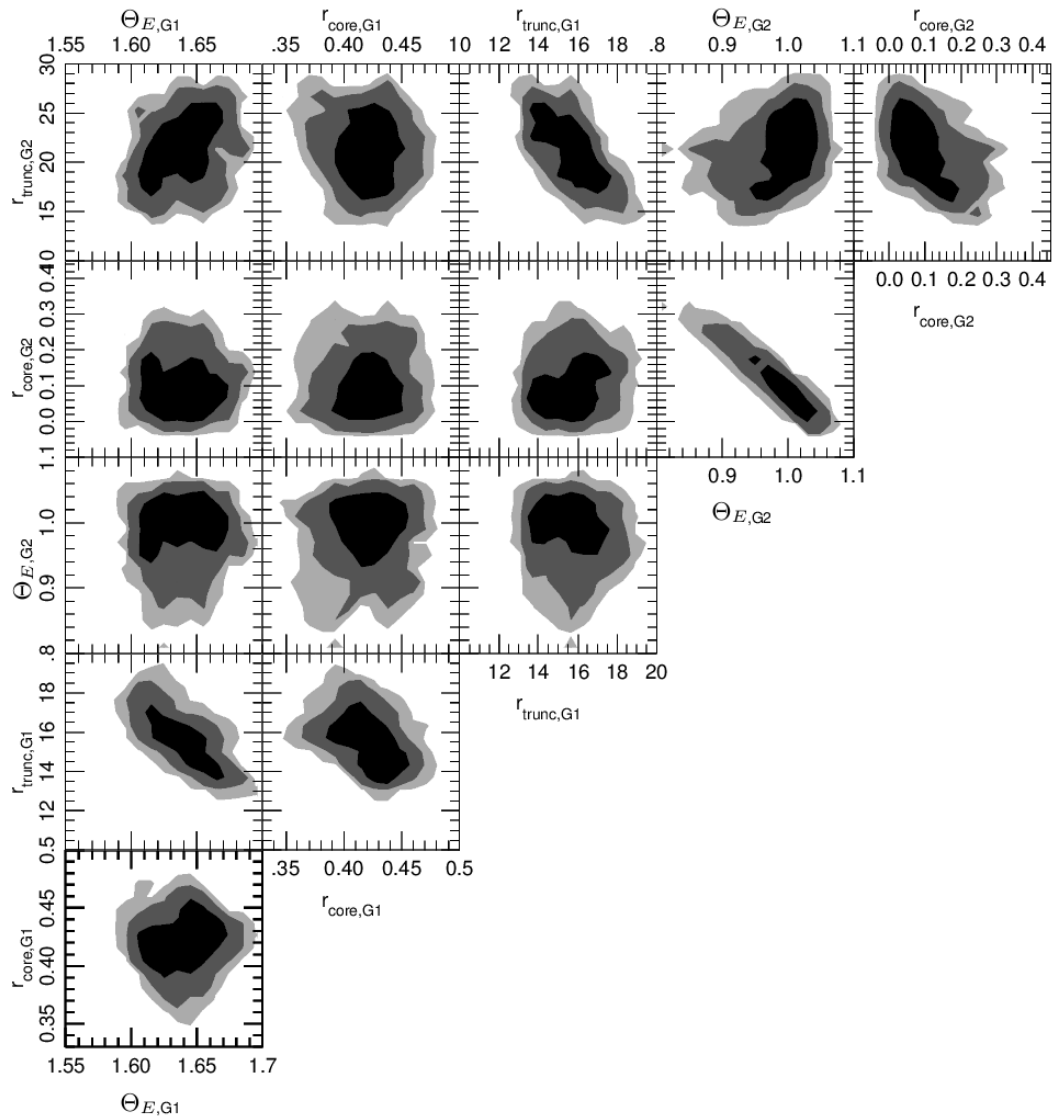


Figure 8.13: MCMC sampling of the parameters describing the DH mass profiles of G1 and G2 resulting from the surface brightness reconstruction. The truncation and core radii and Θ_E are given in arcseconds as in the previous plots.

agreement with the measured values at the 1σ level (see Fig. 8.7). Only few galaxies have σ_{SL} slightly different from the measured velocity dispersions, which are faint galaxies with large errors on the measured velocity dispersions. However these also agree at the 2σ level with the spectroscopic measurements.

In particular, when we optimise the mass profiles of cluster members individually, taking advantage of stronger constraints from lensing, the σ_{SL} predictions are in great agreement with the σ_{sp} measurements.

The galaxy chosen as reference for the luminosity scaling relations has measured velocity dispersion. Thus, once we fix the exponents of the scaling relations (Eq. 4.8 and Eq. 4.9), the only parameter we need to constrain to estimate the global scaling laws is the truncation radius $r_{tr,GR}$. The results of the pointlike models show that knowledge of the cluster members velocity dispersions allows to improve the constraints on the $r_{tr,GR}$ and on the scaling relation by 50%. Faber et al. (2007) investigated the luminosity function for red and blue galaxies in several redshift bins up to $z \sim 1$. For the red galaxy sample with redshift $0.2 \leq z < 0.4$, a typical L^* galaxy has $M_B^* = -20.95_{-0.17}^{+0.16}$ in AB system. According to our final scaling relation w/σ (Eq. 8.3), such a typical L^* red galaxy at $z \sim 0.2$ has a truncation radius of $r_{tr}^* = 20.5_{-6.7}^{+9.6}$ kpc, velocity dispersion of $\sigma_* = 324 \pm 17$ km/s and total mass $M_{tot}^* = 1.57_{-0.54}^{+0.75} \times 10^{12} M_\odot$.

Natarajan et al. (2009), combining strong and weak lensing analyses, investigated the dark halo of galaxies in the core of CL 0024+16 at $z = 0.39$ for early and late type galaxies as a function of their distance from the cluster centre. They found that the dark halo mass of a fiducial L^* early type galaxy increases with the distance from the cluster centre, from $M^* = 6.3_{-2.0}^{+2.7} \times 10^{11} M_\odot$ in the core ($r < 0.6$ Mpc) to $M^* = 3.7_{-1.1}^{+1.4} \times 10^{12} M_\odot$ in the outskirts. This is consistent with our results for a L^* galaxy in the core of A383 at the 2σ level.

Limousin et al. (2009), using N-body hydrodynamical simulations, probed the tidal stripping of galaxy dark halos in clusters in the redshift range $z_{cl} = [0, 0.7]$. They used the half mass radii $r_{1/2}$ of galaxies to quantify the extent of their dark halos, which correspond to our r_{tr} for dPIE profile with vanishing core radius. They found that the $r_{1/2}$ and the total dark halo mass of the galaxies decrease moving from the outskirts to the core of the clusters, showing that galaxies in the core experience stronger stripping than the ones in the outer regions. In particular, galaxies in the core ($r < 0.6$ Mpc) are expected to have $r_{1/2} < 20$ kpc. In this work we analysed the halo properties of galaxies in the core of A383, with projected radial distance $R < 1.5' = 0.3$ Mpc. Our results from the model w/σ are in great agreement with the predictions of Limousin et al. (2009), confirming that the sample of cluster members we investigated in the core of A383 experienced strong tidal stripping.

In Fig. 8.14 we compare our results for the scaling law between the truncation radii and velocity dispersions with results from previous analyses. In Eichner et al. (2013) we measured the galaxies' scaling relation in the cluster MACS1206 at $z = 0.439$ performing an analysis similar to the one presented here for A383, but without the knowledge of cluster members' velocity dispersions. For MACS1206 we obtained $r_{tr} = 35 \pm 8 \text{ kpc}(\sigma/186 \text{ km/s})^{4/3}$, which is consistent with the result for A383 from the pointlike model w/σ , but it is not in agreement at the 1σ level with the tighter scaling relation we get from the model w/σ . This is also the case when we compare our results with the ones presented in Halkola et al. (2007), where strong lensing is used to derive the sizes of the halos of galaxies in the core of Abell 1689. They tested the assumption of two different exponents for the r_{tr} - σ relation, using $\alpha/\delta = 1, 2$ (see

Eq. 4.9). The reference truncation radii resulting from their two models are consistent and they conclude that galaxies in the core of the cluster are strongly truncated. For simplicity in Fig. 8.14 we plot only their results for $\alpha/\delta = 1$, which is closer to the exponent assumed in our analyses. The scaling relations from Eichner et al. (2013) and Halkola et al. (2007) deviate from our relations. This can be a result of the different clusters analysed. Another reason could be that, by scaling all the cluster members (including the brighter ones) with the same law, the resulting sizes are overestimated. Bright cluster members, which have been central galaxies before accretion to the cluster, have not yet been strongly stripped as fainter galaxies which have been satellites for a long time. Indeed one expects that the dispersion of halo mass is larger for bright galaxies than for fainter ones, depending on whether they have been a satellite or central galaxy at accretion of the cluster. In our analysis several brighter central galaxies (GR, BCG, G1, G2) are individually optimised, and the scaling laws mainly applies to galaxies which have been satellites for a long time.

Suyu & Halkola (2010) derived the size for a satellite halo in a galaxy group at $z = 0.35$, which has a projected distance from the centre of galaxy group of $R \sim 26$ kpc. The truncation radii and velocity dispersion estimated for this satellite are $r_{tr} = 6.0^{+2.9}_{-2.0}$ kpc for $\sigma_{sat} = 127^{+22}_{-12}$ km/s respectively. This is in good agreement with predictions from our scaling law w/σ at low velocity dispersions, and support that our scaling law is representative for satellite galaxies.

Natarajan et al. (2002), combining strong and weak lensing analyses, investigated properties of galaxies in 6 massive clusters spanning the redshift range $z = 0.17 - 0.58$, using archival HST data. They found that galaxies are tidally truncated in clusters, and in particular their results for 3 clusters of the sample (A2390, AC114, CL0054-27) are in good agreement with our results from the modelling w/σ .

Limousin et al. (2007) used weak lensing to measure the size of galaxies in 5 clusters at $z \sim 0.2$, including A383, covering a wide FOV with $R < 2$ Mpc. Globally they find that galaxies with velocity dispersion within $[150, 250]$ km/s have truncation radii lower than 50 kpc, with mean value of 13 kpc, which is consistent with predictions from our scaling laws. In particular for A383 they predicted $r_{tr} = 13^{+37}_{-12}$ kpc for a galaxy with $\sigma = 175^{+66}_{-143}$ km/s (in agreement with our results).

Finally Richard et al. (2010) and Donnarumma et al. (2011) measured the halos sizes of individual galaxies in the core of Abell 370 ($z = 0.375$) and Abell 611 ($z = 0.288$) respectively, taking advantage of direct strong lensing constraints on the galaxies. Their analyses predict larger truncation radii for these galaxies when compared to our w/σ scaling law, but they are consistent with our results from the model w/σ at the 1σ level (see Fig. 8.14).

The estimates from these previous works, are still degenerate with the velocity dispersions they used. Here in this work, for the first time we broke this degeneracy using measurements of cluster members velocity dispersions.

To improve the constraints on the halo size of individual galaxies in the core of the cluster, we performed the surface brightness reconstruction of the southern giant arcs. This allowed us to measure the halo size of two close cluster members, G1 and G2, for which we have measured velocity dispersions. With this analysis we improved the constraints by more than 30% on the halo size of these two galaxies. The results are also plotted in Fig. 8.14, which shows that these two galaxies deviate from the global scaling law derived for the cluster. This could mean that G1 and G2 have been central galaxies before accretion to the cluster and suffered less stripping than fainter galaxies which have been satellites. However, using Eq. 3.65 we estimated the total mass associated with the dark halos for G1 and G2 and compared these

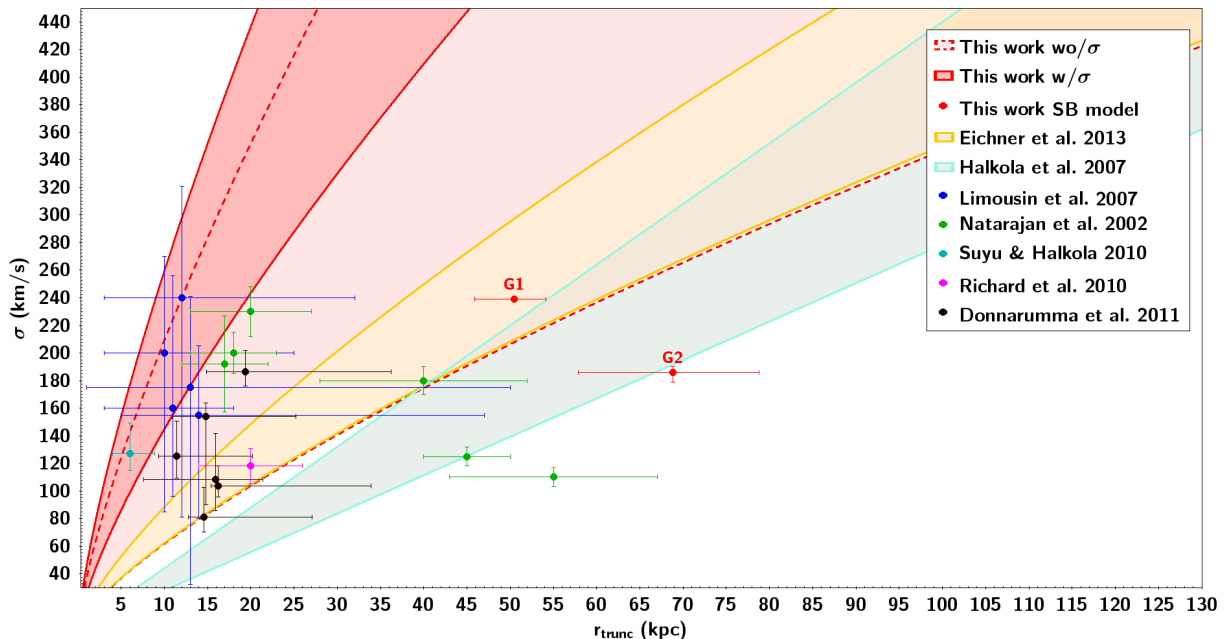


Figure 8.14: Galaxy scaling relations resulting from our and previous lensing analyses. The red lines are the 68% confidence levels of the scaling relations obtained in this work from the model w/σ (red dashed lines) and w/σ (red lines). We also plot the measurements of the dark halo sizes of G1 and G2 resulting from the surface brightness reconstruction of the southern giant arcs. In yellow and cyan we plot the 68% confidence levels of the scaling relations derived in Eichner et al. (2013) and Halkola et al. (2007) respectively. Natarajan et al. (2002) and Limousin et al. (2007) derive the halo sizes of galaxies in the core of several clusters, using respectively strong and weak lensing analyses. Their results are plotted as green (Natarajan et al. (2002)) and blue circles (Limousin et al. (2007)). The uncertainties on the measurements of Limousin et al. (2007) are 1- 2- and 3- σ errors, depending on the cluster (see Limousin et al., 2007, for details). In addition we plot individual measurements of galaxies halos in a group, from Suyu & Halkola (2010) (plotted in cyan), and in clusters, from Richard et al. (2010) (in magenta) and Donnarumma et al. (2011) (in black). The measurements from Donnarumma et al. (2011) are the parameters for the six galaxies individually optimised in the core of A 611, corresponding to the “case 6” presented in their paper. Our scaling relation from the modelling w/σ is in agreement with all the previous measurements, except for two clusters from Natarajan et al. (2002), while the tighter relation resulting from our model w/σ is consistent with the results from Limousin et al. (2007), Suyu & Halkola (2010) and part of results from Natarajan et al. (2002). See text for more details.

values with the mass they would have without suffering any stripping for the interaction with the cluster dark halo and the other galaxies. It resulted that 93% and 83% of the mass has been stripped respectively for G1 and G2, in agreement with results from numerical simulations which predict that galaxies in cluster cores loose 90% of their mass due to tidal stripping.

In this paper we have shown that the degeneracy in the analytic scaling relation, adopted for cluster members in lens modeling, can be broken using measured velocity dispersions of individual cluster galaxies. The knowledge of cluster members σ_{sp} yields to improvements both on the fit and on the constraints on the mass shape and composition. We found that galaxies in cluster cores are strongly truncated, which is overall in agreement with previous measurements and also with prediction from numerical simulations. High resolution photometric and spectroscopic data, combined with galaxy kinematics, allow to constrain to a

higher level the galaxy scaling law in core of clusters, and also to individually identify cluster members which deviate from the global scaling law measured for the cluster, as G1 and G2. This was a first case study on a well studied lensing cluster, A383. In the near future we plan to apply this new technique to a larger sample of clusters, and explore further the treasury of using cluster members measured velocity dispersions in lensing analysis.

Acknowledgements

This work is supported by the Transregional Collaborative Research Centre TRR 33 - The Dark Universe and the DFG cluster of excellence “Origin and Structure of the Universe”. The CLASH Multi-Cycle Treasury Program (GO-12065) is based on observations made with the NASA/ESA Hubble Space Telescope. The Space Telescope Science Institute is operated by the Association of Universities for Research in Astronomy, Inc. under NASA contract NAS 5-26555. The Dark Cosmology Centre is funded by the DNRF. Support for AZ is provided by NASA through Hubble Fellowship grant #HST-HF-51334.01-A awarded by STScI. The Smithsonian Institution supports the research of DGF, MJG, and HSH. We thank Daniel Gruen for his contribution to the improvement of the text.

Summary and Conclusions

In this Thesis I presented the research projects I carried out in the last three years at the Astronomical Observatory of Munich, under the supervision of Ralf Bender and Stella Seitz. I used Strong Gravitational Lensing by massive galaxy clusters to investigate the nature of galaxies strongly lensed by the clusters as well as the mass distribution of the cluster and in particular of its galaxy members.

Through a systematic photometric analysis of the sources observed in the field of some CLASH clusters, I identified several photometric $z > 5$ candidates and discovered a $z \sim 6$ galaxy quintuple lensed by the cluster RXC J2248. This lensed system appears as optical dropouts in the 16 HST filters of the CLASH dataset.

Four of its multiple images are clearly detected in the ACS/F814W, ACS/F850LP and redder filters. Through a detailed photometric analysis I showed that these images are robust high redshift candidates and have same photometric redshifts and colours within the 1σ uncertainties. The fifth central image is detected in the NIR filters after subtracting the light of the BCG.

I analyzed the strong lensing effect of this cluster using as constraints 11 multiple lensed sources, for a total of 32 multiple images. I derived the mass model of the cluster and predicted the deflection angle over the field of cluster core. The lensing model predicts a quintuple $z \sim 6$ lensed source associated with the four $z \sim 6$ optical dropouts. The position of these lensed images are predicted with accuracy of $0.8''$. The fifth central image is actually detected in agreement with the lensing prediction and is observed in the same NIR filters as the other four images once that the BCG light is subtracted. The joint photometric and lensing analyses support the high redshift quintuple lensed nature of this system and allow to rule out the low-redshift early type and galactic stellar contaminants, given the extended nature of the images. The magnifications of the five images are between 2.4 and 10, which leads to a delensed UV luminosity of $L_{1600} \sim 0.4L_{1600}^*$ at $z = 6$. I also estimate its restframe UV slope β from the observed NIR colours, finding a steep $\beta = -2.89 \pm 0.25$.

Through a detailed SED fit analysis this $z \sim 6$ galaxy is shown to be a very young (age < 300 Myr) galaxy with mass of $M \sim 10^8 M_\odot$, subsolar metallicity ($Z < 0.2Z_\odot$) and low dust content ($A_V \sim 0.2 - 0.4$).

Thanks to the lensing magnification of the fluxes, 4 lensed images of this $z \sim 6$ galaxy are bright enough to be spectroscopically investigate with current 8m class telescopes, like the

ESO/VLT at Paranal. Thus the candidate was included as a target in the CLASH-VLT survey. It was confirmed to be at $z_{sp} = 6.11$ (Balestra et al., 2013; Boone et al., 2013; Karman et al., 2014) and also the physical properties estimated from its spectrum are in great agreement with the results from the photometric analysis.

The case of this quintuple lensed galaxy spectroscopically confirmed at z_{sp} is a clear example of the robustness of combining gravitational lensing and photometric analyses to identify and investigate the properties of $z > 5$ galaxies that could not be analyzed to the same detail without their gravitational lensing magnification.

In this thesis I also presented my effort in constraining the mass associated with cluster galaxies, to finally study how they are stripped relative to field galaxies. I applied a new approach to constrain the mass distribution in the clusters core with strong lensing, which uses as additional constraints the measurements of the velocity dispersion of several cluster members to estimate the amplitude of the galaxy halo density profiles.

I performed the strong lensing analysis of the core of the CLASH cluster Abell 383 using measured velocity dispersion of 21 cluster members from the Hectospec survey (P.I. Geller M.). Lensing usually constrains the overall, projected mass density. Using velocity dispersion measurements of individual cluster members breaks inherent degeneracies between the galaxy mass parameters, and allows us to refine the constraints on single galaxy masses and on the galaxy mass-to-light scaling relation. As a result, the constraints on the DM-only map are also refined. I show that the knowledge of cluster member velocity dispersions improves the lensing fit by 17% in terms of the image reproduction χ^2 . The constraints on the cluster smooth DM halo are refined by $\sim 10\%$, while for a fiducial reference galaxy used to scale the member galaxy masses they are corroborated correspondingly by $\sim 50\%$, breaking the degeneracy between the velocity dispersions and sizes of the galaxies. For a fiducial L^* galaxy with $M_B^* = -20.96$, for example, we obtain best fitting truncation radius $r_{tr}^* = 20.5_{-6.7}^{+9.6}$ kpc and velocity dispersion $\sigma_* = 324 \pm 17$ km/s.

I found that galaxies in cluster cores are strongly truncated and have lost $\sim 90\%$ of their halo mass due to tidal stripping, which is overall in agreement with previous measurements and also with numerical simulations.

In addition, by performing a detailed surface brightness reconstruction of the southern giant arcs, I improved the constraints on the truncation radius of two close by cluster members which have measured velocity dispersions by more than 30%.

I conclude that high resolution photometric and spectroscopic data, combined with galaxy kinematics, allow to constrain the galaxy luminosity scaling laws in core of clusters at a higher level. Moreover, when one can use additional information due to giant arcs and multiple images nearby cluster members, these galaxies can be investigated in greater details and one can also identify members which deviate from the global scaling law measured for the cluster. In the near future I plan to apply this new technique to a larger sample of clusters within the CLASH survey and the Frontier Field program (P.I. Lotz J.) to improve our constraints on the galaxy scaling law in different clusters and investigate if and how these are affected by the properties of the individual cluster, and whether a general galaxy scaling law can be actually measured and used to describe galaxies in cluster cores.

Bibliography

- Abdelsalam, H. M., Saha, P., & Williams, L. L. R. 1998: *Non-parametric reconstruction of cluster mass distribution from strong lensing - Modelling Abell 370*, Mon. Not. Roy. Astron. Soc., 294, 734
- Allen, S. W., Schmidt, R. W., Ebeling, H., Fabian, A. C., & van Speybroeck, L. 2004: *Constraints on dark energy from Chandra observations of the largest relaxed galaxy clusters*, Mon. Not. Roy. Astron. Soc., 353, 457
- Arnouts, S., Cristiani, S., Moscardini, L., Matarrese, S., Lucchin, F., Fontana, A., & Giallongo, E. 1999: *Measuring and modelling the redshift evolution of clustering: the Hubble Deep Field North*, Mon. Not. Roy. Astron. Soc., 310, 540
- Balestra, I., Mainieri, V., Popesso, P., Dickinson, M., Nonino, M., Rosati, P., Teimoorinia, H., Vanzella, E., Cristiani, S., Cesarsky, C., Fosbury, R. A. E., et al. 2010: *The Great Observatories Origins Deep Survey. VLT/VIMOS spectroscopy in the GOODS-south field: Part II*, A&A, 512, A12
- Balestra, I., Vanzella, E., Rosati, P., Monna, A., Grillo, C., Nonino, M., Mercurio, A., Biviano, A., Bradley, L., Coe, D., Fritz, A., et al. 2013: *CLASH-VLT: spectroscopic confirmation of a $z = 6.11$ quintuply lensed galaxy in the Frontier Fields cluster RXC J2248.7-4431*, A&A, 559, L9
- Barkana, R. & Loeb, A. 2001: *In the beginning: the first sources of light and the reionization of the universe*, Physics Reports, 349, 125
- Bartelmann, M. 1996: *Arcs from a universal dark-matter halo profile.*, A&A, 313, 697
- Bartelmann, M. 2010: *TOPICAL REVIEW Gravitational lensing*, Classical and Quantum Gravity, 27, 233001
- Bartelmann, M. & Meneghetti, M. 2004: *Do arcs require flat halo cusps?*, A&A, 418, 413
- Bender, R., Burstein, D., & Faber, S. M. 1992: *Dynamically hot galaxies. I - Structural properties*, ApJ, 399, 462
- Benítez, N. 2000: *Bayesian Photometric Redshift Estimation*, ApJ, 536, 571
- Bertin, E. & Arnouts, S. 1996: *SExtractor: Software for source extraction.*, A&AS, 117, 393

- Binney, J. & Merrifield, M. 1998, *Galactic Astronomy*
- Binney, J. & Tremaine, S. 1987, *Galactic dynamics*
- Boone, F., Clément, B., Richard, J., Schaerer, D., Lutz, D., Weiß, A., Zemcov, M., Egami, E., Rawle, T. D., Walth, G. L., Kneib, J.-P., et al. 2013: *An extended Herschel drop-out source in the center of AS1063: a normal dusty galaxy at $z = 6.1$ or SZ substructures?*, A&A, 559, L1
- Bouwens, R. J., Illingworth, G. D., Blakeslee, J. P., Broadhurst, T. J., & Franx, M. 2004: *Galaxy Size Evolution at High Redshift and Surface Brightness Selection Effects: Constraints from the Hubble Ultra Deep Field*, ApJ, 611, L1
- Bouwens, R. J., Illingworth, G. D., Oesch, P. A., Franx, M., Labbé, I., Trenti, M., van Dokkum, P., Carollo, C. M., González, V., Smit, R., & Magee, D. 2012: *UV-continuum Slopes at $z \sim 4-7$ from the HUDF09+ERS+CANDELS Observations: Discovery of a Well-defined UV Color-Magnitude Relationship for $z > 4$ Star-forming Galaxies*, ApJ, 754, 83
- Bouwens, R. J., Illingworth, G. D., Oesch, P. A., Trenti, M., Labbé, I., Bradley, L., Carollo, M., van Dokkum, P. G., Gonzalez, V., Holwerda, B., Franx, M., et al. 2014: *UV Luminosity Functions at redshifts $z \sim 4$ to $z \sim 10$: 11000 Galaxies from HST Legacy Fields*, ArXiv e-prints
- Boylan-Kolchin, M., Springel, V., White, S. D. M., Jenkins, A., & Lemson, G. 2009: *Resolving cosmic structure formation with the Millennium-II Simulation*, Mon. Not. Roy. Astron. Soc., 398, 1150
- Bradley, L. D., Bouwens, R. J., Zitrin, A., Smit, R., Coe, D., Ford, H. C., Zheng, W., Illingworth, G. D., Benítez, N., & Broadhurst, T. J. 2012: *Through the Looking Glass: Bright, Highly Magnified Galaxy Candidates at $z \sim 7$ behind A1703*, ApJ, 747, 3
- Bradley, L. D., Zitrin, A., Coe, D., Bouwens, R., Postman, M., Balestra, I., Grillo, C., Monna, A., Rosati, P., Seitz, S., Host, O., et al. 2014: *CLASH: A Census of Magnified Star-forming Galaxies at $z \sim 6-8$* , ApJ, 792, 76
- Brimioulle, F., Seitz, S., Lerchster, M., Bender, R., & Snigula, J. 2013: *Dark matter halo properties from galaxy-galaxy lensing*, Mon. Not. Roy. Astron. Soc., 432, 1046
- Bruzual, G. & Charlot, S. 2003: *Stellar population synthesis at the resolution of 2003*, Mon. Not. Roy. Astron. Soc., 344, 1000
- Calzetti, D., Armus, L., Bohlin, R. C., Kinney, A. L., Koornneef, J., & Storchi-Bergmann, T. 2000: *The Dust Content and Opacity of Actively Star-forming Galaxies*, ApJ, 533, 682
- Calzetti, D., Kinney, A. L., & Storchi-Bergmann, T. 1994: *Dust extinction of the stellar continua in starburst galaxies: The ultraviolet and optical extinction law*, ApJ, 429, 582
- Carlstrom, J. E., Holder, G. P., & Reese, E. D. 2002: *Cosmology with the Sunyaev-Zel'dovich Effect*, ARA&A, 40, 643
- Chabrier, G. 2003: *Galactic Stellar and Substellar Initial Mass Function*, PASP, 115, 763

- Clowe, D., Bradač, M., Gonzalez, A. H., Markevitch, M., Randall, S. W., Jones, C., & Zaritsky, D. 2006: *A Direct Empirical Proof of the Existence of Dark Matter*, ApJ, 648, L109
- Coe, D., Benítez, N., Broadhurst, T., & Moustakas, L. A. 2010: *A High-resolution Mass Map of Galaxy Cluster Substructure: LensPerfect Analysis of A1689*, ApJ, 723, 1678
- Coe, D., Fuselier, E., Benítez, N., Broadhurst, T., Frye, B., & Ford, H. 2008: *LensPerfect: Gravitational Lens Mass Map Reconstructions Yielding Exact Reproduction of All Multiple Images*, ApJ, 681, 814
- Coe, D., Umetsu, K., Zitrin, A., Donahue, M., Medezinski, E., Postman, M., Carrasco, M., Anguita, T., Geller, M. J., Rines, K. J., Diaferio, A., et al. 2012: *CLASH: Precise New Constraints on the Mass Profile of the Galaxy Cluster A2261*, ApJ, 757, 22
- Coil, A. L. 2013, *The Large-Scale Structure of the Universe*, ed. T. D. Oswalt & W. C. Keel, 387
- Cole, S. & Lacey, C. 1996: *The structure of dark matter haloes in hierarchical clustering models*, Mon. Not. Roy. Astron. Soc., 281, 716
- Conselice, C. J., Blackburne, J. A., & Papovich, C. 2005: *The Luminosity, Stellar Mass, and Number Density Evolution of Field Galaxies of Known Morphology from $z = 0.5$ to 3*, ApJ, 620, 564
- Cushing, M. C., Rayner, J. T., & Vacca, W. D. 2005: *An Infrared Spectroscopic Sequence of M , L , and T Dwarfs*, ApJ, 623, 1115
- D'Aloisio, A. & Natarajan, P. 2011: *Cosmography with cluster strong lenses: the influence of substructure and line-of-sight haloes*, Mon. Not. Roy. Astron. Soc., 411, 1628
- Dickinson, M. 2000: *The first galaxies: structure and stellar populations*, in Royal Society of London Philosophical Transactions Series A, Vol. 358, Astronomy, physics and chemistry of H_3^+ , 2001
- Diego, J. M., Protopapas, P., Sandvik, H. B., & Tegmark, M. 2005: *Non-parametric inversion of strong lensing systems*, Mon. Not. Roy. Astron. Soc., 360, 477
- Djorgovski, S. & Davis, M. 1987: *Fundamental properties of elliptical galaxies*, ApJ, 313, 59
- Donnarumma, A., Ettori, S., Meneghetti, M., Gavazzi, R., Fort, B., Moscardini, L., Romano, A., Fu, L., Giordano, F., Radovich, M., Maoli, R., et al. 2011: *Abell 611. II. X-ray and strong lensing analyses*, A&A, 528, A73
- Dressler, A. 1980: *Galaxy morphology in rich clusters - Implications for the formation and evolution of galaxies*, ApJ, 236, 351
- Dressler, A., Lynden-Bell, D., Burstein, D., Davies, R. L., Faber, S. M., Terlevich, R., & Wegner, G. 1987: *Spectroscopy and photometry of elliptical galaxies. I - A new distance estimator*, ApJ, 313, 42
- Drory, N., Bender, R., & Hopp, U. 2004: *Comparing Spectroscopic and Photometric Stellar Mass Estimates*, ApJ, 616, L103

- Dunlop, J. S. 2013: *Observing the First Galaxies*, in *Astrophysics and Space Science Library*, Vol. 396, Astrophysics and Space Science Library, ed. T. Wiklind, B. Mobasher, & V. Bromm, 223
- Eddington, A. S. 1920, *Space, time and gravitation. an outline of the general relativity theory*
- Eichner, T., Seitz, S., Suyu, S. H., Halkola, A., Umetsu, K., Zitrin, A., Coe, D., Monna, A., Rosati, P., Grillo, C., Balestra, I., et al. 2013: *Galaxy halo truncation and Giant Arc Surface Brightness Reconstruction in the Cluster MACSJ1206.2-0847*, ArXiv e-prints
- Einstein, A. 1916: *Die Grundlage der allgemeinen Relativitätstheorie*, *Annalen der Physik*, 354, 769
- Einstein, A. 1917: *Kosmologische Betrachtungen zur allgemeinen Relativitätstheorie*, *Sitzungsberichte der Königlich Preußischen Akademie der Wissenschaften (Berlin)*, Seite 142-152., 142
- Elíasdóttir, Á., Limousin, M., Richard, J., Hjorth, J., Kneib, J.-P., Natarajan, P., Pedersen, K., Jullo, E., & Paraficz, D. 2007: *Where is the matter in the Merging Cluster Abell 2218?*, ArXiv e-prints
- Faber, S. M., Dressler, A., Davies, R. L., Burstein, D., & Lynden-Bell, D. 1987: *Global scaling relations for elliptical galaxies and implications for formation*, in *Nearly Normal Galaxies. From the Planck Time to the Present*, ed. S. M. Faber, 175–183
- Faber, S. M. & Jackson, R. E. 1976: *Velocity dispersions and mass-to-light ratios for elliptical galaxies*, *ApJ*, 204, 668
- Faber, S. M., Willmer, C. N. A., Wolf, C., Koo, D. C., Weiner, B. J., Newman, J. A., Im, M., Coil, A. L., Conroy, C., Cooper, M. C., Davis, M., et al. 2007: *Galaxy Luminosity Functions to $z \sim 1$ from DEEP2 and COMBO-17: Implications for Red Galaxy Formation*, *ApJ*, 665, 265
- Fabricant, D., Chilingarian, I., Hwang, H. S., Kurtz, M. J., Geller, M. J., Del’Antonio, I. P., & Rines, K. J. 2013: *Measuring Galaxy Velocity Dispersions with Hectospec*, *PASP*, 125, 1362
- Fabricant, D., Fata, R., Roll, J., Hertz, E., Caldwell, N., Gauron, T., Geary, J., McLeod, B., Szentgyorgyi, A., Zajac, J., Kurtz, M., et al. 2005: *Hectospec, the MMT’s 300 Optical Fiber-Fed Spectrograph*, *PASP*, 117, 1411
- Fan, X., Carilli, C. L., & Keating, B. 2006: *Observational Constraints on Cosmic Reionization*, *ARA&A*, 44, 415
- Focardi, P. & Malavasi, N. 2012: *The Effect of the Environment on the Faber-Jackson Relation*, *ApJ*, 756, 117
- Ford, H. C., Clampin, M., Hartig, G. F., Illingworth, G. D., Sirianni, M., Martel, A. R., Meurer, G. R., McCann, W. J., Sullivan, P. C., Bartko, F., Benitez, N., et al. 2003: *Overview of the Advanced Camera for Surveys on-orbit performance*, in *Society of Photo-Optical Instrumentation Engineers (SPIE) Conference Series*, Vol. 4854, Future EUV/UV

- and Visible Space Astrophysics Missions and Instrumentation., ed. J. C. Blades & O. H. W. Siegmund, 81–94
- Friedmann, A. 1922: *Über die Krümmung des Raumes*, Zeitschrift für Physik, 10, 377
- Fritz, A., Bohm, A., & Ziegler, B. L. 2009: *Field early-type galaxies at $0.2 < z < 0.8$* , VizieR Online Data Catalog, 739, 31467
- Geller, M. J., Hwang, H. S., Diaferio, A., Kurtz, M. J., Coe, D., & Rines, K. J. 2014: *A Redshift Survey of the Strong Lensing Cluster Abell 383*, ArXiv e-prints
- Gioia, I. M., Maccacaro, T., Schild, R. E., Wolter, A., Stocke, J. T., Morris, S. L., & Henry, J. P. 1990: *The Einstein Observatory Extended Medium-Sensitivity Survey. I - X-ray data and analysis*, ApJS, 72, 567
- Glazebrook, K., Ellis, R., Santiago, B., & Griffiths, R. 1995: *The morphological identification of the rapidly evolving population of faint galaxies*, Mon. Not. Roy. Astron. Soc., 275, L19
- Gómez, P. L., Valkonen, L. E., Romer, A. K., Lloyd-Davies, E., Verdugo, T., Cantalupo, C. M., Daub, M. D., Goldstein, J. H., Kuo, C. L., Lange, A. E., Lueker, M., et al. 2012: *Optical and X-Ray Observations of the Merging Cluster AS1063*, AJ, 144, 79
- Gregg, M. D., Lacy, M., White, R. L., Glikman, E., Helfand, D., Becker, R. H., & Brotherton, M. S. 2002: *The Reddest Quasars*, ApJ, 564, 133
- Greisel, N., Seitz, S., Drory, N., Bender, R., Saglia, R. P., & Snigula, J. 2013: *Photometric Redshifts and Systematic Variations in the Spectral Energy Distributions of Luminous Red Galaxies from SDSS DR7*, ApJ, 768, 117
- Grillo, C., Suyu, S. H., Rosati, P., Mercurio, A., Balestra, I., Munari, E., Nonino, M., Caminha, G. B., Lombardi, M., De Lucia, G., Borgani, S., et al. 2014: *CLASH-VLT: Insights on the mass substructures in the Frontier Fields Cluster MACS J0416.1-2403 through accurate strong lens modeling*, ArXiv e-prints
- Gruen, D., Brimiouille, F., Seitz, S., Lee, C.-H., Young, J., Koppenhoefer, J., Eichner, T., Riffeser, A., Vikram, V., Weidinger, T., & Zenteno, A. 2013: *Weak lensing analysis of RXC J2248.7-4431*, Mon. Not. Roy. Astron. Soc.
- Guzzo, L., Schuecker, P., Böhringer, H., Collins, C. A., Ortiz-Gil, A., de Grandi, S., Edge, A. C., Neumann, D. M., Schindler, S., Altucci, C., & Shaver, P. A. 2009: *The REFLEX galaxy cluster survey. VIII. Spectroscopic observations and optical atlas*, A&A, 499, 357
- Halkola, A., Seitz, S., & Pannella, M. 2006: *Parametric strong gravitational lensing analysis of Abell 1689*, Mon. Not. Roy. Astron. Soc., 372, 1425
- Halkola, A., Seitz, S., & Pannella, M. 2007: *The Sizes of Galaxy Halos in Galaxy Cluster Abell 1689*, ApJ, 656, 739
- Hatziminaoglou, E., Pérez-Fournon, I., Polletta, M., Afonso-Luis, A., Hernán-Caballero, A., Montenegro-Montes, F. M., Lonsdale, C., Xu, C. K., Franceschini, A., Rowan-Robinson, M., Babbedge, T., et al. 2005: *Sloan Digital Sky Survey Quasars in the Spitzer Wide-Area Infrared Extragalactic Survey (SWIRE) ELAIS N1 Field: Properties and Spectral Energy Distributions*, AJ, 129, 1198

- Hinshaw, G., Weiland, J. L., Hill, R. S., Odegard, N., Larson, D., Bennett, C. L., Dunkley, J., Gold, B., Greason, M. R., Jarosik, N., Komatsu, E., et al. 2009: *Five-Year Wilkinson Microwave Anisotropy Probe Observations: Data Processing, Sky Maps, and Basic Results*, ApJS, 180, 225
- Hoekstra, H., Franx, M., Kuijken, K., Carlberg, R. G., & Yee, H. K. C. 2003: *Lensing by galaxies in CNOC2 fields*, Mon. Not. Roy. Astron. Soc., 340, 609
- Hoekstra, H. & Jain, B. 2008: *Weak Gravitational Lensing and Its Cosmological Applications*, Annual Review of Nuclear and Particle Science, 58, 99
- Host, O. 2012: *Galaxy cluster strong lensing: image deflections from density fluctuations along the line of sight*, Mon. Not. Roy. Astron. Soc., 420, L18
- Hu, E. M., Cowie, L. L., McMahan, R. G., Capak, P., Iwamuro, F., Kneib, J.-P., Maihara, T., & Motohara, K. 2002: *A Redshift $z=6.56$ Galaxy behind the Cluster Abell 370*, ApJ, 568, L75
- Hubble, E. 1929: *A Relation between Distance and Radial Velocity among Extra-Galactic Nebulae*, Proceedings of the National Academy of Science, 15, 168
- Hubble, E. P. 1936, Realm of the Nebulae
- Ilbert, O., Arnouts, S., McCracken, H. J., Bolzonella, M., Bertin, E., Le Fèvre, O., Mellier, Y., Zamorani, G., Pellò, R., Iovino, A., Tresse, L., et al. 2006: *Accurate photometric redshifts for the CFHT legacy survey calibrated using the VIMOS VLT deep survey*, A&A, 457, 841
- Ilbert, O., Capak, P., Salvato, M., Aussel, H., McCracken, H. J., Sanders, D. B., Scoville, N., Kartaltepe, J., Arnouts, S., Le Floch, E., Mobasher, B., et al. 2009: *Cosmos Photometric Redshifts with 30-Bands for 2-deg²*, ApJ, 690, 1236
- Jorgensen, I., Franx, M., & Kjaergaard, P. 1995: *Spectroscopy for E and S0 galaxies in nine clusters*, Mon. Not. Roy. Astron. Soc., 276, 1341
- Jouvel, S., Host, O., Lahav, O., Seitz, S., Molino, A., Coe, D., Postman, M., Moustakas, L., Benítez, N., Rosati, P., Balestra, I., et al. 2014: *CLASH: Photometric redshifts with 16 HST bands in galaxy cluster fields*, A&A, 562, A86
- Jullo, E., Kneib, J.-P., Limousin, M., Elíasdóttir, Á., Marshall, P. J., & Verdugo, T. 2007: *A Bayesian approach to strong lensing modelling of galaxy clusters*, New Journal of Physics, 9, 447
- Karman, W., Caputi, K. I., Grillo, C., Balestra, I., Rosati, P., Vanzella, E., Coe, D., Christensen, L., Koekemoer, A. M., Kruehler, T., Lombardi, M., et al. 2014: *MUSE integral-field spectroscopy towards the Frontier Fields Cluster Abell S1063: I. Data products and redshift identifications*, ArXiv e-prints
- Kassiola, A. & Kovner, I. 1993: *Analytic lenses with elliptic mass distributions, pseudo-isothermal and others, instead of elliptic potentials*, in Liege International Astrophysical Colloquia, Vol. 31, Liege International Astrophysical Colloquia, ed. J. Surdej, D. Fraipont-Caro, E. Gosset, S. Refsdal, & M. Remy, 571

- Kassiola, A., Kovner, I., & Fort, B. 1992: *Perturbations of cluster cusps by galaxies - The triple arc in CL 0024+1654*, ApJ, 400, 41
- Kennicutt, J. R. C. 1998: *Star Formation in Galaxies Along the Hubble Sequence*, ARA&A, 36, 189
- Kessler, R., Becker, A. C., Cinabro, D., Vanderplas, J., Frieman, J. A., Marriner, J., Davis, T. M., Dilday, B., Holtzman, J., Jha, S. W., Lampeitl, H., et al. 2009: *First-Year Sloan Digital Sky Survey-II Supernova Results: Hubble Diagram and Cosmological Parameters*, ApJS, 185, 32
- Kimble, R. A., MacKenty, J. W., O'Connell, R. W., & Townsend, J. A. 2008: *Wide Field Camera 3: a powerful new imager for the Hubble Space Telescope*, in Society of Photo-Optical Instrumentation Engineers (SPIE) Conference Series, Vol. 7010, Society of Photo-Optical Instrumentation Engineers (SPIE) Conference Series
- Kneib, J.-P., Ellis, R. S., Santos, M. R., & Richard, J. 2004: *A Probable $z \sim 7$ Galaxy Strongly Lensed by the Rich Cluster A2218: Exploring the Dark Ages*, ApJ, 607, 697
- Kneib, J.-P. & Natarajan, P. 2011: *Cluster lenses*, A&ARv, 19, 47
- Koekemoer, A. M., Faber, S. M., Ferguson, H. C., Grogin, N. A., Kocevski, D. D., Koo, D. C., Lai, K., Lotz, J. M., Lucas, R. A., McGrath, E. J., Ogaz, S., et al. 2011: *CANDELS: The Cosmic Assembly Near-infrared Deep Extragalactic Legacy Survey—The Hubble Space Telescope Observations, Imaging Data Products, and Mosaics*, ApJS, 197, 36
- Koleva, M., Prugniel, P., Bouchard, A., & Wu, Y. 2009: *ULySS: a full spectrum fitting package*, A&A, 501, 1269
- Komatsu, E., Bennett, C. L., Barnes, C., Bean, R., Bennett, C. L., Doré, O., Dunkley, J., Gold, B., Greason, M. R., Halpern, M., Hill, R. S., et al. 2014: *Results from the Wilkinson Microwave Anisotropy Probe*, Progress of Theoretical and Experimental Physics, 2014, 060000
- Komatsu, E., Smith, K. M., Dunkley, J., Bennett, C. L., Gold, B., Hinshaw, G., Jarosik, N., Larson, D., Nolte, M. R., Page, L., Spergel, D. N., et al. 2011: *Seven-year Wilkinson Microwave Anisotropy Probe (WMAP) Observations: Cosmological Interpretation*, ApJS, 192, 18
- Kormendy, J. & Bender, R. 2013: *The $L_{\nu\text{prop}\sigma^8}$ Correlation for Elliptical Galaxies with Cores: Relation with Black Hole Mass*, ApJ, 769, L5
- Kriek, M., van Dokkum, P. G., Franx, M., Förster Schreiber, N. M., Gawiser, E., Illingworth, G. D., Labbé, I., Marchesini, D., Quadri, R., Rix, H.-W., Rudnick, G., et al. 2006: *Direct Measurements of the Stellar Continua and Balmer/4000 Å Breaks of Red $z > 2$ Galaxies: Redshifts and Improved Constraints on Stellar Populations₁*, ApJ, 645, 44
- Kurtz, M. J. & Mink, D. J. 1998: *RVSAO 2.0: Digital Redshifts and Radial Velocities*, PASP, 110, 934
- Lauer, T. R. 1986: *Photometric decomposition of the multiple-nucleus galaxy NGC 6166*, ApJ, 311, 34

- Le Fèvre, O., Saisse, M., Mancini, D., Brau-Nogue, S., Caputi, O., Castinel, L., D’Odorico, S., Garilli, B., Kissler-Patig, M., Lucuix, C., Mancini, G., et al. 2003: *Commissioning and performances of the VLT-VIMOS instrument*, in Society of Photo-Optical Instrumentation Engineers (SPIE) Conference Series, Vol. 4841, Instrument Design and Performance for Optical/Infrared Ground-based Telescopes, ed. M. Iye & A. F. M. Moorwood, 1670–1681
- Liddle, A. 2003, *An Introduction to Modern Cosmology*, Second Edition
- Lilly, S. J., Carollo, C. M., Pipino, A., Renzini, A., & Peng, Y. 2013: *Gas Regulation of Galaxies: The Evolution of the Cosmic Specific Star Formation Rate, the Metallicity-Mass-Star-formation Rate Relation, and the Stellar Content of Halos*, *ApJ*, 772, 119
- Limousin, M., Kneib, J. P., Bardeau, S., Natarajan, P., Czoske, O., Smail, I., Ebeling, H., & Smith, G. P. 2007: *Truncation of galaxy dark matter halos in high density environments*, *A&A*, 461, 881
- Limousin, M., Sommer-Larsen, J., Natarajan, P., & Milvang-Jensen, B. 2009: *Probing the Truncation of Galaxy Dark Matter Halos in High-Density Environments from Hydrodynamical N-Body Simulations*, *ApJ*, 696, 1771
- Loeb, A., Ferrara, A., & Ellis, R. S. 2008, *First Light in the Universe*
- Mantz, A., Allen, S. W., Rapetti, D., & Ebeling, H. 2010: *The observed growth of massive galaxy clusters - I. Statistical methods and cosmological constraints*, *Mon. Not. Roy. Astron. Soc.*, 406, 1759
- Maraston, C., Pforr, J., Renzini, A., Daddi, E., Dickinson, M., Cimatti, A., & Tonini, C. 2010: *Star formation rates and masses of $z \sim 2$ galaxies from multicolour photometry*, *Mon. Not. Roy. Astron. Soc.*, 407, 830
- Markevitch, M., Gonzalez, A. H., Clowe, D., Vikhlinin, A., Forman, W., Jones, C., Murray, S., & Tucker, W. 2004: *Direct Constraints on the Dark Matter Self-Interaction Cross Section from the Merging Galaxy Cluster 1E 0657-56*, *ApJ*, 606, 819
- Meneghetti, M., Rasia, E., Vega, J., Merten, J., Postman, M., Yepes, G., Sembolini, F., Donahue, M., Ettori, S., Umetsu, K., Balestra, I., et al. 2014: *The MUSIC of CLASH: Predictions on the Concentration-Mass Relation*, *ApJ*, 797, 34
- Merritt, D. 1983: *Relaxation and tidal stripping in rich clusters of galaxies. I. Evolution of the mass distribution*, *ApJ*, 264, 24
- Merten, J., Meneghetti, M., Postman, M., Umetsu, K., Zitrin, A., Medezinski, E., Nonino, M., Koekemoer, A., Melchior, P., Gruen, D., Moustakas, L. A., et al. 2014: *CLASH: The Concentration-Mass Relation of Galaxy Clusters*, *ArXiv e-prints*
- Miralda-Escudé, J. 2003: *The Dark Age of the Universe*, *Science*, 300, 1904
- Monna, A., Seitz, S., Greisel, N., Eichner, T., Drory, N., Postman, M., Zitrin, A., Coe, D., Halkola, A., Suyu, S. H., Grillo, C., et al. 2014a: *CLASH: $z \sim 6$ young galaxy candidate quintuply lensed by the frontier field cluster RXC J2248.7-4431*, *Mon. Not. Roy. Astron. Soc.*, 438, 1417

- Monna, A., Seitz, S., Zitrin, A., Geller, M. J., Grillo, C., Mercurio, A., Greisel, N., Halkola, A., Suyu, S. H., Postman, M., Rosati, P., et al. 2014b: *Constraining the galaxy mass content in the core of A383 using velocity dispersion measurements for individual cluster members*, ArXiv e-prints
- Murdin, P. 2001, *Encyclopedia of astronomy and astrophysics*
- Narayan, R. & Bartelmann, M. 1996: *Lectures on Gravitational Lensing*, ArXiv Astrophysics e-prints
- Narayan, R. & Bartelmann, M. 1999: *Gravitational lensing*, in *Formation of Structure in the Universe*, ed. A. Dekel & J. P. Ostriker, 360
- Natarajan, P. & Kneib, J.-P. 1997: *Lensing by galaxy haloes in clusters of galaxies*, *Mon. Not. Roy. Astron. Soc.*, 287, 833
- Natarajan, P., Kneib, J.-P., & Smail, I. 2002: *Evidence for Tidal Stripping of Dark Matter Halos in Massive Cluster Lenses*, *ApJ*, 580, L11
- Natarajan, P., Kneib, J.-P., Smail, I., Treu, T., Ellis, R., Moran, S., Limousin, M., & Czoske, O. 2009: *The Survival of Dark Matter Halos in the Cluster Cl 0024+16*, *ApJ*, 693, 970
- Navarro, J. F., Frenk, C. S., & White, S. D. M. 1997: *A Universal Density Profile from Hierarchical Clustering*, *ApJ*, 490, 493
- Navarro, J. F., Ludlow, A., Springel, V., Wang, J., Vogelsberger, M., White, S. D. M., Jenkins, A., Frenk, C. S., & Helmi, A. 2010: *The diversity and similarity of simulated cold dark matter haloes*, *Mon. Not. Roy. Astron. Soc.*, 402, 21
- Newman, A. B., Treu, T., Ellis, R. S., & Sand, D. J. 2011: *The Dark Matter Distribution in A383: Evidence for a Shallow Density Cusp from Improved Lensing, Stellar Kinematic, and X-ray Data*, *ApJ*, 728, L39
- Newman, A. B., Treu, T., Ellis, R. S., Sand, D. J., Richard, J., Marshall, P. J., Capak, P., & Miyazaki, S. 2009: *The Distribution of Dark Matter Over Three Decades in Radius in the Lensing Cluster Abell 611*, *ApJ*, 706, 1078
- Newton, E. R., Marshall, P. J., Treu, T., Auger, M. W., Gavazzi, R., Bolton, A. S., Koopmans, L. V. E., & Moustakas, L. A. 2011: *The Sloan Lens ACS Survey. XI. Beyond Hubble Resolution: Size, Luminosity, and Stellar Mass of Compact Lensed Galaxies at Intermediate Redshift*, *ApJ*, 734, 104
- Oesch, P. A., Carollo, C. M., Stiavelli, M., Trenti, M., Bergeron, L. E., Koekemoer, A. M., Lucas, R. A., Pavlovsky, C. M., Beckwith, S. V. W., Dahlen, T., Ferguson, H. C., et al. 2009: *The UDF05 Follow-Up of the Hubble Ultra Deep Field. II. Constraints on Reionization from Z-Dropout Galaxies*, *ApJ*, 690, 1350
- Paczynski, B. 1996: *Gravitational Microlensing in the Local Group*, *ARA&A*, 34, 419
- Peebles, P. J. & Ratra, B. 2003: *The cosmological constant and dark energy*, *Reviews of Modern Physics*, 75, 559

- Peebles, P. J. E. 1993, *Principles of Physical Cosmology*
- Peng, C. Y., Ho, L. C., Impey, C. D., & Rix, H.-W. 2010: *Detailed Decomposition of Galaxy Images. II. Beyond Axisymmetric Models*, AJ, 139, 2097
- Pickles, A. J. 1998: *A Stellar Spectral Flux Library: 1150-25000 Å*, PASP, 110, 863
- Pierre, M., Valtchanov, I., Altieri, B., Andreon, S., Bolzonella, M., Bremer, M., Disseau, L., Dos Santos, S., Gandhi, P., Jean, C., Pacaud, F., et al. 2004: *The XMM-LSS survey. Survey design and first results*, 9, 11
- Planck Collaboration, Ade, P. A. R., Aghanim, N., Armitage-Caplan, C., Arnaud, M., Ashdown, M., Atrio-Barandela, F., Aumont, J., Baccigalupi, C., Banday, A. J., & et al. 2013: *Planck 2013 results. XVI. Cosmological parameters*, ArXiv e-prints
- Polletta, M. d. C., Wilkes, B. J., Siana, B., Lonsdale, C. J., Kilgard, R., Smith, H. E., Kim, D.-W., Owen, F., Efstathiou, A., Jarrett, T., Stacey, G., et al. 2006: *Chandra and Spitzer Unveil Heavily Obscured Quasars in the Chandra/SWIRE Survey*, ApJ, 642, 673
- Postman, M., Coe, D., Benítez, N., Bradley, L., Broadhurst, T., Donahue, M., Ford, H., Graur, O., Graves, G., Jouvel, S., Koekemoer, A., et al. 2012a: *The Cluster Lensing and Supernova Survey with Hubble: An Overview*, ApJS, 199, 25
- Postman, M., Lauer, T. R., Donahue, M., Graves, G., Coe, D., Moustakas, J., Koekemoer, A., Bradley, L., Ford, H. C., Grillo, C., Zitrin, A., et al. 2012b: *A Brightest Cluster Galaxy with an Extremely Large Flat Core*, ApJ, 756, 159
- Prevot, M. L., Lequeux, J., Prevot, L., Maurice, E., & Rocca-Volmerange, B. 1984: *The typical interstellar extinction in the Small Magellanic Cloud*, A&A, 132, 389
- Rayner, J. T., Cushing, M. C., & Vacca, W. D. 2009: *The Infrared Telescope Facility (IRTF) Spectral Library: Cool Stars*, ApJS, 185, 289
- Reid, B. A., Percival, W. J., Eisenstein, D. J., Verde, L., Spergel, D. N., Skibba, R. A., Bahcall, N. A., Budavari, T., Frieman, J. A., Fukugita, M., Gott, J. R., et al. 2010: *Cosmological constraints from the clustering of the Sloan Digital Sky Survey DR7 luminous red galaxies*, Mon. Not. Roy. Astron. Soc., 404, 60
- Richard, J., Kneib, J.-P., Ebeling, H., Stark, D. P., Egami, E., & Fiedler, A. K. 2011: *Discovery of a possibly old galaxy at $z=6.027$, multiply imaged by the massive cluster Abell 383*, Mon. Not. Roy. Astron. Soc., 414, L31
- Richard, J., Kneib, J.-P., Limousin, M., Edge, A., & Jullo, E. 2010: *Abell 370 revisited: refurbished Hubble imaging of the first strong lensing cluster*, Mon. Not. Roy. Astron. Soc., 402, L44
- Riess, A. G., Filippenko, A. V., Challis, P., Clocchiatti, A., Diercks, A., Garnavich, P. M., Gilliland, R. L., Hogan, C. J., Jha, S., Kirshner, R. P., Leibundgut, B., et al. 1998: *Observational Evidence from Supernovae for an Accelerating Universe and a Cosmological Constant*, AJ, 116, 1009

- Riess, A. G., Macri, L., Casertano, S., Sosey, M., Lampeitl, H., Ferguson, H. C., Filippenko, A. V., Jha, S. W., Li, W., Chornock, R., & Sarkar, D. 2009a: *A Redetermination of the Hubble Constant with the Hubble Space Telescope from a Differential Distance Ladder*, ApJ, 699, 539
- Riess, A. G., Macri, L., Li, W., Lampeitl, H., Casertano, S., Ferguson, H. C., Filippenko, A. V., Jha, S. W., Chornock, R., Greenhill, L., Mutchler, M., et al. 2009b: *Cepheid Calibrations of Modern Type Ia Supernovae: Implications for the Hubble Constant*, ApJS, 183, 109
- Rosati, P., Borgani, S., & Norman, C. 2002: *The Evolution of X-ray Clusters of Galaxies*, ARA&A, 40, 539
- Rubin, V. C. & Ford, J. W. K. 1970: *Rotation of the Andromeda Nebula from a Spectroscopic Survey of Emission Regions*, ApJ, 159, 379
- Rusin, D., Kochanek, C. S., Falco, E. E., Keeton, C. R., McLeod, B. A., Impey, C. D., Lehár, J., Muñoz, J. A., Peng, C. Y., & Rix, H.-W. 2003: *The Evolution of a Mass-selected Sample of Early-Type Field Galaxies*, ApJ, 587, 143
- Rybicki, G. B. & Lightman, A. P. 1979, Radiative processes in astrophysics
- Ryden, B. 2003, Introduction to cosmology
- Saha, P. & Williams, L. L. R. 1997: *Non-parametric reconstruction of the galaxy lens in PG 1115+080*, Mon. Not. Roy. Astron. Soc., 292, 148
- Sand, D. J., Treu, T., & Ellis, R. S. 2002: *The Dark Matter Density Profile of the Lensing Cluster MS 2137-23: A Test of the Cold Dark Matter Paradigm*, ApJ, 574, L129
- Sand, D. J., Treu, T., Ellis, R. S., Smith, G. P., & Kneib, J.-P. 2008: *Separating Baryons and Dark Matter in Cluster Cores: A Full Two-dimensional Lensing and Dynamic Analysis of Abell 383 and MS 2137-23*, ApJ, 674, 711
- Sand, D. J., Treu, T., Smith, G. P., & Ellis, R. S. 2004: *The Dark Matter Distribution in the Central Regions of Galaxy Clusters: Implications for Cold Dark Matter*, ApJ, 604, 88
- Sarazin, C. L. 1988, X-ray emission from clusters of galaxies
- Schneider, P. 2003: *Gravitational lensing as a probe of structure*, ArXiv Astrophysics e-prints
- Schneider, P., Ehlers, J., & Falco, E. E. 1992, Gravitational Lenses
- Schrabback, T., Hartlap, J., Joachimi, B., Kilbinger, M., Simon, P., Benabed, K., Bradač, M., Eifler, T., Erben, T., Fassnacht, C. D., High, F. W., et al. 2010: *Evidence of the accelerated expansion of the Universe from weak lensing tomography with COSMOS*, A&A, 516, A63
- Scodreggio, M., Franzetti, P., Garilli, B., Zanichelli, A., Paltani, S., Maccagni, D., Bottini, D., Le Brun, V., Contini, T., Scaramella, R., Adami, C., et al. 2005: *The VVDS Data-Reduction Pipeline: Introducing VIPGI, the VIMOS Interactive Pipeline and Graphical Interface*, PASP, 117, 1284

- Smith, G. P., Kneib, J.-P., Ebeling, H., Czoske, O., & Smail, I. 2001: *A Hubble Space Telescope Lensing Survey of X-Ray Luminous Galaxy Clusters. I. A383*, ApJ, 552, 493
- Smith, G. P., Kneib, J.-P., Smail, I., Mazzotta, P., Ebeling, H., & Czoske, O. 2005: *A Hubble Space Telescope lensing survey of X-ray luminous galaxy clusters - IV. Mass, structure and thermodynamics of cluster cores at $z = 0.2$* , Mon. Not. Roy. Astron. Soc., 359, 417
- Springel, V., White, S. D. M., Jenkins, A., Frenk, C. S., Yoshida, N., Gao, L., Navarro, J., Thacker, R., Croton, D., Helly, J., Peacock, J. A., et al. 2005: *Simulations of the formation, evolution and clustering of galaxies and quasars*, Nat, 435, 629
- Stanford, S. A., Dickinson, M., Postman, M., Ferguson, H. C., Lucas, R. A., Conselice, C. J., Budavári, T., & Somerville, R. 2004: *The Evolution of Early-Type Field Galaxies Selected from a NICMOS Map of the Hubble Deep Field North*, AJ, 127, 131
- Steidel, C. C. 1996: *Normal galaxies at extreme redshifts.*, in Bulletin of the American Astronomical Society, Vol. 28, Bulletin of the American Astronomical Society, 1312
- Steidel, C. C., Giavalisco, M., Dickinson, M., & Adelberger, K. L. 1996a: *Spectroscopy of Lyman Break Galaxies in the Hubble Deep Field*, AJ, 112, 352
- Steidel, C. C., Giavalisco, M., Pettini, M., Dickinson, M., & Adelberger, K. L. 1996b: *Spectroscopic Confirmation of a Population of Normal Star-forming Galaxies at Redshifts $Z > 3$* , ApJ, 462, L17
- Sunyaev, R. A. & Zeldovich, Y. B. 1972: *The Observations of Relic Radiation as a Test of the Nature of X-Ray Radiation from the Clusters of Galaxies*, Comments on Astrophysics and Space Physics, 4, 173
- Suyu, S. H., Auger, M. W., Hilbert, S., Marshall, P. J., Tewes, M., Treu, T., Fassnacht, C. D., Koopmans, L. V. E., Sluse, D., Blandford, R. D., Courbin, F., et al. 2013: *Two Accurate Time-delay Distances from Strong Lensing: Implications for Cosmology*, ApJ, 766, 70
- Suyu, S. H. & Halkola, A. 2010: *The halos of satellite galaxies: the companion of the massive elliptical lens SL2S J08544-0121*, A&A, 524, A94
- Suyu, S. H., Hensel, S. W., McKean, J. P., Fassnacht, C. D., Treu, T., Halkola, A., Norbury, M., Jackson, N., Schneider, P., Thompson, D., Auger, M. W., et al. 2012: *Disentangling Baryons and Dark Matter in the Spiral Gravitational Lens B1933+503*, ApJ, 750, 10
- Suyu, S. H., Marshall, P. J., Auger, M. W., Hilbert, S., Blandford, R. D., Koopmans, L. V. E., Fassnacht, C. D., & Treu, T. 2010: *Dissecting the Gravitational lens B1608+656. II. Precision Measurements of the Hubble Constant, Spatial Curvature, and the Dark Energy Equation of State*, ApJ, 711, 201
- Suyu, S. H., Marshall, P. J., Hobson, M. P., & Blandford, R. D. 2006: *A Bayesian analysis of regularized source inversions in gravitational lensing*, Mon. Not. Roy. Astron. Soc., 371, 983
- Talia, M., Cimatti, A., Mignoli, M., Pozzetti, L., Renzini, A., Kurk, J., & Halliday, C. 2014: *Listening to galaxies tuning at $z \sim 2.5-3.0$: The first strikes of the Hubble fork*, A&A, 562, A113

- Tully, R. B. & Fisher, J. R. 1977: *A new method of determining distances to galaxies*, A&A, 54, 661
- Udalski, A., Szymanski, M., Kaluzny, J., Kubiak, M., Krzemiński, W., Mateo, M., Preston, G. W., & Paczyński, B. 1993: *The optical gravitational lensing experiment. Discovery of the first candidate microlensing event in the direction of the Galactic Bulge*, Acta Astronomica, 43, 289
- Umetsu, K., Medezinski, E., Nonino, M., Merten, J., Postman, M., Meneghetti, M., Donahue, M., Czakon, N., Molino, A., Seitz, S., Gruen, D., et al. 2014: *CLASH: Weak-lensing Shear-and-magnification Analysis of 20 Galaxy Clusters*, ApJ, 795, 163
- Umetsu, K., Medezinski, E., Nonino, M., Merten, J., Zitrin, A., Molino, A., Grillo, C., Carrasco, M., Donahue, M., Mahdavi, A., Coe, D., et al. 2012: *CLASH: Mass Distribution in and around MACS J1206.2-0847 from a Full Cluster Lensing Analysis*, ApJ, 755, 56
- van Paradijs, J. & Bleeker, J. A. M., eds. 1999, Lecture Notes in Physics, Berlin Springer Verlag, Vol. 520, X-Ray Spectroscopy in Astrophysics
- Vanzella, E., Giavalisco, M., Dickinson, M., Cristiani, S., Nonino, M., Kuntschner, H., Popesso, P., Rosati, P., Renzini, A., Stern, D., Cesarsky, C., et al. 2009: *Spectroscopic Observations of Lyman Break Galaxies at Redshifts $\sim 4, 5$, and 6 in the GOODS-South Field*, ApJ, 695, 1163
- Verhamme, A., Schaerer, D., Atek, H., & Tapken, C. 2008: *3D Ly α radiation transfer. III. Constraints on gas and stellar properties of $z \sim 3$ Lyman break galaxies (LBG) and implications for high- z LBGs and Ly α emitters*, A&A, 491, 89
- Vikhlinin, A., Kravtsov, A. V., Burenin, R. A., Ebeling, H., Forman, W. R., Hornstrup, A., Jones, C., Murray, S. S., Nagai, D., Quintana, H., & Voevodkin, A. 2009: *Chandra Cluster Cosmology Project III: Cosmological Parameter Constraints*, ApJ, 692, 1060
- von der Linden, A., Best, P. N., Kauffmann, G., & White, S. D. M. 2007: *How special are brightest group and cluster galaxies?*, Mon. Not. Roy. Astron. Soc., 379, 867
- Wambsganss, J. 2006: *Gravitational Microlensing*, ArXiv Astrophysics e-prints
- Warnick, K., Knebe, A., & Power, C. 2008: *The tidal streams of disrupting subhaloes in cosmological dark matter haloes*, Mon. Not. Roy. Astron. Soc., 385, 1859
- Warren, S. J. & Dye, S. 2003: *Semilinear Gravitational Lens Inversion*, ApJ, 590, 673
- Weinberg, S. 1972, Gravitation and Cosmology: Principles and Applications of the General Theory of Relativity
- Weinberg, S. 2008, Cosmology (Oxford University Press)
- Weller, J., Battye, R. A., & Kneissl, R. 2002: *Constraining Dark Energy with Sunyaev-Zel'dovich Cluster Surveys*, Physical Review Letters, 88, 231301
- Will, C. M. 2014: *The 1919 measurement of the deflection of light*, ArXiv e-prints

- Wu, K. K. S., Lahav, O., & Rees, M. J. 1999: *The large-scale smoothness of the Universe*, Nat, 397, 225
- Zheng, W., Postman, M., Zitrin, A., Moustakas, J., Shu, X., Jouvel, S., Høst, O., Molino, A., Bradley, L., Coe, D., Moustakas, L. A., et al. 2012: *A magnified young galaxy from about 500 million years after the Big Bang*, Nat, 489, 406
- Ziegler, B. L. & Bender, R. 1997: *The Mg(b)-sigma relation of elliptical galaxies at Z of about 0.37*, Mon. Not. Roy. Astron. Soc., 291, 527
- Zitrin, A., Broadhurst, T., Coe, D., Umetsu, K., Postman, M., Benítez, N., Meneghetti, M., Medezinski, E., Jouvel, S., Bradley, L., Koekemoer, A., et al. 2011: *The Cluster Lensing and Supernova Survey with Hubble (CLASH): Strong-lensing Analysis of A383 from 16-band HST/WFC3/ACS Imaging*, ApJ, 742, 117
- Zitrin, A., Broadhurst, T., Umetsu, K., Coe, D., Benítez, N., Ascaso, B., Bradley, L., Ford, H., Jee, J., Medezinski, E., Rephaeli, Y., et al. 2009: *New multiply-lensed galaxies identified in ACS/NIC3 observations of C10024+1654 using an improved mass model*, Mon. Not. Roy. Astron. Soc., 396, 1985
- Zitrin, A., Moustakas, J., Bradley, L., Coe, D., Moustakas, L. A., Postman, M., Shu, X., Zheng, W., Benítez, N., Bouwens, R., Broadhurst, T., et al. 2012a: *CLASH: Discovery of a Bright $z \sim 6.2$ Dwarf Galaxy Quadruply Lensed by MACS J0329.6-0211*, ApJ, 747, L9
- Zitrin, A., Rosati, P., Nonino, M., Grillo, C., Postman, M., Coe, D., Seitz, S., Eichner, T., Broadhurst, T., Jouvel, S., Balestra, I., et al. 2012b: *CLASH: New Multiple Images Constraining the Inner Mass Profile of MACS J1206.2-0847*, ApJ, 749, 97

SED Fitting Results for the $z \sim 6$ quintuple lensed galaxy in RXC J2248

We show here the results of the SED fitting from Sec. 6.7 of the multiple lensed system in greater detail. We concentrate again only on ID2&3 which have the cleanest photometry. Figs. A.1 and A.2 display the results for exponentially increasing ($\tau < 0$) and decreasing ($\tau > 0$) SFRs. Fig. A.3 shows the fitting results with SSP models only, whereas Fig. A.4 displays the results when we perform the SED fit to all models (SSPs and CSPs) combined. The lower panels of Figs. A.1 to A.4 display the best fitting SED and the photometry. The panels in the middle and upper rows show the 2-dimensional likelihood distributions of fitting parameters (Z , τ , model age, A_V), whereas the probability distributions of the mass-to-light ratios (M/L) in the V band are shown in the upper panels. The blue contours in the likelihood distributions outline the 1σ - (solid), 2σ - (dashed), and 3σ (dotted) confidence levels. The filter bands in which the S/N ratio does not exceed 1 (the dropout filters f225w to f775w) are considered upper limits in the SED fit (lower panels).

Figs. A.6 to A.8 show furthermore the probability distributions of the model ages, marginalized over the other fitting parameters. The upper limits of the 2σ interval in age is smallest for the fit with SSP models (Fig. A.7). This is because all stars are assumed to form at the time of formation and therefore the mean stellar age of a SSP is higher than that of a CSP with the same formation redshift observed at the same cosmic time.

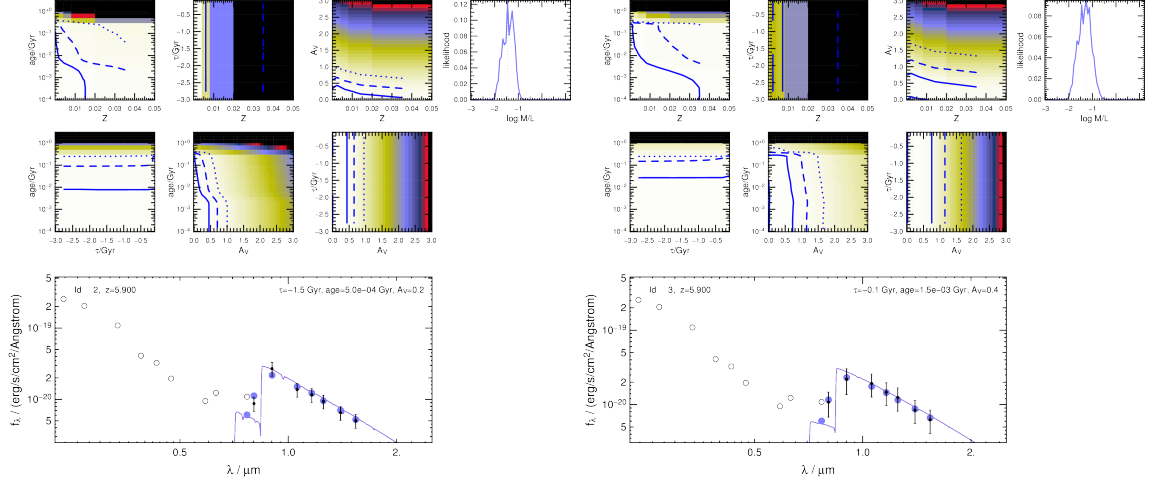


Figure A.1: SED fitting results for ID2&3 and models with negative τ SFRs. The lower panel shows the input photometry and errors with black points. Empty circles denote the fluxes in the dropout filters where the fluxes are considered upper limits. The best fitting model SED is shown in blue and the convolved fluxes in the detection bands are displayed by filled circles. The density plots in the upper panels show the likelihood distributions of the SED fit in two-dimensional parameter spaces. Blue lines denote the 1σ (dotted), 2σ (dashed), and 3σ (solid) confidence levels. Finally, the likelihood distribution of the mass-to-light ratio in the V band is plotted in the upper right panel. The dotted line in this panel denotes the M/L ratio of the best fitting model.

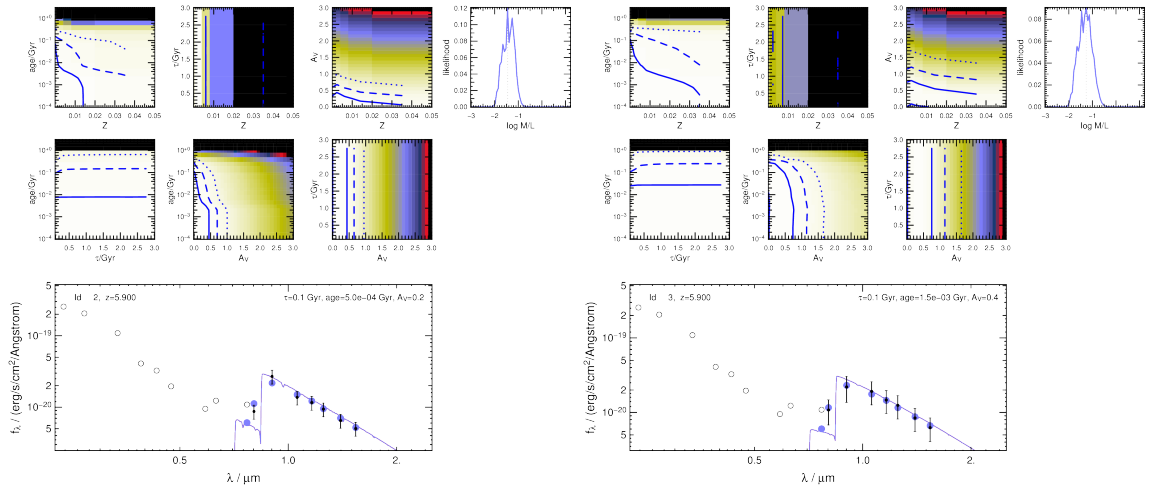


Figure A.2: SED fitting results for ID2&3 and models with positive τ SFRs. For a detailed description on the plot see Fig. A.1.

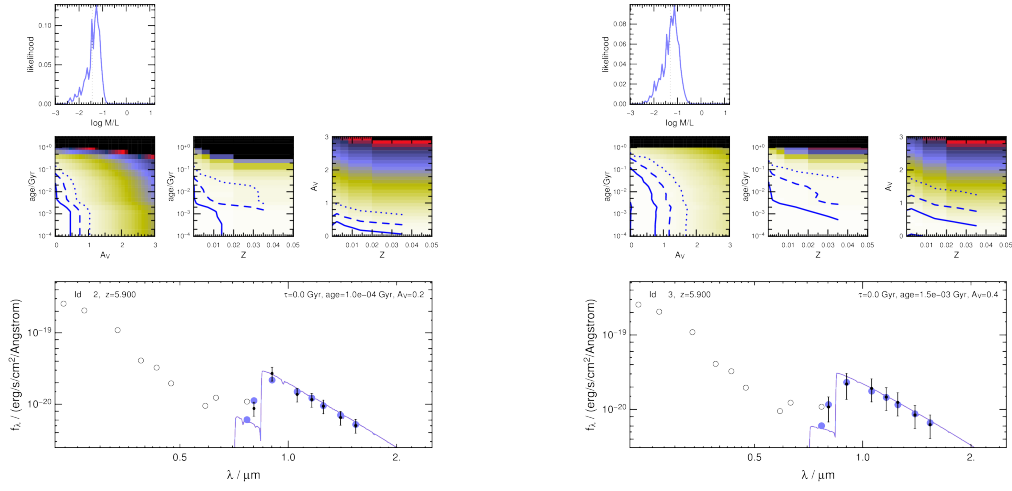


Figure A.3: SED fitting results for ID2&3 and SSP models. For a detailed description on the plot see Fig. A.1.

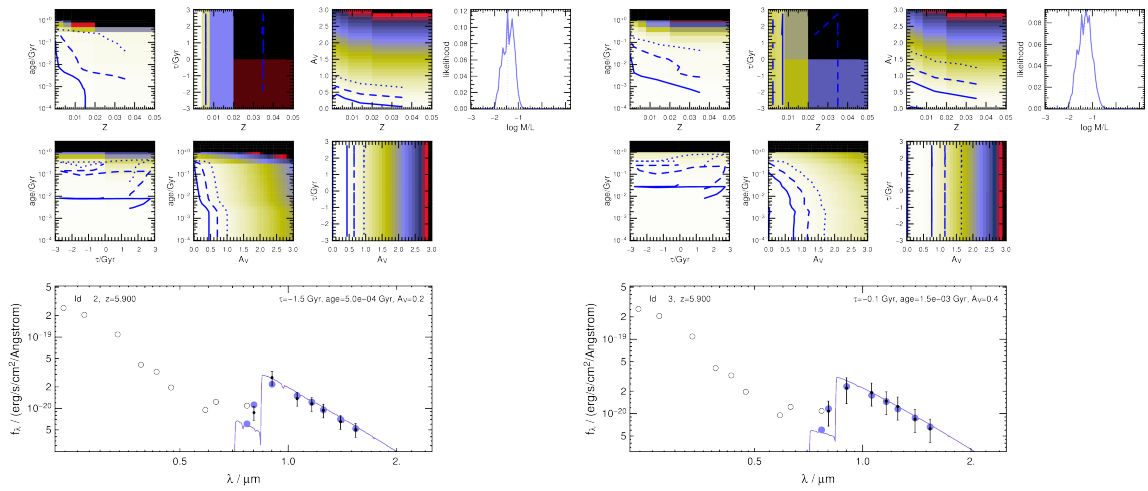


Figure A.4: SED fitting results for ID2&3 and all models (CSPs and SSPs). For a detailed description on the plot see Fig. A.1.

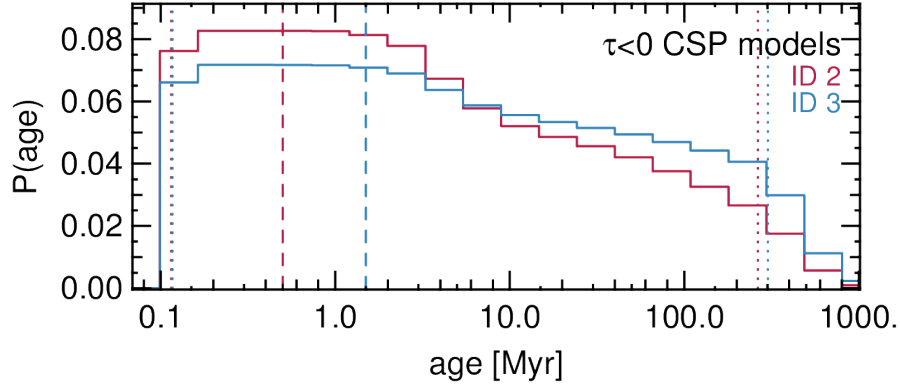


Figure A.5: : PDF of the model age for ID2&3, marginalized over the other fitting parameters for a fit with $\tau < 0$ SFR models. The dashed lines are the ages of the best fitting models. Between the dotted lines the total probability is 95.45% (corresponding to a 2σ confidence interval).

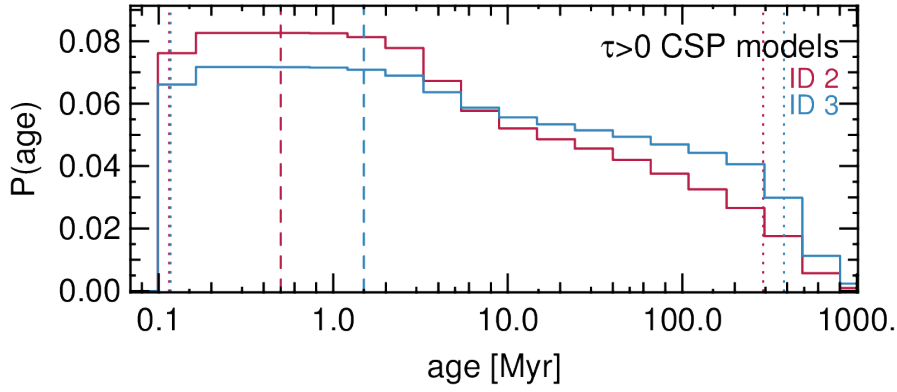


Figure A.6: : PDF of the model age for ID2&3, marginalized over the other fitting parameters for a fit with $\tau > 0$ SFR models. The dashed lines are the ages of the best fitting models. Between the dotted lines the total probability is 95.45% (corresponding to a 2σ confidence interval).

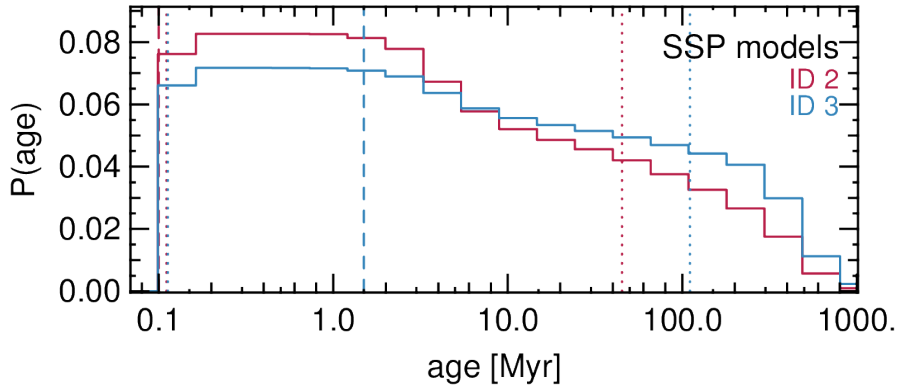


Figure A.7: : PDF of the model age for ID2&3, marginalized over the other fitting parameters for a fit with SSPs only. The dashed lines are the ages of the best fitting models. Between the dotted lines the total probability is 95.45% (corresponding to a 2σ confidence interval). The best fitting age does not necessarily lie within the interval, as is the case for ID2.

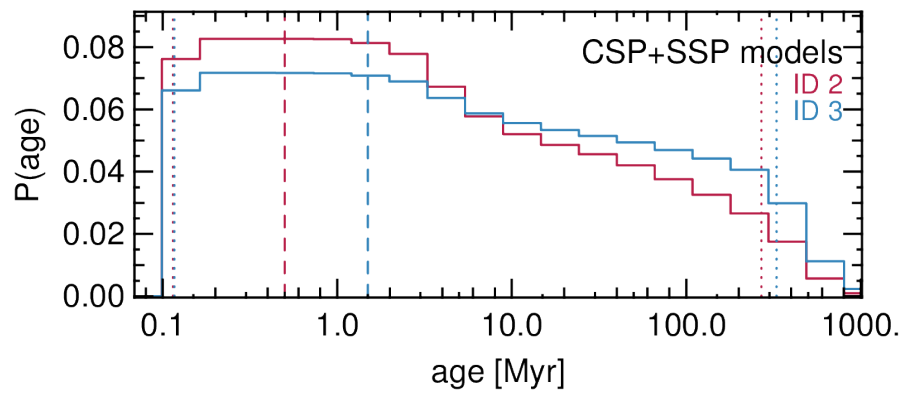


Figure A.8: : PDF of the model age for ID2&3, marginalized over the other fitting parameters where the model set comprises all created model SEDs (SSPs and CSPs). The dashed lines are the ages of the best fitting models. Between the dotted lines the total probability is 95.45 % (corresponding to a 2σ confidence interval).

Publications

Constraining the galaxy mass content in the core of A383 using velocity dispersion measurements for individual cluster members,

Monna A., Seitz S., Zitrin A. et al., 2014arXiv1412.0023M

accepted for publication on MNRAS

CLASH: $z \sim 6$ young galaxy candidate quintuply lensed by the frontier field cluster RXC J2248.7-4431,

Monna A., Seitz S., Greisel N. et al., 2014MNRAS.438.1417M

Searching primeval galaxies through gravitational telescopes,

Monna A. & Covone G., 2012MSAIS..19..258M

Acknowledgments

I would like to thank my supervising professor Ralf Bender, for making this thesis possible. I would also like to thank Stella Seitz. She was my thesis advisor during these years, and I feel to thank her for her guidance. She provided a relevant contribution in defining the guidelines of my work, following my interests and matching them with appealing and promising research projects. Stella was always available for discussions and supported the development of my work with a lot of suggestions and ideas.

I also want to thank all colleagues and friends of our Lensing Group and in particular, Natascha Greisel, Thomas Eichner and Fabrice Brimiouille. They were here when I started the PhD, and were always available when help was needed during these years. It was very nice to share with you part of the time I spent here, both in work-related and extra-work situations.

A particular thanks goes to the people which I feel more as friends, which are Natascha, again, and my office-mates Jesus and Konstantine(a). It was always so great having you around, and you made me feel the USM like a kind of home.

And Ugo, thanks to you too. You know that you made the difference in this last three years. Every single moment was better since you were here on my side.

A row of these acknowledgments goes to our Moona, to save you in my memories of these years.

Dulcis in fundo, il mio pensiero va alla mia famiglia. A mio padre e mia madre, ad Ivana e Stefy, e a Dario. Ed a Nonna. Perché so che avete sempre creduto che io potessi distinguermi, e continuate a farlo, forse più di me. Ed anche se a volte é difficile essere lontana da casa, é casa che mi ha sempre dato la forza di continuare anche nei momenti di tristezza ed abbattimento. E casa siete voi.